Investigating Alternative Green Methods for Carbon Dioxide Utilisation and Carbon Capture and Storage

Katie Joanna Lamb

PhD

University of York

Chemistry

June 2017

Abstract

Reducing carbon dioxide emissions is vital to reducing the effects of global warming. Numerous industrial methods exist, but developing alternative, greener and more energy-efficient methods is essential. Two pieces of work were investigated in this thesis towards developing alternative methods and are presented as two individual chapters, each with their own introduction, results, discussion, conclusion and future work sections. A general introduction to carbon dioxide and the vitality of decreasing carbon dioxide emissions acts as a preface to these chapters and is presented in Chapter 1. Chapter 2 examines promoting Carbon Dioxide Utilisation with new chromium(III) salophen complexes and Chapter 3 investigates a novel electrochemical carbon capture and mineralisation methodology.

A range of chromium(III) salophen complexes were synthesised and were found to catalyse the synthesis of cyclic carbonates from carbon dioxide and terminal or internal epoxides at ambient conditions. The most active catalyst contained methoxy and *tert*-butyl groups on the salicylaldehyde and a bromide counterion, and is one of the most active catalysts in this field. Some of these catalysts were also used to catalyse the synthesis of the oxazolidinone diphenyloxazolidin-2-one from styrene oxide and phenyl isocyanate with successful results.

A new electrochemical method was developed to perform carbon dioxide mineralisation, forming an amorphous aluminium hydroxycarbonate, at ambient conditions. The most energy efficient methods captured carbon with an energy requirement of 231-250 kJ mol^{-1} of carbon dioxide. This methodology worked with sustainable energy and materials, such as solar energy, seawater and "waste" aluminium. The carbon capture and energy efficiency of this methodology however could be improved to promote future developments and industrialisation, but nonetheless provides an interesting and alternative method to capture and mineralise carbon dioxide.

List of Contents

List of Tables

Appendices

List of Figures

Appendices

List of Schemes

Acknowledgements

I would like to give thanks to my supervisor, Professor Michael North, for helping and guiding me throughout my PhD, providing me with the fantastic opportunity to undertake this research, and for his support throughout the whole process. I would also like to thank Dr Alison Parkin for her help and guidance on the electrochemistry based work, and for having the kindness and patience of training and helping me with many of the challenges that can be faced when performing electrochemistry. My new love and appreciation for Origin is all thanks to you. I also thank Professor Robin Perutz for being on my thesis advisory panel, his words of wisdom and guidance during my PhD and for putting me first when it mattered.

Without the support of fellow University of York researchers, experimental officers and technicians many parts of this thesis would have been difficult to obtain. I would therefore like to thank Dr Pedro M. Aguiar, for his solid state NMR analysis expertise, patience and wisdom throughout the electrochemistry project. Dr Roland Kröger, Dr Zhan Wei Scullion, and Dr Konstantinos Chatzipanagis from the Physics Department for Raman and SEM analysis and guidance. Dr James D. Lee from WACL, for loaning the H_2-GC detector and for your help and guidance with gas analysis overall. Paul Elliot for his upmost kindness, support and help with using equipment in the Green Chemistry Centre of Excellence. Karl Heaton and Heather Fish from the Chemistry Department for MS analysis and help with NMR analysis respectively. Professor Ian Fairlamb, for XRF training and guidance. Dr Adrian Whitwood, for powder XRD analysis training and for guidance in crystal growth and analysis. Everyone at the Chemistry Mechanical, Glass and Electronic workshops past and present, for helping with day-to-day problems and especially with building the electrochemical cell.

The day-to-day motivation and support from fellow researchers, friends and colleagues helped me throughout my research. I would therefore like to thank old and present

Friends I have met during my time at York, old and new, since I started my studies in 2009, helped me to not only reach this stage but continue to the end. Past and present members of YSC were always there throughout my time at York, especially Ben Bristow, Martha Cattell and Molly Dennis for all the trips, friendship and support. I would like to thank Dr Jonathan Booth, for helping me relax and come away from work when I needed to, the continuous unconditional support and helping me even when you had to deal with your own problems. His family also deserve my thanks for their kindness.

Last, but by no means least, I would love to give thanks to my family, my Mum, Dad and Brother. Without their unconditional love and support, I would not be where I am today or made it this far in my life.

Author's Declaration

I declare that this thesis is a presentation of original work and I am the sole author. Any data obtained or figures created in conjunction with the work presented in this thesis but was not obtained by me personally is stated clearly in the text, and when required presented in appendices. Part of this work was published as a paper titled "Cr(salophen) Complex Catalyzed Cyclic Carbonate Synthesis at Ambient Temperature And Pressure" in ACS Catalysis in 2016 (DOI: 10.1021/acscatal.6b01386). Only work obtained by me for this publication is described in further detail in the thesis. Any work from this publication that was not obtained by me but mentioned is stated clearly in the text. This work has not been previously presented for an award at this, or any other, University. All sources are acknowledged as references.

Chapter 1: General Introduction

The world is constantly changing. In 2014, the world population reached 7.3 billion and is predicted to keep growing and reach 10 billion by 2050. Furthermore 1.3 billion people, approx. 18% of the population, currently live in less economically developed countries.[1] Not only is the human population ever-increasing, but the demand for a better quality of life is growing. Hence carbon based fuels are becoming more and more essential across the globe.

Modern society in developed countries, and the economic growth of less economically developed countries, is reliant on the combustion of carbonaceous fossil fuels, such as coal, oil and natural gas. The combustion of carbonaceous fossil fuels accounted for 81% of the world's commercial energy supply in 2009.[2] Fossil fuel combustion is performed in car engines for transportation, electrical power plants to produce electricity and as a source of energy for chemical production.[3] Fossil fuel consumption however has had a detrimental effect on the planet. The combustion (and incomplete combustion) of fossil fuels leads to the emission of greenhouse gases (GHGs) into the atmosphere, such as methane, nitrous oxides (NO_x), sulfur oxides (SO_x) and carbon dioxide (CO_2). The global growth in fuel utilisation since the industrial revolution correlates to an increase in GHG emissions, and is believed to have caused a gradual rise in the Earth's mean global temperature.

If GHG emissions are not reduced sufficiently, it is predicted that worldwide disasters will occur, such as drought, increased desertification and animal extinction. This was discussed at the Paris COP21 conference, where world leaders met and agreed to implement and research new methods for decreasing global emissions to prevent a 2 °C rise in global temperature increase by 2050, and thus prevent these disasters from occurring. Carbon dioxide is the biggest contributor to GHG emissions, accounting for approx. 74% and 80% of global and UK GHG emissions respectively in 2014.[4-6] Needless to say, research

towards reducing global CO_2 emissions is a field of huge interest. New and innovative ways of providing energy without wasting or using carbon based feedstocks are also highly desired, as natural fuel based resources are unsustainable and are projected to run out in the future. Oil/natural gas and coal are predicted to last for 10-40 and 300 years respectively.[7,8] Changing energy sources is however a long-term solution. Research is therefore driven towards the more short-term solution of reducing GHG emissions, especially CO_2 emissions, in a useful, economical and sustainable manner.

1.1 Carbon Dioxide

1.1.1 General Properties

Carbon dioxide is a linear triatomic molecule, which exists as a gas at room temperature and pressure, with electronegative oxygen atoms and an electropositive carbon centre (Figure 1).[5] The carbon-oxygen bond of CO_2 has an equilibrium C-O bond length of 116 pm, shorter than a standard saturated single C-O bond (142 pm) and carbonyl double C=O bond (121 pm).[5,9] Carbon dioxide can exist as a supercritical fluid, which is when "*compounds, mixtures or elements are above their critical pressure and temperature but below the pressure required to condense it into a solid*".[10] Carbon dioxide becomes a supercritical fluid at temperatures and pressures above its critical point of 31 °C and 74 bar respectively (Figure 2).[5] Carbon dioxide can also coordinate to metals via numerous modes of coordination,[5,11] including through the central carbon atom, the oxygen atoms and as a bridging ligand (Figure 3).[9,11,12]

$$\delta\text{-} \quad \delta\text{+} \quad \delta\text{-}$$
$$\text{O}=\text{C}=\text{O}$$
$$116 \text{ pm}$$
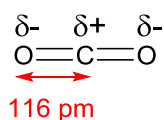
Figure 1: Representative structure of CO_2.[5,9]
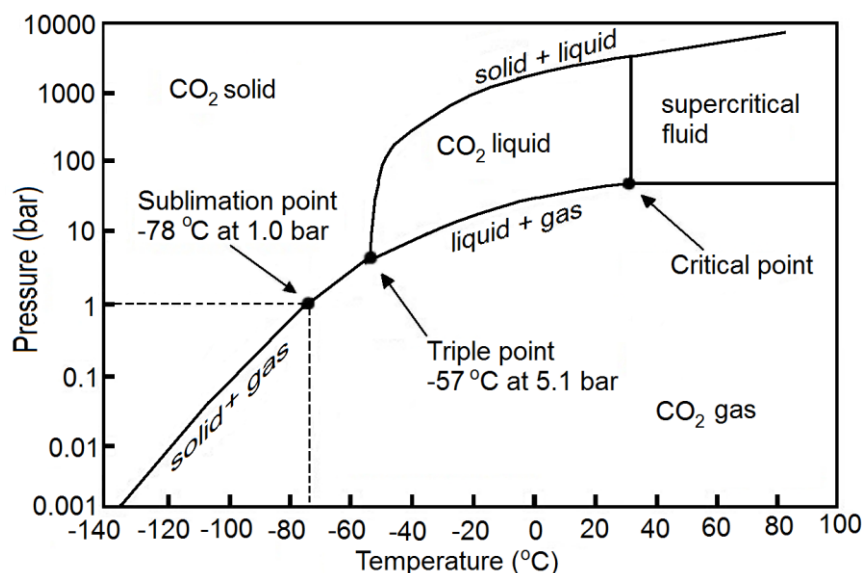
Figure 2: Phase diagram of CO_2 (from *Carbon Dioxide Utilisation: Closing the Carbon Cycle*).[5]
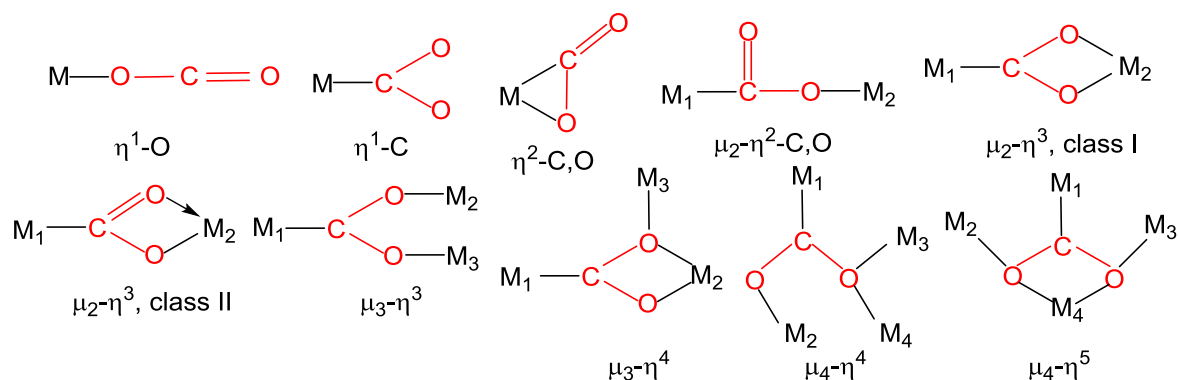
Figure 3: Coordination modes that can be exhibited between CO_2 and metal atoms (M).[9,11,12]

1.1.2 Infrared Properties and Global Warming

Carbon dioxide naturally occurs in the Earth's atmosphere, from sources such as animal and plant respiration, forest fires and volcanic eruptions.[5] Carbon dioxide was vital for the origin of life on Earth, as research has shown that CO_2 was present prior to primitive life on Earth.[13] Carbon dioxide is still important today in the carbon cycle, and plants require CO_2 to grow via photosynthesis, using >750 gigatonnes of CO_2 per year.[14] Carbon dioxide is therefore intrinsic to the formation of life.[15]

The infrared active vibrations of CO_2 are responsible for its GHG properties. When visible light from the sun hits the Earth's surface, it is re-emitted as infrared light. Many gases in the Earth's atmosphere are transparent to infrared light, whereas CO_2 absorbs infrared light and thus traps in heat. This process is vital for the natural regulation of Earth's

temperature, but ever-increasing anthropogenic CO_2 emissions caused by transportation, electricity, and industrial processes (Figure 4 and Figure 5) have offset the natural balance of CO_2.
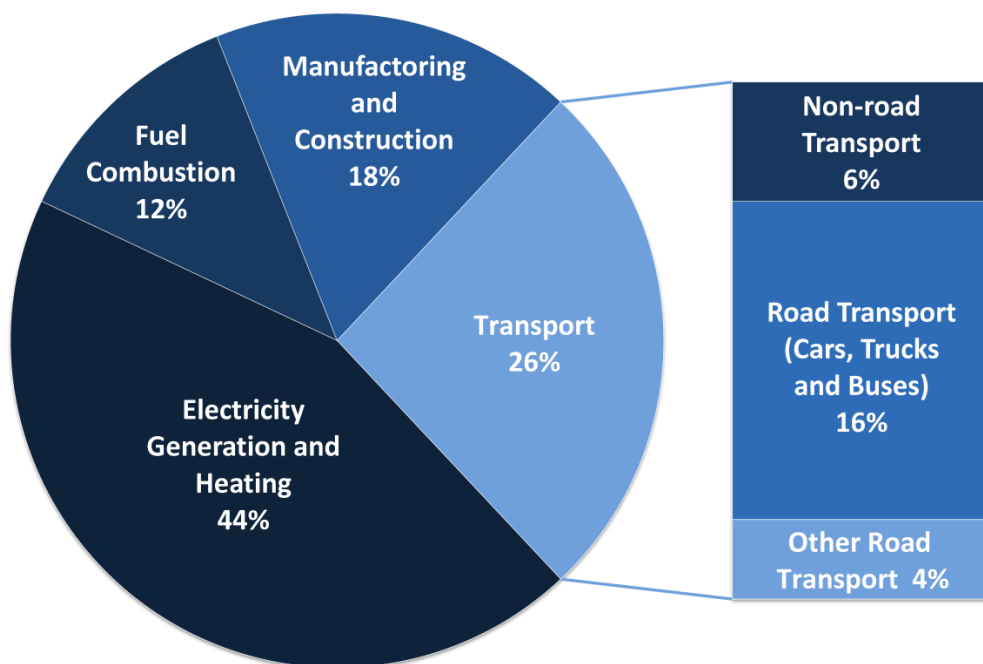
Figure 4: Anthropogenic global CO_2 emissions from different energy sectors in 2014.[14]
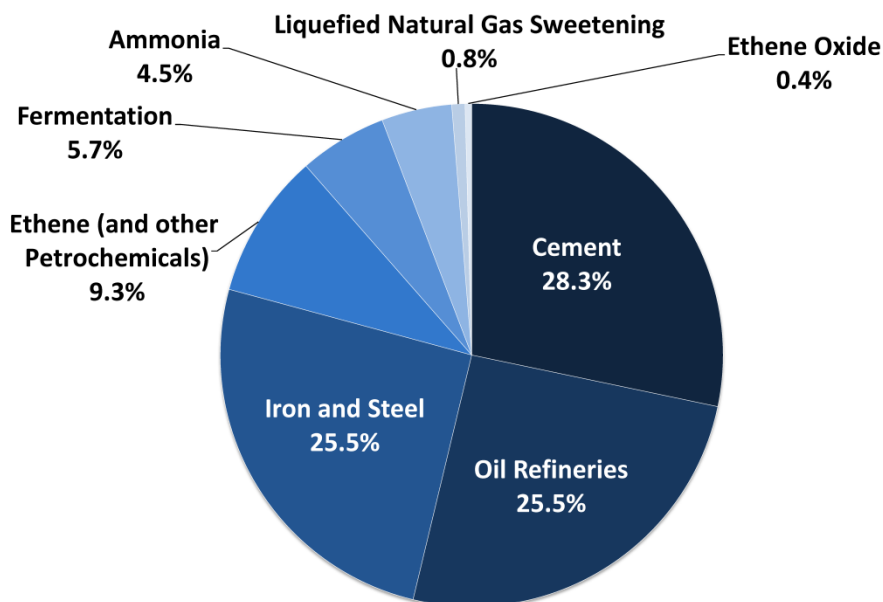
Figure 5: Contribution of industrial processes to global anthropogenic CO_2 emissions in 2014.[14]

Atmospheric CO_2 levels have increased by >43% since the industrial revolution (from 270 ppm to over 400 ppm).[16] As a result, more infrared light and heat is being trapped in the Earth's atmosphere and leading to global warming.[5] Although anthropogenic emissions

only account for approx. 33% of CO_2 in the atmosphere, with approx. 3300-3500 million tonnes of CO_2 emitted per year from industrial processes, Earth cannot cope with this surplus.[14]

1.1.3 Kinetics and Thermodynamics

Carbon dioxide is a very thermodynamically stable molecule, with a standard enthalpy of formation ($\Delta_f H$) of -393 kJ mol^{-1}.[17-19] Despite the extreme negative value of $\Delta_f H$ for CO_2, it can be used in exothermic reactions. For example, the formation of calcium carbonate ($CaCO_3$), which is essential for cement manufacturing,[20] has a negative enthalpy of reaction ($\Delta_r H$) of -178 kJ mol^{-1} (Scheme 1).[5,18]

$$CO_2 + X \longrightarrow Y + Z \qquad \Delta_r H = [\Delta_f H(Y) + \Delta_f H(Z)] - [\Delta_f H(CO_2) + \Delta_f H(X)]$$

$$CO_{2(g)} + CaO_{(s)} \longrightarrow CaCO_{3(s)} \qquad \Delta_r H = -(1207) - (-394 + -635) = -178 \text{ kJ mol}^{-1}$$
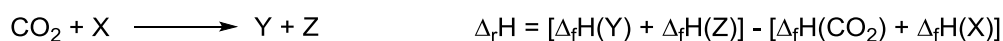
Scheme 1: Synthesis of $CaCO_3$ from CO_2 and CaO and its enthalpy of reaction ($\Delta_r H$).[5,18]

Reaction equilibrium, and thus the Gibbs free energy of the reaction ($\Delta_r G$), enables the spontaneity of a reaction to be determined and is related to the enthalpy and entropy of a reaction ($\Delta_r G = \Delta_r H - T\Delta_r S$). Entropies of CO_2 reactions are usually negative, as the conversion of CO_2 from a gas into a solid or liquid product leads to a decrease in entropy. If reaction entropy however becomes too negative, thus creating a positive $T\Delta_r S$, the Gibbs free energy becomes positive and dictates that the reaction is unfavourable.

Despite the exothermic nature of some CO_2 reactions, not all of them are spontaneous due to high activation energies. For example, the formation of $CaCO_3$ from CO_2 and CaO has a $\Delta_r G$ of -185 kJ mol^{-1} and therefore is favourable in terms of reaction equilibrium. In nature however, this reaction takes years, due to its slow kinetics as a result of the reaction's high activation energy. As a result many CO_2 reactions, such as carbonate formation, require high temperatures and pressures to occur over a realistic timescale. Catalysis is therefore often employed to lower the activation energy, thus enabling reactions to occur at less strenuous, or near ambient, reaction conditions.

Many industrially relevant chemicals can be synthesised with CO_2, but are endothermic reactions with high activation energies, as the Gibbs free energy of formation ($\Delta_f G$) of the products is higher than the starting materials. For these reactions, it is especially challenging for catalysts to lower the activation energy and thus the reaction temperature and pressure. The formation of cyclic carbonates from CO_2 and diols is one such example.

1.2 Reducing Carbon Dioxide Emissions

It is predicted that current CO_2 emissions must be reduced by 50-80% by 2050 to avoid major global catastrophes. More than 3.5 billion tonnes of CO_2 must therefore be captured every year, and global use of fossil fuels must remain at 7 billon tonnes of carbon per year (although they are predicted to rise to 14 billion tonnes of carbon per year by around 2050).[21] Reducing CO_2 emissions however is not a simple task due to the stability of CO_2 (as discussed in "1.1.3 Kinetics and Thermodynamics"). There is therefore no simple "dream" answer to this humongous challenge,[22] and many alternative methods must be used collectively to reach and maintain these goals.[21,23] Although these goals will be demanding, predictions indicate that this task could be possible.

Research since the late 19th Century has illustrated that CO_2 can be used in organic chemistry, and is currently a component of many global industrial processes. Since 2010, industry uses approx. 120 million tonnes of CO_2 per year.[24] Using atmospheric or waste CO_2 gas as a C_1 renewable feedstock, would not only increase the lifetime of non-renewable carbon resources, such as coal, natural gas and fuel, but also reduce anthropogenic CO_2 levels. The abundance of anthropogenic CO_2 emissions also means using waste CO_2 is economically viable.

The two key and most favoured methodologies for currently reducing CO_2 emissions are:

1) Carbon Dioxide Utilisation (CDU), and

2) Carbon (dioxide) Capture and Storage (CCS)

Carbon Dioxide Utilisation (CDU) is when "*CO$_2$ is transformed from waste or recycled CO$_2$ into a useful chemical product.*"[25] Carbon Capture and Storage (CCS) is "*a process consisting of the separation of CO$_2$ from industrial and energy-related sources and* "*long-term isolation from the atmosphere*".[26] Both methods have their advantages and disadvantages, but can effectively reduce CO$_2$ emissions on an industrial scale.[14,27]

1.3 Carbon Dioxide and Green Chemistry

One major issue of performing CDU or CCS is the thermodynamic and kinetic stability of CO$_2$ (as discussed in "1.1.3 Kinetics and Thermodynamics"). In order to utilise or capture CO$_2$, a high input of energy or catalysis is usually required to overcome this stability. However, use of an unsustainable catalyst or a very energy intensive, and thus expensive, process offers no benefit to diminishing CO$_2$ emissions and hinders future industrialisation.[28] Recent emphasis has therefore been given towards green, sustainable and energy efficient CDU and CCS methodology, to ensure CO$_2$ emissions can be depleted without simultaneously impacting the environment. This ties in with the paradigm shift towards promoting greener chemical processes across the globe since the establishment of Green Chemistry in the 1990s.

The principle of Green Chemistry started in 1983, when the World Commission on Environment and Development defined sustainable development as "*meeting the needs of the present generation without compromising the ability of future generations to meet their own needs*".[29] Following this report, research devoted to promoting sustainable, environmentally friendly chemical reactions increased dramatically, and Green Chemistry obtained its official name in the 1990s. The concept of Green Chemistry was summarised into 12 principles by Anastas and Warner in 1998 (Figure 6).[30,31] Carbon dioxide itself has ideal properties for Green Chemistry, as it is non-toxic, extremely abundant, non-flammable, non-explosive and potentially renewable.[5] Supercritical CO$_2$ can be

Figure 6: A simplistic approach to the 12 principles of Green Chemistry (from *ACS*).[31,32]

reached at fairly mild temperatures and pressures, and can be removed by simply evaporating off CO_2 as a gas. Supercritical CO_2 has therefore also been researched extensively as an alternative to organic solvents, and is currently employed in the decaffeination of coffee beans. Nonetheless, the development of new, greener, energy efficient and sustainable CDU and CCS methodology is vital.

1.4 Research Aims and Thesis Outline

Carbon dioxide emissions must be diminished in order to avoid an increase in global warming. The two main ways to reduce CO_2 emissions currently are CDU and CCS, but more greener and more energy efficient methodology must be investigated. This area of research became of interest and two separate pieces of work were pursued (and are presented) in this thesis, one in CDU and the other in CCS, with the common theme of reducing CO_2 emissions using green methodology. Chapter 2 discusses work performed towards promoting CDU, via "The development of chromium(III) salophen complexes for cyclic carbonate and oxazolidinone synthesis", and Chapter 3 describes work in developing an alternative electrochemical based CCS technique, titled "A novel mixed anode approach for electrochemical CO_2 sequestration and mineralisation under near ambient conditions".

Chapter 2: The Development of Chromium(III) Salophen Complexes for Cyclic Carbonate and Oxazolidinone Synthesis

2.1 Introduction

2.1.1 Carbon Dioxide Utilisation (CDU)

The continuous growth in anthropogenic CO_2 emissions is a global issue. One methodology that can reduce CO_2 emissions is the conversion of "waste" CO_2 into useful and valuable products. This process is Carbon Dioxide Utilisation (CDU) and has been known since 1869, when the synthesis of salicylic acid using CO_2 and phenol salts was discovered. Salicylic acid synthesis is now an important industrial use of CO_2, as well as the Solvay process, which makes sodium bicarbonate and carbonate solutions, and the conversion of CO_2 and ammonia into urea.[33] Today, CDU has been thoroughly researched and can form many products (Figure 7).[14,34,35]

Despite the versatility of CO_2 in forming different products via CDU, only a few of these processes have been industrialised (Figure 8). The major hindrance in utilising CO_2 is its thermodynamic stability and kinetic inertness. Only a few CDU reactions are spontaneous, and many require a catalyst to lower the activation energy of the reaction (see "1.1.3 Kinetics and Thermodynamics"). Consequently, very few methods can be employed at near ambient conditions. Developing methods which therefore cannot only perform CDU but proceed using near ambient conditions is highly desired. This research also concerns green chemistry, as the principle of *"Design for Energy Efficiency"* states that *"if possible, synthetic methods should be conducted at ambient temperature and pressure"*.[31] The
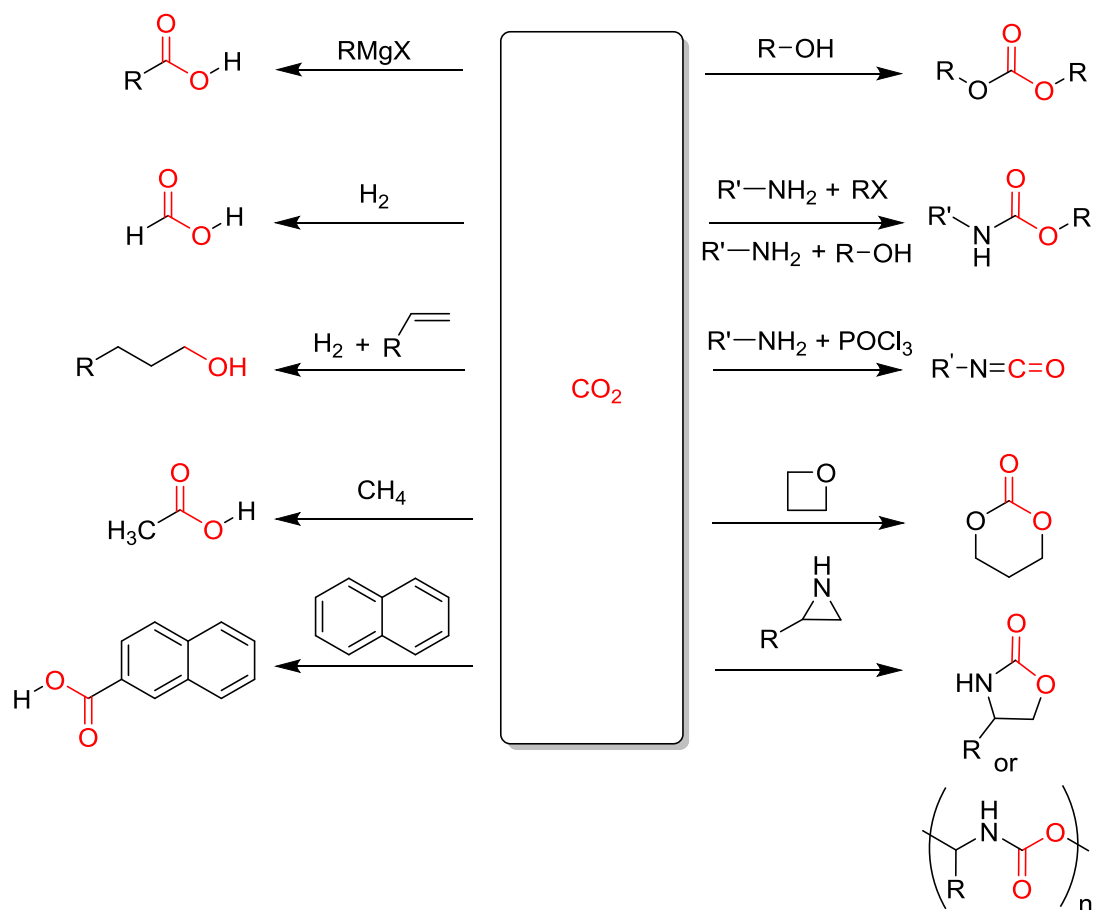
Figure 7: Examples of CDU methodology reported in the literature.[14,34,35]
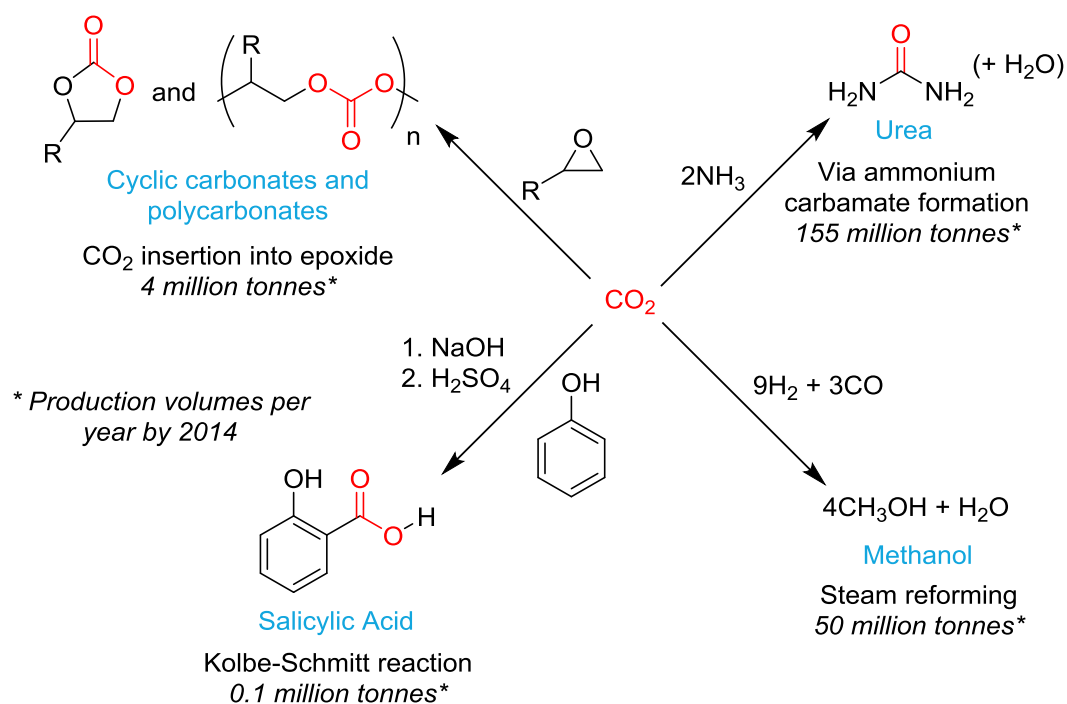
Figure 8: Industrialised CDU methods.[14,24,34,36]

development of CDU using green chemistry principles is vitally important, to ensure CO_2

emissions are reduced without compromising the environment further for future

generations. One important branch of compounds that can be formed via CDU and green methodology are organic carbonates.

2.1.2 Organic Carbonates

Organic carbonates can be classed into three main groups: acyclic, cyclic and polycarbonates (or polymeric carbonates, Figure 9).

Acyclic carbonates

Dimethyl carbonate **1**

Diethyl carbonate **2**

Cyclic carbonates

Ethylene carbonate **3**

Propylene carbonate **4**

Cyclohexene carbonate **5**

Glycerol carbonate **6**

Styrene carbonate **7**

Polycarbonates or polymeric carbonates

Poly(cyclohexene carbonate) **8**

Poly(propylene carbonate) **9**
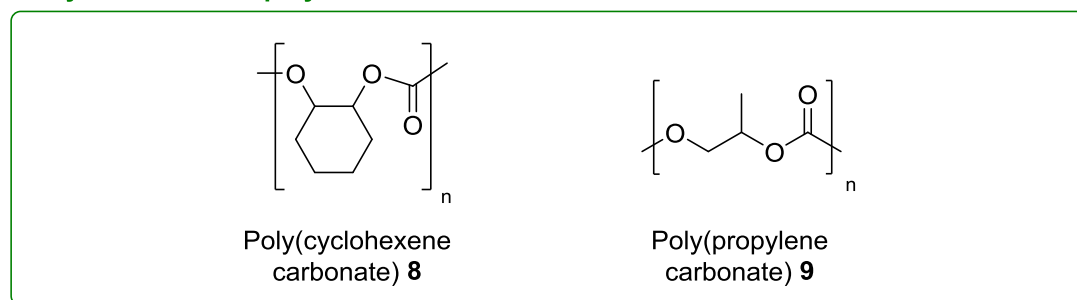
Figure 9: Classes of organic carbonates used in industry today.[37,38]

Organic carbonates were first commercialised in the mid-1950s,[39] and are now industrially important chemicals. Acyclic carbonates, such as dimethyl carbonate (**1**) and diethyl carbonate (**2**), are used as gasoline additives, cosmetic thickeners, pharmaceutical intermediates and pesticides.[9,40,41] Cyclic carbonates can be used in lithium-ion batteries, in paint stripper, act as drug intermediates and precursors for polymer synthesis.[9] They have

been researched as alternative "green" dipolar aprotic solvents, as they are non-toxic, biodegradable and non-corrosive chemicals, making them excellent alternative solvents,[37] for example the Heck reaction.[42] Polycarbonates can be used to make CDs, DVDs and aircraft windows due to their optical transparency and impact resistant properties.[43]

The synthesis of organic carbonates is a huge and growing market. In 2016, worldwide production of organic carbonates reached approx. 7 million tonnes per year, and is predicted to reach 20 million tonnes per year by 2030.[9] Cyclic carbonates are not industrialised to the same scale as acyclic and polycarbonates. For example, the worldwide synthesis of polycarbonates in 2014 reached approx. 4 million tonnes per year, whereas cyclic carbonates only reached 0.1 million tonnes in the same year.[14,44] Research is therefore not only driven towards increasing the industrialisation and commercialisation of cyclic carbonates, but also towards investigating alternative synthetic methods.

2.1.3 Synthesis of Organic Carbonates and Cyclic Carbonates

Traditional Methods

The traditional method of synthesising organic carbonates is now considered extremely inefficient and uneconomical (Scheme 2). This reaction requires the toxic reagent phosgene (**10**), an excess of pyridine and solvents such as benzene which are now considered unsustainable.[45] The reaction also forms HCl, which is not only corrosive but generates extra waste.[24,37,46]
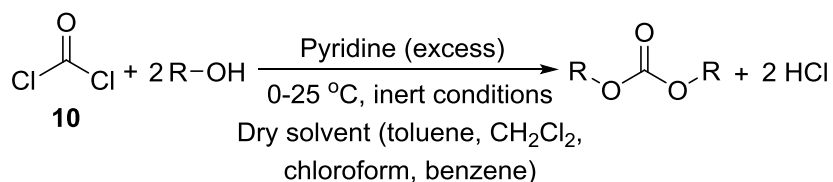
Scheme 2: Example of a traditional cyclic carbonate synthesis route.[9,24]

Today, the traditional method is not ideal from a green chemistry and financial perspective. The currently employed industrial process for (some) cyclic carbonates is greener and more sustainable than the traditional method, and uses tetrabutylammonium bromide

(TBAB, Bu$_4$NBr, **11**), attached to silica. This creates a heterogeneous catalyst which can convert epoxides and CO_2 into cyclic carbonates (Scheme 3). This method however requires high temperatures and pressures and is extremely energy inefficient. There is therefore a lot of interest in performing cyclic carbonate synthesis using ambient reaction conditions (i.e. 25 °C and 1 bar of CO_2) and green chemistry principles.[40]

R = CH$_3$, CH$_2$Cl, Ph, CH$_2$OPh, CH$_2$O^{i}Pr

Scheme 3: Current industrial synthesis for (some) cyclic carbonates.[40]

Modern Methods

Since the 1990s, numerous synthetic routes have been researched towards the formation of five- and six-membered ring cyclic carbonates via CDU (Figure 10).[40,47-50] However, many of these are not "green" synthetic routes. Oxidative cycloaddition (**1**, Figure 10) requires solvents such as DMF and is heavily catalyst dependent, with metals such as niobium or vanadium giving the best conversions.[9,51,52] Alcohols, including diols (**2**, Figure 10) and glycerol, have been successfully employed in cyclic carbonate synthesis.[53-57] The reaction of alcohols and CO_2 however is extremely difficult to drive to high conversions and yields, as this reaction is thermodynamically unfavourable, requires a drying agent to shift the equilibrium towards product formation, and high temperatures and pressures.[58,59]

Using ionic liquids with epoxides (**3**, Figure 10) can successfully form cyclic carbonates using milder conditions than current industrial methods (Scheme 3),[47,60-64] but are expensive, require complicated synthetic routes to make them and add complications to purification and isolation of the cyclic carbonate. Alkyl and metal salts can be used but often require strenuous reaction temperatures and pressures (**5**, Figure 10). The electrochemical formation of cyclic carbonates has also been reported,[65,66] with a notable
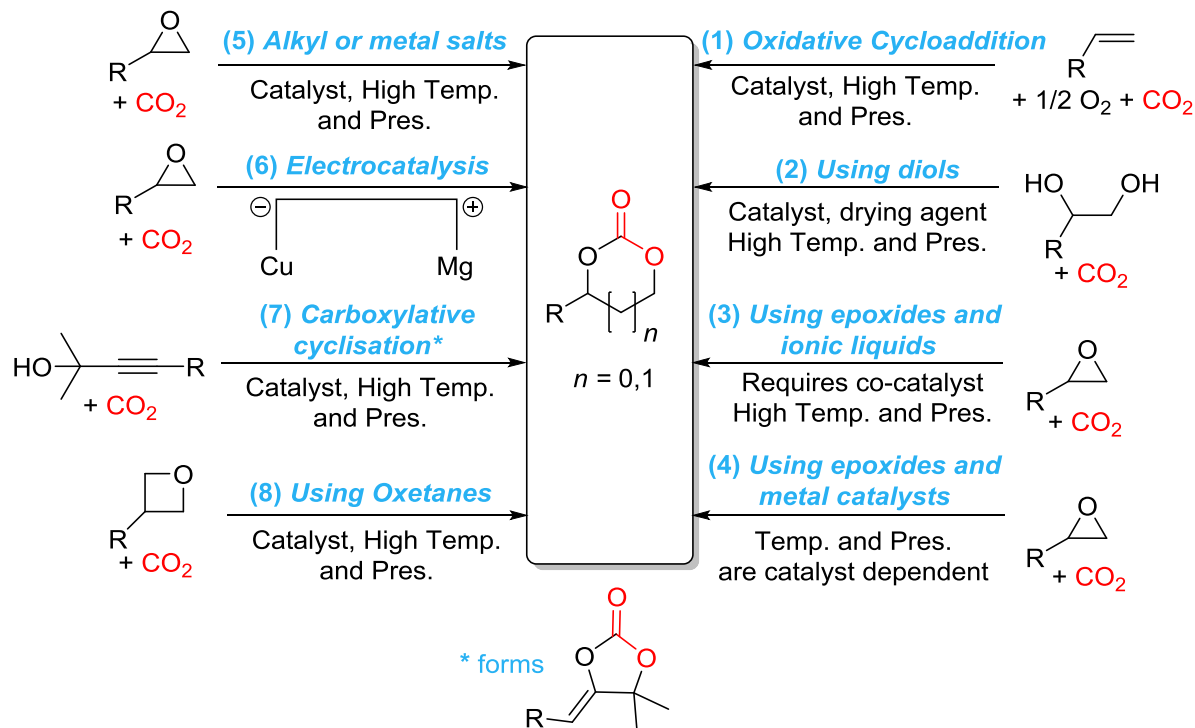
Figure 10: Modern examples of cyclic carbonates synthesis via CDU in the literature.[40,47-50]

example from Buckley *et al.* in 2011 (**6**, Figure 10),[50] who reported the electrochemical conversion of epoxides to cyclic carbonates at atmospheric pressures using a magnesium anode and copper cathode. This method however may not be the best method to pursue in the interest of metal sustainability.

The carboxylative cyclisation (**7**, Figure 10) of propargylic alcohols, to form cyclic carbonates has been reported, but requires a large excess of copper salts and an organic base for effective conversions and is problematic towards product selectivity.[67-69] The transformation of oxetanes (**8**, Figure 10) into six-membered cyclic carbonates has been reported, but the low reactivity of oxetanes hinders this reaction, and the formation of a six-membered cyclic carbonate is thermodynamic unfavourable.[48,70]

Despite the thermodynamic stability of CO_2, some CDU synthetic routes have shown the potential to occur using ambient reaction conditions. One of the most promising and thermodynamically favoured reactions for promoting "green" CDU is CO_2 insertion into epoxides (**4**, Figure 10),[40,48,49,58] as this reaction is 100% atom economical, uses non-toxic reagents and forms innocuous products. The main problem is that very few metal, or

non-metal, based systems operate under ambient conditions. The possibility of creating such desired catalytic systems was intriguing and became of interest in this work.

2.1.4 Carbon Dioxide Insertion into Epoxides

A vast range of synthetic methods have been reported for CO_2 insertion into terminal and internal epoxides to form five-membered cyclic carbonates (Scheme 4).[40,47-49,71]
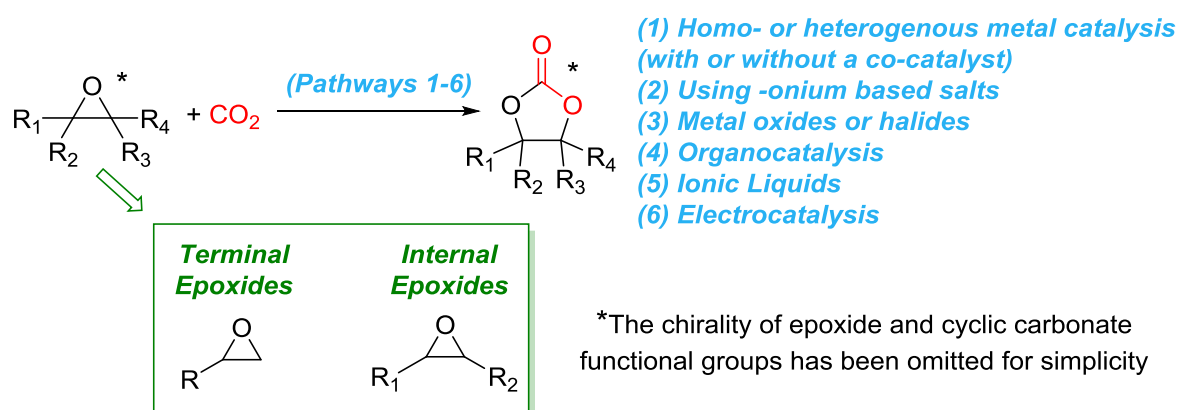
Scheme 4: Reported methods for five-membered cyclic carbonates synthesis via CO_2 insertion into epoxides.[40,47-49,71]

In the interest of investigating simple and near ambient catalytic systems, only notable examples of homogenous metal based systems (Pathway 1, Scheme 4) and the formation of five-membered cyclic carbonates will be considered. Parameters such as reaction temperature, CO_2 pressure, catalytic loading (with respect to the epoxide) and turnover frequency (TOF), defined as "*the number of revolutions of the catalytic cycle per unit time*" will be considered.[72] When possible, the ability of the catalytic system to perform CO_2 insertion into styrene oxide (**12**) to form styrene carbonate (**7**) will be considered to facilitate a fair comparison of catalytic activity.
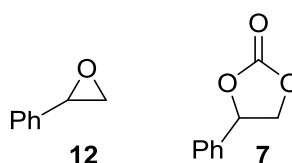
2.1.5 Carbon Dioxide Insertion in the Absence of Metal Complexes

Using -onium Based Salts

In 2002, Caló *et al.* reported the synthesis of cyclic carbonates from epoxide precursors using molten tetrabutylammonium (TBA) salts, such as TBAB (**11**) and tetrabutylammonium iodide (TBAI, Bu_4NI, **13**), 1 bar of CO_2 and temperatures as high as 120 °C (Scheme 5).[73]
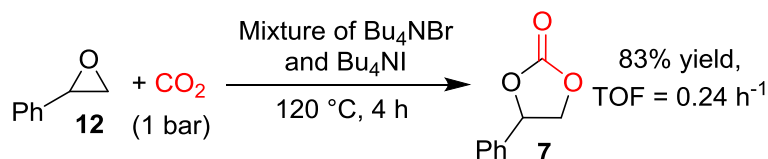
Scheme 5: Caló's method of cyclic carbonate synthesis.[73]

Despite the harsh reaction conditions and the low TOF, acceptable yields were obtained. Caló's work also helped establish the reaction mechanism explaining how TBA salts can catalyse CO_2 insertion into epoxides. The TBA salt halide anion induces a ring-opening of the epoxide via nucleophilic addition, enabling CO_2 to then undergo addition into the alkoxide intermediate, followed by cyclisation to form the cyclic carbonate (Scheme 6).
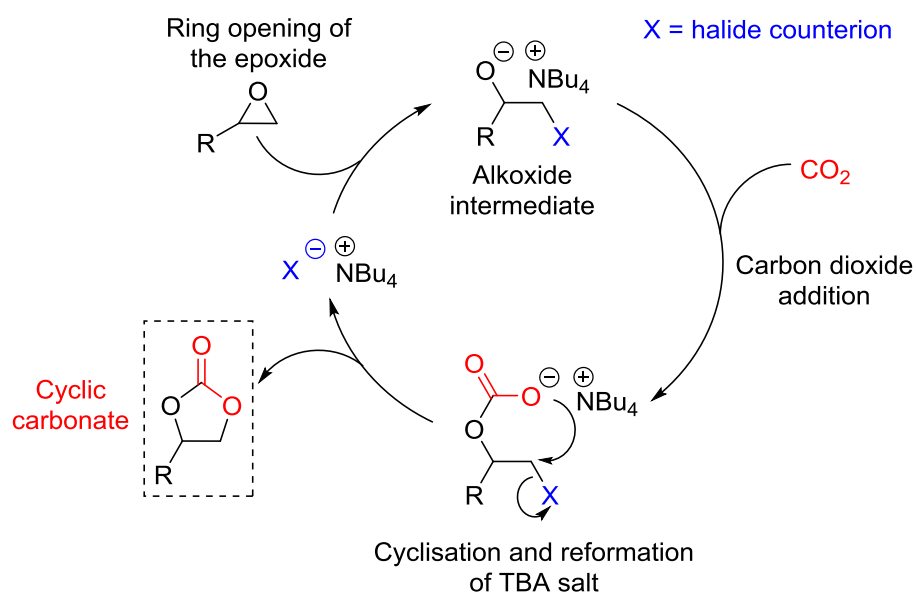
Scheme 6: Formation of cyclic carbonates using epoxides and CO_2 with TBA salts.[39,73]

Caló discovered that the better the nucleophilicity of the halide counterion, the faster the conversion of the epoxide.[73] Caló also hypothesised that the lack of solvent led to greater

reactivity of the nucleophilic anion, as solvation effects are eliminated. Hence it is now common practice to use the epoxide (and cyclic carbonate product) as the reaction solvent (use neat conditions), thereby also creating a greener reaction. Caló's method however required high temperatures and a large catalytic amount (approx. 80%) of the TBA salts, making the definition of TBAB and TBAI as catalysts in this reaction questionable. Numerous -onium based salts have been researched since,[40,74,75] as well as quaternary ammonium hydroxides,[76] however in the absence of a metal complex sufficient conversions are unachievable, especially at near ambient conditions. Many of these compounds are also ineffective at ring-opening sterically hindered internal epoxides.

Other Methodology

Different non-metal based catalytic systems have shown promise in reaching near ambient reaction conditions.[77] Perhaps the most intriguing example was developed by Hirose *et al.* in 2016, who developed the binary system of pyridine based reagents and TBA salts (**14**) to produce cyclic carbonates. No solvent is required and sufficient conversions are achievable using ambient conditions (Scheme 7). High catalytic loadings of **14** are however required for good conversions, the reaction reported low TOFs, and was inefficient at ring-opening internal epoxides.[78]
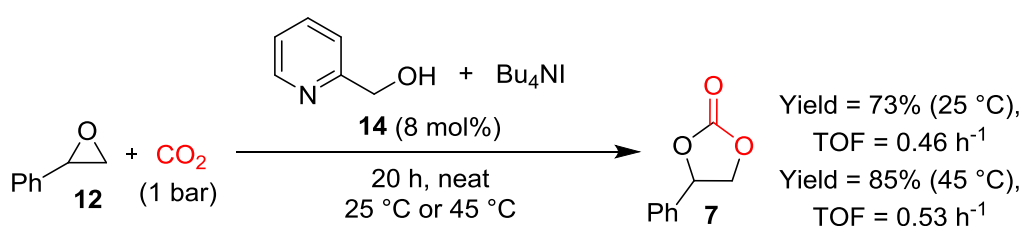
Scheme 7: Hirose's alternative "green" synthesis of cyclic carbonates.[78]

2.1.6 Carbon Dioxide Insertion in the Presence of Metal Complexes

Metal Complex and Co-catalyst: A Co-operative Mechanism

Simple salt based systems require metal complexes in order to obtain sufficient conversions and yields of cyclic carbonates. Interestingly, the majority of metal complexes that have shown promise in cyclic carbonate formation also require co-catalysts to obtain

sufficient yields and conversions. Tetraalkylammonium (TAA) salts, phosphonium salts, and nitrogen based compounds are some examples of co-catalysts reported in the literature (Figure 11).[40,48,79] Only a few metal complexes give sufficient conversions in the absence of a nucleophilic co-catalyst.

TAA salts

N-Methylimidazole
(N-MeIm) **15**

4-(Dimethylamino)pyridine
(DMAP) **16**

Bis(triphenylphosphine)iminium
halides
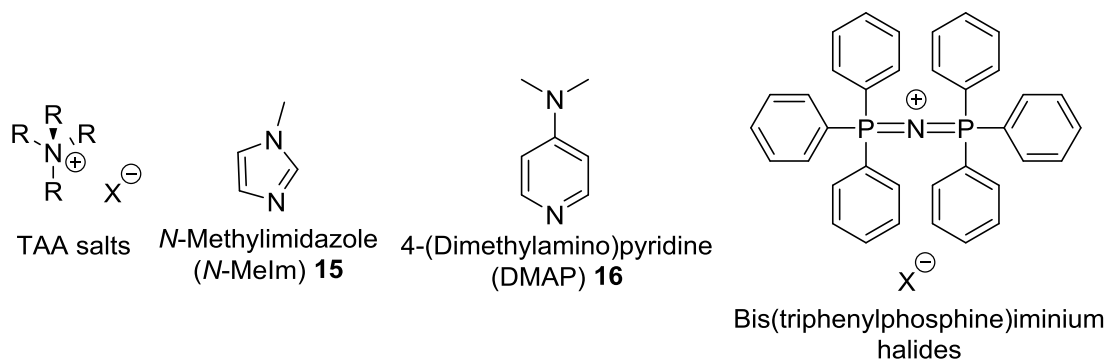
Figure 11: Some co-catalysts that have been used for CO_2 insertion into epoxides.[79]

When a metal catalyst and co-catalyst are used together, a co-operative mechanism occurs. There are four proposed co-operative reaction mechanisms, each of which are dependent on the reaction conditions and catalytic system used.[79] These include:

1) A monometallic mechanism involving one nucleophile (Scheme 8),

2) A monometallic mechanism involving two nucleophiles,

3) A bimetallic mechanism involving two different metal complexes, and

4) A bimetallic mechanism involving two metal centres from the same complex.

In the generally accepted reaction mechanism (Scheme 8), the metal catalyst acts as a Lewis acid, to create an activated epoxide which is then ring-opened by a nucleophile (usually the co-catalyst) to form a metal-alkoxide intermediate. Carbon dioxide addition then forms a metal-carbonate, which can undergo ring closure (or "back-biting") to form the cyclic carbonate, or undergo further CO_2 addition reactions to form polycarbonates.[48,79] Numerous metals have successfully promoted CO_2 insertion into epoxides in the form of metal complexes,[40,48,49,80] such as acen,[81] amino-tris(phenolate),[82] scorpionate,[83,84] salen[85-87] and salophen (or salphen) complexes[88-90] (Figure 12). Only some of the more notable metal complex catalytic systems will be discussed further.
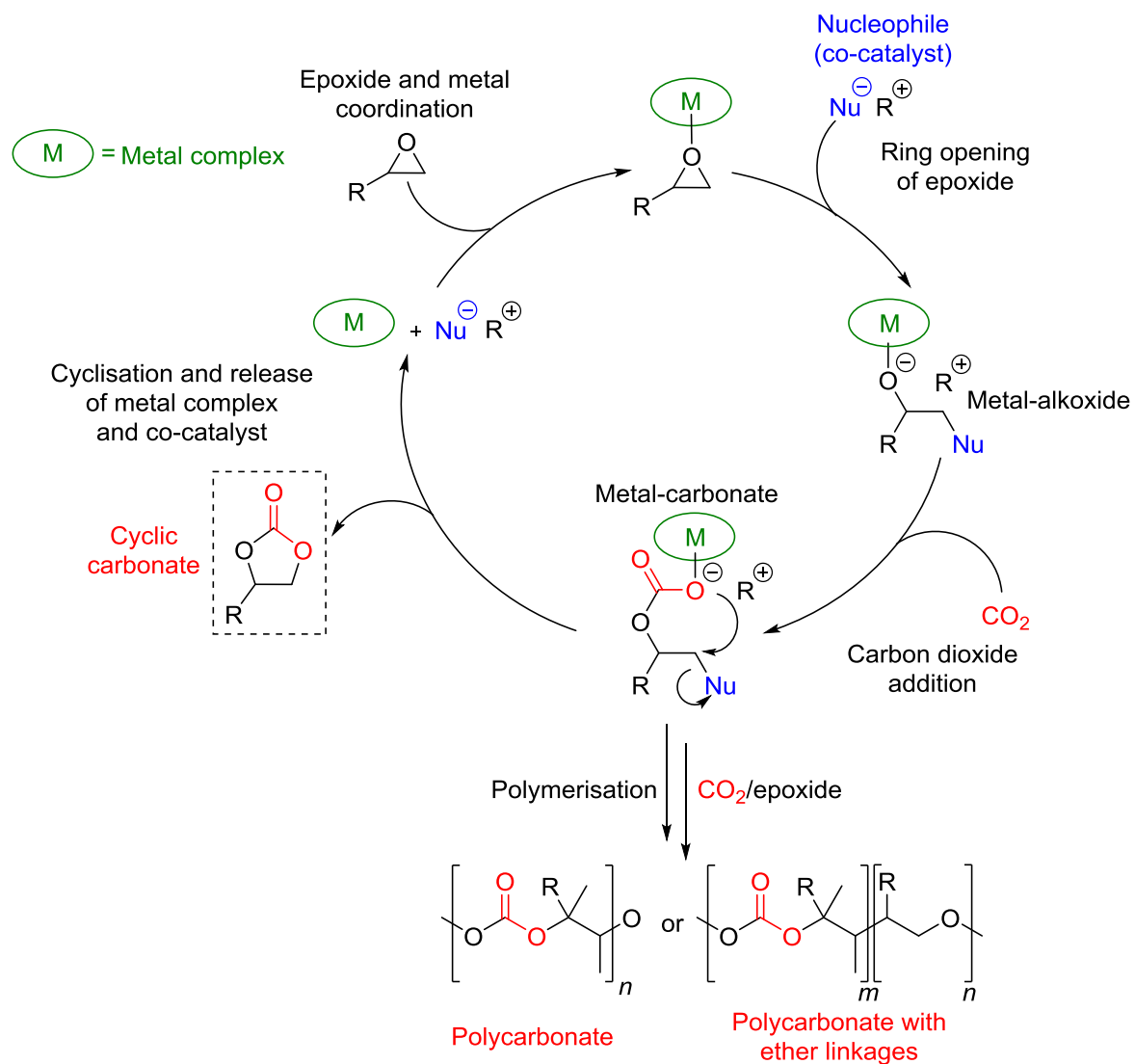
Scheme 8: The generally accepted co-operative mechanism of cyclic carbonate or polycarbonate synthesis, using epoxides and CO_2 with a metal catalyst and co-catalyst.[48,79]
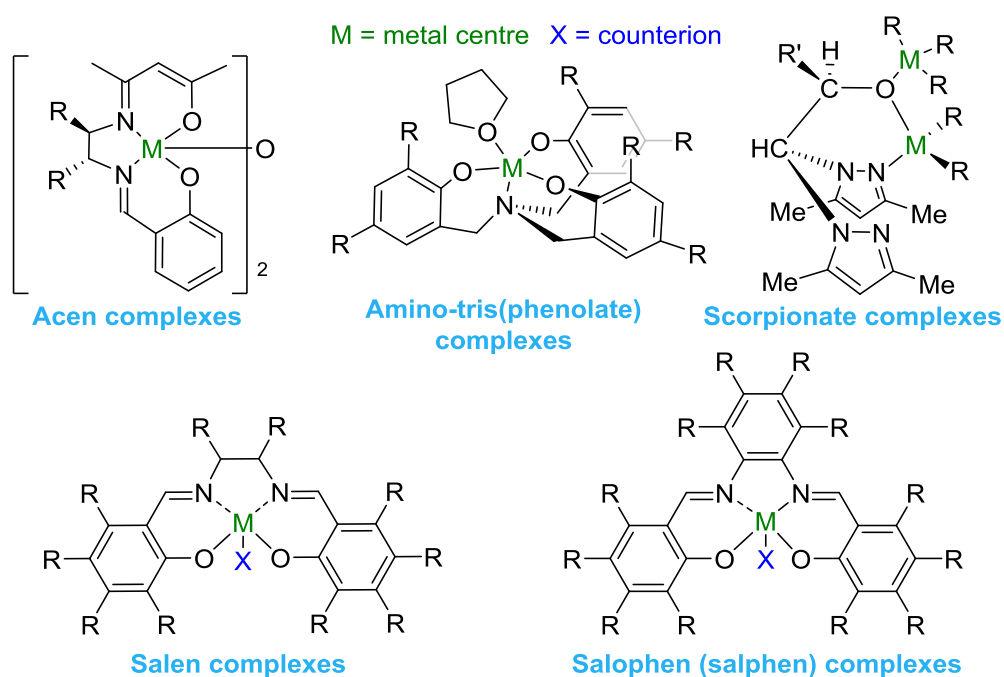
Figure 12: Metal complexes that have been researched for cyclic carbonate formation.

Acen Complexes

In 2011, bimetallic aluminium(acen) complexes **17-19** were developed by Young *et al.*, in the search for more cost-effective and cheaper aluminium complexes for cyclic carbonate synthesis. These complexes along with the co-catalyst TBAB (**11**) were able to convert terminal epoxides into cyclic carbonates with reasonable conversions, using only 2.5 mol% of metal catalyst and co-catalyst under ambient conditions. The potential for further developing the functionality of these complexes is however limited and they remain untested in ring-opening internal epoxides (Scheme 9).[81]
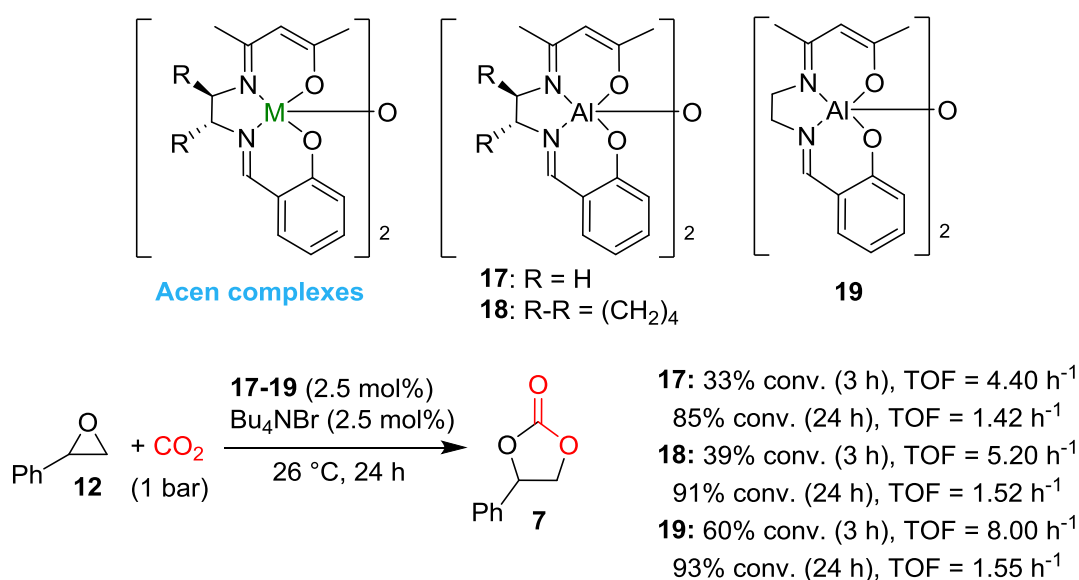
Scheme 9: Cyclic carbonate synthesis with Young's complexes **17**-**19**.[81]

Amino-tris(phenolate) Complexes

In 2014, Kleij *et al.* investigated aluminium amino-tris(phenolate) complexes, and found that complex **20**, with TAA or phosphine based co-catalysts, provided an extremely active catalytic system for terminal epoxides, such as epichlorohydrin (**21**) into 3-chloropropylene carbonate (**22**, Scheme 10).[82] Using only 0.0005 mol% of (**20**) and 0.05 mol% of bis(triphenylphosphine)iminium bromide (PPNBr, **23**) gave good conversions of 1,2-epoxyhexane (**24**) into 1,2-hexylene carbonate (**25**) with a TOF of 36,000 h^{-1}. Achieving good conversions and high TOFs with such low catalytic loadings

was unprecedented. These complexes however require high pressures of CO_2 (10 bar) and sometimes non-ambient temperatures (90 °C) to obtain quicker TOFs.[82]
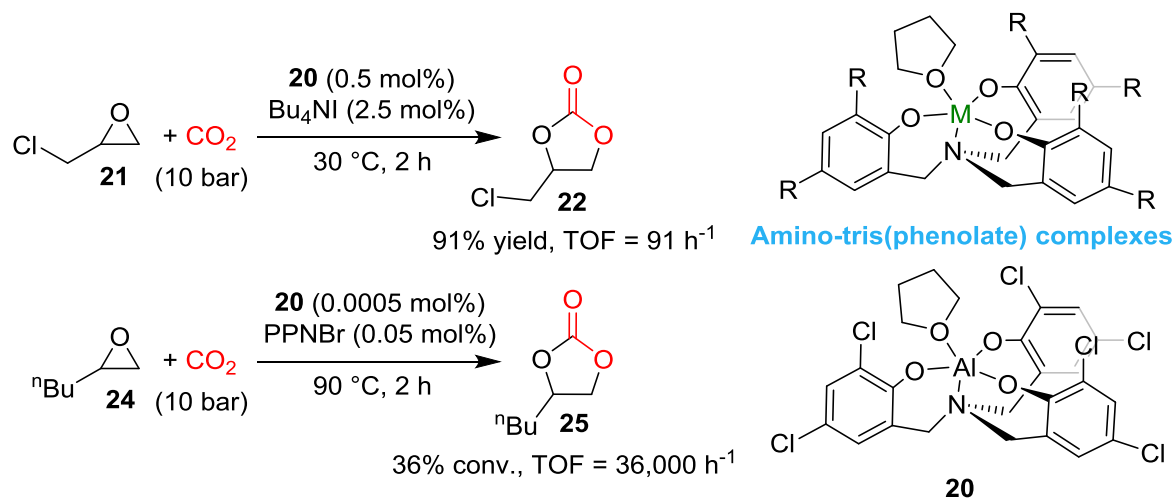
Scheme 10: Cyclic carbonate synthesis with Kleij's complex **20**.[82]

Scorpionate Complexes

Aluminium scorpionate complexes have been researched by North *et al.* since 2012 with **26** (and TBAB, **11**) currently reported as the most active complex.[83,84,91] Complex **26** however required high pressures of CO_2 (10 bar) for good conversions and TOFs, and a moderate catalytic loading of 5 mol% (Scheme 11). Some scorpionate complexes can ring-open internal epoxides but require increased temperatures and pressures of 50 °C and 10 bar of CO_2 respectively and reported low conversions.[84,91]
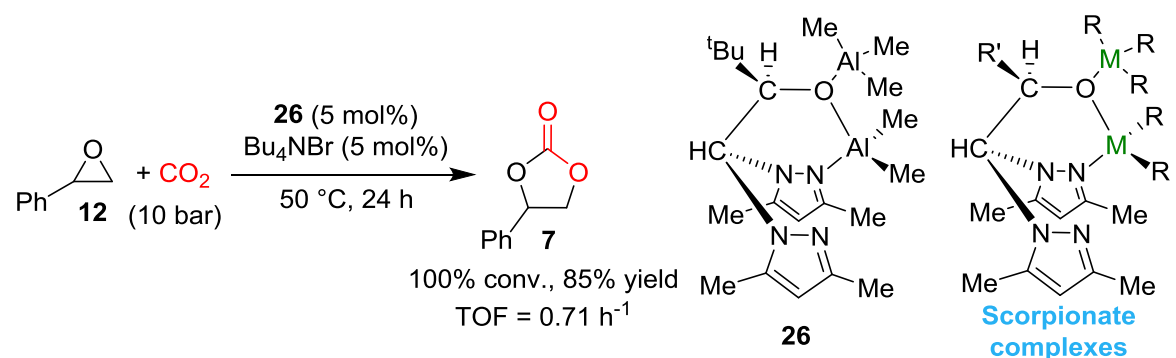
Scheme 11: Cyclic carbonate synthesis with North's complex **26**.[84]

Salen Complexes

Perhaps one of the most widely researched complex structures for cyclic carbonate synthesis are salen complexes (Figure 13). These ligands have been researched extensively

due to three main factors. Firstly, the ligands and complexes require a simple and cost-effective "green" synthesis, by reacting two equivalents of a salicylaldehyde with one equivalent of a chiral or achiral diamine, which can then coordinate to a metal precursor.[92] Secondly, the functional groups present on the salicylaldehyde and diamine backbone can be adjusted with ease, enabling the electronic and steric effects of the complex to be fine-tuned for desired purposes.[40,93] Thirdly, these ligands can coordinate to numerous metals, and thus form various complexes. Only notable chromium(III), cobalt(III) and aluminium(III) complexes are discussed and by no means provide a comprehensive list.
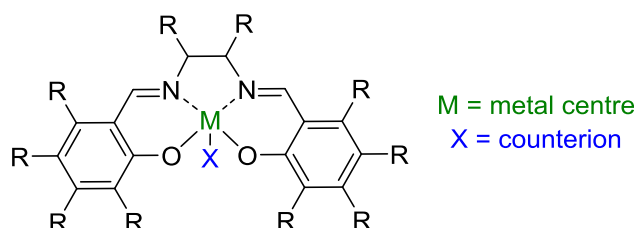
Figure 13: General structure of salen complexes.

Chromium(III) Salen Complexes

In 2001, Paddock *et al.* first highlighted the catalytic ability of chromium(III) salen complexes, illustrating that complexes **27-30**, with 4-(dimethylamino)pyridine (DMAP, **16**), could convert epoxides into cyclic carbonates (Scheme 12). The most active complex was **30**, which Paddock hypothesised was due to less steric crowding round the chromium metal. Complex **30** nevertheless required increased temperatures and pressures (85 °C and 3.5 bar of CO_2) and dichloromethane (DCM) to obtain faster conversions.[94]
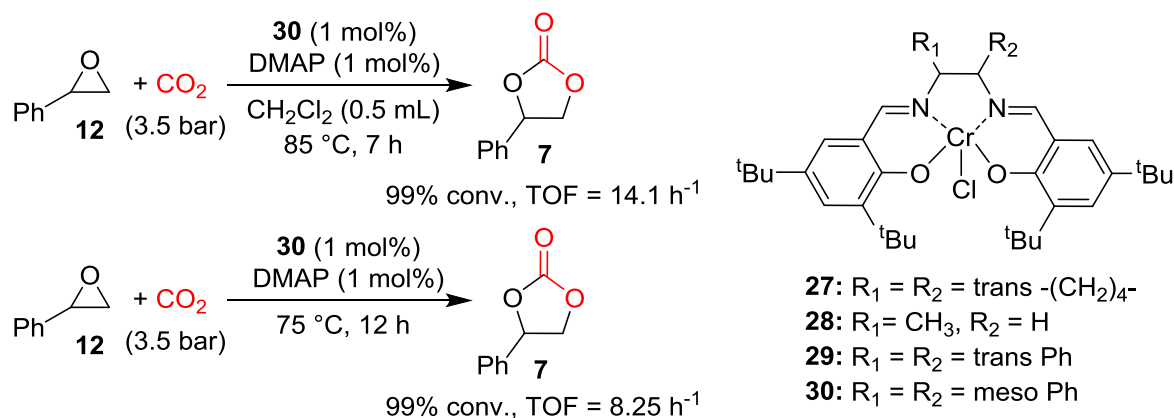
Scheme 12: Cyclic carbonate synthesis using **27-30**.[94]

In 2004, Darensbourg *et al.* synthesised a range of chromium(III) salen complexes to investigate their ability in epoxide polymerisation.[95] Darensbourg determined that the combination of electron donating functional groups on the salicylaldehyde, less bulky diamine backbone functional groups and more nucleophilic metal counterions created more active catalysts. Complex **31** combined with *N*-methylimidazole (*N*-MeIm, **15**) provided the most active catalytic system for converting cyclohexene oxide (**32**) to its corresponding polymer with 99% carbonate linkages. Cyclic carbonate formation however did not occur.
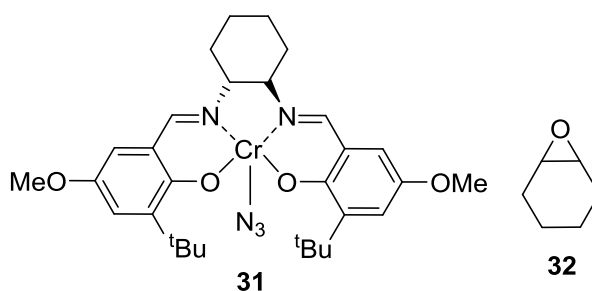
In 2004, Garcia demonstrated that the formation of cyclic carbonates was possible using chromium(III) salen complex **27** an extremely low mol%, co-catalyst *N*-MeIm (**15**) and ionic liquid BMIM-PF$_6$ as a co-solvent (Scheme 13).[96] Garcia's method however required 80 °C and 100 bar of CO$_2$ to obtain a conversion of only 50% for styrene oxide (**12**). Using expensive ionic liquids also decreases the cost-efficiency of this process.
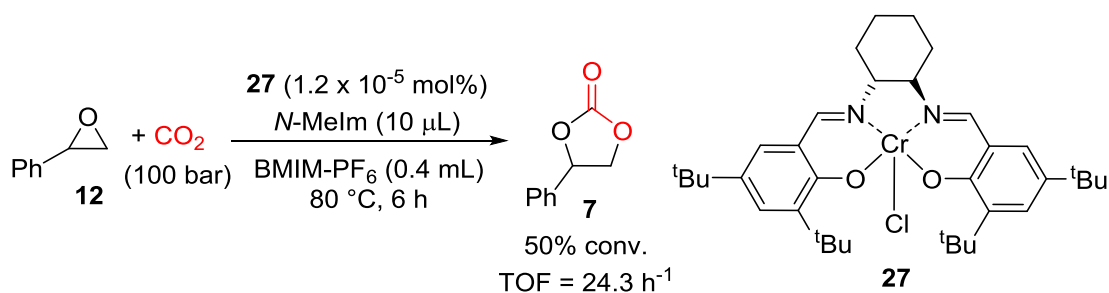
Scheme 13: Cyclic carbonate synthesis using complex **27**.[96]

In 2010, North studied the activity of numerous monometallic salen complexes, including complex **27**, to compare their activity to bimetallic aluminium(III) salen complexes. Complex **27** was found to only achieve 20% conversion of styrene oxide with TBAB (**11**) into styrene carbonate under ambient conditions after 24 h (Scheme 14), and was less active than bimetallic aluminium(III) salen complexes (described later).[87]
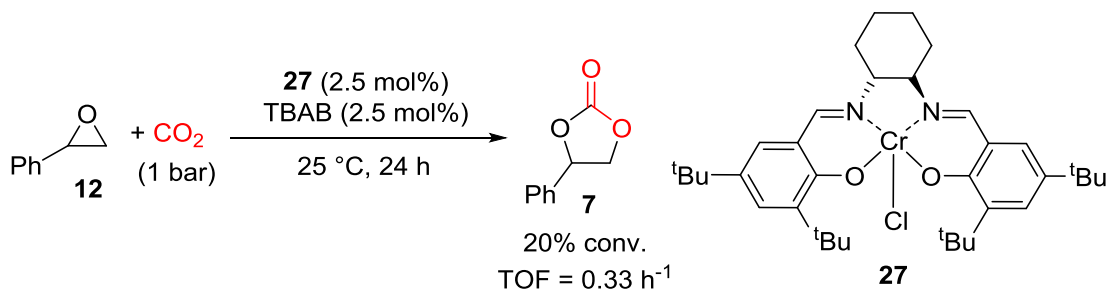
Scheme 14: Cyclic carbonate synthesis using complex **27**.[87]

Cobalt(III) Salen Complexes

Only a few cobalt(III) salen complexes favour cyclic carbonate formation over polycarbonates. In 2004, Paddock *et al.* synthesised a range of extremely active cobalt(III) salen complexes. The most active complex **33**, with DMAP, had a TOF of 65.3 h^{-1} after only 1.5 h (Scheme 15), and could ring-open internal epoxides, but required harsh conditions (100 °C and 20 bar of CO_2).[97] Although only a low catalytic loading of complex **33** was required (1 mol%), the reaction was extremely temperature dependent, required DCM and would form a mixture of poly- and cyclic carbonates at lower temperatures.
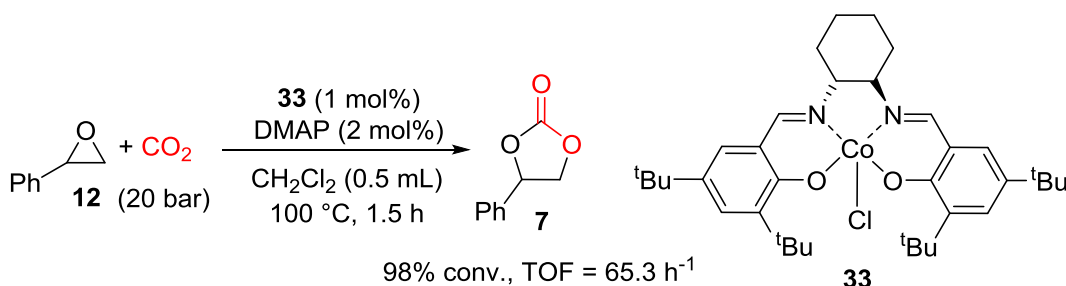
Scheme 15: Cyclic carbonate synthesis using complex **33**.[97]

In 2009, Jing *et al.* synthesised one-component cobalt(III) salen complexes **34** and **35** with phosphonium salts on the phenyl rings (Scheme 16). The most active catalyst **34** could convert propylene oxide (**36**) into propylene carbonate (**4**) with 45% conversion using only 0.1 mol% of catalyst over 20 h without a co-catalyst. The bromide complex **34** was more active than its chloride analogue **35**, illustrating that the more nucleophilic the phosphonium salt anions the more active the catalyst,[98] akin to results determined by Caló and Darensbourg.[73,95] Faster conversions and higher yields have however been reported for other catalytic systems and required a moderate pressure of 6 bar of CO_2.

50
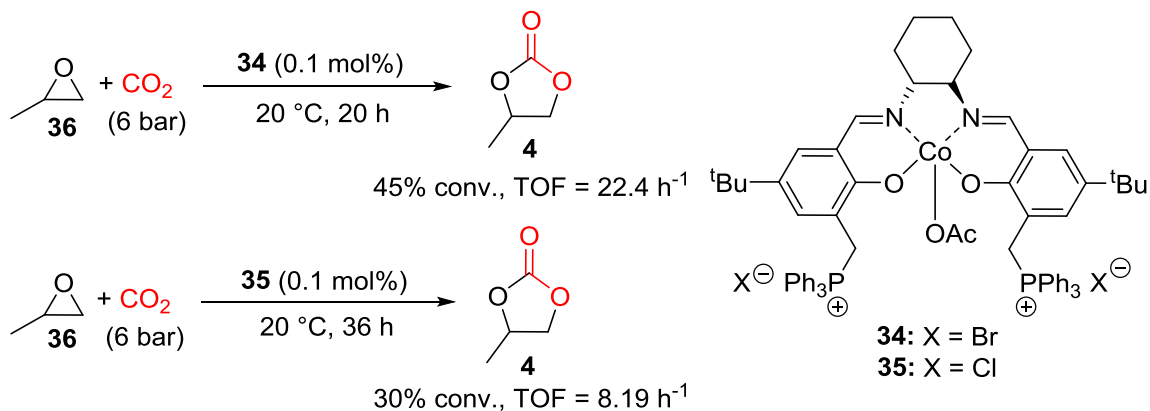
Scheme 16: Cyclic carbonate synthesis using Jing's one-component complexes **35-36**.[98]

Aluminium(III) Salen Complexes

In 2005, Darensbourg *et al.* reported the use of aluminium(III) salen complexes (**37-41**) for the conversion of cyclohexene oxide (**32**) into its polycarbonate derivative. Darensbourg reported that electron deficient groups on the ligand were required to promote the formation of polycarbonates,[99] whereas interestingly chromium(III) salen complexes required electron donating groups to promote the reaction.[95] None of these complexes however were more active than their chromium(III) salen analogues, and cyclic carbonates were only formed as minor products.

37: R_1 = -C_2H_4-, R_2 = ^tBu, R_3 = NO_2, X = Et
38: R_1 = -C_2H_4-, R_2 = ^tBu, R_3 = NO_2, X = Cl
39: R_1 = -C_2H_4-, R_2 = R_3 = Cl, X = Et
40: R_1 = -C_2H_4-, R_2 = H, R_3 = NO_2, X = Et
41: R_1 = -C_2H_4-, R_2 = R_3 = ^tBu, X = Cl
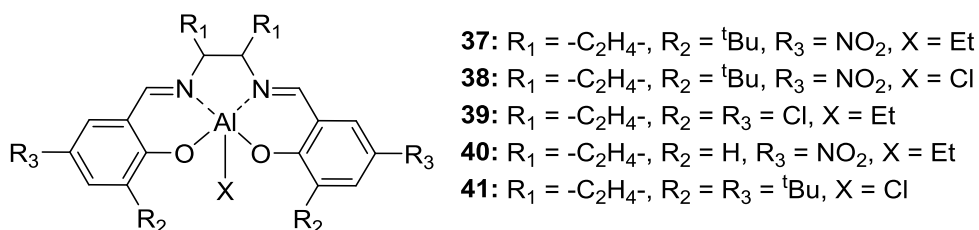
In 2007, North *et al.* reported the synthesis and catalytic ability of bimetallic aluminium(III) salen complexes such as complex **42** and **43**. These complexes could convert many terminal epoxides into cyclic carbonates under 24 h at ambient reaction conditions with high yields (Scheme 17).[87,100] One-component bimetallic complex **43** could be used without a co-catalyst and achieve a TOF of 9.47 h^{-1} after just 3 h at a catalytic loading of 2.5 mol%.[101] Efficient ring-opening of epoxides without the requirement of a co-catalyst is extremely rare for metal complexes, especially at the mild
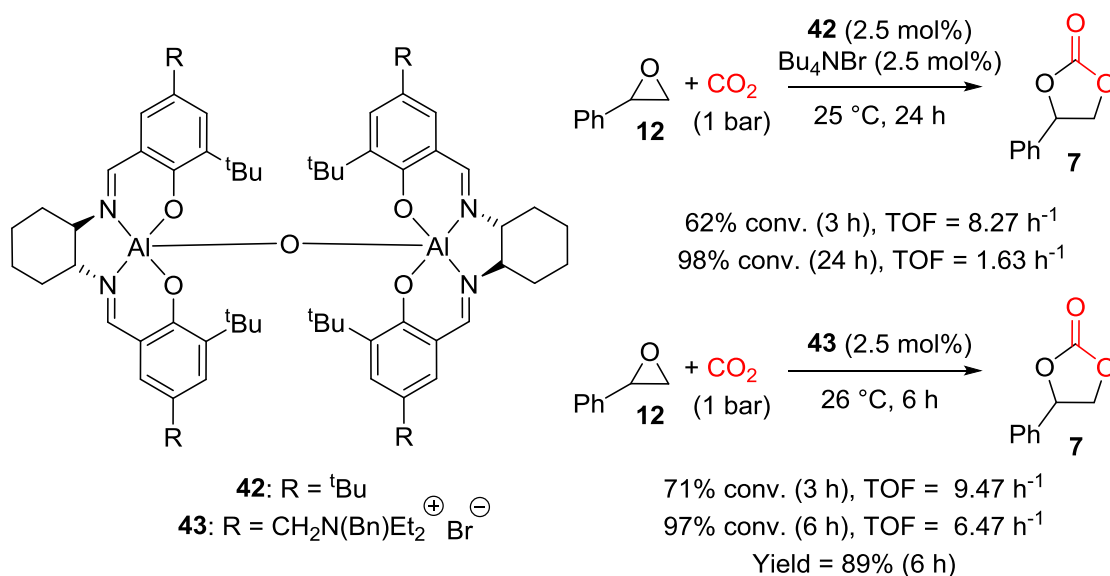
Scheme 17: Cyclic carbonate synthesis using North's bimetallic complex **42** and **43**.[100,101]

Conditions reported with complex **43**.[101] Increased reaction temperatures and pressures (50 °C and 50 bar of CO_2) also enabled complex **42** to ring-open terminal epoxides without the requirement of a co-catalyst.[102] These catalysts are therefore extremely active and can work sufficiently under ambient conditions. Bimetallic aluminium(III) salen complexes however still experience difficulties in ring-opening internal epoxides, especially at near ambient conditions.

Salophen Complexes

Salophen complexes are very similar to salen complexes, with the exception that the diamine backbone is aromatic.[103] Salophen complexes therefore create achiral catalysts, compared to their chiral salen analogues (Figure 14).
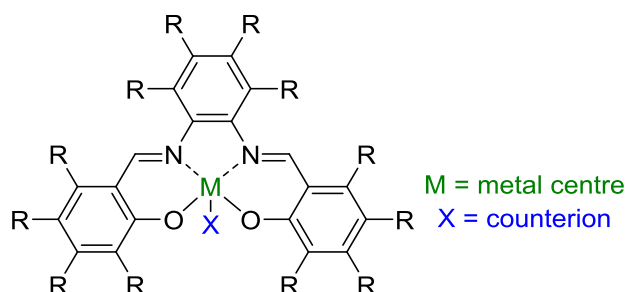
Figure 14: General structure of salophen complexes.

Despite this difference, the electronic and steric properties of salophen complexes can be adjusted in the same manner as salen complexes. Salophen ligands have a π-conjugated

system running throughout the ligand, and therefore contain a more restricted ligand scaffold which can change the Lewis acidity of coordinated metals with ease. Salophen ligands are also more cost-effective than salen complexes.[103] Despite these advantages, only a few salophen complexes have been researched compared to salen complexes. Only notable examples of chromium(III), aluminium(III) and zinc(II) complexes are discussed further and again does not provide a comprehensive list.

Chromium(III) Salophen Complexes

In 2004, Darensbourg *et al.* synthesised numerous chromium complexes to test their efficiency in synthesising cyclic carbonates.[95] A few salophen complexes (44-49) were synthesised, and complexes containing electron donating groups created more active catalysts. Complexes 44-49 however favoured polycarbonate formation, and synthesised cyclic carbonates as minor products.[95]

44: $R_1 = R_2 = H$, X = Cl
45: $R_1 = R_2 = {}^tBu$, X = Cl
46: $R_1 = R_2 = {}^tBu$, X = N_3
47: $R_1 = {}^tBu$, R_2 = OMe, X = Cl
48: $R_1 = {}^tBu$, R_2 = OMe, X = N_3
49: $R_1 = R_2 = Cl$, X = Cl
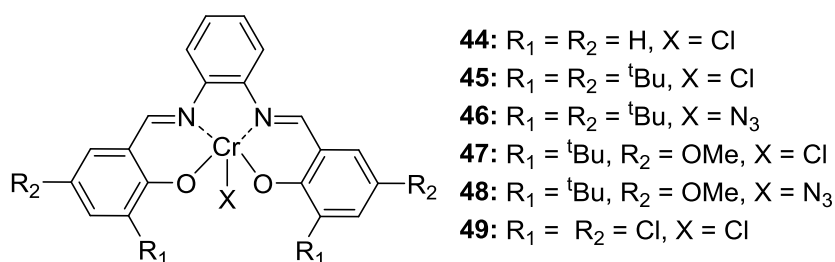
In 2012, Reiger *et al.* synthesised bimetallic complex 50,[104] but could only form polycarbonates, akin to Darensbourg's chromium(III) salophen complexes.[95] Interestingly, Reiger reported that monometallic equivalents of 50 were less active catalysts for polycarbonate formation but synthesised traces of cyclic carbonate. Reiger hypothesised that the smaller and simpler monometallic complexes enabled easier "back-biting" of the epoxide to promote cyclic carbonate formation, due to less steric hindrance around the metal centre.[104]

In 2016, North *et al.* investigated the ability of complex 51 to form cyclic carbonates, and is one of the few metal complexes capable of achieving sufficient conversions at ambient

50
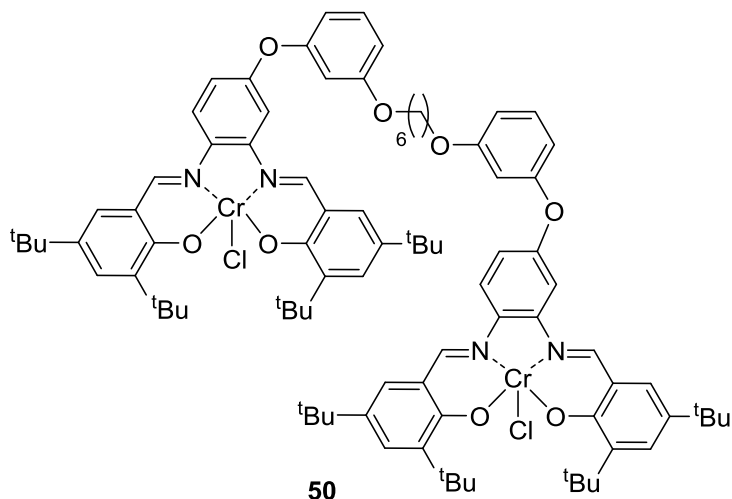
temperatures and pressures for terminal and internal epoxides (Scheme 18). The ability for

chromium complexes to successfully promote cyclic carbonate synthesis from internal

epoxides was unprecedented prior to this research.[105]

51 (1.5 mol%)
PPNBr (1.5 mol%)
25 °C, 24 h

Ph **12** + CO_2 (1 bar) → Ph **7**

41% conv. (3 h), TOF = 9.11 h^{-1}
100% conv. (24 h), TOF = 2.78 h^{-1}

51 (2.5 mol%)
TBAB (2.5 mol%)
25 °C, 24 h

Ph **12** + CO_2 (1 bar) → Ph **7**

63% conv. (3 h), TOF = 8.40 h^{-1}
100% conv. (24 h), TOF = 1.67 h^{-1}
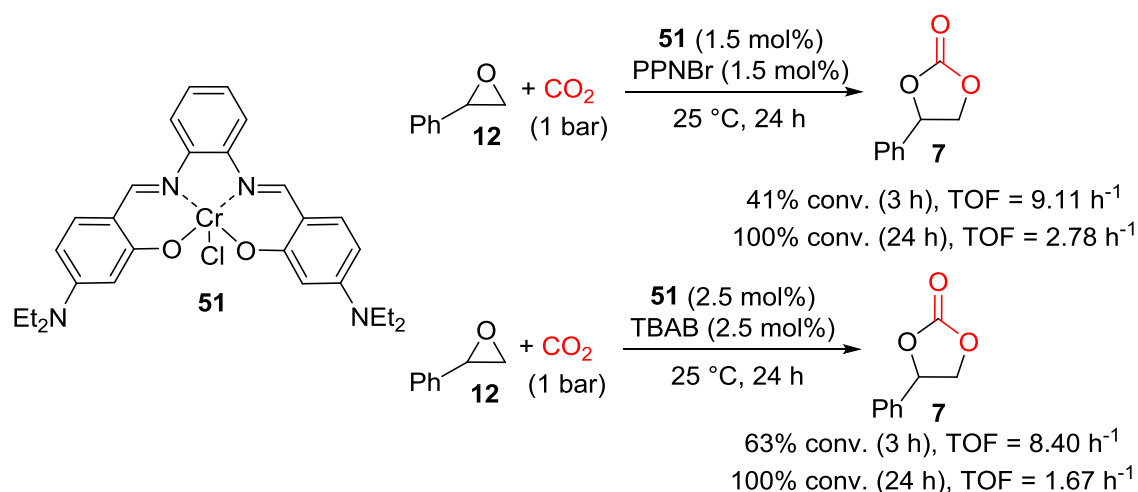
Scheme 18: Cyclic carbonate synthesis using North's complex **51**.[105]

Aluminium(III) Salophen Complexes

In 2005, Darensbourg *et al.* not only studied aluminium(III) salen complexes in cyclic

carbonate formation but also aluminium(III) salophen complexes **52-56**. These complexes

however favoured polycarbonate synthesis, akin to Darensbourg's work on chromium(III)

salophen[95] and aluminium(III) salen complexes,[99] and Reiger's bimetallic chromium(III)

salophen complex.[104]

In 2016, North *et al.* investigated the ability of aluminium(III) salophen complex **57** to

convert terminal and internal epoxides into cyclic carbonates. Complex **57** gave

52: $R_1 = {}^tBu$, $R_2 = NO_2$, X = Et
53: $R_1 = {}^tBu$, $R_2 = NO_2$, X = Cl
54: $R_1 = R_2 = Cl$, X = Et
55: $R_1 = R_2 = H$, X = Cl
56: $R_1 = R_2 = Cl$, X = Cl
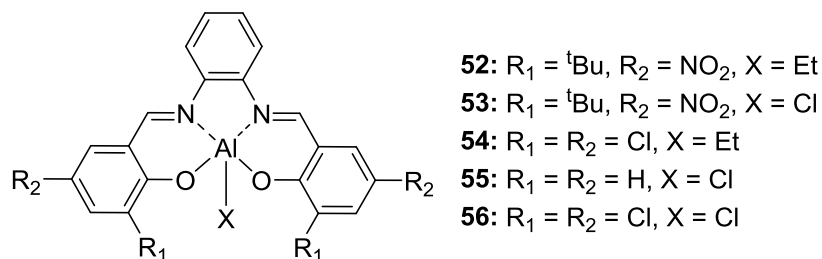
satisfactory conversions for terminal epoxides at ambient conditions (Scheme 19). Complex **57** could also ring-open internal epoxides, but required more strenuous reaction conditions (50 °C and 10 bar of CO_2) for reasonable conversions and was less active than North's chromium(III) salophen complex **51**.[105]

50% conv. (3 h), TOF = 11.1 h^{-1}
100% conv. (24 h), TOF = 2.78 h^{-1}
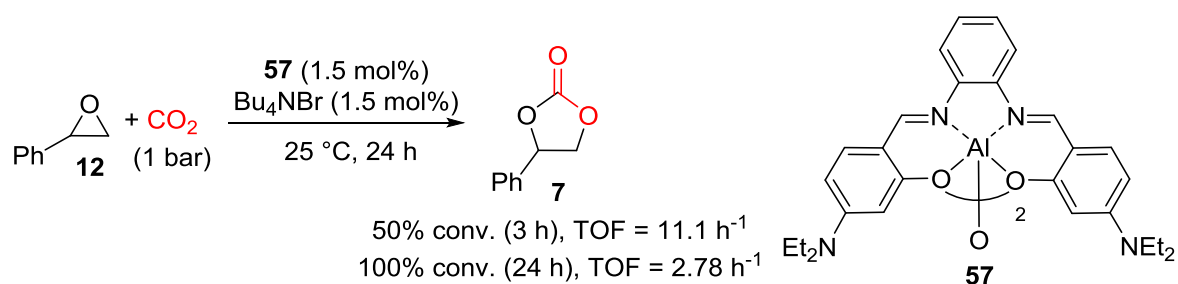
Scheme 19: Cyclic carbonate synthesis using North's complex **57**.[105]

Zinc(II) Salophen Complexes

In 2014, Kleij *et al.* synthesised zinc(II) salophen complexes **58-60**, which were all more active than their zinc(II) salen analogues. The salophen complexes were hypothesised to be more active due to the increased Lewis acidity of the zinc(II) metal cation, as a result of the geometry enforced by the planar ligand system.[90,103,106] Complex **58** was the most active complex in ring-opening terminal epoxides (Scheme 20).[106] Non-ambient temperatures and pressures (80 °C and 10 bar of CO_2) however were used, nor was the ring-opening of internal epoxides investigated.

58: $R_1 = R_2 = {}^tBu$, $R_3 = Me$, X = I
59: $R_1 = {}^tBu$, $R_2 = H$, $R_3 = Me$, X = Br or I
60: $R_1 = R_2 = {}^tBu$, $R_3 = Bn$, X = Br or I

91% conv.
TOF = 10.1 h^{-1}
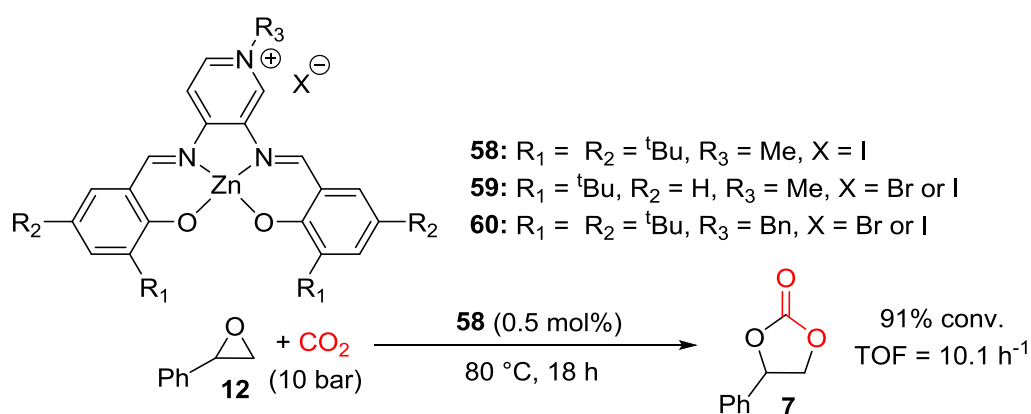
Scheme 20: Cyclic carbonate synthesis using Kleij's complexes **58-60**.[106]

In 2013, Kleij *et al*. synthesised trimetallic zinc(II) salophen complexes **61-62**, which were capable of forming cyclic carbonates from epoxides, such as glycidyl methyl ether (**63**), in high conversions and yields in just 18 h (Scheme 21). Complex **61** could also be recycled up to four times and required no co-catalyst. The nucleophilicity of the zinc counterion was crucial to the catalyst activity, as when the less nucleophilic acetate (OAc) counterion was present (complex **62**) poor conversions were obtained. Unfortunately, non-ambient reaction conditions were required for reasonable conversions. Complexes **61-62** were reusable, unlike their monometallic analogues, but were similar in activity, arguably making the synthesis of complex **61** not economically viable.[89]
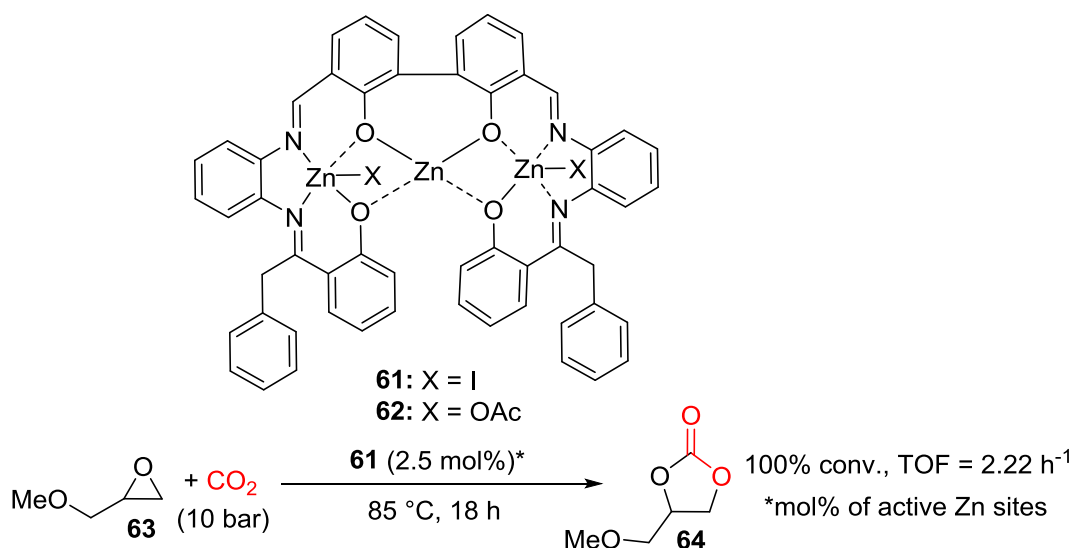
Scheme 21: Cyclic carbonate synthesis using Kleij's trimetallic complexes **61**-**62**.[89]

2.1.7 Summary of Catalytic Systems

All of the non-metal and metal based catalytic systems discussed in "Carbon dioxide insertion into epoxides" are summarised in 4.1 Appendix 1, Section 4.1.1, Table A1 and Table A2 respectively.

2.1.8 General Summary and Project Aims

Organic carbonates are one of many compounds that can be synthesised via CDU, but often require strenuous reaction conditions to manufacture. Developing alternative "green" methodology to perform carbonate synthesis via epoxide conversion at ambient conditions,

to therefore increase their production level, greenness and sustainability is intriguing. Currently, only a handful of complexes in the literature can fulfil this task, with salophen complexes showing great promise. A potential gap in the research was therefore identified and we became interested in investigating alternative salophen complexes to convert epoxides and CO_2 into cyclic carbonates.

As shown by North *et al.*, chromium(III) salophen based complexes have shown promise in forming cyclic carbonates from epoxides and CO_2 at near ambient conditions, and were more effective at ring-opening internal epoxides compared to aluminium(III) salophen complexes.[105] Only one chromium(III) complex **51** however was synthesised and studied in this work. The synthesis of more varied chromium(III) complexes, especially chromium(III) salophen complexes, was therefore of interest. The aim of this work was to synthesise a range of chromium(III) salophen complexes, and to investigate their ability to convert epoxides and CO_2 into cyclic carbonates via CDU using ambient reaction conditions. Reaction conditions such as salophen complex and co-catalyst combinations, and catalytic loading will be varied to find optimum reaction conditions. If the salophen complexes show promise in cyclic carbonate formation, the effect of varying functional groups on the salicylaldehyde, diamine backbone and the chromium metal counterion on epoxide conversion, and thus the electronic and steric effects of chromium(III) salophen complexes, on cyclic carbonate synthesis will be investigated. The optimum catalyst from a range of salophen complexes will also be determined and then screened against numerous terminal and internal epoxides, to study its versatility in cyclic carbonate formation at ambient conditions. Investigations into the mechanism of cyclic carbonate formation will also be performed. Metal complexes that are capable of forming cyclic carbonates can be used for other catalytic processes.[71] The ability of some chromium(III) salophen complexes to also synthesise oxazolidinones from isocyanates and epoxides will also be considered, to investigate the versatility of these complexes in other catalytic applications.

2.2 Results and Discussion Part 1: Cyclic Carbonate Synthesis

2.2.1 Synthesis and Optimisation of Chromium(III) salophen complexes

The steric and electronic effects of salophen complexes can be fine-tuned as desired.[103] A synthesis plan was therefore devised, so that numerous chromium(III) salophen complexes were synthesised with different functional groups present on the salicylaldehyde, diamine backbone, and as the chromium counterion. The steric and electronic effects of these complexes on cyclic carbonate synthesis could therefore be investigated (Figure 15).

Cr15
Catalyst synthesised prior to this study
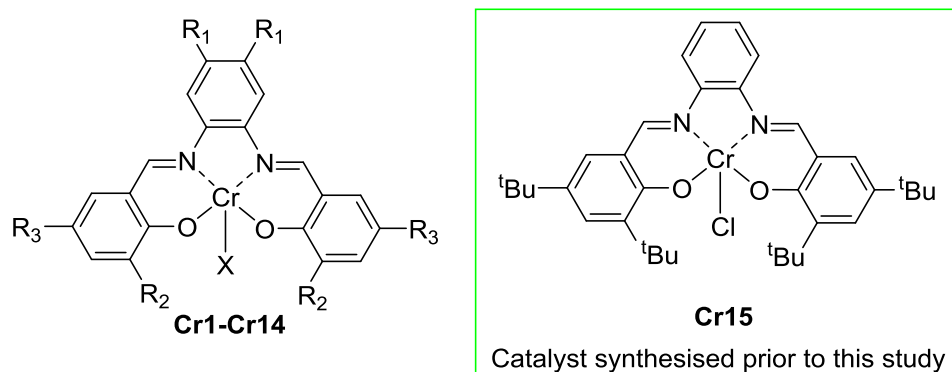
Cr1: R_1 = H, R_2 = R_3 = H, X = Cl; **Cr2**: R_1 = H, R_2 = ^{t}Bu, R_3 = H, X = Cl;
Cr3: R_1 = H, R_2 = H, R_3 = ^{t}Bu, X = Cl; **Cr4**: R_1 = H, R_2 = ^{t}Bu, R_3 = OMe, X = Cl;
Cr5: R_1 = H, R_2 = ^{t}Bu, R_3 = NO_2, X = Cl; **Cr6**: R_1 = Me, R_2 = R_3 = H, X = Cl;
Cr7: R_1 = Cl, R_2 = R_3 = H, X = Cl; **Cr8**: R_1 = -(CH)$_4$-, R_2 = R_3 = H, X = Cl;
Cr9: R_1 = Cl, R_2 = ^{t}Bu, R_3 = H, X = Cl; **Cr10**: R_1 = Cl, R_2 = ^{t}Bu, R_3 = OMe, X = Cl;
Cr11: R_1 = H, R_2 = ^{t}Bu, R_3 = OMe, X = Br; **Cr12**: R_1 = H, R_2 = ^{t}Bu, R_3 = OMe, X = I;
Cr13: R_1 = H, R_2 = ^{t}Bu, R_3 = OMe, X = OAc; **Cr14:** R_1 = H, R_2 = ^{t}Bu, R_3 = OMe, X = OTs

Figure 15: Catalysts synthesised in this study (see "2.4 Experimental" for full details).

A plan to optimise the chromium(III) salophen catalysts for cyclic carbonate synthesis was also devised (Steps 1-4, Figure 16, Scheme 22, Scheme 23 and Figure 17 respectively).

Step 1

Co-catalyst:
65: Bu$_4$NF
66: Bu$_4$NCl
11: Bu$_4$NBr
13: Bu$_4$NI
67: PPNCl
23: PPNBr
16: DMAP
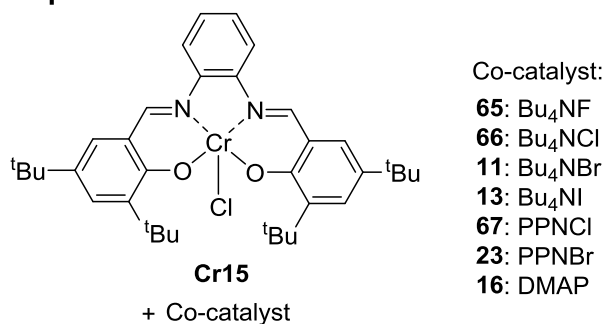
Cr15
+ Co-catalyst

(a) Test catalyst **Cr15** with different co-catalysts to find the most active co-catalyst.
(b) Screen most active combination against different epoxides.

Figure 16: Co-catalyst optimisation and epoxide screening (Step 1).

Step 2
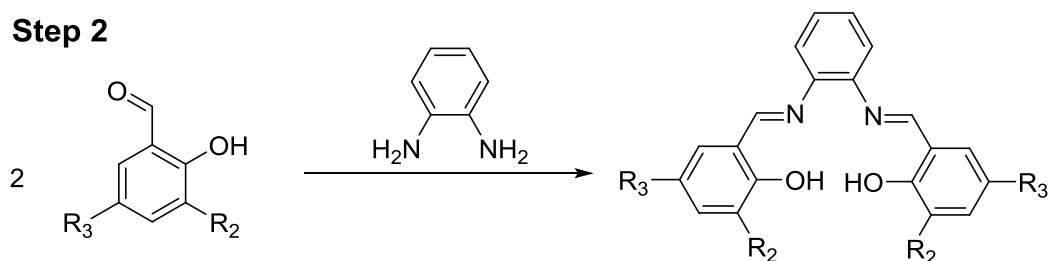
Ald1: $R_2 = R_3 = H$
Ald2: $R_2 = {}^tBu$, $R_3 = H$
Ald3: $R_2 = H$, $R_3 = {}^tBu$
Ald4: $R_2 = {}^tBu$, $R_3 = OMe$
Ald5: $R_2 = {}^tBu$, $R_3 = NO_2$

Sal1: $R_2 = R_3 = H$
Sal2: $R_2 = {}^tBu$, $R_3 = H$
Sal3: $R_2 = H$, $R_3 = {}^tBu$
Sal4: $R_2 = {}^tBu$, $R_3 = OMe$
Sal5: $R_2 = {}^tBu$, $R_3 = NO_2$
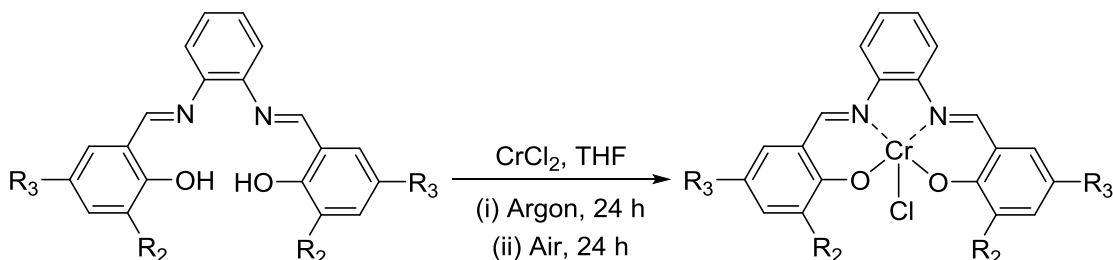
Test catalysts **Cr1-Cr5** with the most active co-catalyst (Step 1) to find the optimal salicylaldehyde functional groups.

Cr1: $R_2 = R_3 = H$
Cr2: $R_2 = {}^tBu$, $R_3 = H$
Cr3: $R_2 = H$, $R_3 = {}^tBu$
Cr4: $R_2 = {}^tBu$, $R_3 = OMe$
Cr5: $R_2 = {}^tBu$, $R_3 = NO_2$

Scheme 22: Salicylaldehyde optimisation (Step 2).

Step 3
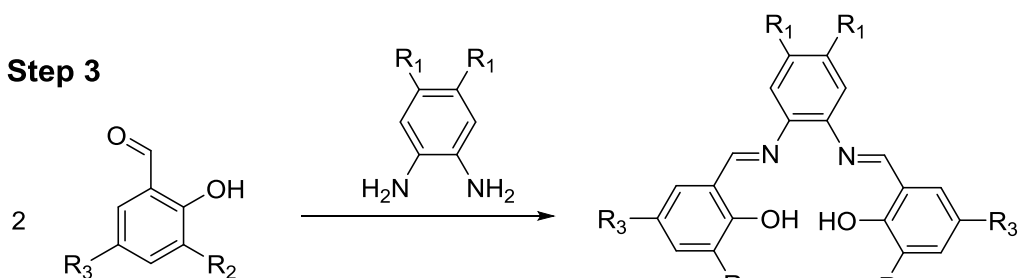
Ald6: $R_1 = Me$, $R_2 = R_3 = H$
Ald7: $R_1 = Cl$, $R_2 = R_3 = H$
Ald8: $R_1 = -(CH)_4-$, $R_2 = R_3 = H$

Sal6: $R_1 = Me$, $R_2 = R_3 = H$
Sal7: $R_1 = Cl$, $R_2 = R_3 = H$
Sal8: $R_1 = -(CH)_4-$, $R_2 = R_3 = H$
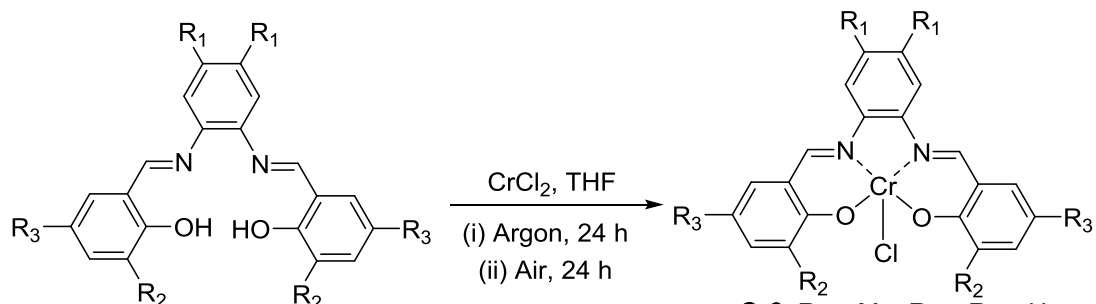
(a) Test catalysts **Cr6-Cr8** with the most active co-catalyst (Step 1), to find the optimal diamine functional groups.
(b) Combine most active salicylaldehyde (Step 2) and diamine backbone functional groups to see if activity is increased
Cr9-Cr10

Cr6: $R_1 = Me$, $R_2 = R_3 = H$
Cr7: $R_1 = Cl$, $R_2 = R_3 = H$
Cr8: $R_1 = -(CH)_4-$, $R_2 = R_3 = H$
Cr9: $R_1 = Cl$, $R_2 = {}^tBu$, $R_3 = H$
Cr10: $R_1 = Cl$, $R_2 = {}^tBu$, $R_3 = OMe$

Scheme 23: Diamine backbone optimisation (Step 3).

Step 4
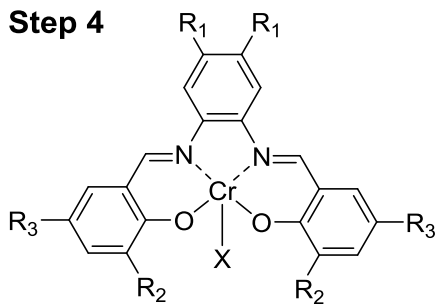
Cr4: R_1 = H, R_2 = ^{t}Bu, R_3 = OMe, X = Cl
Cr11: R_1 = H, R_2 = ^{t}Bu, R_3 = OMe, X = Br
Cr12: R_1 = H, R_2 = ^{t}Bu, R_3 = OMe, X = I
Cr13: R_1 = H, R_2 = ^{t}Bu, R_3 = OMe, X= OAc
Cr14: R_1 = H, R_2 = ^{t}Bu, R_3 = OMe, X = OTs

Cr4, Cr11-Cr14

Test different chromium counterions on the most active catalyst from steps 2-3 with the most active co-catalyst (Step 1). Find the most active catalyst and screen against numerous epoxides.

Figure 17: Chromium counterion optimisation (Step 4).

Catalyst **Cr15** (Figure 15) was synthesised by Dr José Antonio Castro-Osma prior to performing this study. Consequently, catalyst **Cr15** was tested with different co-catalysts to investigate whether a co-catalyst was needed, and if so determine the most active catalyst and co-catalyst combination. This combination was then screened against different epoxides to ensure there was potential scope for this catalyst and to decide which epoxide to use in further optimisations (Step 1a and Step 1b, Figure 16). Different functional groups on the salicylaldehyde (Step 2, Scheme 22) and the diamine backbone (Step 3a, Scheme 23) were then screened with the most active co-catalyst (determined from Step 1) to find the most active salophen framework. The most active groups on the salicylaldehyde and diamine backbone were also combined to investigate if this increased epoxide conversion (Step 3b, Scheme 23). Counterions on the chromium were varied to find the most active functional group combination and thus the most active catalyst overall (Step 4, Figure 17). All standard deviation values quoted with conversions where possible in this chapter refer to standard deviation values of at least three repeat experiments. Tests were then conducted in which the catalytic loading of the catalyst was varied to ensure that a sufficient quantity was being used. The most active catalyst was then screened against a variety of epoxides to explore its versatility in forming cyclic carbonates via CDU. Investigations into ring-opening internal epoxides with the most active catalyst, along with a kinetic and mechanistic study of this catalyst, will be performed. The efficiency of this catalyst will also be compared to notable catalysts reported in the literature.

Step 1a: Optimising the Co-catalyst

Catalyst **Cr15** with different TBA and PPN salts as co-catalysts were all efficient systems in the formation of styrene carbonate (**7**, **CC1**) from styrene oxide and CO_2 gas from dry ice pellets (**12**, **EP1**, Table 1).

Table 1: Optimisation of co-catalysts using catalyst **Cr15**.
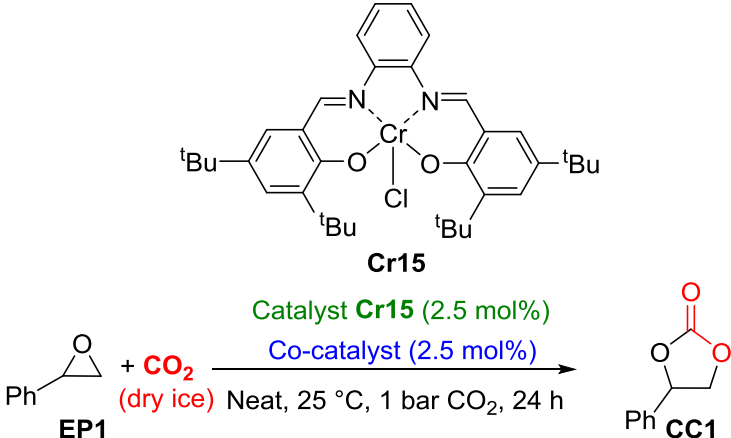
Cr15

Catalyst **Cr15** (2.5 mol%)
Co-catalyst (2.5 mol%)
Neat, 25 °C, 1 bar CO_2, 24 h

Entry[a,b]	Co-catalyst	Conv. 3 h / %	TOF / h^{-1}	Conv. 6 h / %	TOF / h^{-1}	Conv. 24 h / %	TOF / h^{-1}
1	-	0	0.00	0	0.00	0	0.00
2	Bu_4NBr[c]	0	0.00	0	0.00	1	0.02
3	Bu_4NF	3	0.40	9	0.60	34	0.57
4	Bu_4NCl	10	1.33	20	1.33	62	1.03
5	Bu_4NBr	37	4.93	60	4.00	100	1.67
6	Bu_4NBr (5 mol%)	41	5.46	65	4.33	100	1.67
7	Bu_4NI	34	4.53	53	3.53	93	1.55
8	PPNCl	18	2.40	29	1.93	62	1.03
9	PPNBr	31	4.13	47	3.13	91	1.52
10	DMAP	0	0.00	0	0.00	2	0.03

a) Conversions were obtained from ^{1}H NMR analysis of the unpurified reaction mixture.
b) TOF = mol of product / ((mol of catalyst) x time).
c) Catalyst **Cr15** was not used in the reaction.

Control tests using catalyst or co-catalyst only (Entries 1 and 2, Table 1) showed low conversions as expected.[107-109] Co-catalyst optimisation showed that order of reactivity for TBA salts was TBAB > TBAI > TBAC > TBAF (Entries 3-7, Table 1). Increasing TBAB concentration to 5 mol% only slightly increased the conversion, indicating that there was no advantage to increasing co-catalyst loading or catalyst to co-catalyst ratios (Entry 6, Table 1). In all cases, the reaction required 24 h using ambient conditions, as the reaction was not complete after 3 or 6 h (Entries 1-10, Table 1).

The PPN salts were active co-catalysts, and the order of reactivity was (PPNBr) > bis(triphenylphosphine)iminium chloride (PPNCl, Entries 8-9, Table 1). bis(triphenylphosphine)iminium chloride was more active than TBAC (Entries 8 and 4 respectively, Table 1, whereas PPNBr was slightly less active than TBAB (Entries 9 and 5 respectively, Table 1). 4-(Dimethylamino)pyridine (DMAP) was a very poor co-catalyst for this catalytic system (Entry 10, Table 1). Charged anions provided by TBA salts, such as Br⁻, are more nucleophilic than neutral species such as DMAP, which may therefore be a poor co-catalyst due to its low nucleophilicity.

The most active co-catalyst overall was TBAB (Entries 5-6, Table 1). Bis(triphenylphosphine)iminium bromide and PPNCl were similar in activity (Entries 7-8, Table 1) but are more expensive than TAA halide salts, not as commercially available and can have solubility problems.[99] It was therefore more beneficial to use TBA salts as co-catalysts.

The activity trend for TBA salt anions was Br > I > Cl > F, and for PPN salt anions was Br > Cl. In the formation of cyclic carbonates, TBA and PPN salts dissociate to form TBA^+ and PPN^+ cations respectively and a halide anion. This anion can act as nucleophile and ring-open the epoxide, thus driving cyclic carbonate formation.[40,48,49] Thus the trend in terms of activity can also be stated as $Br^- > I^- > Cl^- > F^-$ and $Br^- > Cl^-$ for TBA and PPN salts respectively. The greater the nucleophilicity of the halide anion from the co-catalyst,

the faster the anion can ring-open the epoxide and initiate the reaction,[110] thus the trend seen in Table 1 with the exception of the iodide anion.[111] The iodide anion is an extremely bulky anion, and therefore may be less active than the bromide anion due to steric hindrance.[112] Doubling the concentration of TBAB, and therefore Br⁻, concentration also had no significant change on the conversion, suggesting there is an optimum salophen catalyst and co-catalyst loading. Investigations into the reaction mechanism are discussed further in "2.2.5 Kinetic and Mechanistic Studies". As TBAB was the optimum co-catalyst, this was used in further optimisation tests.

Step 1b: Screening Different Epoxides

Catalyst **Cr15** was screened with different epoxides **EP1-EP10** in the presence of TBAB to investigate if this catalytic system was worthwhile optimising (Table 2). When screened with different epoxides, catalyst **Cr15** could convert a wide scope of terminal epoxides to their corresponding cyclic carbonates under ambient conditions, giving high conversions and reasonable yields (Entries 1-10, Table 2). This suggested that optimisation of chromium(III) salophen catalysts was worth pursuing.

With halogen groups on the epoxide phenyl ring, conversions and consequent yields were lower than expected (Entries 9-10, Table 2). This may be due to the electron withdrawing effect of the halogen groups hindering the ability of the epoxide to coordinate to the chromium metal centre.[95,113,114] Epoxide **EP10** is also a solid at room temperature and a liquid at 26-29 °C,[115] which will directly affect its conversion. When the reaction temperature was raised to 50 °C, faster conversions and higher yields were obtained as expected (Entries 11-12, Table 2). After testing different epoxides, styrene oxide **EP1** was identified as an ideal substrate for further catalyst optimisation, as the highest isolated yield was obtained for styrene carbonate **CC1** (Entry 1, Table 2).

Table 2: Screening of **Cr15** against epoxides **EP1-EP10**.
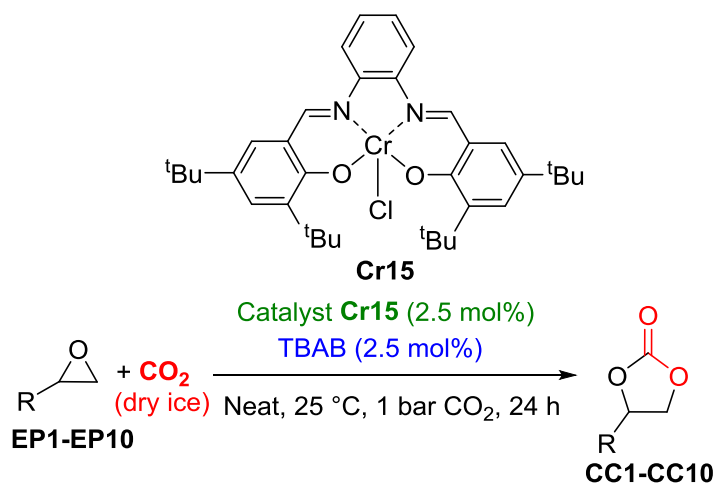
Cr15

Catalyst **Cr15** (2.5 mol%)
TBAB (2.5 mol%)

R–(epoxide) + CO_2 (dry ice) → Neat, 25 °C, 1 bar CO_2, 24 h → (cyclic carbonate) R

EP1-EP10 → **CC1-CC10**

1: R = Ph; **2**: R = Me; **3**: R = Et; **4**: R = ^nBu; **5**: R = ^nOct; **6**: R = CH_2Cl;
7: R = CH_2OH; **8**: R = CH_2OPh; **9**: R = 4-ClC_6H_4; **10**: R = 4-BrC_6H_4

Entry[a]	Epoxide (EP)	Temperature / °C	Conv. 24 h / %	Yield[d] / %
1	**1**	25	100	93
2[b]	**2**	0	N/A[c]	71
3	**3**	25	100	84
4	**4**	25	100	88
5	**5**	25	100	79
6	**6**	25	100	91
7	**7**	25	67	64
8	**8**	25	77	72
9	**9**	25	80	73
10	**10**	25	60	50
11	**9**	50	100	85
12	**10**	50	100	89

a) Conversions were obtained from ^{1}H NMR analysis of the unpurified reaction mixture.
b) Due to the volatility of the epoxide, the reaction was performed at 0 °C.
c) Due to the volatility of the epoxide, the conversion after 24 h was not determined.
d) Yields quoted are isolated yields, obtained by purifying the reaction mixture via column chromatography.

Steps 2-4: Synthesis and Optimisation of Chromium(III) Salophen Catalysts

The synthesise of the new chromium(III) salophen complexes **Cr1-Cr14** (steps 2-4) were all achieved with reasonable yields (51-94%, 2.4 Methods and Experimental). In all further optimisation tests, 2.5 mol% of **Cr1-Cr15** and TBAB were used in the synthesis of styrene carbonate **CC1**, at room temperature and 1 bar of CO_2 pressure over 24 h (Scheme 24).
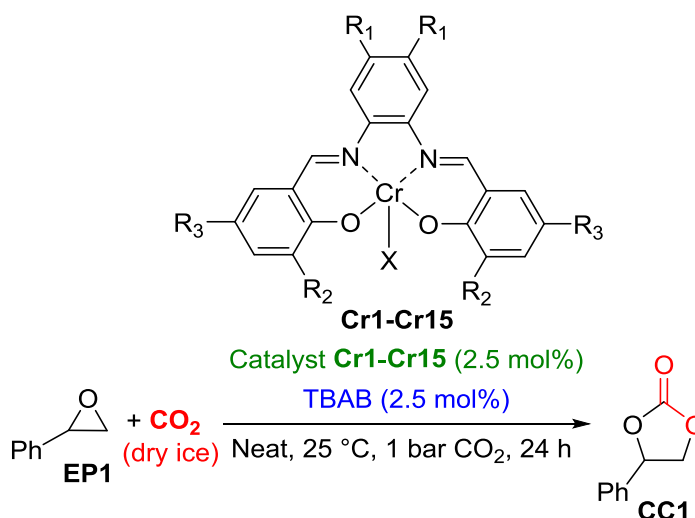
Scheme 24: Reaction conditions used in catalyst optimisation steps 2-4.

Step 2: Optimising Salicylaldehyde Functional Groups

Changing functional groups on the salicylaldehyde affected reaction conversions as expected (Table 3). Without taking into account the standard deviation of duplicate runs (quoted as error bars in Table 3), the order of activity for salicylaldehyde functional groups was methoxy > ortho and para *tert*-butyl ≈ H ≈ ortho *tert*-butyl > para *tert*-butyl > nitro (Entries 1-6, Table 3).

Changing hydrogen groups for *tert*-butyl groups had no major effect on catalytic conversions (Entries 1-4, Table 3), suggesting steric effects of the salicylaldehyde functional groups had no significant influence on catalytic activity. In terms of electronic effects, it was predicted that more electron donating groups would increase catalyst reactivity, because electron donating groups, such as +M methoxy and +I *tert*-butyl groups, push electron density towards the chromium metal centre; thus weakening the interaction between the metal and chloride counterion. Consequently it becomes easier for the epoxide

Table 3: Optimisation of salicylaldehyde functional groups.
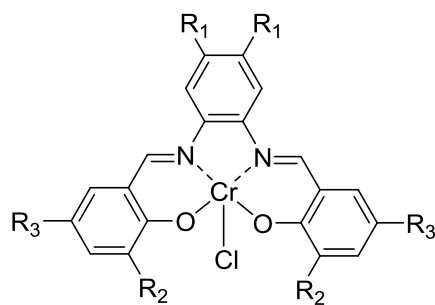
Cr15, Cr1-Cr5

Cr15: R_1 = H, R_2 = R_3 = ^tBu; **Cr1**: R_1 = H, R_2 = H, R_3 = H;
Cr2: R_1 = H, R_2 = ^tBu, R_3 = H; **Cr3**: R_1 = H, R_2 = H, R_3 = ^tBu;
Cr4: R_1 = H, R_2 = ^tBu, R_3 = OMe; **Cr5**: R_1 = H, R_2 = ^tBu, R_3 = NO_2

Entry[a,b,c,d]	Catalyst	Conv. 3 h / %	TOF / h^{-1}	Conv. 6 h / %	TOF / h^{-1}	Conv. 24 h / %	TOF / h^{-1}
1	**Cr15**	29 ± 3	3.87	48 ± 7	3.18	91 ± 2	1.52
2	**Cr1**	28 ± 2	3.73	48 ± 2	3.18	90 ± 4	1.49
3	**Cr2**	28 ± 3	3.70	52 ± 6	3.44	97 ± 4	1.62
4	**Cr3**	20 ± 3	2.67	38 ± 4	2.55	89 ± 10	1.48
5	**Cr4**	40 ± 4	5.27	64 ± 5	4.28	98 ± 4	1.63
6	**Cr5**[e]	7	0.93	13	0.87	41	0.68

a) Conversions were obtained from ^1H NMR analysis of the unpurified reaction mixture.
b) TOF = mol of product / ((mol of catalyst) x time).
c) Conversions are the average result obtained from at least three duplicate runs and are quoted with standard deviation values.
d) Performed using reaction conditions in Scheme 24.
e) Due to catalyst stability and synthesis difficulties, only one run with catalyst **Cr5** was performed.

to coordinate to the chromium metal centre.[88,95,113,114] Electron withdrawing groups are therefore expected to have the opposite effect. *Tert*-butyl and/or methoxy groups can also increase the solubility of the catalyst in epoxides and thus reactivity.[95,114]

After 24 h, the conversions obtained using catalysts **Cr1-Cr4** and **Cr15** (Entries 1-5, Table 3) were within the same error margin, therefore indicating that replacing salicylaldehyde hydrogens with +I ortho and para *tert*-butyl groups, or +M methoxy groups, does not lead to any significant changes in epoxide conversion. After 3 h and 6 h, **Cr4** reported higher conversions than the other catalysts (Entry 4, Table 3), whereas **Cr1-Cr3** and **Cr15**

obtained similar conversions. This indicated that the combination of a para *tert*-butyl and methoxy group created a more active catalyst during the early stages of the reaction, thus following previously reported trends. Only catalyst **Cr5** reported a significant difference in conversion, with the lowest conversions at each time period (Entry 6, Table 3). This was expected due to the presence of the electron withdrawing –M nitro group in **Cr5**.

Step 3a: Optimising Diamine Backbone Functional Groups

The next area of catalyst optimisation was altering the diamine backbone groups. Changing these functional groups again affected catalyst activity (Table 4). In terms of diamine backbone groups, the order of reactivity was chloride > naphthalene ≈ dimethyl groups (Entry 1-3, Table 4). As reported by Darensbourg, the steric effects of functional groups on the diamine backbone can have a huge effect on catalyst activity, as sterically hindering groups will hinder access of the epoxide to the chromium centre. In contrast, electronic properties of these functional groups had no major effects on activity.[95,113,114]

Table 4: Optimisation of diamine backbone functional groups.
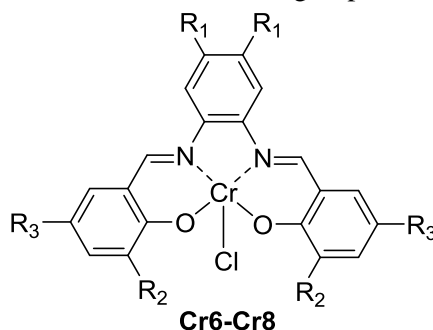
Cr6: R_1 = Me, R_2 = H, R_3 = H; **Cr7**: R_1 = Cl, R_2 = H, R_3 = H;
Cr8: R_1 = -(CH)$_4$-, R_2 = H, R_3 = H

Entry[a,b,c,d]	Catalyst	Conv. 3 h / %	TOF / h^{-1}	Conv. 6 h / %	TOF / h^{-1}	Conv. 24 h / %	TOF / h^{-1}
1	**Cr6**	11 ± 3	1.50	22 ± 4	1.45	73 ± 10	1.21
2	**Cr7**	21 ± 5	2.76	41 ± 6	2.73	97 ± 3	1.62
3	**Cr8**	14 ± 2	1.91	29 ± 3	1.91	87 ± 8	1.46

a) Conversions were obtained from ^{1}H NMR analysis of the unpurified reaction mixture.
b) TOF = mol of product / ((mol of catalyst) x time).
c) Conversions are the average result obtained from at least three duplicate runs and are quoted with standard deviation values.
d) Performed using reaction conditions in Scheme 24.

All of the catalysts (Entry 1-3, Table 4) were less active than catalysts with only hydrogens present on the diamine backbone (Entries 1-6, Table 3). This may be due to the absence of *tert*-butyl groups, meaning these catalysts were less soluble in styrene oxide **EP1** and thus hindering the reaction.[113,114,116,117] The overall trend in terms of sterics (and electronics) was not clear, as the catalyst with bulky Cl atoms on the diamine backbone (**Cr7**) was the most active catalyst compared to when less bulky Me groups were present. Catalyst **Cr7** may have been more soluble than the other catalysts, hence its greater activity.

Step 3b: Combining Salicylaldehyde and Diamine Backbone Functional Groups

After discovering the most active salicylaldehyde and diamine backbone functional groups, complexes were synthesised containing both optimised functional groups, to determine if these could create more active catalysts (Table 5).

Table 5: Combining the most active salicylaldehyde and diamine backbone functional groups.

Cr9-Cr10
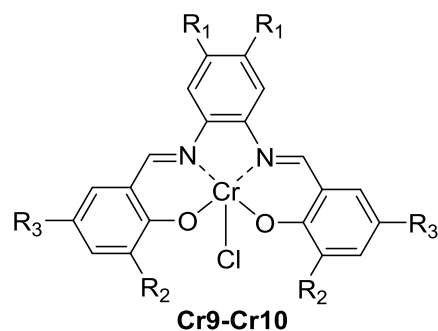
Cr9: R_1 = Cl, R_2 = ^{t}Bu, R_3 = H; **Cr10**: R_1 = Cl, R_2 = ^{t}Bu, R_3 = OMe

Entry[a,b,c,d]	Catalyst	Conv. 3 h / %	TOF / h^{-1}	Conv. 6 h / %	TOF / h^{-1}	Conv. 24 h / %	TOF / h^{-1}
1	Cr9	19 ± 10	2.47	35 ± 12	2.30	91 ± 0	1.52
2	Cr10	27 ± 5	3.53	47 ± 7	3.13	95 ± 3	1.58

a) Conversions were obtained from ^{1}H NMR analysis of the unpurified reaction mixture.
b) TOF = mol of product / ((mol of catalyst) x time).
c) Conversions shown are the average result obtained from at least two duplicate runs and are quoted with standard deviation values.
d) Performed using reaction conditions in Scheme 24.

In terms of activity, catalyst **Cr10** was slightly more active than **Cr9** (Entries 1 and 2 respectively, Table 5), and both were more active than the diamine functionalised catalysts, with the exception of when chlorine groups were present on the diamine backbone (**Cr6-**

Cr8, Entries 1-3, Table 4). The presence of the *tert*-butyl groups may have increased the solubility, and thus activity, of these catalysts.[95,106,114] These catalysts however were not always more active than those with only hydrogen groups on the diamine backbone (catalysts **Cr1-Cr2**, **Cr4** and **Cr15**, Entries 1-3 and 5, Table 3). The presence of the chloride groups may lead to an increase in catalytic activity but the combined presence of chloride and bulky *tert*-butyl groups could sterically hinder epoxides interacting with the chromium metal centre.[114] This trend has been previously reported in the literature.[95,114] The combination of the most active functional groups therefore offered no overall benefit.

Step 4: Optimising Catalyst Counterion

The chromium counterions present in the (currently) most active catalyst (**Cr4**, when considering conversions after 3 h and 6 h) were varied, to investigate how the nucleophilicity of different counterions affected catalyst activity (Table 6).

Table 6: Optimisation of catalyst counterion.

Cr4, Cr11-Cr14
Cr4: X = Cl; **Cr11**: X = Br; **Cr12**: X = I;
Cr13: X = OAc; **Cr14**: X = OTs
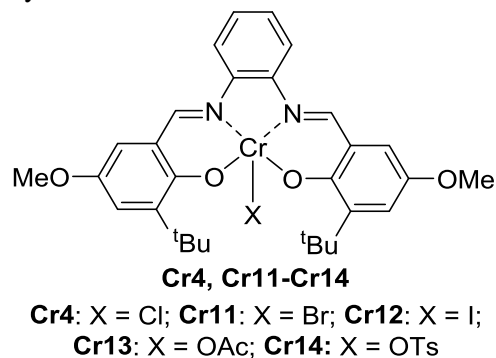
Entry[a,b,c,d]	Catalyst	Conv. 3 h / %	TOF / h^{-1}	Conv. 6 h / %	TOF / h^{-1}	Conv. 24 h / %	TOF / h^{-1}
1	**Cr4**	40 ± 4	5.27	64 ± 5	4.28	98 ± 4	1.63
2	**Cr11**	47 ± 4	6.27	75 ± 5	4.97	100 ± 0	1.67
3	**Cr12**	26 ± 4	3.40	43 ± 4	2.87	100 ± 0	1.67
4	**Cr13**	34 ± 1	4.47	56 ± 1	3.73	100 ± 0	1.67
5	**Cr14**	4 ± 0	0.53	7 ± 1	0.43	32 ± 14	0.53

a) Conversions were obtained from ^{1}H NMR analysis of the unpurified reaction mixture.
b) TOF = mol of product / ((mol of catalyst) x time).
c) Conversions are the average result obtained from at least two duplicate runs and are quoted with standard deviation values.

In terms of activity, the trend for different counterions was Br > Cl > OAc > I > OTs (Entries 1-5, Table 6). The activity of the counterions follows the general periodic trend of nucleophilicity,[118-120] and the empirical scales of nucleophilicity defined by Swain and Scott[121] and by Edwards,[122] as the more nucleophilic the counterion the faster the conversion of epoxide into cyclic carbonate. This trend has been previously reported in the literature when chromium counterions were varied in chromium(III) salen complexes.[95] The only exceptions were the iodide and tosylate counterion, which due to their large size may have hindered epoxides coordinating to the chromium. The most active catalyst hence was thus catalyst **Cr11**, with the combination of *tert*-butyl and methoxy groups on the salicylaldehyde and a bromide counterion.

2.2.2 Catalytic Loading

To ensure that a catalytic loading of 2.5 mol% of the chromium(III) salophen catalysts and TBAB (in a 1:1 ratio) was sufficient for high epoxide conversions, catalyst **Cr2** was tested at different catalytic loadings in the conversion of styrene oxide **EP1** to styrene carbonate **CC1** (Table 7). Catalyst **Cr2** was used in these experiments due to its ideal solubility in numerous epoxides and it was the largest batch of catalyst available at the time.

As expected, a decrease in conversion occurred concurrently with a reduction in catalytic loading (Entries 1-6, Table 7). With catalytic loadings of 0.1-1.5 mol%, the conversions of styrene oxide **EP1** to cyclic carbonate were slower after 3 and 6 h (Entries 1-4, Table 7) compared to >1.5 mol% (Entries 5-6, Table 7). Using 1.5 mol% of catalyst **Cr2** obtained adequate conversions after 24 h, but not over a shorter time frame (Entry 4, Table 7). Using 2.0 and 2.5 mol% of catalyst **Cr2** achieved the highest conversions overall (Entries 5-6, Table 7), with 2.5 mol% obtaining the fastest conversions at each time point (Entry 6, Table 7). Using 2.5 mol% of catalyst was therefore deemed necessary for cyclic carbonate formation and used in all further tests.

Table 7: Optimisation of catalyst loading with catalyst **Cr2**.

Catalyst **Cr2** (0.1, 0.5, 1.0, 1.5, 2.0, 2.5 mol%)

TBAB (0.1, 0.5, 1.0, 1.5, 2.0, 2.5 mol%)

EP1 + CO_2 (dry ice) → Neat, 25 °C, 1 bar CO_2, 24 h → CC1
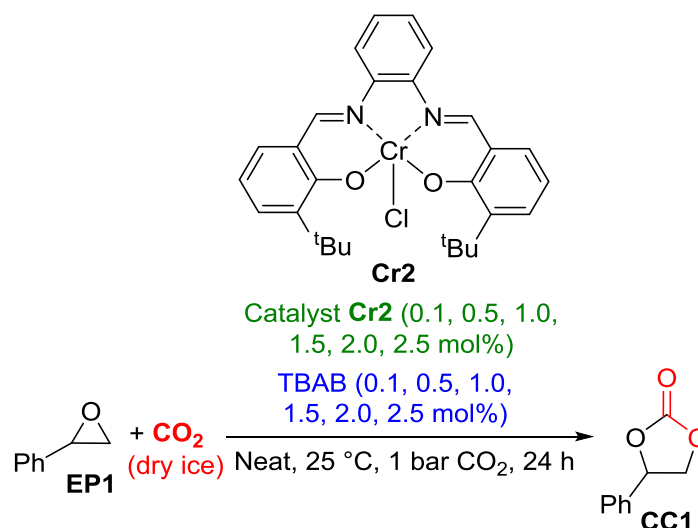
Entry[a,b,c,d]	Cr2 / mol%	Conv. 3 h / %	TOF / h^{-1}	Conv. 6 h / %	TOF / h^{-1}	Conv. 24 h / %	TOF / h^{-1}
1	0.1	1	3.33	3	5.00	14	5.83
2	0.5	7	4.67	14	4.67	56	4.67
3	1.0	17	5.67	30	5.00	79	3.29
4	1.5	18	4.00	36	4.00	90	2.50
5	2.0	25	4.17	48	4.00	97	2.03
6	2.5	28 ± 3	3.70	52 ± 6	3.44	97 ± 4	1.62

a) Conversions were obtained from ^{1}H NMR analysis of the unpurified reaction mixture.
b) TOF = mol of product / ((mol of catalyst) x time).
c) Conversions obtained using 2.5 mol% of catalyst **Cr2** are the average results obtained from four duplicate runs and are quoted with standard deviation values.
d) Catalyst **Cr2** and TBAB were kept in a 1:1 ratio in each test.

2.2.3 Epoxide Screening

When catalyst **Cr11** was screened against different epoxides, in a similar manner to the screening of catalyst **Cr15**, its broad scope of activity was illustrated. Catalyst **Cr11** was capable of converting aromatic, aliphatic, halogen and hydroxyl containing epoxides into their corresponding cyclic carbonate using CO_2 from dry ice (Table 8).

The conversions obtained with catalyst **Cr15** and **Cr11** were very similar (Table 2 and Table 8 respectively), with catalyst **Cr11** noticeably showing greater reactivity for epoxides **EP1**, **EP7**, **EP9** and **EP10**. Catalyst **Cr11** was therefore deemed more versatile

71

Table 8: Screening of **Cr11** against epoxides **EP1-EP10**.
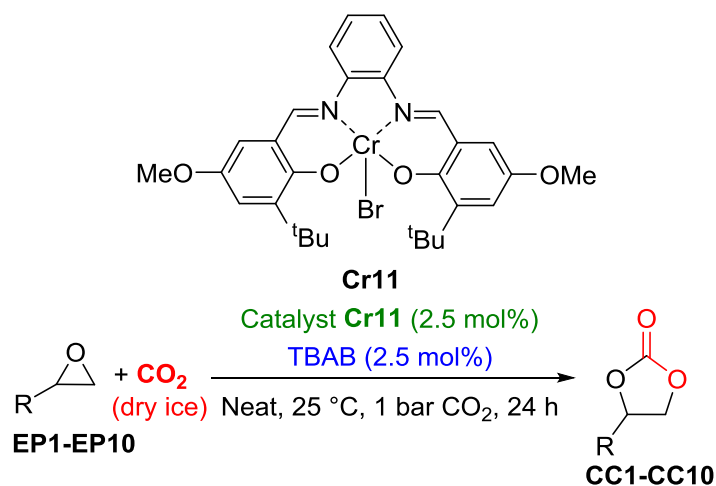
Cr11

Catalyst **Cr11** (2.5 mol%)

TBAB (2.5 mol%)

$+ CO_2$ (dry ice) Neat, 25 °C, 1 bar CO_2, 24 h

EP1-EP10

CC1-CC10

1: R = Ph; **2**: R = Me; **3**: R = Et; **4**: R = ^{n}Bu; **5**: R = ^{n}Oct; **6**: R = CH_2Cl;
7: R = CH_2OH; **8**: R = CH_2OPh; **9**: R = 4-ClC_6H_4; **10**: R = 4-BrC_6H_4

Entry[a]	Epoxide (EP)	Temperature / °C	Conv. 24 h / %	Yield[d] / %
1	1	25	100	92
2[b]	2	0	N/A[c]	57
3	3	25	100	86
4	4	25	95	81
5	5	25	89	82
6	6	25	100	78
7	7	25	86	72
8	8	25	71	71
9	9	25	100	78
10	10	25	71	49
11	9	50	100	91
12	10	50	100	89

a) Conversions were obtained from ^{1}H NMR analysis of the unpurified reaction mixture.
b) Due to the volatility of the epoxide, the reaction was performed at 0 °C.
c) Due to the volatility of the epoxide, the conversion after 24 h was not determined.
d) Yields quoted are isolated yields, obtained by purifying the reaction mixture via column chromatography

overall than catalyst **Cr15**. Interestingly there was no clear trend in terms of epoxide reactivity with catalyst **Cr11**, as yields and conversions did not correlate to epoxide size or functionality. This may be due to the ease at which epoxides can coordinate to mononuclear salophen catalysts, and the stability of the salophen framework.

2.2.4 Conversion of Internal Epoxides

After performing this analysis, further research was performed in collaboration with Dr José Antonio Castro-Osma at the University of Castilla-La Mancha in Spain. Dr Castro-Osma performed the synthesis of internal, or disubstituted, cyclic carbonates with the most active catalyst **Cr11**. Pleasingly, catalyst **Cr11** with TBAB was capable of transforming internal epoxides and CO_2 into cyclic carbonates at elevated temperatures and pressures or 50 °C and 50 bar of CO_2 respectively.[112] Catalyst **Cr11** was also able to polymerise cyclohexene oxide, with a 76% yield, narrow polydispersity ($Đ$ = 1.13), and high selectivity towards polymer formation (>99%).[112] The conversion of internal epoxides occurred with a retention of stereochemistry. This supports the general mechanism for cyclic carbonate formation from ring-opening epoxides and CO_2 insertion, with a nucleophile and a Lewis acidic chromium metal complex[94,108,123] performing two substitution reactions at the less sterically hindered carbon of the epoxide.[124-126] This was investigated further (*vide infra*).

2.2.5 Kinetic and Mechanistic Studies

One important consideration in cyclic carbonate synthesis from epoxides and CO_2 is the nucleophilicity and leaving group ability of the nucleophile. Getting the right balance between a strong nucleophile and a good leaving group is vital. This ensures the nucleophile can effectively ring-open the epoxide and subsequently be displaced to form a cyclic carbonate. If the nucleophile however exhibits excellent leaving group properties, then the reformation of the epoxide becomes a competing reaction.[83]

When using chromium(III) salophen catalysts with a co-catalyst, the ring-opening of epoxides can occur via a monometallic pathway or bimetallic pathway. In the monometallic pathway the co-catalyst, or nucleophile, will ring-open an epoxide coordinated to a metal centre and is first-order rate dependent on catalyst concentration. In the bimetallic pathway, a metal coordinated co-catalyst, or metal coordinated nucleophile, will ring-open a metal coordinated epoxide interacting with a different metal centre and is second-order rate dependent on catalyst concentration (Scheme 25).[110,114]
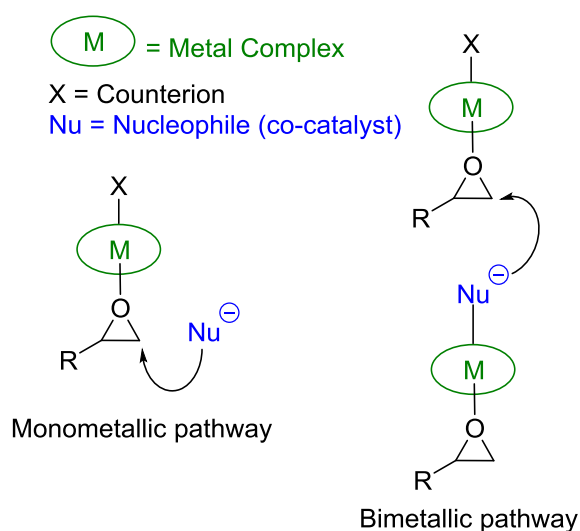
Scheme 25: Monometallic and bimetallic pathways for ring-opening epoxides.[114]

To investigate which pathway occurs when using catalyst **Cr11** and TBAB, and to further study the reaction mechanism, a kinetic study of the synthesis of styrene carbonate using catalyst **Cr11** and TBAB (Bu$_4$NBr) was performed under solvent-free conditions, 50 °C and 1 bar of CO_2. HPLC analysis was used to determine the conversion of styrene oxide **EP1** into styrene carbonate **CC1**. The kinetic study was performed by Dr José Antonio Castro-Osma, thus a summary of his findings is presented. Further information, including the kinetic plots obtained in his study, can be found in the paper published in this work.[112]

It has been shown in the literature with different catalysts that the conversion of styrene oxide to styrene carbonate, with the reaction conditions used in Jose's kinetic study, follows zero-order kinetics in the early stages of the reaction, as the epoxide is acting as a substrate and reaction solvent. As the reaction progresses the reaction then obeys

first-order kinetics, as the cyclic carbonate becomes the main species in the reaction mixture.[84,102,127]

The rate equations used throughout the kinetic study are shown in Figure 18. The general rate equation for the studied reaction is summarised by Equation 1 (Figure 18). The concentrations of CO_2, **Cr11**, and TBAB do not change during the reaction; therefore Equation 1 can be rewritten as Equation 2 (Figure 18). As already stated, the concentration of styrene oxide **EP1** remains constant in the early stages of the reaction. Therefore, the kinetics can be fitted to zero-order kinetics and the rate equation can be expressed as Equation 3 (Figure 18). As the reaction proceeds, it starts to follow first-order kinetics with respect to styrene oxide **EP1** concentration; therefore the rate equation may be expressed as Equation 4 (Figure 18).

$$\text{Rate} = k[\textbf{EP1}]^a[CO_2]^b[\textbf{Cr11}]^c[Bu_4NBr]^d \tag{1}$$

$$\text{Rate} = k_{obs}[\textbf{EP1}]^a \quad \text{where } k_{obs} = k[CO_2]^b[\textbf{Cr11}]^c[Bu_4NBr]^d \tag{2}$$

$$\text{Rate} = k_{0,obs}[\textbf{EP1}]^a \quad \text{where } k_{0,obs} = k_0[\textbf{EP1}]^a[CO_2]^b[\textbf{Cr11}]^c[Bu_4NBr]^d \tag{3}$$

$$\text{Rate} = k_{1,obs}[\textbf{EP1}] \quad \text{where } k_{1,obs} = k_1[CO_2]^b[\textbf{Cr11}]^c[Bu_4NBr]^d \tag{4}$$

Figure 18: Rate equations proposed in the formation of styrene carbonate **CC1** from styrene oxide **EP1**, CO_2 and catalyst **Cr11**.

Reaction order with respect to **Cr11** and TBAB concentration were studied by carrying out two sets of reactions using four different concentrations of **Cr11** or TBAB, keeping the concentration of the other reagent constant. When the order with respect to TBAB concentration was studied (by varying the concentration of TBAB and keeping **Cr11** concentration constant), the kinetic plot of the observed first-order rate constant vs TBAB concentration showed that the reaction followed first-order kinetics with respect to TBAB concentration (d in Figure 18 = 1).[112]

On the other hand, when the order with respect to TBAB was studied (by varying the concentration of **Cr11** and keeping TBAB concentration constant), the kinetic plot of the observed first-order rate constant vs **Cr11** concentration showed that the reaction followed

zero-order kinetics with respect to **Cr11** concentration (when [Bu$_4$NBr] < [**Cr11**], c in Figure 18 = 0). However, when the kinetic study was repeated, when [Bu$_4$NBr] > [**Cr11**], kinetic plots of the observed first-order rate constant vs **Cr11** concentration showed that the reaction followed first-order kinetics with respect to **Cr11** concentration (c in Figure 18 = 1).[112]

Consequently, the rate equation for the synthesis of styrene carbonate **CC1** from styrene oxide **EP1** catalysed by **Cr11** and TBAB, when [Bu4NBr] > [**Cr11**] at 25 °C and 1 bar of CO$_2$, may be expressed as shown in Equation 5 during the early stages of the reaction and Equation 6 during the latter stages (Figure 19). The reaction mechanism thus follows the monometallic pathway (Scheme 25).

$$\text{Rate} = k_{0,obs} \quad \text{where } k_{0,obs} = k_0[\textbf{EP1}][\text{CO}_2][\textbf{Cr11}][\text{Bu}_4\text{NBr}] \quad\quad (5)$$

$$\text{Rate} = k_{1,obs}[\textbf{EP1}] \quad \text{where } k_{1,obs} = k_1[\text{CO}_2][\textbf{Cr11}][\text{Bu}_4\text{NBr}] \quad\quad (6)$$

Figure 19: The kinetically determined rate equations for the synthesis of styrene carbonate **CC1** from styrene oxide **EP1**, CO$_2$ and catalyst **Cr11**, at 25 °C, 1 bar of CO2 and when [Bu$_4$NBr] > [**Cr11**].

From the kinetic experiments it is apparent that the chromium salophen complex **Cr11** and TBAB interact to form a new 1:1 species, the concentration of which depends upon the concentration of the limiting catalyst component. It was hypothesised that a six coordinate species, with two bromide anions coordinating to the chromium could be forming (Scheme 26).
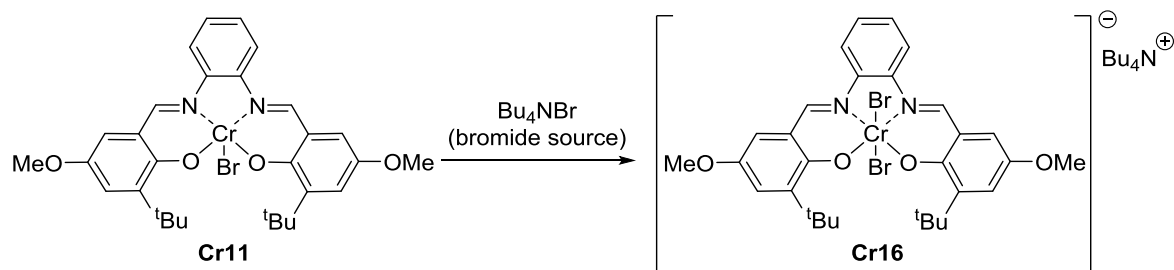
Scheme 26: Proposed formation of [Cr(salophen)Br$_2$]$^-$ **Cr16**.

This is not an unusual proposal, as Darensbourg reported a similar phenomenon with Cl⁻, NO₃⁻, CN⁻, and NCO⁻ anions coordinating to chromium in chromium(III) salen based catalysts,[110,128] and would explain the need for an excess of TBAB to study the reaction order with respect to **Cr11** concentration in the chromium salophen/TBAB catalyst system.

The formation of complex **Cr16** was further studied via UV-Vis and ATR-IR analysis, in which TBAB was added to catalyst **Cr11** in a solution of DCM in 0.5 equivalents from 0.5 to 5.0 equivalents. The catalyst solution was analysed after each 0.5 equivalent addition of TBAB. UV-Vis analysis showed an increase in absorbance at 418 and 506 nm for catalyst **Cr11** upon the addition of 0.5 equivalents to 3.5 equivalents of TBAB. Shifts in these peaks also occurred from 506 to 512 nm and 423 to 413 nm respectively, suggesting the catalyst structure was changing (Figure 20).
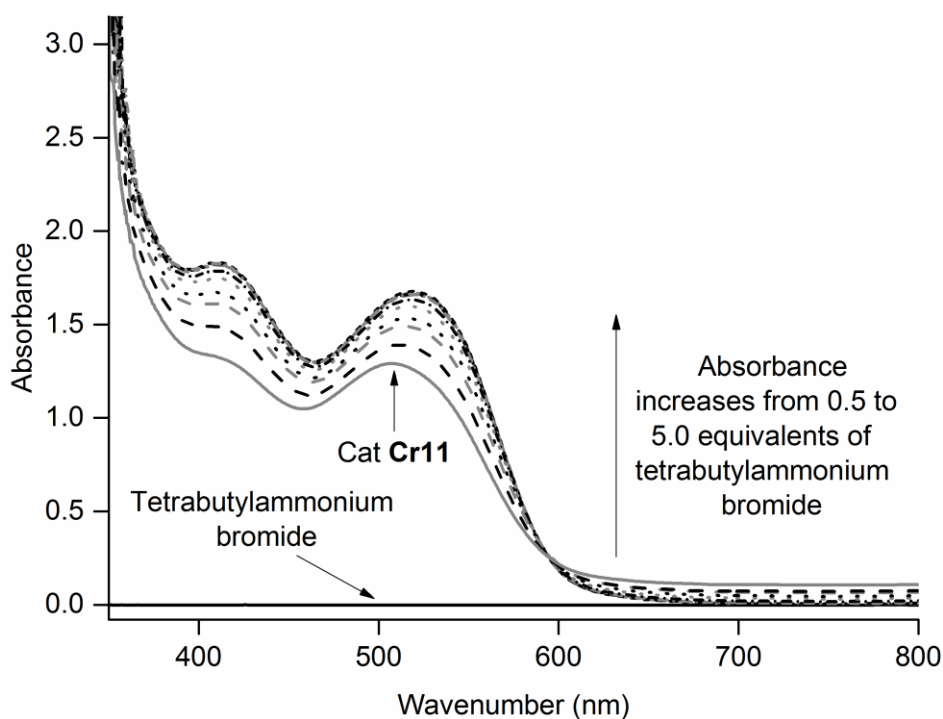
Figure 20: UV-Vis analysis of catalyst **Cr11** upon the addition of TBAB in 0.5 equivalent increments in CH₂Cl₂. Catalyst **Cr11** spectra are normalised to TBAB absorbance (+0.65).

In ATR-IR analysis, two new peak appears at 697 cm⁻¹ and 738 cm⁻¹ after adding 1.5 equivalents of TBAB, both of which were absent in the spectrum of catalyst or TBAB alone. No major changes occurred for both peaks after 3-3.5 additions of TBAB. (Figure

21). ATR-IR analysis therefore suggests that some perturbation to the catalyst structure occurred upon adding TBAB (or bromide anions). No other significant changes occurred.
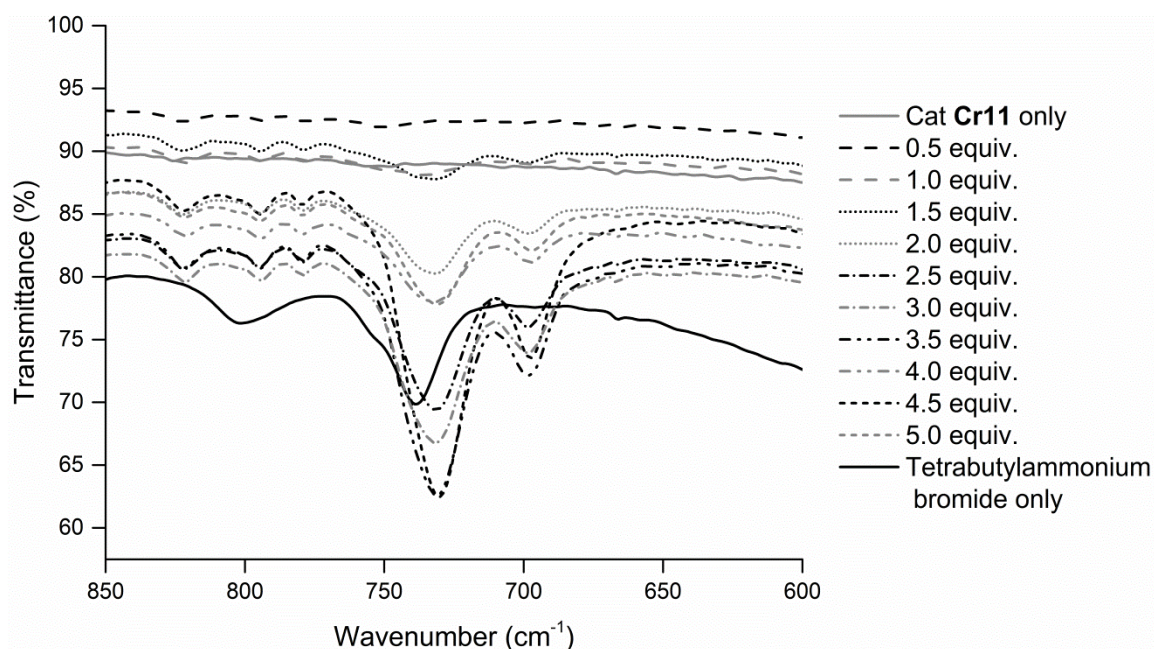
Figure 21: ATR-IR analysis of catalyst **Cr11** upon the addition of TBAB in 0.5 equivalent increments in CH_2Cl_2.

The addition of TBAB and TBAC to catalyst **Cr4** was also performed and analysed via ATR-IR analysis, to investigate whether a six coordinate [Cr(salophen)ClBr]$^-$ or [Cr(salophen)Cl$_2$]$^-$ species could be formed and subsequently detected (Figure 22 and Figure 23 respectively). No distinctive changes in the IR spectra occurred, suggesting the formation of these complexes did not occur.

Although these UV-Vis and IR studies did not unequivocally prove the formation of a [Cr(salophen)Br$_2$]$^-$ type species, the analysis suggested it was possible. Attempts to grow a crystal structure of the [Cr(salophen)Br$_2$]$^-$ species **Cr16**, similar to Darensbourg's work, to prove the formation of **Cr16** were unsuccessful.[110,128] With the kinetic, UV-Vis and ATR-IR analysis in mind, indicating a first-order dependence on the concentration of the catalyst and TBAB and the knowledge that internal epoxides are ring-opened with a retention in epoxide stereochemistry, an overall reaction mechanism was proposed (Scheme 27). On addition of 1 equiv. of TBAB to **Cr11**, the six-coordinate dibromide complex [Cr(salophen)Br$_2$]$^-$ (**Cr16**) is formed. Upon addition of the epoxide to the catalyst system
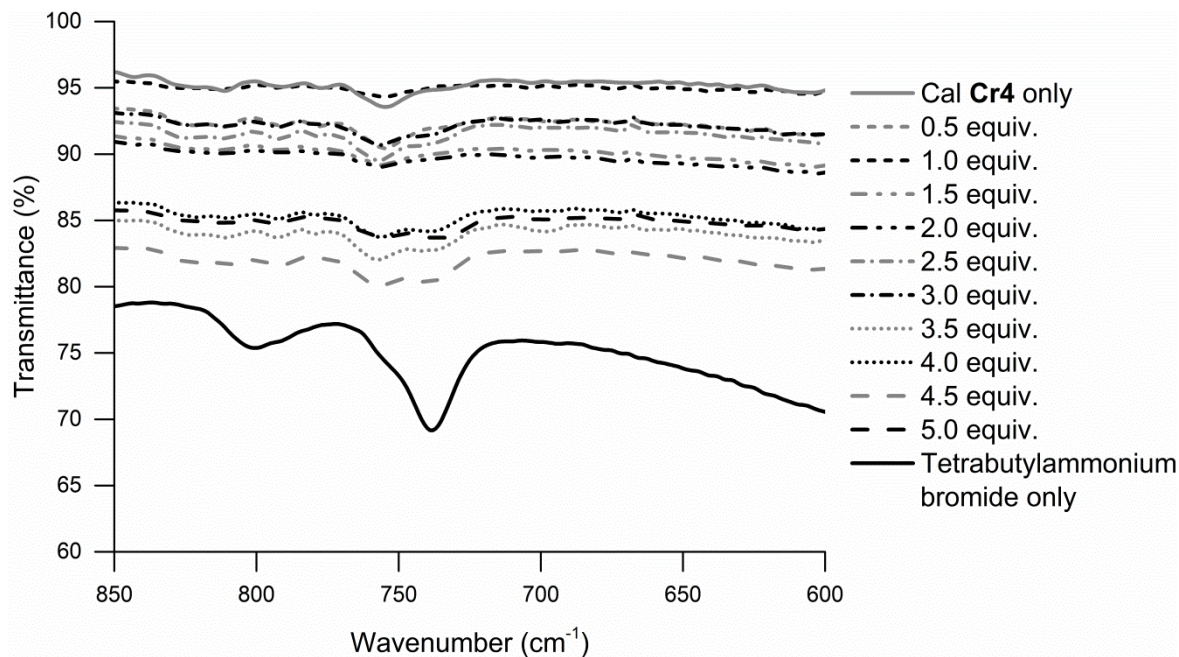
Figure 22: ATR-IR analysis of catalyst **Cr4** upon the addition of TBAB in 0.5 equivalent increments in CH_2Cl_2.
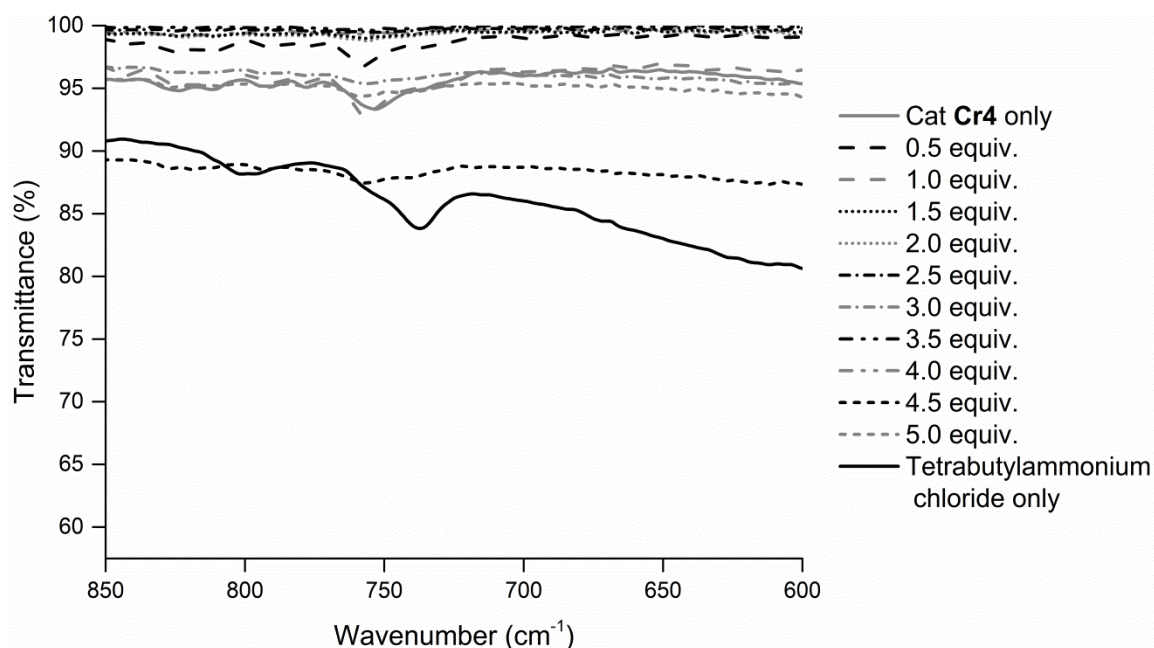
Figure 23: ATR-IR analysis of catalyst **Cr4** upon the addition of TBAC in 0.5 equivalent increments in CH_2Cl_2.

an equilibrium is established between the dibromide complex **Cr16** and the epoxide adduct. It has been reported that this equilibrium is shifted toward the neutral epoxide adduct in pure epoxide solution.[128] The non-coordinated bromide attacks the less hindered carbon of the epoxide, causing the first inversion in stereochemistry. Then, CO_2 is inserted

into the chromium-oxygen bond to form a metal carbonate which ring closes with a second inversion to afford the cyclic carbonate with overall retention of epoxide stereochemistry.
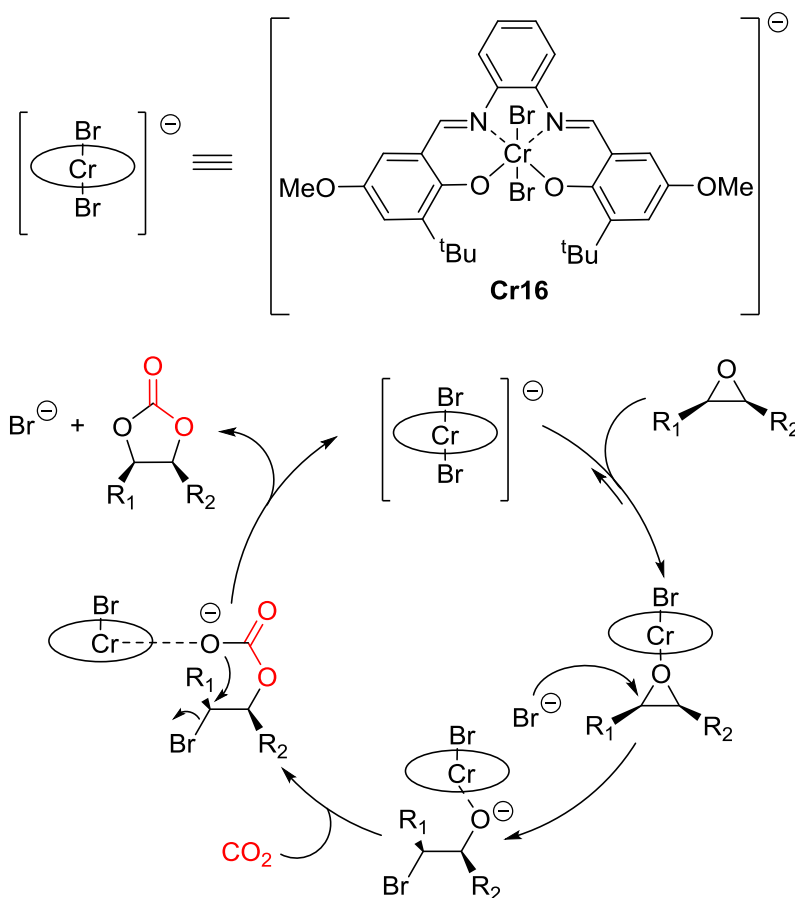
Scheme 27: Proposed reaction mechanism for the synthesis of cyclic carbonates from epoxides and CO_2 with catalyst **Cr11** (and hence **Cr16**) and TBAB as the catalytic system.[112]

In summary, the conversion of epoxides into cyclic carbonates, using catalyst **Cr11** with TBAB as the catalytic system, occurs via a monometallic pathway, obeying first-order kinetics, and is hypothesised to occur via the formation of the six-coordinate dibromide complex [Cr(salophen)Br$_2$]⁻ **Cr16** (Scheme 27).[112]

2.2.6 Crystallisation experiments

When attempting crystallisation of catalyst **Cr4**, by leaving aliquots of **Cr4** in THF for at least two months, white crystals were isolated. These crystals were not of **Cr4** but intriguingly of piperazine derivative **Cry1** (Figure 24 and Figure 25, see 4.1 Appendix 1, Section 4.1.2 for crystal data). A search of the Cambridge Structural Database showed **Cry1** to be a novel class of compound. The formation of **Cry1** from the salophen ligand

Sal4 can be explained by the hypothesised mechanism shown in Scheme 28. Salophen ligand **Sal4** is presumably formed by slow hydrolysis of **Cr4** by adventitious water on prolonged standing in solution. Traces of Cr^{2+} present can result in formation of the radical anion of ligand **Sal4** which can then undergo a 6-endo-trig ring closure. Protonation, further one-electron reduction and a second protonation would then give **Cry1**.
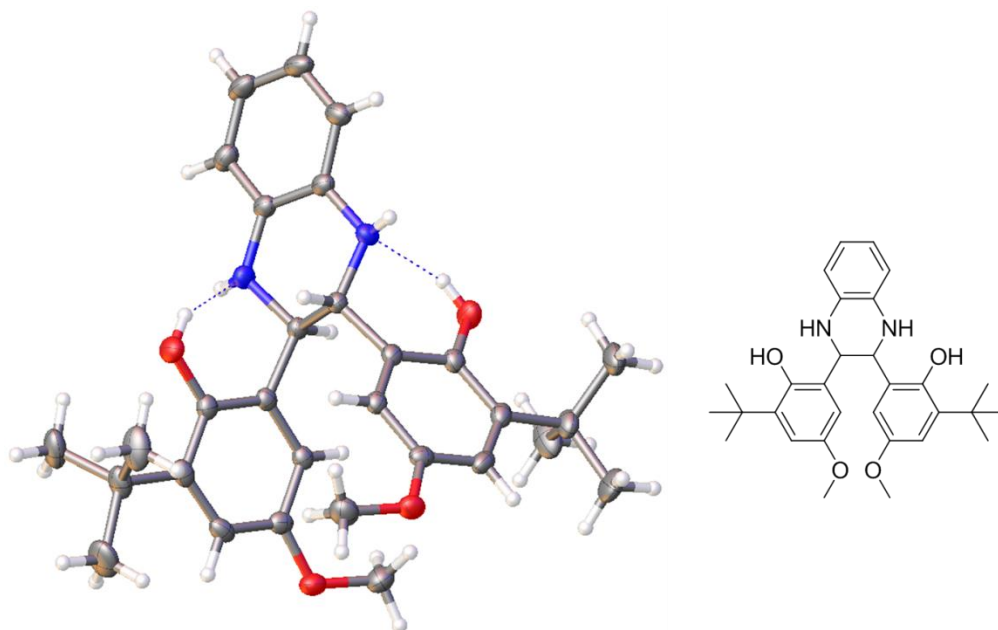
Figure 24: Ball-and-stick diagram (LHS) and structure of **Cry1** (RHS).
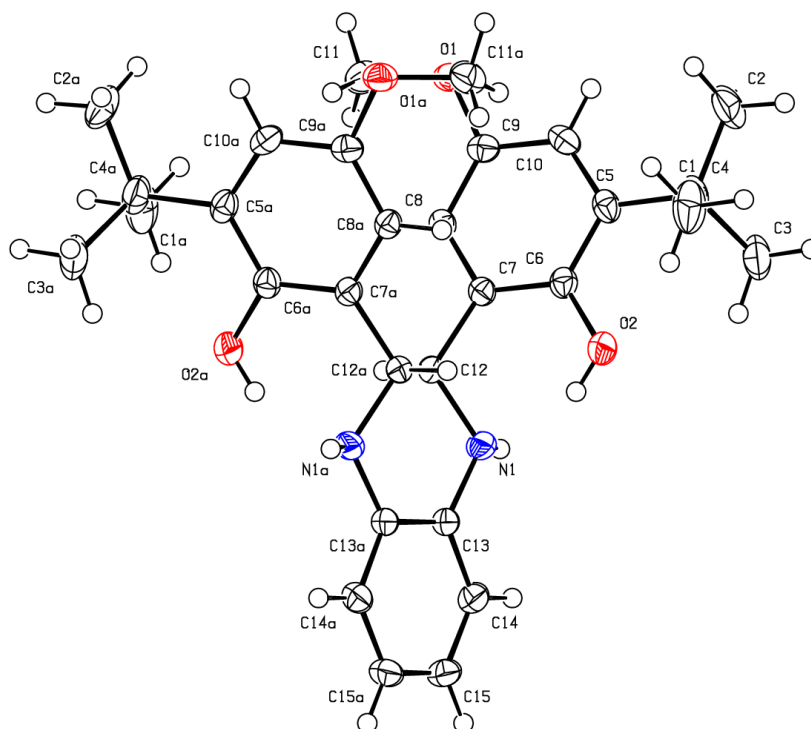
Figure 25: Thermal ellipsoid plot of **Cry1**. Ellipsoids are shown at 50% probability and structure was recorded at 110 K.
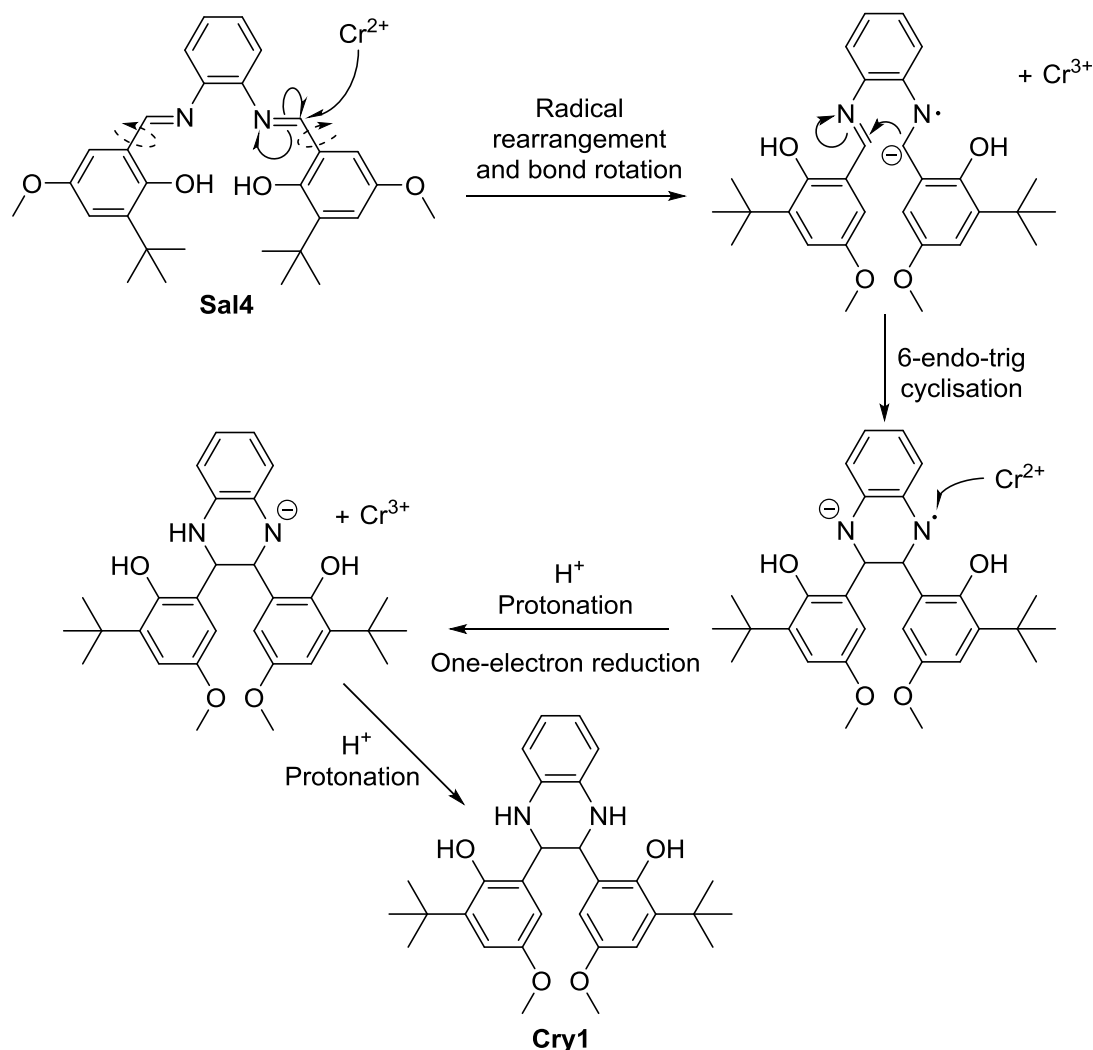
Scheme 28: Hypothesised mechanism towards the formation of **Cry1**.

Due to lack of time, no further studies on the formation of piperazine derivative **Cry1** were performed. Product **Cry1** was never detected during the synthesis or analysis of complex **Cr4**, or after **Cr4** was used catalytically to form cyclic carbonates. The potential formation of complexes such as **Cry1** should be considered for the future synthesis and long-term storage of chromium(III) salophen complexes.

2.2.7 Comparison of Results to Literature

The catalytic system of chromium(III) salophen complex **Cr11** and TBAB is fairly active compared to some catalytic systems in the literature, which were discussed in 2.1 Introduction. Catalyst **Cr11** was similar in activity to bimetallic(acen) complexes **17-19**, with conversions for styrene oxide **EP1** to styrene carbonate **CC1** reported as 85-93% after

24 h using identical reaction conditions, compared to 100% conversion with catalyst **Cr11** (Entry 2, Table 6 and Entry 1, Table 8).[81]

Aluminium amino-tris(phenolate) complex **20** only required 0.0005 mol% of catalyst and 0.05 mol% of PPNBr at 90 °C, to convert terminal epoxides such as 1,2-epoxyhexane **24** over a 2 h period with a TOF of 36 000 h^{-1}.[82] Complex **20** is therefore more active, and efficient in terms of catalytic loading, than the combination of catalyst **Cr11** and TBAB.

17: R = H
18: R-R = (CH$_2$)$_4$

19

20
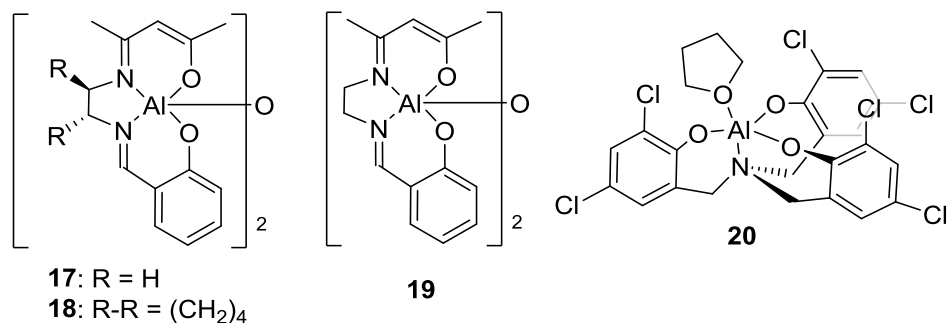
The conversion of styrene oxide **EP1** into styrene carbonate **CC1** after 24 h using catalyst **Cr11** (100%, Entry 2, Table 6 and Entry 1, Table 8) was on a par with the most active heteroscorpionate catalyst (**26**). Aluminium heteroscorpionate complexes usually require higher catalytic loadings (5 mol%) to achieve similar conversions, are more efficient with 10 bar pressure of CO_2 and 50 °C, and are not all effective in ring-opening internal epoxides.[83,84] Catalyst **Cr11** is therefore more effective at ring-opening terminal epoxides under ambient conditions and internal epoxides overall.

26
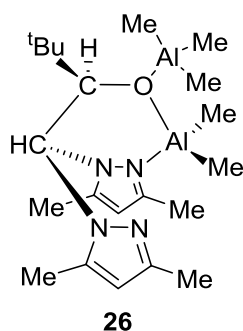
Bimetallic aluminium(III) salen complexes such as **43** form styrene carbonate **CC1** with 62% conversion and a TOF of 8.27 h^{-1} after just 3 h with 2.5 mol% of catalyst and TBAB at 25 °C, whereas catalyst **Cr11** achieved 47% conversion and a TOF of 6.27 h^{-1} under identical conditions (Entry 2, Table 6).[100] At 50 bar of CO_2 and 50 °C, complex **42** could achieve 95% conversion and 78% yield of styrene oxide **EP1** after 24 h, with just

0.5 mol% of **42** and without a co-catalyst.[102] One-component bimetallic aluminium(III) salen complex **43** could achieve 71% conversion after just 3 h with only 2.5 mol% of catalyst and no co-catalyst.[101] Catalysts **42** and **43** are therefore more active than **Cr11** with TBAB. These bimetallic catalysts however achieve lower conversions for internal epoxides into cyclic carbonates compared to catalyst **Cr11**.

42   **43**
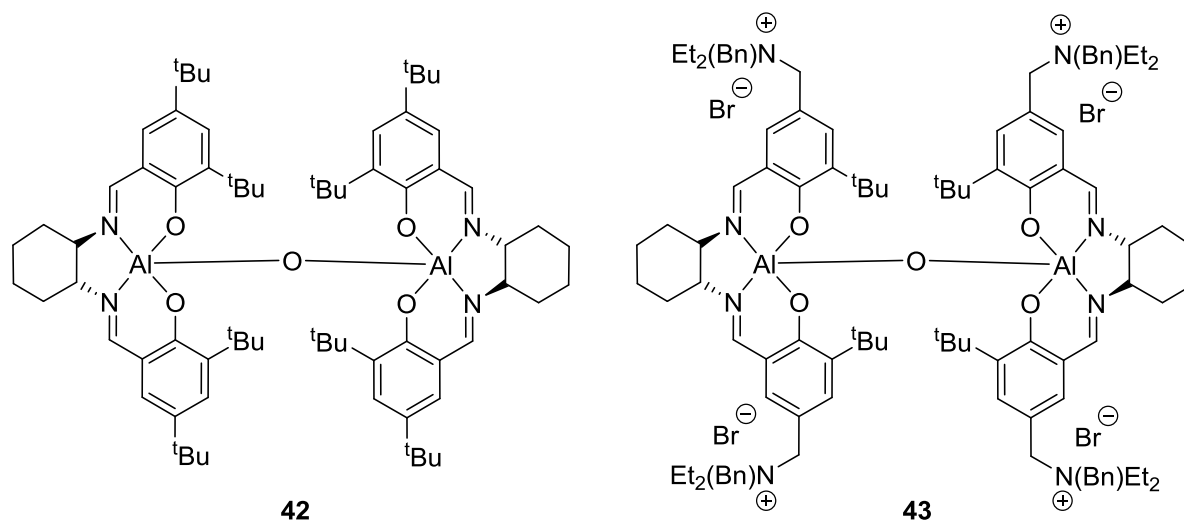
Catalyst **Cr11** with TBAB was more active than some reported monometallic chromium(III) salen complexes. Complex **27** only achieved 20% conversion under identical reaction conditions.[87] Paddock's chromium(III) salen complex **30** achieved 99% conversion of styrene oxide **EP1** into styrene carbonate **CC1** with only 1 mol% of catalyst and DMAP after 12 h.[94] This catalytic system was faster than **Cr11** with TBAB, with a TOF of 8.25 h^{-1} (after 12 h)[94] compared to 6.27 h^{-1} (after 3 h, Entry 2, Table 6). A temperature of 75 °C was used to obtain this TOF value, therefore it is unknown if **Cr11** and TBAB would be slower or quicker than **30** under identical conditions.[94]

27   **30**
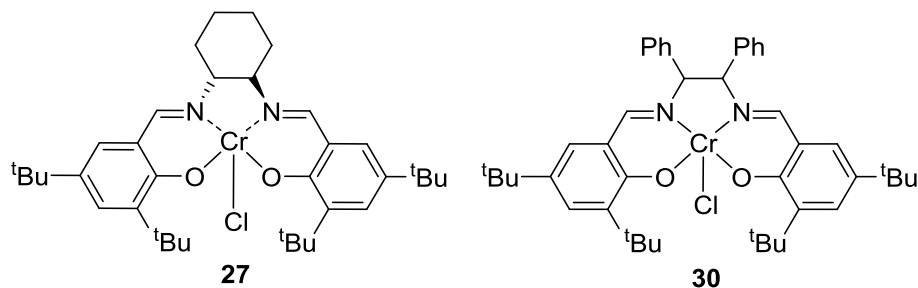
Perhaps the most similar research in the literature compared to this study was performed by the North group in 2016, when the monometallic chromium(III) (**51**) and bimetallic

aluminium(III) salophen (**57**) complexes were synthesised. Both of these complexes are extremely active in synthesising cyclic carbonates from epoxides.[105]
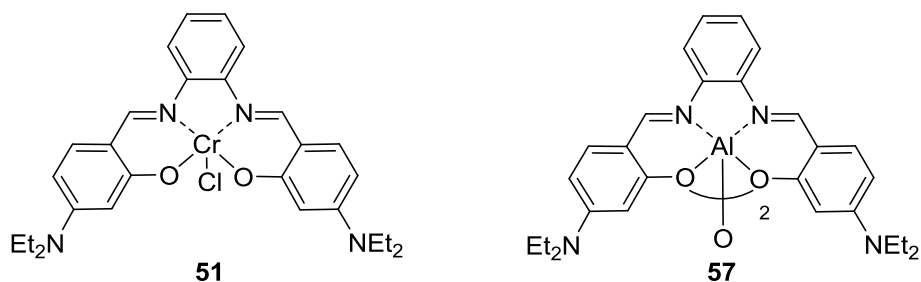
Complex **51** with TBAB was more active than **Cr11** with TBAB, achieving 63% conversion after only 3 h, compared to 47% conversion under identical conditions (Entry 2, Table 6). Complex **51** could also ring-open internal epoxides, with higher conversions and yields in comparison to catalyst **Cr11** and TBAB.[105] Complex **57** could achieve 50% conversion of styrene oxide **EP1** to styrene carbonate **CC1**, after 3 h at 25 °C and 1 bar CO_2 pressure with only 1.5 mol% of **57** and TBAB, and obtained 41-97% conversion for numerous terminal epoxides using the same conditions. Complex **57** and TBAB therefore provide a more active catalytic system than **Cr11** and TBAB. Complex **57** could also ring-open internal epoxides, under identical conditions to those used with **Cr11** and TBAB, and was more active than **Cr11** and TBAB. Complex **57** however required higher catalytic loadings, such as 5 mol%, to achieve sufficient conversions for some internal epoxides compared to **51** and TBAB.

2.2.8 Conclusion and Future Work

Chromium(III) salophen complexes are suitable catalysts for the formation of cyclic carbonate from epoxides and CO_2, via green, 100% atom economy reactions, and provide an alternative and ambient CDU methodology. Cyclic carbonate formation proceeded sufficiently with gaseous CO_2 from dry ice and therefore did not require dry or extremely pure CO_2. Optimisation tests of the chromium(III) salophen structure revealed that the most active catalyst was catalyst **Cr11** with electron donating *tert*-butyl and methoxy groups on the salicylaldehyde and a bromide counterion. A catalytic loading of 2.5 mol%

for chromium(III) salophen catalysts and TBAB was required for sufficient conversions. Catalyst **Cr11** in conjunction with TBAB was capable of converting numerous terminal epoxides and CO_2 into their cyclic carbonate products under neat and ambient conditions. The conversion of internal epoxides was also possible at increase temperatures and pressures. The reaction mechanism for cyclic carbonate formation was proposed to obey first-order kinetics and occur via the formation of a six coordinate $[Cr(salophen)Br_2]^-$ type species. This catalytic system of catalyst **Cr11** and TBAB was not the most active system reported in the literature but was one of the most efficient under ambient conditions.

In terms of future work, further optimisation for cyclic carbonate synthesis could be performed. For example more reaction variables could be investigated, including catalyst to co-catalyst ratio, to determine the optimum ratio is 1:1, and temperature and pressure, to determine if increased temperature and pressures could reduce the required catalytic loading. Synthesising bimetallic chromium(III) salophen catalysts to see if these complexes could increase catalyst activity would be intriguing. In the interest of improving the recycling capability of the catalysts, placing catalysts onto a solid support so that the catalyst could be used repeatedly would be a fascinating endeavour. Further studies into the mechanism and generality of formation of **Cry1** and related piperazines would be interesting.

2.3 Results and Discussion Part 2: Oxazolidinone Synthesis

The development of new chromium(III) salophen catalysts for cyclic carbonate synthesis was successful. Synthesising catalysts which are efficient for many chemical reactions increases their economical value and usefulness overall. Many catalysts that are capable of synthesising cyclic carbonates can catalyse the formation of oxazolidinones,[84,105,129-131] which are important building blocks for pharmaceutical drugs.[132] The ability of chromium(III) salophen catalysts to synthesise oxazolidinones, specifically diphenyloxazolidin-2-one (**OX1**), was therefore investigated.

2.3.1 Screening Reaction Conditions

Solvent Use and Catalytic Loading

In the first tests conducted, catalyst **Cr3** and TBAB (the most active co-catalyst in cyclic carbonate synthesis) was chosen as the initial catalytic system to investigate, due to previous reports suggesting TBAB was an extremely efficient co-catalyst for oxazolidinone synthesis.[129,133-135] Control tests were performed in which the catalytic components were tested as separate entities and together, to ensure both were required for oxazolidinone synthesis. Eliminating the requirement of solvent for reactions is one of the main principles of green chemistry, which states "*the use of auxiliary substances (e.g., solvents) should be made unnecessary wherever possible*".[31] Therefore, tests were also performed to determine if solvent (initially acetonitrile) was required in conjunction with chromium(III) salophen catalysts and TBAB (Table 9).

As expected, control tests indicated that without a catalyst or co-catalyst, regardless of solvent presence, no product formation occurred (Entries 1-2, Table 9). Using TBAB alone was a very inactive system, giving low conversions with or without solvent (22 and 27% respectively) and preference towards the 3,5-isomer **OX1B** (Entries 3-4, Table 9).

Using catalyst **Cr3** alone resulted in a low conversion in the presence of solvent (10%, Entry 5, Table 9), but was exceptionally high in the absence of solvent (>99%, Entry 6, Table 9). The catalytic loading of **Cr3** was tested at 2.5 and 1.0 mol% without solvent to investigate whether high catalytic loadings were essential (Entries 7-8 respectively, Table 9). Conversions dropped significantly, indicating 5 mol% of catalyst was required. Catalyst **Cr3** at 5 mol% had a slight preference for the 3,5-isomer in the absence of solvent, but favoured the 3,4-isomer when the catalytic loading was decreased to 2.5 mol% (Entries 6 and 7 respectively, Table 9).

When catalyst **Cr3** and co-catalyst TBAB were used simultaneously, high conversions were obtained with or without solvent (93 and >99% respectively, Entries 9-10, Table 9).

Table 9: Screening catalyst **Cr3**, TBAB and acetonitrile in the formation of oxazolidinone **OX1**.

3,4 isomer (**OX1A**) 3,5 isomer (**OX1B**)
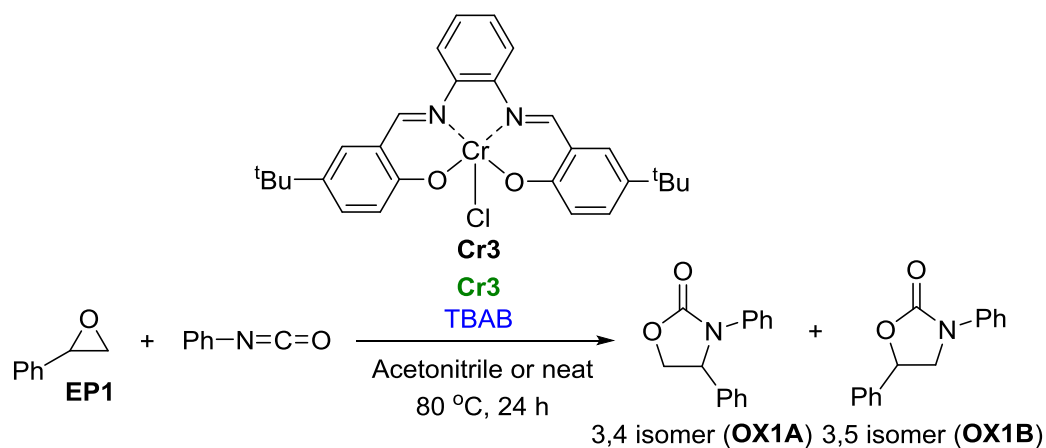
Entry[a]	Catalyst Cr3 / mol%	TBAB / mol%	Acetonitrile / mL	Conv. 24 h / % [b]	A:B ratio
1	0	0	2	0	N/A
2	0	0	0	0	N/A
3	0	5	2	22	26:74
4	0	5	0	27	40:60
5	5	0	2	10	Could not determine[c]
6	5	0	0	>99	48:52
7	2.5	0	0	42	53:47
8	1	0	0	<1	Could not determine
9	5	5	2	93	41:59
10	5	5	0	>99	64:36
11	2.5	2.5	0	64	56:44
12	1	1	0	25	49:51

a) Conversions and **A:B** ratios were obtained from ^{1}H NMR analysis of the unpurified reaction mixture
b) Conversions are quoted for both isomer A and B compared to the epoxide starting material.
c) Paramagnetic nature of catalyst **Cr3** meant that the ratio could not be determined.

The regioselectivity of the combined catalytic system appeared to be solvent dependent, as

in the presence of solvent the 3,5-isomer was favoured and in the absence of solvent the

3,4-isomer **OX1A** was favoured (Entries 9 and 10 respectively, Table 9). The combination of both catalysts with a solvent may therefore be creating a steric effect which results in ring-opening of styrene oxide **EP1** at the least hindered carbon, and thus favours the 3,5-isomer. When both catalytic ratios of catalyst **Cr3** and TBAB were lowered from 5 to 2.5 and 1.0 mol%, in the absence of solvent, the conversions dropped significantly and isomer preference changed from the 3,4-isomer to the 3,5-isomer (Entries 10-12, Table 9). When TBAB or catalyst **Cr3** were used alone the 3,5-isomer was favoured, regardless of solvent presence (Entries 3-4 and 6, Table 9). This therefore indicated that the combination of catalyst **Cr3** and TBAB at high catalytic loadings without a solvent was promoting a slight preference towards the 3,5-isomer, and with a solvent could promote slight favourability for the 3,4-isomer. The experiments which obtained the highest conversions (Entry, 6, 9 and 10, Table 9) were further purified via column chromatography, to determine the most effective reaction conditions for further optimisation tests (Table 10).

Table 10: Comparing isolated yields of oxazolidinone **OX1** using different reaction conditions.
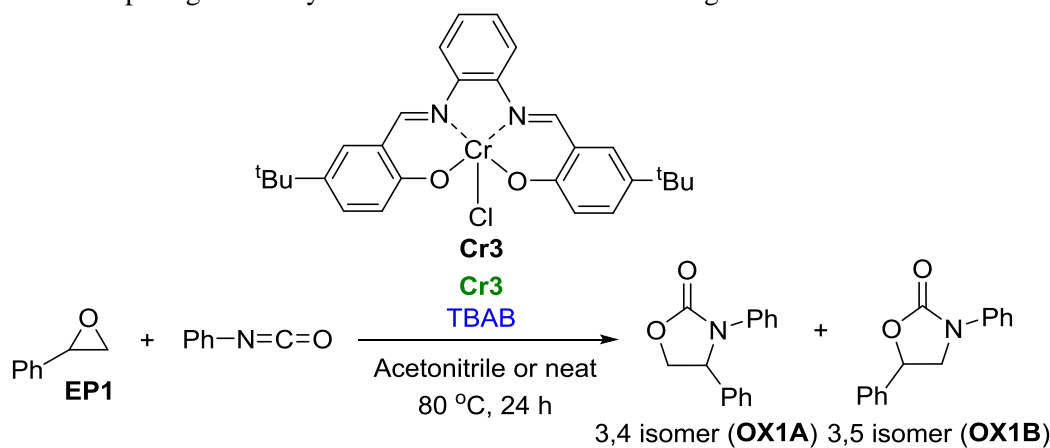
Entry[a]	Acetonitrile / mL	Conv. 24 h / %[b]	A:B ratio	Yield A / %	Yield B / %	Total yield / %
1[c]	0	>99	48 : 52	36	39	75
2[d]	2	93	41 : 59	47	39	87
3[e]	2	>99	64 : 36	47	22	69

a) Conversions and **A:B** ratios were obtained from ^{1}H NMR analysis of the unpurified reaction mixture
b) Conversions are quoted for both isomer A and B compared to the epoxide starting material.
c) No TBAB was used (Entry 6 in Table 9).
d) TBAB was used at 5 mol% (Entry 9 in Table 9).
e) TBAB was used at 5 mol% (Entry 10 in Table 9).

The isolated yields for oxazolidinone **OX1** were reasonable (Entries 1-3, Table 10), with the highest yield reported when 5 mol% of both catalyst and co-catalyst were used in the presence of acetonitrile (Entry 2, Table 10). This matched well with previous literature reports indicating that solvent with a catalyst and co-catalyst was required for high conversions.[129] Catalyst **Cr3** and TBAB, both at 5 mol% in the presence of a solvent were therefore used in further tests.

Solvent Screening

After deciding upon the use of a solvent, numerous solvents were trialled in the formation of oxazolidinone **OX1** (Table 11). Non-polar and alternative green solvents were examined in the interest of achieving high conversions whilst promoting sustainability. A low catalytic loading of 1 mol% of both catalyst **Cr3** and TBAB were used in order to monitor differences in conversion more effectively (Table 11).

The non-polar solvent toluene provided the highest conversion (Entry 3, Table 11), compared to the standard organic solvents ethyl acetate and acetonitrile (Entries 1-2, Table 11), similar to previous findings in the literature.[129,133,136] Non-polar solvents are often used instead of polar solvents, despite sometimes obtaining slower conversions, as they promote the synthesis of oxazolidinones whilst preventing side reactions such as isocyanate trimerisation.[136] Cyclic and acyclic carbonates have been highlighted as alternative green solvents,[37,45] and can also be used as an alternative solvent to toluene.[129] When ethylene, propylene, dimethyl and diethyl carbonate were tested (EC, PC, DMC and DEC respectively), no increase in conversion was observed (Entries 4-7, Table 11). Using *p*-cymene was disastrous (Entry 8, Table 11). As expected, isomer regioselectivity changed for each solvent (Entries 1-8, Table 11). Toluene was therefore deemed the most suitable solvent to use in all further tests.

Table 11: Screening solvents in the synthesis of oxazolidinone **OX1**.
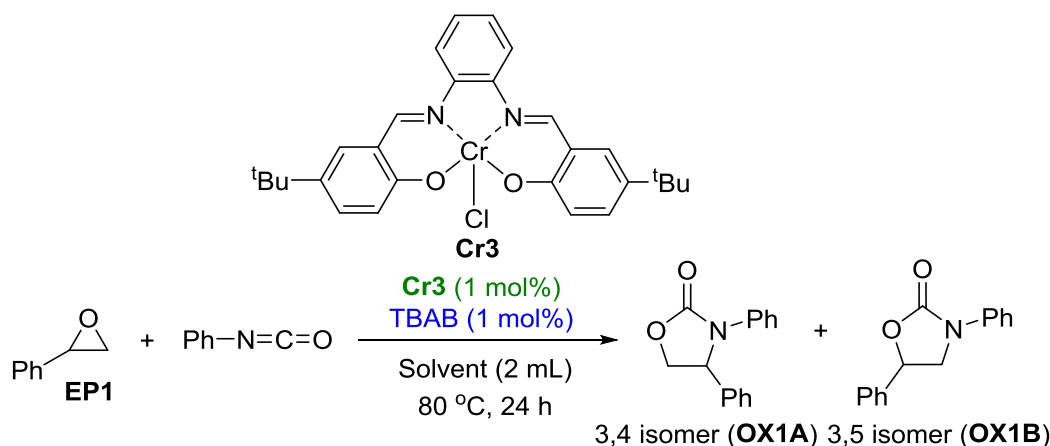
Entry[a,b]	Solvent / 2 mL	Conv. 24 h / %[c]	A:B ratio
1	Ethyl acetate	60	52 : 48
2	Acetonitrile	63	65 : 35
3	Toluene	69	43 : 57
4	EC	45	54 : 46
5	PC	45	64 : 36
6	DMC	36	53 : 47
7	DEC	29	47 : 53
8	*p*-Cymene	5	Could not determine

a) Conversions and **A:B** ratios were obtained from ^{1}H NMR analysis of the unpurified reaction mixture
b) Both catalyst **Cr3** and TBAB were used at 1 mol% to see differences in conversion more clearly.
c) Conversions are quoted for both isomer A and B compared to the epoxide starting material.

2.3.2 Screening Catalysts

To investigate if chromium(III) salophen catalysts with different functional groups could synthesise **OX1**, six catalysts (**Cr1-Cr3**, **Cr6-Cr8**) were trialled using the optimised reaction conditions of 5 mol% of catalyst and TBAB in toluene at 80 °C for 24 h (Table 12). All six catalysts were able to synthesise **OX1** (Entries 1-6, Table 12). Intriguingly, only catalyst **Cr8** showed a major difference in catalytic conversion, reaching 78%

conversion after 24 h (Entry 6, Table 12), compared to >99% conversion with catalysts **Cr1-Cr3** and **Cr6-Cr8** (Entries 1-5, Table 12).

Table 12: Screening different catalysts in the formation of oxazolidinone **OX1**.

Cr1: R_1 = H, R_2 = H, R_3 = H
Cr2: R_1 = H, R_2 = ^{t}Bu, R_3 = H
Cr3: R_1 = H, R_2 = H, R_3 = ^{t}Bu
Cr6: R_1 = Me, R_2 = H, R_3 = H
Cr7: R_1 = Cl, R_2 = H, R_3 = H
Cr8: R^1 = -(CH)$_4$-, R_2 = H, R_3 = H

Cr1-Cr3; Cr6-Cr8

3,4 isomer (**OX1A**) 3,5 isomer (**OX1B**)
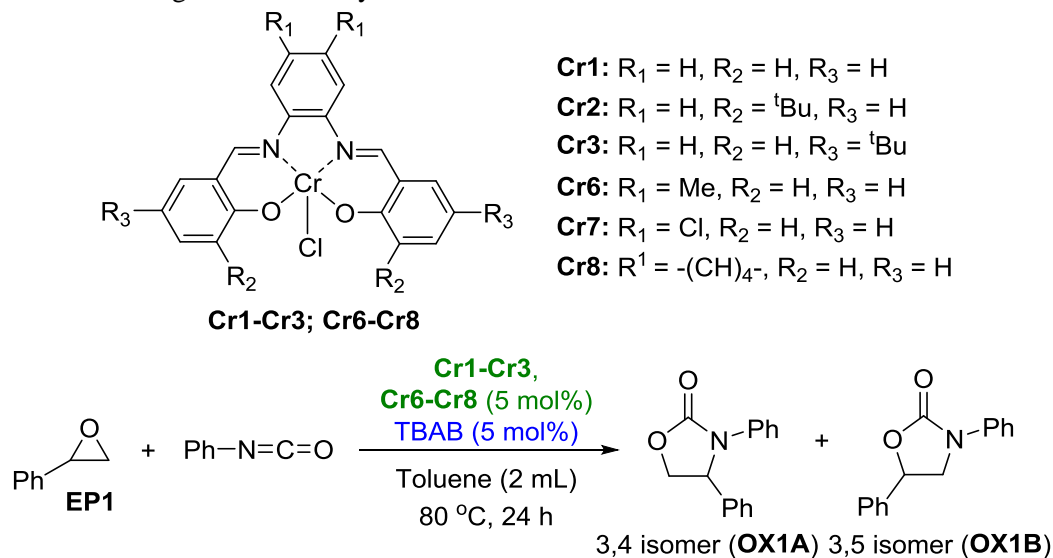
Entry[a]	Catalyst	Conv. 24 h / %[b]	A:B ratio	Yield A / %	Yield B / %	Total yield[c] / %
1	**Cr1**	>99%	55 : 45	62	29	91
2	**Cr2**	>99%	54 : 46	54	44	98
3	**Cr3**	>99%	53 : 47	56	34	90
4	**Cr6**	>99%	53 : 47	50	31	81
5	**Cr7**	>99%	55 : 45	59	30	89
6	**Cr8**	78%	51 : 49	23	33	56

a) Conversions and **A:B** ratios were obtained from ^{1}H NMR analysis of the unpurified reaction mixture
b) Conversions are quoted for both isomer A and B compared to the epoxide starting material.
c) Yields quoted are isolated yields, obtained by purifying the reaction mixture via column chromatography.

The electronic and steric importance of functional groups on the catalysts appeared insignificant, as most catalysts reached >99% conversion after 24 h. All six catalysts also showed a slight preference for the formation of the 3,4-isomer, whereas the 3,5-isomer was favoured with 5 mol% of catalyst **Cr3** and co-catalyst in the presence of acetonitrile (Entry 9, Table 9). This again indicated that regioselectivity was solvent dependent. The highest total yield reported was 98% when catalyst **Cr2** was employed (Entry 2, Table 12).

Due to using a high loading of catalyst and co-catalyst for each run, it was difficult to determine which catalyst provided the fastest conversions. Experiments were therefore conducted in which only 2.5 mol% of catalyst and co-catalyst was used, in order to analyse differences in activity between catalysts **Cr1**-**Cr3** and **Cr6**-**Cr8** more easily (Table 13).

Table 13: Screening different catalysts in the formation of oxazolidinone **OX1**.

Cr1: R_1 = H, R_2 = H, R_3 = H
Cr2: R_1 = H, R_2 = ^{t}Bu, R_3 = H
Cr3: R_1 = H, R_2 = H, R_3 = ^{t}Bu
Cr6: R_1 = Me, R_2 = H, R_3 = H
Cr7: R_1 = Cl, R_2 = H, R_3 = H
Cr8: R^1 = -(CH)$_4$-, R_2 = H, R_3 = H

Cr1-Cr3; Cr6-Cr8

3,4 isomer (**OX1A**) 3,5 isomer (**OX1B**)
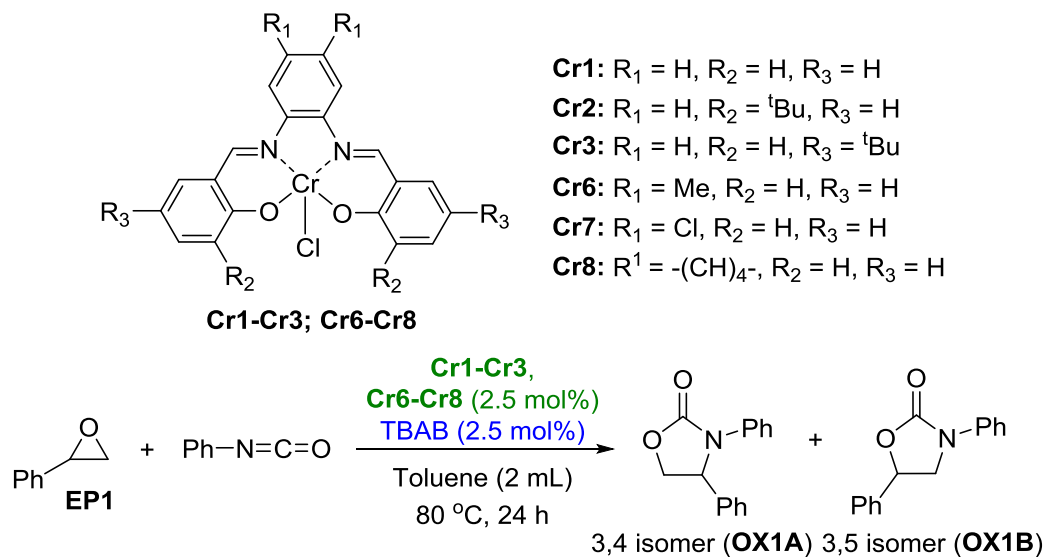
Entry[a,b]	Catalyst	Conv. 3 h / %	Conv. 6 h / %	Conv. 24 h / %	A:B ratio
1	**Cr1**	55	67	82	48 : 52
2	**Cr2**	67	73	86	51 : 49
3	**Cr3**	39	48	64	47 : 53
4	**Cr6**	47	68	84	54 : 46
5	**Cr7**	24	36	55	51 : 49
6	**Cr8**	10	17	27	46 : 54

a) Conversions and **A:B** ratios were obtained from ^{1}H NMR analysis of the unpurified reaction mixture
b) Conversions are quoted for both isomer A and B compared to the epoxide starting material.

Varying the steric and electronic effects of functional groups on chromium(III) salophen complexes influences oxazolidinone synthesis (Entries 1-6, Table 13). The activity trends reported (when considering conversions reported after 3 h) for salicylaldehyde group was ortho *tert*-butyl > H > para *tert*-butyl (Entries 1-3, Table 13) and for diamine backbone

groups was methyl > chloride > naphthalene (Entries 4-6, Table 13). This trend was similar to the isolated yields reported when 5 mol% of catalysts **Cr1-Cr3** and **Cr6-Cr8** was used with TBAB (Table 12). The fastest catalyst overall (during the early stages of the reaction) was **Cr2** (Entry 2, Table 13) potentially due to the *tert*-butyl group's electron donating +I inductive effect pushing electron density onto the chromium metal.

When comparing conversion reported for catalyst **Cr2** compared to **Cr1** and **Cr3**, conversion dropped slightly when the *tert*-butyl group was in the para position (**Cr3**, Entry 3, Table 13) but was on a par when only hydrogens were present (**Cr1**, Entry 1, Table 13). The electronic properties of salicylaldehyde functional groups therefore have an effect on oxazolidinone synthesis, whereas steric effects appeared to have less influence.

In terms of varying the diamine backbone groups, steric and electronic effects influence reaction conversion (Entries 4-6, Table 13). When considering catalysts **Cr6-Cr8**, placing methyl groups onto the catalyst created a more active catalyst (**Cr6**, Entry 4, Table 13). This suggests that the +I inductive effect of the methyl groups was beneficial for the reaction. The slowest catalyst (and overall) was **Cr8** (Entry 6, Table 13). The presence of an extra aromatic ring on the diamine backbone may hinder product formation due to steric effects, and may also explain why there was a drop in activity with Cl groups on the diamine backbone (**Cr7**, Entry 5, Table 13). Differences in solubility of the catalysts in acetonitrile would also undoubtedly affect the conversion.

Interestingly, preferences in isomer formation changed with catalytic loading (as previously reported) and for each catalyst, with no overall distinct trend (Entries 1-6, Table 13). Subtle differences in catalyst electronic and steric effects may therefore affect product formation. As only a handful of catalysts were analysed, and no kinetic study into the reaction mechanism was performed, these differences in regioselectivity were unclear.

2.3.3 Comparison of Results to Literature

This catalytic system was not the most active system reported for oxazolidinone **OX1** synthesis but nevertheless was reasonably active. The catalytic loading required was low compared to reported catalytic systems and did not require toxic solvents. For example in 2010, Chen *et al.* reported that 50 mol% of MgI_2 etherate was required for good conversions,[137] and Baba reported using antimony catalysts such as Ph_4SbI in the extremely toxic solvent benzene to obtain sufficient conversions.[138]

In terms of conversions, more active catalysts have been reported. For example, in 2014 North reported that vanadium(V) salen complexes and TBAB were capable of synthesising oxazolidinones. In forming diphenyloxazolidin-2-one (**OX1**), conversions of 90% were reported using **68** under the same reaction conditions employed in this study after only 4 h.[135] Both vanadium(V) salen catalysts **68** and **69** were more active than catalysts **Cr1**-**Cr3** and **Cr6**-**Cr8**, as catalyst **68** obtained higher conversions in the absence of TBAB compared to **Cr3** (26% after 4 h vs 10% after 24 h, Entry 5, Table 9). Only 1 mol% of the more active vanadium(V) salen catalyst **69** and co-catalyst would achieve 90% conversion after 24 h, whereas 5 mol% of **Cr3** was required to reach high conversions (Table 9).[135]
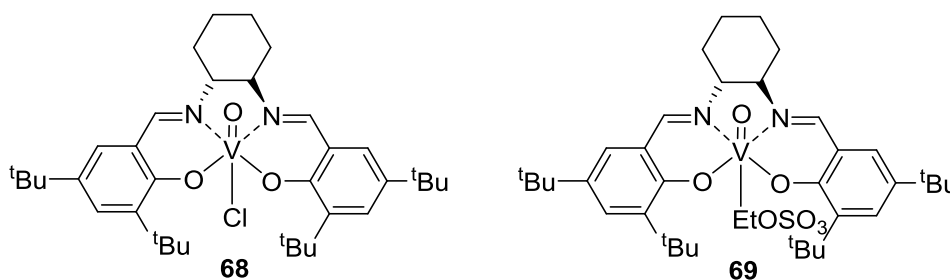
Paddock's chromium(III) salen complex **27** is more active than the tested chromium(III) salophen complexes. Complex **27** only required 3 mol% of catalyst, and triphenylphosphine oxide (PPh$_3$O) as a co-catalyst, to achieve 85-100% isolated yield of numerous oxazolidinones (99% of **OX1**) at 60 °C after 6 h.[136]

Catalysts **Cr1**-**Cr3** and **Cr6**-**Cr8** were more active than monometallic aluminium salen complexes **70-72**, which are all inactive in forming oxazolidinones, but were less active

than bimetallic aluminium(III) salen complex **42**, which could give 100% conversion for **OX1** with no co-catalyst under the same reaction conditions.[133] The activity of these catalysts were on a par with aluminium heteroscorpionate complexes such as **73**, which obtained 100% conversion for **OX1** under the same conditions used in this study.[129]

27

70: X = Et
71: X = OEt
72: X = Cl

42

73
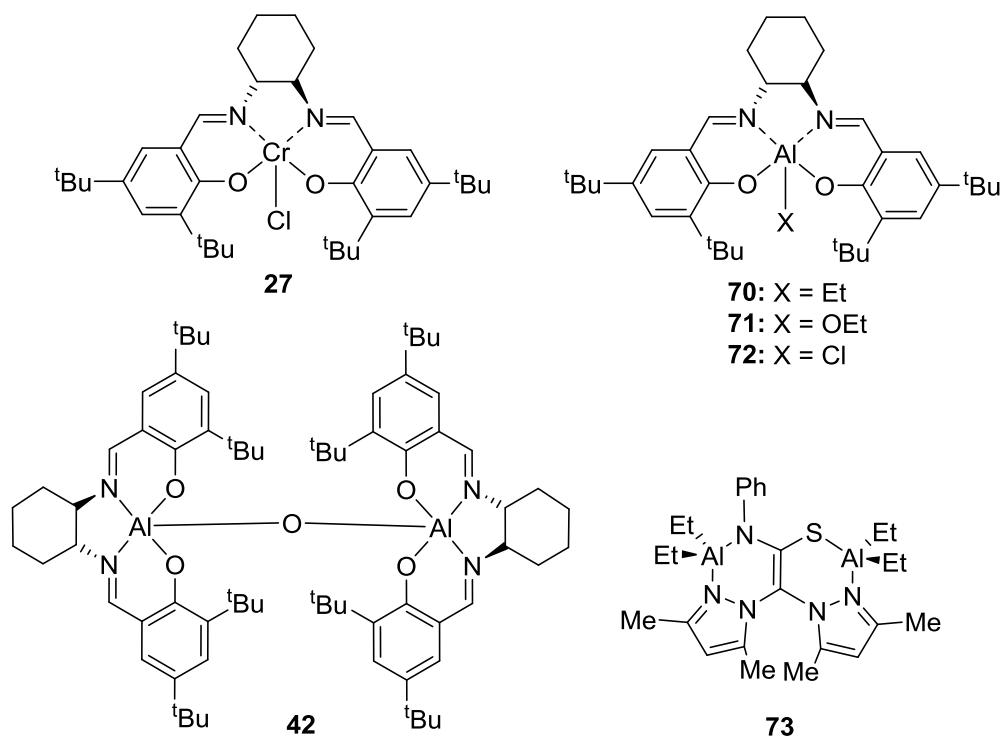
The catalytic system of chromium(III) salophen complexes and TBAB varied in regioselectivity, with no clear trend or overall preference for the 3,4-isomer or 3,5-isomer of diphenyloxazolidin-2-one (**OX1**) reported (Table 13). This was different to systems developed by Chen[137] or Baba,[138,139] who reported selective formation of the 3,4-isomer.

North also reported a preference for the 3,4-isomer when ring-opening styrene oxide **EP1** with vanadium(V) salen complexes and TBAB. In the case of styrene oxide **EP1**, the 3,4-isomer is usually favoured, despite the steric hindrance of the phenyl group, as ring-opening is electronically preferred at the secondary carbon atom, or benzylic C_α-O bond.[133,140,141] Variations in isomer preference is however not uncommon, and was reported by Paddock and North for chromium(III) salen complexes[136] and certain mononuclear aluminium heteroscorpionate complexes respectively.[129] It was predicted that sterically hindered aluminium centres in certain aluminium heteroscorpionate complexes

favoured ring-opening at the least sterically hindered carbon and hence the 3,5-isomer of diphenyloxazolidin-2-one, despite the electronic favourability of forming the 3,4-isomer.[129] Subtle steric effects in chromium(III) salophen complexes, may therefore sometimes favour the 3,5-isomer and subtle differences in electronic effects, and therefore Lewis acidity of the chromium metal, may sometimes be sufficient to drive regioselectivity towards the 3,4-isomer. The slight differences in isomer preference, and in repeated experiments (Table 12 and Table 13), may also be due to the solvent and reagents not being vigorously dried before use. Adventitious water may therefore be acting as a nucleophile and also ring-open the epoxide at the 3,5-isomer position.[141]

2.3.4 Conclusion and Future Work

Chromium(III) salophen complexes are suitable catalysts for the formation of diphenyloxazolidin-2-one (**OX1**), from styrene oxide and phenyl isocyanate, and therefore show promise in forming other oxazolidinones. Optimum reaction conditions were 5 mol% of catalyst and TBAB in the presence of toluene. Catalysts **Cr1**-**Cr3** and **Cr6-Cr8** could form oxazolidinone **OX1** with satisfactory yields, and conversions were influenced by the steric and electronic properties of the catalysts. The preferential formation of the 3,4- or 3,5-isomer of **OX1** varied with catalysts and reaction conditions. Due to time restrictions, the research into oxazolidinone synthesis using chromium(III) salophen catalysts was only an initial study, therefore a lot of questions remain unanswered.

In future work, all chromium(III) salophen complexes **Cr1**-**Cr15** should be tested in the synthesis of oxazolidinones, as only some of the catalysts tested in the synthesis of cyclic carbonates were trialled in oxazolidinone synthesis. It is therefore unknown if the most active catalyst for cyclic carbonate formation is the same for oxazolidinone synthesis. Co-catalyst screening experiments should be performed, to investigate if other co-catalysts provide a more active catalytic system, as TBAB may not the most active co-catalyst in combination with chromium(III) salophen complexes. The catalytic system of complexes

Cr1-**Cr3** and **Cr6**-**Cr8** combined with TBAB was only investigated in the formation of diphenyloxazolidin-2-one (**OX1**). Screening numerous ranges of epoxides and isocyanate combinations in order to form different oxazolidinones should therefore be pursued, to determine the versatility of these complexes in oxazolidinone synthesis. Performing a kinetic and mechanistic study into the formation of oxazolidinones would also be intriguing, in order to gain a deeper understanding of the catalytic process.

2.4 Methods and Experimental

2.4.1 General

All chemicals, including Salicylaldehyde **Ald1**, were provided by Alfa Aesar, Acros Organics, Sigma-Aldrich or Fischer Scientific and were used without further purification. Carbon dioxide was used in the form of Cardice® pellets (BOC). All reaction solvents were HPLC grade from Fischer Scientific. Solvents were dried using a Pure Solv MD-7 solvent purification system. For anhydrous conditions, all glassware was pre-dried in an oven (110-120 °C), placed *in vacuo* and then kept under an argon atmosphere. For column purification, 40-60 nm silica gel was used (Fluorochem) and monitored using aluminium backed TLC silica gel F_{254} plates (Fisher Scientific). Ultrapure water was obtained from a Milli-Q® water purification system (Purite, ONDEO, average resistivity of 18 MΩ cm^{-1} at 25 °C). In all other cases, de-ionised water was used.

2.4.2 Nuclear Magnetic Resonance (NMR) Spectroscopy

All ^{1}H, ^{13}C and ^{31}P NMR spectra were obtained from a Jeol ECS-400 or Jeol ECX-400 NMR spectrometer (400 MHz) at room temperature and analysed using MestReNova software (Mestrelab). ^{1}H NMR spectra were referenced using the CHCl$_3$ peak of CDCl$_3$ at 7.26 ppm or TMS at 0.00 ppm, and ^{13}C NMR spectra were referenced using the middle peak of the CDCl$_3$ triplet at 77 ppm.[142]

2.4.3 Mass Spectrometry (MS)

MS analysis was run using a Bruker microTOF MS, twinned with an Agilent series 1200 LC for Electrospray Ionisation (ESI) analysis, or a Water GCT Premier MS, twinned with an Agilent (HP) 7890A GC for Electron Ionisation (EI) and Liquid Injection Field Desorption ionization (LIFDI) analysis. Samples were run and analysed by Karl Heaton from the Chemistry Department at the University of York.

2.4.4 Attenuated Total Reflectance-Infrared Spectroscopy (ATR-IR)

ART-IR spectroscopy was performed using a PerkinElmer UATR Two ATR-IR spectrometer and analysed with Spectrum software (PerkinElmer). Samples were analysed neat. In the case of the mechanistic studies (Section 2.2.5), aliquots of the samples in DCM were placed onto the spectrometer and analysed.

2.4.5 Melting Points

Melting points were measured with a Stuart SMP3 (25-350 °C) or SMP20 (25-300 °C) melting point apparatus.

2.4.6 Inductively Coupled-Plasma Mass Spectrometry (ICP-MS)

Samples were digested in 5 mL of nitric acid (HNO_3, TraceSELECT® solvent grade, Sigma-Aldrich) and heated at 110 °C for 3 h. After cooling, the sample was dissolved in 100 mL of ultrapure water and diluted further if required. Samples were analysed with an Agilent 7700x ICP-MS spectrometer, using nickel sample and skimmer cones whilst under helium. Each sample was taken up for 60 s, stabilised for 40 s, and washed for 60 s (with 5% HCl for 30 s, and 2% HNO_3 for 30 s). Samples were run three times and the mean chromium ppm or ppb value was used to determine Cr% of samples. Samples were run and analysed by Dr Helen Parker, Andrea Muñoz García or Dr María García Gallarreta from the Green Chemistry Centre of Excellence at the University of York, at the Biorenewables Development Centre (BDC) in the York Science Park.

2.4.7 X-Ray Fluorescence (XRF) Analysis

XRF analysis was performed using a Horiba XGT-7000 XRF spectrometer with an Rh X-Ray generator. Analysis was performed with no X-Ray filter, a pre-set time of 60 s, and an X-Ray voltage of 30 keV with a beam size of 1.2 mm. The spectrometer was calibrated to quantify chromium and halide concentrations, using standards with known chromium and/or halide concentrations, which were mixed together with a pestle and mortar and then pelletised. Intensity (cps/mA) of the desired element was plotted vs known element concentrations to produce calibration curves (Figure 26).
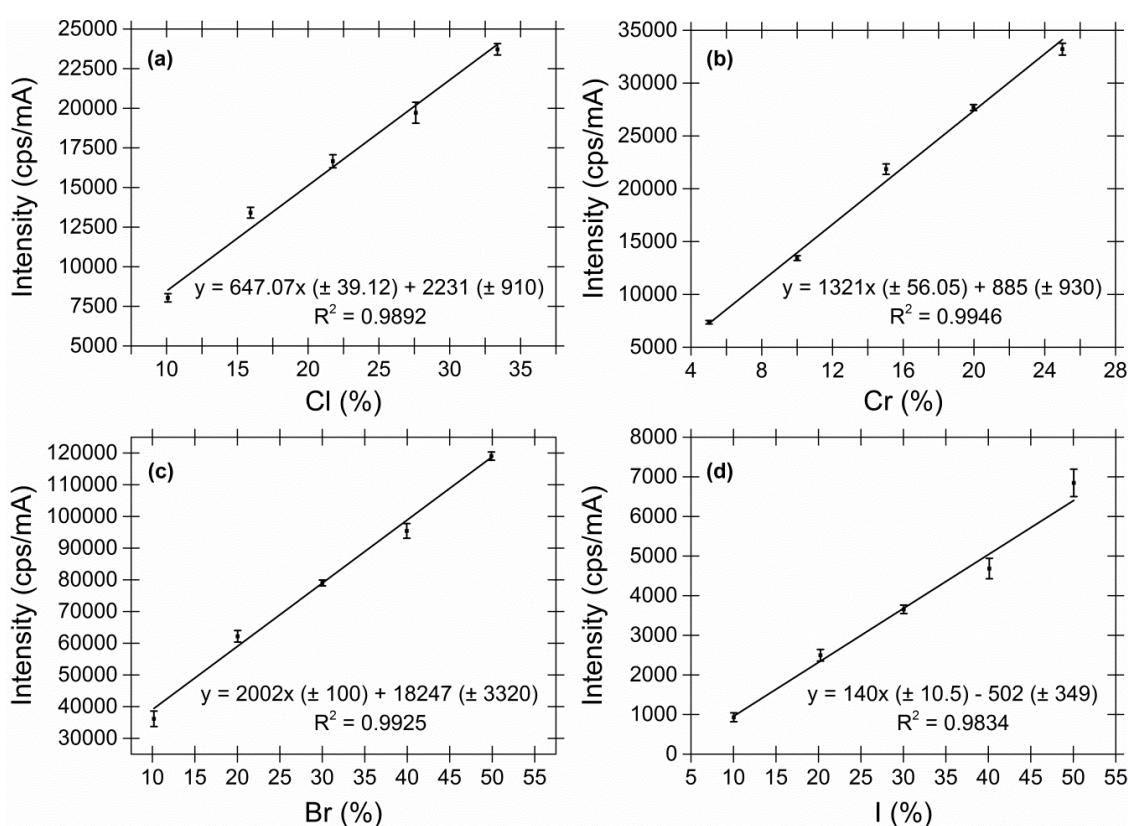
Figure 26: XRF calibration curve for (a) Cl (10-33%), (b) Cr (5-25%), (c) Br (10-50%), and (d) I (10-50%).

Samples and standards were analysed eight times, and the average intensity value was used in subsequent calculations.

2.4.8 HPLC (High Performance Liquid Chromatography) Spectroscopy

All HPLC analysis was performed by Dr José Antonio Castro-Osma to determine reaction kinetics. Analysis was performed using an Agilent 1220 instrument fitted with a diode-

array detector using a Chiralcel OD column (25 cm by 4.6 mm), using hexane/isopropyl alcohol (80:20 v/v) as eluent and a flow rate of 1 mL min^{-1}.[112]

2.4.9 Reaction Kinetics

Styrene oxide **EP1** (0.2 g, 1.66 mmol), catalyst **Cr11** (1, 2, 3, 4 or 5 mol%) and TBAB (1, 2, 3, 4 or 5 mol%) were placed in a sample vial fitted with a magnetic stirrer bar and placed in a large conical flask. Cardice$^{®}$ pellets were added to the conical flask which was then fitted with a rubber stopper, with a needle inserted through the rubber seal and a deflated balloon attached to the needle (see Section 2.4.13 for further information). The reaction mixture was stirred at 50 °C. Samples were taken at convenient intervals (approximately every 30 min) and analysed by HPLC.[112]

2.4.10 Ultraviolet-Visible (UV-Vis) Spectroscopy

UV-Vis spectroscopy was performed using a Shimadzu UV-1800 spectrometer. Analysis was performed in solution using Quartz UV-Vis cells (Starna Scientific, 1 cm).

2.4.11 Synthesis towards Chromium(III) Salophen Catalysts

Synthesis of Aldehydes: General Procedure
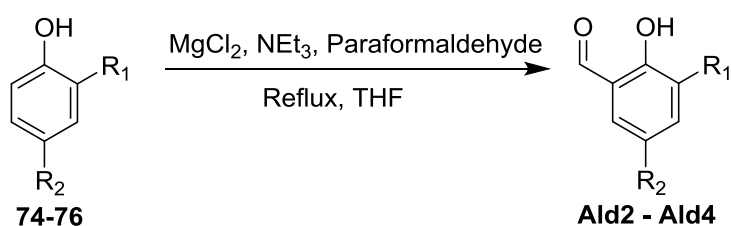
Ald2: R$_1$ = ^{t}Bu, R$_2$ = H; **Ald3**: R$_1$ = H, R$_2$ = ^{t}Bu;
Ald4: R$_1$ = ^{t}Bu, R$_2$ = OMe

Salicylaldehydes were synthesised by a magnesium chloride-triethylamine *ortho*-formylation reaction.[143] The phenol **74-76** dissolved in THF was added to a stirring solution of MgCl$_2$ (2 equiv.) and paraformaldehyde (2 or 6 equiv.) in THF. Triethylamine (2 equiv.) was added dropwise then the reaction mixture was refluxed (16 h). Water was then added before extracting with CH$_2$Cl$_2$, with the addition of sat. aq. NH$_4$Cl or brine if required to aid layer separation. The CH$_2$Cl$_2$ layer was dried (MgSO$_4$) and then

concentrated *in vacuo* to afford an impure product, which was purified by column chromatography.

3-(Tert-butyl)-2-hydroxybenzaldehyde (Ald2)[144]

Synthesised by the general procedure, using $MgCl_2$ (19.02 g, 0.20 mol) and paraformaldehyde (19.01 g, 0.63 mol) both dissolved in THF (150 mL), 2-*tert*-butyl phenol **74** (15.00 g, 0.10 mol) dissolved THF (50 mL) and triethylamine (27.85 mL, 20.12 g, 0.20 mol). An aliquot (3.71 g) of the isolated impure product (a dark orange oil, 20.35 g) was purified via column chromatography with hexane:CH_2Cl_2 (1:1) to afford the product.

Yield: 1.25 g (light orange oil, 34%, calculated on the basis that the aliquot purified was representative of purifying the whole sample).

R_f (hexane:CH_2Cl_2, 3:1): 0.37.

^{1}H NMR (400 MHz): δ_H(CDCl$_3$) 11.71 (1H, s, OH), 9.71 (1H, s, CHO), 7.39 (1H, dd, J = 7.7, 1.6 Hz, ArH), 7.24 (1H, dd, J = 7.7, 1.6 Hz, ArH), 6.80 (1H, t, J = 7.7 Hz, ArH), 1.30 (9H, s, C(CH$_3$)$_3$) ppm.

^{13}C NMR (100 MHz): δ_C(CDCl$_3$) 196.99 (CHO), 161.07 (C-OH), 138.04 (ArC), 133.96 (ArC), 131.86 (ArC), 120.54 (ArC), 119.11 (ArC), 34.71 (CMe$_3$), 29.09 (C(CH$_3$)$_3$) ppm.

Mass Spec EI: Calc: [C$_{11}$H$_{14}$O$_2$]$^+$: 178.0994 (M$^+$), found: 178.0993.

IR (selected absorbances): 2958, 2912, 2871 (C-H alkyl), 1649 (C=O), 1431 (C=C aromatic), 1195 (C-O), 854 (C-H) cm^{-1}.

5-(Tert-butyl)-2-hydroxybenzaldehyde (Ald3)[144]

Synthesised by the general procedure, using $MgCl_2$ (3.80 g, 0.04 mol) and paraformaldehyde (1.32 g, 0.04 mol) both dissolved in THF (60 mL), 4-*tert*-butyl phenol **75** (3.00 g, 0.02 mol) dissolved in THF (50 mL) and triethylamine (5.57 mL, 4.04 g, 0.04

mol). The isolated impure product (a dark brown oil, 3.82 g) was purified via column chromatography with hexane:CH_2Cl_2 (1:1) to afford the product.

Yield: 1.82 g (light yellow oil, 51%).

R_f (hexane:CH_2Cl_2, 3:1): 0.24.

^{1}H NMR (400 MHz): δ_H(CDCl$_3$) 10.78 (1H, s, OH), 9.76 (1H, s, CHO), 7.46 (1H, dd, J = 8.7, 2.5 Hz, ArH), 7.40 (1H, d, J = 2.5 Hz, ArH), 6.80 (1H, d, J = 8.7 Hz, ArH), 1.21 (9H, s, C(CH$_3$)$_3$) ppm.

^{13}C NMR (100 MHz): δ_C(CDCl$_3$) 196.99 (CHO), 159.32 (C-OH), 142.55 (ArC), 134.52 (ArC), 129.61 (ArC), 119.87 (ArC), 117.05 (ArC), 33.92 (CMe$_3$), 31.08 (C(CH$_3$)$_3$) ppm.

Mass Spec EI: Calc: [C$_{11}$H$_{14}$O$_2$]$^+$: 178.0994 (M$^+$), found: 178.0993.

IR (selected absorbances): 2962, 2868 (C-H alkyl), 1652 (C=O), 1483 (C=C aromatic), 1263 (C-O), 832 (C-H) cm^{-1}.

3-(Tert-butyl)-2-hydroxy-5-methoxybenzaldehyde (Ald4)[145]

Synthesised by the general procedure, using MgCl$_2$ (12.02 g, 0.13 mol) and paraformaldehyde (16.92 g, 0.56 mol) both dissolved in THF (140 mL), 2-*tert*-butyl-3-methoxyphenol **76** (15.01 g, 0.08 mol) dissolved in THF (50 mL) and triethylamine (44 mL, 31.94 g, 0.31 mol). An aliquot (5.01 g) of the isolated impure product (a dark brown oil, 18.16 g) was purified via column chromatography using hexane:ethyl acetate (6:1) to afford the product.

Yield: 4.21 g (light orange oil, 84%, calculated on the basis that the aliquot purified was representative of purifying the whole sample).

R_f (hexane:CH_2Cl_2, 6:1): 0.42.

¹H NMR (400 MHz): δ$_H$(CDCl₃) 11.51 (1H, s, OH), 9.84 (1H, s, CHO), 7.18 (1H, d, *J* = 3.1 Hz, ArH), 6.82 (1H, d, *J* = 3.1 Hz, ArH), 3.81 (3H, s, O-Me), 1.41 (9H, s, C(CH₃)₃) ppm.

¹³C NMR (100 MHz): δ$_C$(CDCl₃) 196.62 (CHO), 156.16 (COH), 151.98 (ArC), 140.11 (ArC), 123.84 (ArC), 119.76 (ArC), 111.64 (ArC), 55.72 (O$\underline{C}$H₃), 34.59 ($\underline{C}$Me₃), 29.06 (C($\underline{C}$H₃)₃) ppm.

Mass Spec EI: Calc: $[C_{12}H_{16}O_3]^+$: 208.1099 (M⁺), found: 208.1109.

IR (selected absorbances): 2999, 2953, 2836 (C-H alkyl), 1651 (C=O), 1428 (C=C aromatic), 1228 (C-O), 1056 (C-O-CH₃) cm⁻¹.

3-(Tert-butyl)-2-hydroxy-5-nitrobenzaldehyde (Ald5)[146,147]
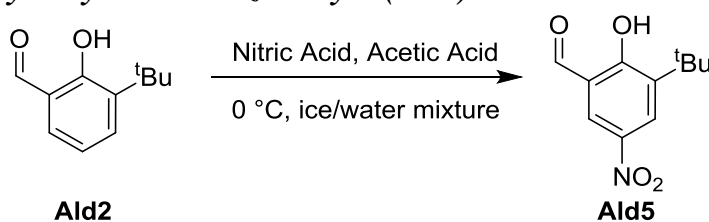
Unpurified 3-(*tert*-butyl)-2-hydroxybenzaldehyde **Ald2** (6.26 g, 0.04 mol) was added to a stirring solution of glacial acetic acid (99.8%, 50 mL, 52.45 g, 0.87 mol) at 0 °C to form a light orange solution. Nitric acid (30 mL, 42.39 g, 0.68 mol) was added to the reaction mixture dropwise over 30 min to form a dark brown/orange solution. The solution was then left to reach room temperature over 2 h. The reaction mixture was added to an ice/water mixture (200 mL) to form a light orange precipitate. This precipitate was collected and washed with water (200 mL). The isolated product was dissolved in acetone and concentrated *in vacuo* to afford a dark coloured foam (5.16 g). The product was purified via column chromatography with hexane:ethyl acetate (6:1).

Yield: 2.12 g (yellow solid, 24%).

***R**$_f$* (hexane:CH₂Cl₂, 6:1): 0.23.

^{1}H NMR (400 MHz): δ$_H$(CDCl$_3$) 12.44 (1H, s, OH), 9.97 (1H, s, CHO), 8.41-8.42 (2H, m, ArH), 1.46 (9H, s, C(CH$_3$)$_3$) ppm.

^{13}C NMR (100 MHz): δ$_C$(CDCl$_3$) 196.22 (CHO), 165.82 (C-OH), 140.66 (ArC), 131.47 (ArC), 128.68 (ArC), 127.88 (ArC), 119.32 (ArC), 35.37 (CMe$_3$), 28.83 (C(CH$_3$)$_3$) ppm.

Mass Spec EI: Calc: [C$_{11}$H$_{13}$NO$_4$]$^+$: 223.0845 (M$^+$), found: 223.0852.

IR (selected absorbances): 2955, 2857 (C-H alkyl), 1660 (C=O), 1560 (NO$_2$), 1428 (C=C aromatic), 1320 (NO$_2$), 1282 (C-O), 723 (C-H) cm^{-1}.

Melting point: 88.9-89.9 °C, literature: 90.4-91.0 °C.[148]

Synthesis of Salophen Ligands: General Procedure
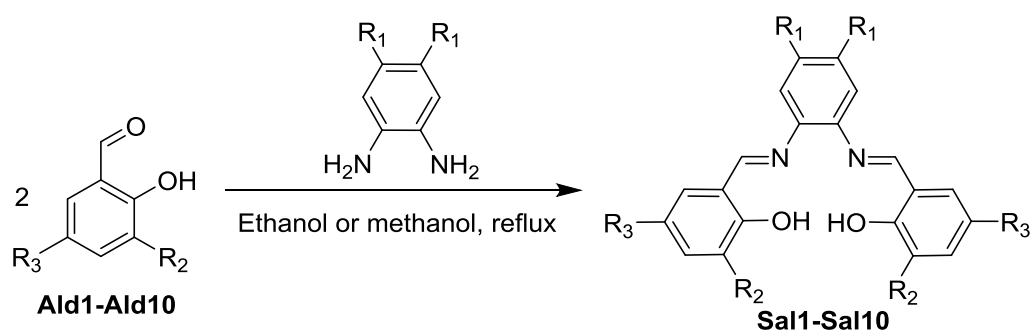
1: R$_1$ = H, R$_2$ = H, R$_3$ = H; **2**: R$_1$ = H, R$_2$ = ^{t}Bu, R$_3$ = H; **3**: R$_1$ = H, R$_2$ = H, R$_3$ = ^{t}Bu;
4: R$_1$ = H, R$_2$ = ^{t}Bu, R$_3$ = OMe; **5**: R$_1$ = H, R$_2$ = ^{t}Bu, R$_3$ = NO$_2$; **6**: R$_1$ = Me, R$_2$ = H, R$_3$ = H;
7: R$_1$ = Cl, R$_2$ = H, R$_3$ = H; **8**: R$_1$ = -(CH)$_4$-, R$_2$ = H, R$_3$ = H; **9**: R$_1$ = Cl, R$_2$ = ^{t}Bu, R$_3$ = H;
10: R$_1$ = Cl, R$_2$ = ^{t}Bu, R$_3$ = OMe

The synthesis of salophen ligands was performed via condensation of a salicylaldehyde (2 equiv.) with a diamine (1 equiv.) in the minimum volume of methanol or ethanol required. The amine solution was added slowly to the salicylaldehyde solution, followed by addition of a catalytic amount of glacial acetic acid (99.8%). The solution was refluxed overnight (16 h) forming a precipitate in the reaction mixture. If required, the solid was dissolved in CH$_2$Cl$_2$, washed with water, dried (MgSO$_4$), filtered and concentrated *in vacuo* to afford the final product. Alternatively, the solid precipitate was purified via ethanol washes.

N,N'-Bis(salicylidene)-1,2-phenylenediamine (Sal1)[149]

Prepared by the general procedure, using salicylaldehyde **Ald1** (5.04 g, 4.40 mL, 0.04 mol) dissolved in ethanol (50 mL) and 1,2-diaminobenzene (2.22 g, 0.02 mol) dissolved in ethanol (30 mL). After refluxing, a precipitate was isolated from the reaction solution and purified by washing with ethanol (5 x 10 mL).

Yield: 3.56 g (orange solid, 56%).

^{1}H NMR (400 MHz): δ_H(CDCl$_3$) 12.95 (2H, br s, OH), 8.52 (2H, s, HC=N), 7.29-7.20 (4H, m, ArH), 7.16-7.09 (4H, m, ArH), 6.94 (2H, d, J = 8.0 Hz, ArH), 6.81 (2H, td, J = 7.5, 1.1 Hz, ArH) ppm.

^{13}C NMR (100 MHz): δ_C(CDCl$_3$) 163.67 (C-OH), 161.31 (C=N), 142.52 (ArC), 133.34 (ArC), 132.30 (ArC), 127.67 (ArC), 119.68 (ArC), 119.18 (ArC), 118.94 (ArC), 117.52 (ArC) ppm.

Mass Spec ESI: Calc: $[C_{20}H_{17}N_2O_2]^+$: 317.1285 (M+H$^+$), found: 317.1289.

Mass Spec ESI: Calc: $[C_{20}H_{16}N_2O_2Na]^+$: 339.1104 (M+Na$^+$), found: 339.1102.

IR (selected absorbances): 3054 (O-H), 1609 (C=O), 1479 (C=C aromatic), 1275 (C-O), 1190 (C-N), 745 (C-H) cm^{-1}.

Melting point: 164.0-164.3 °C, literature: 163.7-164.5 °C.[150]

N,N'-Bis(3-tert-butylsalicylidene)-1,2-phenylenediamine (Sal2)[149]

Prepared by the general procedure, using 3-*tert*-butyl-2-hydroxybenzaldehyde **Ald2** (0.42 g, 2.37 mmol) dissolved in ethanol (15 mL) and 1,2-diaminobenzene (0.12 g, 1.14 mmol) dissolved in methanol (5 mL). After refluxing, a precipitate was isolated from the reaction solution, dissolved in 20 mL of CH$_2$Cl$_2$ and then washed with water (2 x 30 mL). The organic layer was dried (MgSO$_4$), filtered and concentrated *in vacuo* to afford the product.

Yield: 0.32 g (orange solid, 66%).

¹H NMR (400 MHz): δ_H(CDCl₃) 13.73 (2H, s, OH), 8.66 (2H, s, HC=N), 7.38 (2H, dd, J = 7.7, 1.6 Hz, ArH) 7.35-7.32 (2H, m, ArH), 7.26-7.24 (4H, m, ArH), 6.86 (2H, t, J = 7.7 Hz, ArH), 1.44 (18H, s, 2 x C(CH₃)₃) ppm.

¹³C NMR (100 MHz): δ_c(CDCl₃) 164.30 (C-OH), 160.78 (C=N), 142.54 (ArC), 137.85 (ArC), 130.70 (ArC), 130.48 (ArC), 127.50 (ArC), 119.70 (ArC), 119.12 (ArC), 118.13 (ArC), 34.91 (CMe₃), 29.31 (C(CH₃)₃) ppm.

Mass Spec ESI: Calc: [C₂₈H₃₃N₂O₂]⁺: 429.2537 (M+H⁺), found: 429.2539.

Mass Spec ESI: Calc: [C₂₈H₃₂N₂O₂Na]⁺: 451.2356 (M+Na⁺) found: 451.2349.

IR (selected absorbances): 2944 (C-H alkyl), 1609 (C=N), 1427 (C=C aromatic), 1195 (C-O), 1106 (C-N), 741 (C-H) cm⁻¹.

Melting point: 163.3-164.0 °C.

N,N′-Bis(5-tert-butylsalicylidene)-1,2-phenylenediamine (Sal3)[149]

Prepared by the general procedure, using 5-(*tert*-butyl)-2-hydroxybenzaldehyde **Ald3** (0.51 g, 2.85 mmol) dissolved in ethanol (60 mL) and 1,2-diaminobenzene (0.14 g, 1.30 mmol) dissolved in ethanol (5 mL). After refluxing, a precipitate was isolated from the reaction solution, dissolved in 20 mL of CH₂Cl₂ and washed with water (2 x 30 mL). The organic layer was dried (MgSO₄), filtered and concentrated *in vacuo* to afford the product.

Yield: 0.27 g (orange solid, 48%).

¹H NMR (400 MHz): δ_H(CDCl₃) 12.85 (2H, s, OH), 8.64 (2H, s, HC=N), 7.41 (2H, dd, J = 8.7, 2.5 Hz, ArH) 7.36-7.31 (4H, m, ArH), 7.23 (2H, dd, J = 5.9, 3.4 Hz, ArH), 6.99 (2H, d, J = 8.7 Hz, ArH), 1.31 (18H, s, 2 x C(CH₃)₃) ppm.

13C NMR (100 MHz): δ$_c$(CDCl$_3$) 163.98 (C-OH), 159.09 (C=N), 142.81 (ArC), 141.56 (ArC), 130.85 (ArC), 128.59 (ArC), 127.49 (ArC), 119.57 (ArC), 118.46 (ArC), 117.09 (ArC), 33.98 (CMe$_3$), 31.38 (C(CH$_3$)$_3$) ppm.

Mass Spec ESI: Calc: [C$_{28}$H$_{33}$N$_2$O$_2$]$^+$: 429.2537 (M+H$^+$), found: 429.2534.

Mass Spec ESI: Calc: [C$_{28}$H$_{32}$N$_2$O$_2$Na]$^+$: 451.2356 (M+Na$^+$), found: 451.2345.

IR (selected absorbances): 2949 (C-H alkyl), 1619 (C=N), 1486 (C=C aromatic), 1352 (C-O), 1176 (C-N), 756 (C-H) cm^{-1}.

Melting point: 171.5-172.3 °C.

N,N'-Bis(3-tert-butyl-5-methoxysalicylidene)-1,2-phenylenediamine (Sal4)[151]

Prepared by the general procedure, using 3-(*tert*-butyl)-2-hydroxy-5-methoxybenzaldehyde **Ald4** (5.00 g, 0.024 mol) dissolved in methanol (15 mL) and 1,2-diaminobenzene (1.18 g, 0.011 mol) dissolved in methanol (15 mL). After refluxing, a precipitate was isolated from the reaction solution and purified by washing with ethanol (5 x 10 mL).

Yield: 3.39 g (red solid, 63%).

1H NMR (400 MHz): δ$_H$(CDCl$_3$) 13.37 (2H, s, OH), 8.63 (2H, s, HC=N), 7.34-7.31 (2H, m, ArH) 7.27-7.24 (2H, m, ArH), 7.04 (2H, d, *J* = 3.1 Hz, ArH), 6.72 (2H, d, *J* = 3.1 Hz, ArH), 3.79 (6H, s, OMe), 1.42 (18H, s, 2 x C(CH$_3$)$_3$) ppm.

13C NMR (100 MHz): δ$_c$(CDCl$_3$) 164.05 (C-OH), 155.55 (C=N), 151.36 (ArC), 142.46 (ArC), 139.58 (ArC), 127.47 (ArC), 119.80 (ArC), 119.70 (ArC), 118.53 (ArC), 111.82 (ArC), 55.81 (O-CH$_3$), 35.07 (CMe$_3$), 29.23 (C(CH$_3$)$_3$) ppm.

Mass Spec ESI: Calc: [C$_{30}$H$_{37}$N$_2$O$_4$]$^+$: 489.2748 (M+H$^+$), found: 489.2760.

Mass Spec ESI: Calc: [C$_{30}$H$_{36}$N$_2$O$_4$Na]$^+$: 511.2567 (M+Na$^+$), found: 511.2581.

IR (selected absorbances): 2943, 2907 (C-H alkyl), 1617 (C=N), 1569 (C=C aromatic), 1265 (C-O), 1058 (C-N), 747 (C-H) cm^{-1}.

Melting point: 184.7-185.8 °C.

N,N'-Bis(3-tert-butyl-5-nitrosalicylidene)-1,2-phenylenediamine (Sal5)[149]

Prepared by the general procedure, using 3-(*tert*-butyl)-2-hydroxy-5-nitrobenzaldehyde **Ald5** (0.60 g, 2.68 mmol) dissolved in ethanol (25 mL) and 1,2-diaminobenzene (0.13 g, 1.22 mmol) dissolved in ethanol (25 mL). After refluxing, a precipitate was isolated from the reaction solution and purified by washing with ethanol (3 x 10 mL).

Yield: 0.50 g (red solid, 79%).

^{1}H NMR (400 MHz): δ_H(CDCl$_3$) 14.81 (2H, s, OH), 8.76 (2H, s, HC=N), 8.30 (2H, d, J = 2.4 Hz, ArH), 8.29 (2H, d, J = 2.4 Hz, ArH) 7.47 (2H, dd, J = 5.9, 3.4 Hz, ArH), 7.35 (2H, dd, J = 5.9, 3.4 Hz, ArH), 1.45 (18H, s, 2 x C(CH$_3$)$_3$) ppm.

^{13}C NMR (100 MHz): δ_c(CDCl$_3$) 166.28 (C-OH), 162.96 (C=N), 141.19 (ArC), 139.89 (ArC), 139.40 (ArC), 128.91 (ArC), 125.81 (ArC), 119.68 (ArC), 117.96 (ArC), 117.09 (ArC), 35.37 (CMe$_3$), 28.98 (C(CH$_3$)$_3$) ppm.

Mass Spec ESI: Calc: [C$_{28}$H$_{30}$N$_4$O$_6$Na]$^+$: 541.2058 (M+Na$^+$), found: 541.2047.

IR (selected absorbances): 2957, 2909, 2870 (C-H alkyl), 1607 (C=N), 1587 (NO$_2$), 1467 (C=C aromatic), 1324 (NO$_2$ stretch), 1229(C-O), 1112 (C-N), 756 (C-H) cm^{-1}.

Melting point: 268.1-268.5 °C.

N,N'-Bis(salicylaldehyde)-4,5-dimethyl-1,2-phenylenediamine (Sal6)[149]

Prepared by the general procedure, using salicylaldehyde **Ald1** (1.72 mL, 1.97 g, 16.1 mmol) dissolved in methanol (10 mL) and 4,5-dimethyl-1,2-phenylenediamine (0.99 g, 7.27 mmol) dissolved in ethanol (30 mL). After refluxing, a precipitate was isolated from the reaction solution, dissolved in 40 mL of CH$_2$Cl$_2$ and washed with water

(2 x 40 mL). The organic layer was dried (MgSO$_4$), filtered and concentrated *in vacuo* to afford the product.

Yield: 1.77 g (light brown solid, 71%).

^{1}H NMR (400 MHz): δ$_H$(CDCl$_3$) 13.21 (2H, s, OH), 8.62 (2H, s, HC=N), 7.40-7.32 (4H, m, ArH) 7.05 (2H, d, *J* = 8 Hz, ArH) 7.04 (2H, br s, ArH), 6.91 (2H, t, *J* = 7.5, 1.1 Hz, ArH), 2.33 (6H, s, 2 x CH$_3$) ppm.

^{13}C NMR (100 MHz): δ$_c$(CDCl$_3$) 162.74 (C-OH), 161.27 (C=N), 140.01 (ArC), 136.34 (ArC), 133.02 (ArC), 132.12 (ArC), 120.62 (ArC), 119.31 (ArC), 118.83 (ArC), 117.46 (ArC), 19.53 (CH$_3$) ppm.

Mass Spec ESI: Calc. for [C$_{22}$H$_{21}$N$_2$O$_2$]$^+$: 345.1598 (M+H$^+$), found: 345.1604.

IR (selected absorbances): 2916 (C-H alkyl), 1613 (C=N), 1487 (C=C aromatic), 1276 (C-O), 1182 (C-N), 763 (C-H) cm^{-1}.

Melting point: Decomposes <250 °C.

N,N'-Bis(salicylaldehyde)-4,5-dichloro-1,2-phenylenediamine (Sal7)[149]

Prepared by the general procedure, using salicylaldehyde **Ald1** (1.33 mL, 1.52 g, 12.4 mol) dissolved in ethanol (30 mL) and 4,5-dichloro-1,2-benzenediamine (1.01 g, 5.71 mmol) dissolved in ethanol (30 mL). After refluxing, a precipitate was isolated from the reaction solution and purified by washing with ethanol (3 x 10 mL).

Yield: 1.77 g (yellow solid, 80%).

^{1}H NMR (400 MHz): δ$_H$(CDCl$_3$) 12.62 (2H, s, OH), 8.61 (2H, s, HC=N), 7.44-7.37 (4H, m, ArH) 7.34 (2H, s, ArH), 7.05 (2H, m, ArH), 6.96 (1H, dd, *J* = 7.6, 1.2 Hz, ArH), 6.94 (1H, dd, *J* = 7.6, 1.2 Hz, ArH) ppm.

13C NMR (100 MHz): δ_c(CDCl$_3$) 164.66 (C-OH), 161.37 (C=N), 142.01 (ArC), 134.08 (ArC), 132.67 (ArC), 130.96 (ArC), 121.19 (ArC), 119.27 (ArC), 118.86 (ArC), 117.68 (ArC) ppm.

Mass Spec ESI: Calc. for [C$_{20}$H$_{15}$^{35}Cl$_2$N$_2$O$_2$]$^+$: 385.0505 (M+H$^+$), found: 385.0501.

Mass Spec ESI: Calc. for [C$_{20}$H$_{14}$^{35}Cl$_2$N$_2$O$_2$Na]$^+$: 407.0325 (M+Na$^+$), found: 407.0324.

IR (selected absorbances): 3329 (O-H), 1610 (C=N), 1468 (C=C aromatic), 1278 (C-O), 1151 (C-N), 756 (C-Cl) cm^{-1}.

Melting point: 194.9-195.5 °C.

N,N'-Bis(salicylaldehyde)-2,3-diaminonaphthalene (Sal8)[149]

Prepared using the general procedure, using salicylaldehyde **Ald1** (1.49 mL, 1.71 g, 14.0 mmol) dissolved in methanol (20 mL) and 2,3-diaminonaphthalene (1.01 g, 6.38 mmol) dissolved in ethanol (20 mL) and methanol (30 mL). After refluxing, a precipitate was isolated from the reaction solution and purified by washing with ethanol (4 x 10 mL).

Yield: 1.39 g (dark orange solid, 59%).

1H NMR (400 MHz): δ_H(CDCl$_3$) 13.02 (2H, s, OH), 8.75 (2H, s, HC=N), 7.87 (2H, dd, J = 6.1, 3.3 Hz, ArH), 7.60, (2H, s, ArH), 7.53-7.47 (2H, m, ArH) 7.47-7.34 (4H, m, ArH), 7.07 (2H, d, J = 7.9 Hz, ArH), 6.95 (2H, td, J = 7.5, 1.0 Hz, ArH) ppm.

13C NMR (100 MHz): δ_c(CDCl$_3$) 163.88 (C-OH), 161.45 (C=N), 142.27 (ArC), 133.64 (ArC), 133.48 (ArC), 132.72 (ArC), 132.28 (ArC), 127.69 (ArC), 126.36 (ArC), 119.01 (ArC), 117.59 (ArC), 116.73 (ArC) ppm.

Mass Spec ESI: Calc. for [C$_{24}$H$_{19}$N$_2$O$_2$]$^+$: 367.1441 (M+H$^+$), found: 367.1435.

Mass Spec ESI: Calc. for [C$_{24}$H$_{18}$N$_2$O$_2$Na]$^+$: 389.1260 (M$^+$), found: 389.1249.

IR (selected absorbances): 1604 (C=N), 1491 (C=C aromatic), 1272 (C-O), 1147 (C-N), 746 (C-H) cm^{-1}.

Melting point: 188.6-189.2 °C.

N,N'-Bis(3-tert-butylsalicylidene)-4,5-dichloro-1,2-phenylenediamine (Sal9)

Prepared by the general procedure, using 3-(*tert*-butyl)-2-hydroxybenzaldehyde **Ald2** (0.28 g, 1.57 mmol) dissolved in methanol (5 mL) and dichloro-1,2-benzenediamine (0.14 g, 0.78 mmol) dissolved in methanol (2 mL). After refluxing, a precipitate was isolated from the reaction solution and purified by washing with ethanol (2 x 10 mL).

Yield: 0.22 g (light orange/dark yellow solid, 59%).

^{1}H NMR (400 MHz): δ_H(CDCl$_3$) 13.34 (2H, s, OH), 8.63 (2H, s, HC=N), 7.41 (2H, dd, J = 7.8, 1.5 Hz, ArH), 7.35 (2H, d, J = 1.6 Hz, ArH), 7.26 (1H, d, J = 1.6 Hz, ArH), 7.25 (1H, d, J = 7.8 Hz, ArH), 6.88 (2H, t, J = 7.7 Hz, ArH), 1.42 (18H, s, 2 x C(CH$_3$)$_3$) ppm.

^{13}C NMR (100 MHz): δ_c(CDCl$_3$) 165.18 (C-OH), 160.38 (C=N), 141.97 (ArC), 138.01 (ArC), 131.22 (ArC), 131.04 (ArC), 130.74 (ArC), 121.13 (ArC), 118.80 (ArC), 118.48 (ArC), 34.92 (CMe$_3$), 29.28 (C(CH$_3$)$_3$) ppm.

Mass Spec ESI: Calc: [C$_{28}$H$_{31}$^{35}Cl$_2$N$_2$O$_2$]$^+$= 497.1757 (M+H$^+$), found: 497.1753.

Mass Spec LIFDI: Calc: [C$_{28}$H$_{31}$^{35}Cl$_2$N$_2$O$_2$]$^+$ = 497.17 (M+H$^+$), found: 497.17.

IR (selected absorbances): 2962, 2869 (C-H alkyl), 1607 (C=N), 1460 (C=C aromatic), 1193 (C-O), 1146 (C-N), 874.54 (C-Cl), 741 (C-H) cm^{-1}.

Melting point: 168.0-168.9 °C.

N,N'-Bis(3-tert-butyl-5-methoxysalicylidene)-4,5-dichloro-1,2-phenylenediamine (Sal10)

Prepared by the general procedure, using 3-(*tert*-butyl)-2-hydroxy-5-methoxybenzaldehyde **Ald4** (0.32 g, 1.52 mmol) dissolved in methanol (10 mL) and 4,5-dichloro-1,2-benzenediamine (0.056 g, 0.32 mmol) dissolved in methanol (5 mL). A

precipitate was isolated from the reaction solution and purified by washing with ethanol (2 x 10 mL).

Yield: 0.16 g (red solid, 90%).

¹H NMR (400 MHz): δ_H(CDCl$_3$) 12.95 (2H, s, OH), 8.54 (2H, s, HC=N), 7.29 (2H, s, ArH), 6.99 (2H, d, J = 3.1 Hz, ArH), 6.65 (2H, d, J = 3.1 Hz, ArH), 3.72 (6H, s, O-Me), 1.34 (18H, s, 2 x C(CH$_3$)$_3$) ppm.

¹³C NMR (100 MHz): δ_c(CDCl$_3$) 164.90 (C-OH), 155.70 (C=N), 151.53 (ArC), 141.90 (ArC), 139.78 (ArC), 130.70 (ArC), 121.19 (ArC), 120.61 (ArC), 118.02 (ArC), 111.76 (ArC), 55.77 (O-Me), 35.08 (<u>C</u>Me$_3$), 29.19 (C(<u>C</u>H$_3$)$_3$) ppm.

Mass Spec ESI: Calc [C$_{30}$H$_{35}$^{35}Cl$_2$N$_2$O$_4$]$^+$: 557.1968 (M+H$^+$), found: 557.1972.

Mass Spec LIFDI: Calc: [C$_{30}$H$_{35}$^{35}Cl$_2$N$_2$O$_4$]$^+$: 557.19 (M+H$^+$), found: 556.20.

IR (selected absorbances): 2945, 2908 (C-H alkyl), 1612 (C=N), 1446 (C=C aromatic), 1332 (C-O from COCH$_3$), 1115 (C-O), 1054 (C-N), 846 (C-Cl), 793 (C-H) cm^{-1}.

Melting point: 188.9-189.3 °C.

Synthesis of Chromium(III) Salophen Chloride Complexes: General Procedure
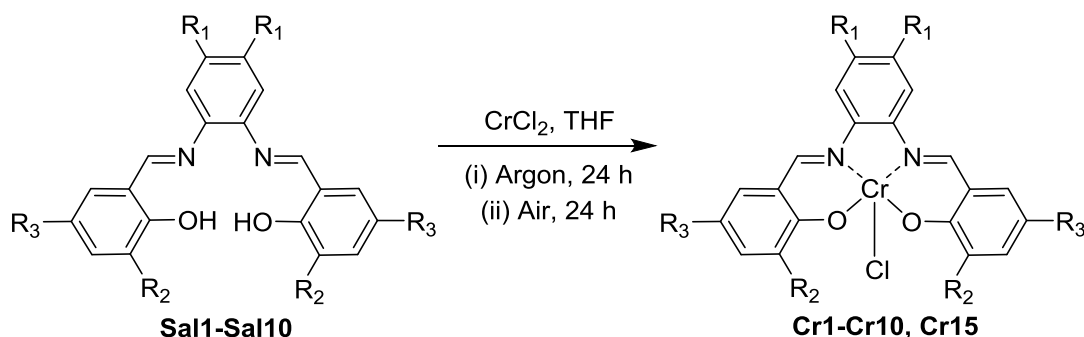
Cr1: R$_1$ = H, R$_2$ = H, R$_3$ = H; **Cr2:** R$_1$ = H, R$_2$ = ^{t}Bu, R$_3$ = H; **Cr3:** R$_1$ = H, R$_2$ = H, R$_3$ = ^{t}Bu;
Cr4: R$_1$ = H, R$_2$ = ^{t}Bu, R$_3$ = OMe; **Cr5:** R$_1$ = H, R$_2$ = ^{t}Bu, R$_3$ = NO$_2$; **Cr6:** R$_1$ = Me, R$_2$ = H, R$_3$ = H;
Cr7: R$_1$ = Cl, R$_2$ = H, R$_3$ = H; **Cr8:** R$_1$ = -(CH)$_4$-, R$_2$ = H, R$_3$ = H; **Cr9:** R$_1$ = Cl, R$_2$ = ^{t}Bu, R$_3$ = H;
Cr10: R$_1$ = Cl, R$_2$ = ^{t}Bu, R$_3$ = OMe; **Cr15:** R$_1$ = H, R$_2$ = ^{t}Bu, R$_3$ = ^{t}Bu;

Chromium(III) salophen chloride complexes were synthesised following the standard method as reported by Darensbourg.[95] The salophen ligand (1 equiv.) and anhydrous CrCl$_2$ (1.0-1.7 equiv., unless otherwise stated) were both placed in a pre-dried round-bottom flask and then purged with argon. Once purged, dry THF was added and the reaction mixture was stirred under argon (24 h). Air was then bubbled through the mixture (24 h). Diethyl ether was added and the organic layer was washed with sat. aq. NH$_4$Cl and sat. brine. The organic layer was dried (Na$_2$SO$_4$ or MgSO$_4$) and the solvent was removed under reduced pressure to give the chromium(III) salophen complex. All complexes were purified by washes or soxhlet washes with hexane. N,N'-Bis(3,5-di-*tert*-butylsalicylidene)-1,2-phenylenediamine chromium(III) chloride catalyst **Cr15** had been previously synthesised by Dr José Antonio Castro-Osma, at the Green Chemistry Centre of Excellence at the University of York. Due to the paramagnetic nature of these catalysts, NMR spectra could not be obtained.

N,N'-Bis(salicylidene)-1,2-phenylenediamine chromium(III) chloride (Cr1)[95]

Prepared by the general procedure, using dry THF (50 mL), *N,N'*-bis(salicylidene)-1,2-phenylenediamine **Sal1** (0.80 g, 2.54 mmol) and CrCl$_2$ (0.32 g, 2.56 mmol). After stirring under argon then air, a solid precipitate formed in the reaction mixture and was isolated to afford the product (0.68 g). To ensure the entire product was collected, diethyl ether (50 mL) was added to the filtrate and then washed with sat. aq. NH$_4$Cl (4 x 40 mL) and sat. brine (4 x 40 mL). The organic layer was dried (MgSO$_4$), filtered and concentrated *in vacuo* to afford more product (0.25 g).

Yield: 0.93 g (dark brown solid, 91%).

Mass Spec ESI: Calc: [C$_{20}$H$_{14}$CrN$_2$O$_2$]$^+$: 336.0455 (M$^+$-Cl), found: 336.0463.

Mass Spec LIFDI: Calc: [C$_{20}$H$_{14}$CrN$_2$O$_2$]$^+$: 336.05 (M$^+$-Cl), found: 336.05.

IR (selected absorbances): 1606 (C=N), 1537 (C=C aromatic), 1189 (C-O), 1150 (C-N), 749 (C-H) cm^{-1}.

Melting point: >350 °C.

XRF: Expected ratio Cr/Cl: 1/1, experimental ratio: 1/1.29 ± 0.10.

ICP-MS: Expected Cr%: 12.9%, experimental Cr%: 12.6% ± 0.80.

N,N'-Bis(3-tert-butylsalicylidene)-1,2-phenylenediamine chromium(III) chloride (Cr2)[95]

Prepared by the general procedure, using dry THF (35 mL), *N,N'*-bis(3-*tert*-butylsalicylidene)-1,2-phenylenediamine **Sal2** (0.20 g, 0.46 mmol) and CrCl$_2$ (0.080 g, 0.65 mmol). After stirring under argon then air, diethyl ether (35 mL) was added and washed with sat. aq. NH$_4$Cl (3 x 50 mL) and sat. brine (3 x 50 mL). The organic layer was dried (MgSO$_4$), filtered and concentrated *in vacuo* to afford the product.

Yield: 0.18 g (dark brown/red solid, 76%).

Mass Spec ESI: Calc: [C$_{28}$H$_{30}$CrN$_2$O$_2$]$^+$: 478.1707 (M$^+$-Cl), found: 478.1715.

Mass Spec LIFDI: Calc: [C$_{28}$H$_{30}$Cr^{35}ClN$_2$O$_2$]$^+$: 513.14 (M$^+$), found: 513.15.

IR (selected absorbances): 2953 (C-H alkyl), 1601 (C=N), 1385 (C=C aromatic), 1185 (C-O), 1026 (C-N), 748 (C-H) cm^{-1}.

Melting point: >350 °C.

XRF: Expected ratio Cr/Cl: 1/1, experimental ratio: 1/0.73 ± 0.05.

ICP-MS: Expected Cr%: 10.12%, experimental Cr%: 9.84% ± 3.20.

N,N'-Bis(5-tert-butylsalicylidene)-1,2-phenylenediamine chromium(III) chloride (Cr3)[95]

Prepared by the general procedure, using dry THF (50 mL), *N,N'*-bis(5-*tert*-butylsalicylidene)-1,2-phenylenediamine **Sal3** (0.51 g, 1.18 mmol) and CrCl$_2$ (0.15 g, 1.19 mmol). After stirring under argon then air, a solid precipitate formed in

the reaction mixture and was isolated to afford the product (0.21 g). To ensure the entire product was collected, diethyl ether (50 mL) was added to the filtrate and then washed with sat. aq. NH_4Cl (3 x 50 mL) and sat. brine (2 x 50 mL). The organic layer was dried ($MgSO_4$), filtered and concentrated *in vacuo* to afford more product (0.36 g).

Yield: 0.57 g (dark brown solid, 94%).

Mass Spec ESI: Calc: $[C_{28}H_{30}CrN_2O_2]^+$: 478.1707 (M^+-Cl), found: 478.1698.

Mass Spec LIFDI: Calc: $[C_{28}H_{30}Cr^{35}ClN_2O_2]^+$: 513.17 ($M^+$), found: 513.18.

IR (selected absorbances): 2956, 2918, 2649 (C-H alkyl), 1614 (C=N), 1579 (C=C aromatic), 1260 (C-O), 1180 (C-N), 746 (C-H) cm^{-1}.

Melting point: >350 °C.

XRF: Expected ratio Cr/Cl: 1/1, experimental ratio: $1/0.97 \pm 0.06$.

ICP-MS: Expected Cr%: 10.1%, experimental Cr%: $10.2\% \pm 0.90$.

N,N'-Bis(3-tert-butyl-5-methoxysalicylidene)-1,2-phenylenediamine chromium(III) chloride (Cr4)[95]

Prepared by the general procedure, using dry THF (10 mL), *N,N'*-bis(3-*tert*-butyl-5-methoxysalicylidene)-1,2-phenylenediamine **Sal4** (0.047 g, 0.096 mmol) and $CrCl_2$ (0.017 g, 0.14 mmol). After stirring under argon then air, diethyl ether (20 mL) was added, and washed with sat. aq. NH_4Cl (2 x 20 mL) and sat. brine (2 x 50 mL). The organic layer was dried ($MgSO_4$), filtered and concentrated *in vacuo* to afford the product.

Yield: 0.050 g (dark red solid, 91%).

Mass Spec ESI: Calc: $[C_{30}H_{34}CrN_2O_4]^+$: 538.1918 (M^+-Cl), found: 538.1918.

Mass Spec LIFDI: Calc: $[C_{30}H_{34}Cr^{35}ClN_2O_4]^+$: 573.16 ($M^+$), found: 573.18.

IR (selected absorbances): 2917 (C-H alkyl), 1601 (C=N), 1532 (C=C aromatic), 1361 (C-O from $COCH_3$), 1211 (C-O), 1050 (C-N), 744 (C-H) cm^{-1}.

Melting point: >350 °C.

XRF: Expected ratio Cr/Cl = 1/1, experimental ratio = $1/0.96 \pm 0.07$.

ICP-MS: Expected Cr%: 9.1%, experimental Cr%: $8.3\% \pm 0.06$.

N,N'-Bis(3-tert-butyl-5-nitrosalicylidene)-1,2-phenylenediamine chromium(III) chloride (Cr5)[95]

Prepared by the general procedure, using dry THF (50 mL), *N,N'*-bis(3-*tert*-butyl-5-nitrosalicylidene)-1,2-phenylenediamine **Sal5** (0.10 g, 0.19 mmol) and $CrCl_2$ (0.032 g, 0.26 mmol). After stirring under argon then air, diethyl ether (50 mL) was added, and washed with sat. aq. NH_4Cl (2 x 50 mL) and sat. brine (2 x 50 mL). The organic layer was dried ($MgSO_4$), filtered and concentrated *in vacuo* to afford the product.

Yield: 0.106 g (dark brown solid, 92%).

Mass Spec ESI: Calc: $[C_{28}H_{28}Cr^{35}ClN_4O_6]^+$: 603.1098 ($M^+$), found: 603.1205.

IR (selected absorbances): 2958, 2921, 2854 (C-H alkyl), 1607 (C=N), 1587 (N-O) 1523 (C=C aromatic), 1323 (C-O), 1285 (N-O) 1199 (C-N), 744 (C-H) cm^{-1}.

Melting point: >350 °C.

N,N'-Bis(salicylaldehyde)-4,5-dimethyl-1,2-phenylenediamine chromium(III) chloride (Cr6)[95]

Prepared by the general procedure, using dry THF (45 mL), *N,N'*-bis(salicylaldehyde)-4,5-dimethyl-1,2-phenylenediamine **Sal6** (0.19 g, 0.55 mmol) and $CrCl_2$ (0.085 g, 0.63 mmol). After stirring under argon then air, a solid precipitate formed in the reaction mixture and was isolated to afford the product (0.086 g). To ensure the entire product was collected, diethyl ether (40 mL) was added to the filtrate and then

washed with sat. aq. NH$_4$Cl (2 x 40 mL) and sat. brine (2 x 40 mL). The organic layer was dried (MgSO$_4$), filtered and concentrated *in vacuo* to afford more product (0.078 g).

Yield: 0.16 g (dark brown solid, 68%).

Mass Spec ESI: Calc: [C$_{22}$H$_{18}$CrN$_2$O$_2$]$^+$: 394.0768 (M$^+$-Cl), found: 394.0756.

Mass Spec LIFDI: Calc: [C$_{22}$H$_{18}$Cr^{35}ClN$_2$O$_2$]$^+$: 429.05 (M$^+$), found: 429.08.

IR (selected absorbances): 2917, 2846 (C-H alkyl), 1592 (C=N), 1461 (C=C aromatic), 1259 (C-O), 1027 (C-N), 751 (C-H) cm^{-1}.

Melting point: >350 °C.

XRF: expected ratio Cr/Cl = 1/1, experimental ratio = 1/0.70 ± 0.11.

ICP-MS: Expected Cr%: 12.1%, experimental Cr%: 10.4% ± 0.90.

N,N'-Bis(salicylaldehyde)-4,5-dichloro-1,2-phenylenediamine chromium(III) chloride (Cr7)[95]

Prepared by the general procedure, using dry THF (25 mL), *N,N'*-bis(salicylaldehyde)-4,5-dichloro-1,2-phenylenediamine **Sal7** (0.29 g, 0.76 mmol) and CrCl$_2$ (0.15 g, 1.22 mmol). After stirring under argon then air, a solid precipitate formed in the reaction mixture and was isolated to afford the product (0.20 g). To ensure the entire product was collected, diethyl ether (30 mL) was added to the filtrate and then washed with sat. aq. NH$_4$Cl (3 x 30 mL) and sat. brine (3 x 30 mL). The organic layer was dried (MgSO$_4$), filtered and concentrated *in vacuo* to afford more product (0.070 g).

Yield: 0.27 g (dark brown/red solid, 75%).

Mass Spec ESI: Calc: [C$_{20}$H$_{12}$^{35}Cl$_2$CrN$_2$O$_2$]$^+$: 433.9676 (M$^+$-Cl), found: 433.9653.

Mass Spec LIFDI: Calc: [C$_{20}$H$_{12}$^{35}Cl$_2$CrN$_2$O$_2$]$^+$: 433.97 (M$^+$-Cl), found: 433.98.

IR (selected absorbances): 2918, 2849 (C-H alkyl), 1607 (C=N), 1530 (C=C aromatic), 1148 (C-O), 1029 (C-N), 752 (C-Cl) cm^{-1}.

Melting point: >350 °C.

XRF: Expected ratio Cr/Cl = 1/3, experimental ratio = 1/3.37 ± 0.08.

ICP-MS: Expected Cr%: 11.1%, experimental Cr%: 8.3 ± 0.80.

N,N'-Bis(salicylaldehyde)-2,3-diaminonaphthalene chromium(III) chloride (Cr8)[95]

Prepared by the general procedure, using dry THF (15 mL), *N,N'*-bis(salicylaldehyde)-2,3-diaminonaphthalene **Sal8** (0.30 g, 0.82 mmol) and CrCl$_2$ (0.15 g, 1.23 mmol). After stirring under argon then air, a solid precipitate formed in the reaction mixture and was isolated to afford the product (0.21 g). To ensure the entire product was collected, diethyl ether (30 mL) was added to the filtrate and then washed with sat. aq. NH$_4$Cl (3 x 30 mL) and sat. brine (3 x 30 mL). The organic layer was dried (MgSO$_4$), filtered and concentrated *in vacuo* to afford more product (0.10 g).

Yield: 0.31 g (dark brown/red solid, 84%).

Mass Spec ESI: Calc: [C$_{24}$H$_{16}$CrN$_2$O$_2$]$^+$: 416.0622 (M$^+$-Cl), found: 416.0634.

Mass Spec LIFDI: Calc: [C$_{24}$H$_{16}$Cr^{35}ClN$_2$O$_2$]$^+$: 451.03 (M$^+$), found: 451.04.

IR (selected absorbances): 2917, 2849 (C-H alkyl), 1604 (C=N), 1530 (C=C aromatic), 1197 (C-O), 1150 (C-N), 747 (C-H) cm^{-1}.

Melting point: >350 °C.

XRF: Expected ratio Cr/Cl = 1/1, experimental ratio = 1/0.79 ± 0.10.

ICP-MS: Expected Cr%: 11.5%, experimental Cr%: 8.8% ± 3.10.

N,N'-Bis(3-tert-butylsalicylidene)-4,5-dichloro-1,2-phenylenediamine **chromium(III)**

chloride (Cr9)

Prepared by the general procedure, using dry THF (20 mL), *N,N′*-bis(3-*tert*-butylsalicylidene)-4,5-dichloro-1,2-phenylenediamine **Sal9** (0.035 g, 0.069 mmol) and CrCl$_2$ (0.015 g, 0.12 mmol). After stirring under argon then air, diethyl ether (15 mL) was added, and washed with sat. aq. NH$_4$Cl (2 x 15 mL) and sat. brine (2 x 15 mL). The organic layer was dried (MgSO$_4$), filtered and concentrated *in vacuo* to afford the product.

Yield: 0.033 g (dark brown solid, 82%).

Mass Spec ESI: Calc: $[C_{28}H_{28}Cl_2CrN_2O_2]^+$: 546.0928 (M$^+$-Cl), found: 546.0913.

Mass Spec LIFDI: Calc: $[C_{28}H_{28}Cl_3CrN_2O_2]^+$: 581.06 (M$^+$), found: 581.08.

IR (selected absorbances): 2917 (C-H alkyl), 1596 (C=N), 1530 (C=C aromatic), 1187 (C-O), 1147 (C-N), 870 (C-Cl), 749 (C-H) cm^{-1}.

Melting point: >350 °C.

XRF: Expected ratio Cr/Cl = 1/3, experimental ratio = 1/2.85 ± 0.17.

ICP-MS: Expected Cr%: 8.9%, experimental Cr%: 8.3% ± 2.30.

N,N'-Bis(3-tert-butyl-5-methoxysalicylidene)-4,5-dichloro-1,2-phenylenediamine

chromium(III) chloride (Cr10)

Prepared by the general procedure, using dry THF (20 mL), *N,N′*-bis(3-*tert*-butyl-5-methoxysalicylidene)-4,5-dichloro-1,2-phenylenediamine **Sal10** (0.016 g, 0.029 mmol) and CrCl$_2$ (0.015 g, 0.12 mmol, 4.1 equiv.). After stirring under argon then air, diethyl ether (20 mL) was added, and washed with sat. aq. NH$_4$Cl (2 x 20 mL) and sat. brine (2 x 20 mL). The organic layer was dried (MgSO$_4$), filtered and concentrated *in vacuo* to afford the product.

Yield: 0.016 (dark brown solid, 86%).

Mass Spec ESI: Calc: $[C_{30}H_{32}{}^{35}Cl_2CrN_2O_4]^+$: 606.1140 (M$^+$-Cl), found: 606.1134.

Mass Spec LIFDI: Calc: $[C_{30}H_{32}{}^{35}Cl_3CrN_2O_4]^+$: 643.11 (M$^+$), found: 643.08.

IR (selected absorbances): 2919, 2850 (C-H alkyl), 1597 (C=N), 1530 (C=C aromatic), 1357 (C-O from COCH$_3$), 1159 (C-O), 1057 (C-N), 822 (C-Cl), 778 (C-H) cm^{-1}.

Melting point: >350 °C.

XRF: Expected ratio Cr/Cl = 1/3, experimental ratio = 1/2.83 ± 0.18.

ICP-MS: Expected Cr%: 8.1%, experimental Cr%: 8.2% ± 2.20.

Synthesis of Chromium(III) Salophen Complexes with Different Counterions

N,N'-Bis(3-tert-butyl-5-methoxysalicylidene)-1,2-phenylenediamine   *chromium(III)*
bromide (Cr11)
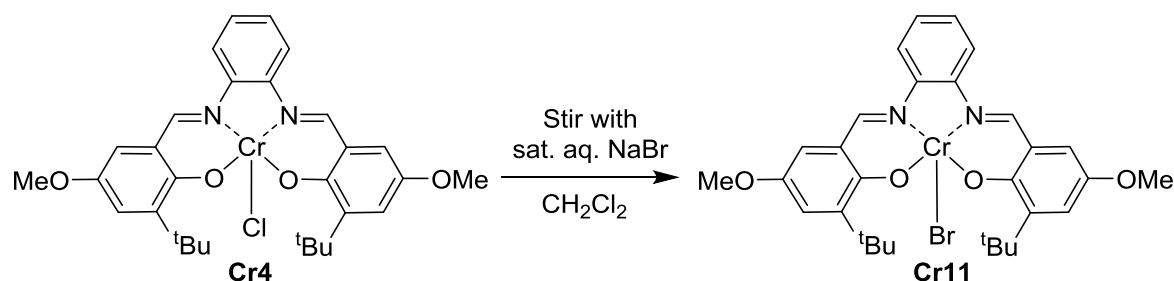
N,N'-Bis(3-*tert*-butyl-5-methoxysalicylidene)-1,2-phenylenediamine   chromium(III)
chloride **Cr4** (0.50 g, 0.86 mmol) was dissolved in CH$_2$Cl$_2$ (45 mL), to form a dark red
solution which was stirred with sat. aq. NaBr solution (65 mL). The reaction mixture was
left stirring vigorously for 5 days. The red organic layer was then extracted from the clear
aqueous layer, dried (MgSO$_4$), filtered and concentrated *in vacuo* to afford a dark red solid.
The solid was then washed with hexane (4 x 10 mL) and dried to give the final product.

Yield: 0.27 g (dark red solid, 51%).

Mass Spec LIFDI: Calc: $[C_{30}H_{34}CrN_2O_4]^+$ = 538.19 (M$^+$-Br), found: 538.21.

Mass Spec LIFDI: Calc: $[C_{30}H_{34}{}^{79}BrCrN_2O_4]^+ = 617.11$ (M$^+$), found: 617.09.

IR (selected absorbances): 2953 (C-H alkyl), 1601 (C=N), 1533 (C=C aromatic), 1359 (C-O from COCH$_3$), 1208 (C-O), 1055 (C-N), 751 (C-H) cm^{-1}.

Melting point: >350 °C.

XRF: Expected Ratio Cr/Br = 1/1, experimental ratio = 1/0.75 ± 0.06. No Cl was detected.

ICP-MS: Expected Cr%: 8.41%, experimental Cr%: 7.00% ± 5.4.

N,N'-Bis(3-tert-butyl-5-methoxysalicylidene)-1,2-phenylenediamine   chromium(III) iodide (Cr12)[152]

N,N'-Bis(3-*tert*-butyl-5-methoxysalicylidene)-1,2-phenylenediamine   chromium(III) chloride **Cr4** (0.082 g, 0.14 mmol) was dissolved in CH$_2$Cl$_2$ (20 mL), to form a dark red solution which was stirred with sat. aq. NaI solution (55 mL). The reaction mixture was left stirring vigorously for 7 h. The red organic layer was then extracted from the clear aqueous layer, washed with water (50 mL), dried (Na$_2$SO$_4$), filtered and concentrated *in vacuo* to afford the product as a dark red, sticky solid (0.071 g). The product was washed with hexane (2 x 5 mL) and dried to give the final product.

Yield: 0.049 g (dark red solid, 53%).

Mass Spec LIFDI: Calc: $[C_{30}H_{34}CrN_2O_4]^+ = 538.19$ (M$^+$-I), found: 538.19.

Mass Spec LIFDI: Calc: $[C_{30}H_{34}CrIN_2O_4]^+ = 665.10$ (M$^+$), found: 665.09.

IR (selected absorbances): 2923 (C-H alkyl), 1602 (C=N), 1533 (C=C aromatic), 1359 (C-O from COCH$_3$), 1207 (C-O), 1057 (C-N), 751 (C-H) cm^{-1}.

Melting point: >350 °C.

XRF: No Cl was detected.

ICP-MS: Expected Cr%: 7.81%, experimental Cr%: 9.65% ± 1.60.

N,N'-Bis(3-tert-butyl-5-methoxysalicylidene)-1,2-phenylenediamine chromium(III) acetate (Cr13)[153,154]
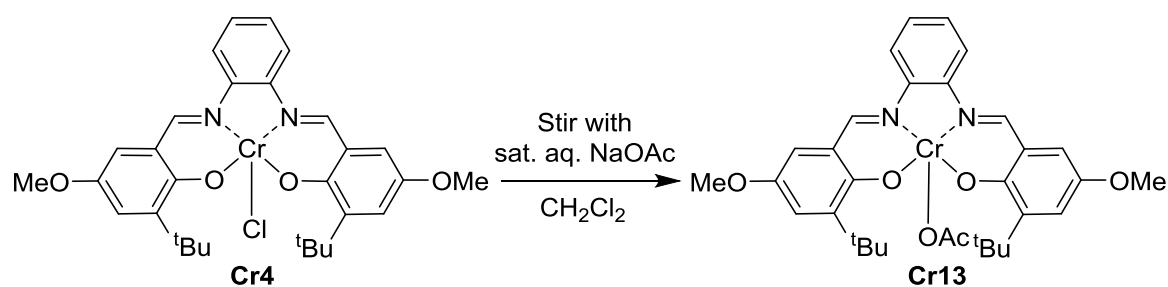
N,N'-Bis(3-*tert*-butyl-5-methoxysalicylidene)-1,2-phenylenediamine chromium(III) chloride **Cr4** (0.10 g, 0.18 mmol) was dissolved in CH$_2$Cl$_2$ (20 mL), to form a dark red solution which was stirred with sat. aq. NaOAc solution (55 mL). The reaction mixture was left stirring vigorously for three days. The red organic layer was then extracted from the clear aqueous layer, washed with water (50 mL), dried (Na$_2$SO$_4$), filtered and concentrated *in vacuo* to afford the product. The dark red solid was then washed with hexane (2 x 5 mL) and dried to afford the final product.

Yield: 0.087 g (dark red solid, 81%).

Mass Spec LIFDI: Calc: [C$_{30}$H$_{34}$CrN$_2$O$_4$]$^+$ = 538.19 (M$^+$-OAc), found: 538.19.

Mass Spec LIFDI: Calc: [C$_{32}$H$_{37}$CrN$_2$O$_6$]$^+$ = 597.21 (M$^+$), found: 597.20.

IR (selected absorbances: 2930 (C-H alkyl), 1602 (C=N), 1531 (C=C aromatic), 1360 (C-O from COCH$_3$), 1207 (C-O), 1058 (C-N), 748 (C-H) cm^{-1}.

Melting point: >350 °C.

XRF: No Cl was detected.

ICP-MS: Expected Cr%: 8.49%, experimental Cr%: 6.83% ± 0.20.

N,N'-Bis(3-tert-butyl-5-methoxysalicylidene)-1,2-phenylenediamine chromium(III) tosylate (Cr14)[154]
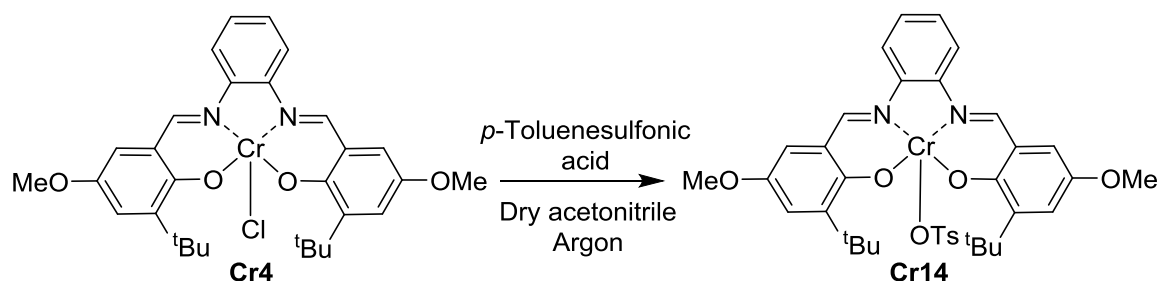
N,N'-Bis(3-*tert*-butyl-5-methoxysalicylidene)-1,2-phenylenediamine chromium(III) chloride **Cr4** (0.079 g, 0.14 mmol) was dissolved in dry acetonitrile (2 mL) to form a dark red solution. *p*-Toluenesulfonic acid (0.052 g, 0.18 mmol) was dissolved in acetonitrile (4 mL) to form a clear solution. The *p*-toluenesulfonic acid solution was added slowly to the catalyst solution, and was left stirring under argon with the round-bottom flask covered with foil. The reaction was left stirring overnight (18 h), filtered through Celite® and washed through with acetonitrile (15 mL). The eluent was concentrated *in vacuo* to afford a dark red solid. The solid was then washed with hexane (2 x 5 mL) and dried to give the final product.

Yield: 0.075 g (dark red solid, 75%).

Mass Spec LIFDI: Calc:$[C_{30}H_{34}CrN_2O_4]^+$ = 538.19 (M$^+$-OTs), found: 538.24.

Mass Spec LIFDI: Calc:$[C_{37}H_{41}CrN_2O_7S]^+$ = 709.20 (M$^+$), found: 709.17.

IR (selected absorbances): 2951 (C-H alkyl), 1601 (C=N), 1534 (C=C aromatic), 1358 (C-O from COCH$_3$), 1150 (C-O), 1057 (C-N), 794 (C-H) cm^{-1}.

Melting point: >350 °C.

XRF: No Cl was detected.

2.4.12 Synthesis of Bis(triphenylphosphine)iminium Bromide (23)[155]
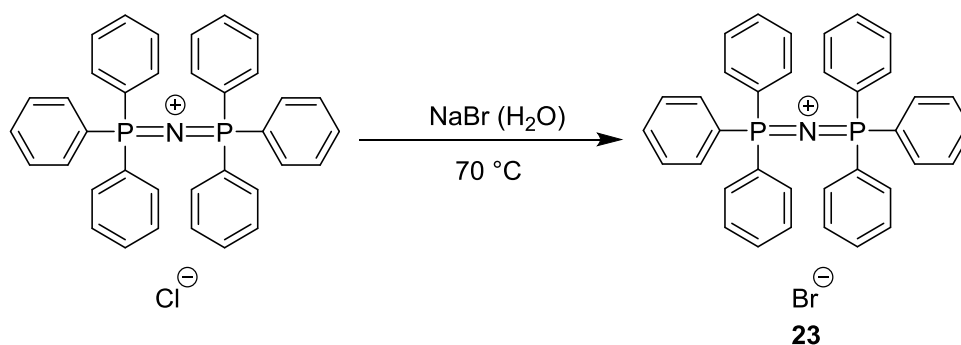
Bis(triphenylphosphine)iminium chloride (1.02 g, 1.77 mmol) was dissolved in warm water (10 mL), and heated to 70 °C whilst stirring. Sodium bromide (7.08 g, 68.80 mmol) was dissolved in a separate aliquot of warm water (25 mL), and heated to 70 °C whilst stirring. With the temperature maintained at 70 °C, the bis(triphenylphosphine)iminium chloride solution was added dropwise to the sodium bromide solution. This led to the immediate formation of a white precipitate. After all of the bis(triphenylphosphine)iminium chloride was added, the mixture was left stirring for 4 h. The white precipitate was filtered from the solution and washed with water (10 mL). The isolated precipitate was then left in an oven (110-120 °C) for three days to the afford the final product.

Yield: 0.92 g (crystalline white solid, 84%).

^{1}H NMR (400 MHz): δ_H(CDCl$_3$) 7.68-7.60 (6H, m, ArH), 7.50-7.35 (24 H, m, ArH) ppm.

^{13}C NMR (100 MHz): δ_C(CDCl$_3$) 133.83 (s, 6C, para ArC), 131.99-129.41 (m, 12C, ArC), 129.60-129.41 (m, 12C, ArC), 126.77 (dd, $^3J_{PC}$ = 1.8 Hz, $^1J_{PC}$ = 103.8 Hz, 6C, ortho ArC).

^{31}P NMR (162 MHz): δ_P(CDCl$_3$) 21.68 (s, 2P) ppm.

Mass Spec ESI: Calc: [C$_{36}$H$_{30}$NP$_2$]$^+$ 538.1848 (M$^+$), found: 538.1871.

IR (selected absorbances): 1586 (C=C aromatic), 1481 (C=C aromatic), 1435 (C=C aromatic) cm^{-1}.

Melting point: 251.0-251.6 °C, literature: 255-256 °C.[156]

2.4.13 General Procedure for Synthesis of Cyclic Carbonates

$$\text{R}\overset{\text{O}}{\triangle} + CO_2 \xrightarrow[\text{25 °C, 1 bar, 24 h}]{\substack{\text{Catalyst Cr1-Cr15 (0-2.5 mol\%)} \\ \text{Bu}_4\text{NBr (0-2.5 mol\%)}}} \text{cyclic carbonate}$$

EP1-EP10 → **EP1-EP10**
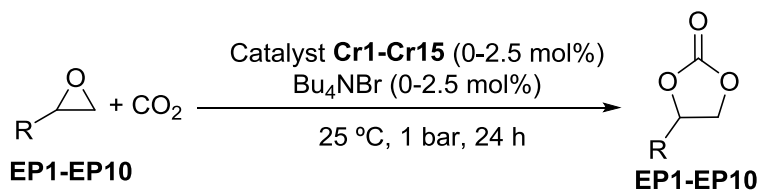
1, R = Ph; **2**, R = Me; **3**, R = Et; **4**, R = ^{n}Bu; **5**, R = ^{n}Oct; **6**, R = CH_2Cl;
7, R = CH_2OH; **8**, R = CH_2OPh; **9,** R = 4-ClC_6H_4; **10,** R = 4-BrC_6H_4

An epoxide (1.66 mmol), chromium(III) salophen complex **Cr1-Cr15** (0.025 mmol), TBAB (Bu$_4$NBr, 0.025 mmol) and a magnetic stirrer bar were placed in a sample vial, which was placed inside a large conical flask. Cardice® pellets were added to the conical flask which was then fitted with a rubber stopper, with a needle inserted through the rubber seal and a deflated balloon attached to the needle. This was to ensure the flask was under 1 bar pressure of CO_2. The reaction mixture was stirred at 25 °C for 24 h. The temperature was controlled by placing the conical flask into an oil bath heated with a stirrer hotplate (Figure 27).

Figure 27: Experimental setup for testing chromium(III) salophen catalysts in converting epoxides to cyclic carbonates.

The conversion of epoxide to cyclic carbonates was determined via ^{1}H NMR spectroscopy by comparing the integral values of the unreacted epoxide peak to its corresponding carbonate peak. The reaction mixture was purified by flash chromatography using a gradient elution solvent system of hexane, hexane:ethyl acetate (9:1), hexane:ethyl acetate (3:1), and then ethyl acetate to isolate the cyclic carbonate. Cyclic carbonates **CC1-CC10** are all known compounds and the spectroscopic data of samples prepared using the chromium(III) salophen catalysts **Cr1-Cr15** were consistent with those reported in the literature.[87,102,157]

Styrene carbonate (CC1)

Yield: 0.251 g (white solid, 92%).

^{1}**H NMR** (400 MHz): δ_H(CDCl$_3$) 7.30-7.19 (5H, m, ArH), 5.52 (1H, t, $J = 8.0$ Hz, OCH), 4.64 (1H, t, $J = 8.0$ Hz, CH$_2$), 4.16 (1H, t, $J = 8.0$ Hz, CH$_2$) ppm.

^{13}**C NMR** (100 MHz): δ_c(CDCl$_3$) 154.7 (C=O), 135.6 (ArC), 129.4 (ArC), 128.9 (ArC), 125.7 (ArC), 77.8 (OCH), 70.9 (OCH$_2$) ppm.

Mass Spec ESI: Calc: [C$_9$H$_8$O$_3$Na]$^+$ 187.0366 (M+Na$^+$), found 187.0363.

IR (selected absorbances): 3068, 3039, 2981, 2925 (C-H alkyl), 1773 (C=O), 1553 (C-O) cm^{-1}.

Melting point: 53-55 °C, literature: 51-53 °C.[158]

Propylene carbonate (CC2)

Yield: 0.097 g (colourless liquid, 57%).

^{1}**H NMR** (400 MHz): δ_H(CDCl$_3$) 4.87-4.79 (1H, m, OCH), 4.52 (1H, t, $J = 8.0$ Hz, CH$_2$), 3.99 (1H, t, $J = 8.0$ Hz, CH$_2$), 1.46 (3H, d, $J = 6.4$ Hz, CH$_3$) ppm.

^{13}**C NMR** (100 MHz): δ_c(CDCl$_3$) 155.0 (C=O), 73.5 (OCH), 70.6 (OCH$_2$), 19.2 (CH$_3$) ppm.

Mass Spec ESI: Calc: $[C_4H_6O_3Na]^+$ 125.0209 (M+Na$^+$), found: 125.0213.

IR (selected absorbances): 2987, 2924 (C-H alkyl), 1782 (C=O) cm^{-1}.

1,2-Butylene carbonate (CC3)

Yield: 0.166 g (colourless liquid, 86%).

^{1}H NMR (400 MHz): δ_H(CDCl$_3$) 4.69-4.62 (1H, m, OCH), 4.52 (1H, t, J = 8.0 Hz, CH$_2$), 4.08 (1H, t, J = 8.0 Hz, CH$_2$), 1.86-1.71 (2H, m, CH$_2$), 1.02 (3H, t, J = 8.0 Hz, CH$_3$) ppm.

^{13}C NMR (100 MHz): δ_c(CDCl$_3$) (100 MHz, CDCl$_3$) 155.1 (C=O), 78.0 (OCH), 69.0 (OCH$_2$), 26.9 (CH$_2$), 8.5 (CH$_3$) ppm.

Mass Spec ESI: Calc: $[C_5H_8O_3Na]^+$ 139.0366 (M+Na$^+$), found: 139.0363.

IR (selected absorbances): 2938, 2942, 2885 (C-H alkyl), 1781 (C=O) cm^{-1}.

1,2-Hexylene carbonate (CC4)

Yield: 0.194 g (colourless liquid, 81%).

^{1}H NMR (400 MHz): δ_H(CDCl$_3$) 4.71-4.65 (1H, m, OCH), 4.51 (1H, t, J = 8.0 Hz, CH$_2$), 4.06 (1H, t, J = 8.0 Hz, CH$_2$), 1.83-1.63 (2H, m, CH$_2$), 1.47-1.29 (4H, m, 2×CH$_2$), 0.91 (3H, t, J = 8.0 Hz, CH$_3$) ppm.

^{13}C NMR (100 MHz): δ_c(CDCl$_3$) 155.1 (C=O), 77.0 (OCH), 69.3 (OCH$_2$), 33.5 (CH$_2$), 26.3 (CH$_2$), 22.2 (CH$_2$), 13.7 (CH$_3$) ppm.

Mass Spec ESI: Calc: $[C_7H_{12}O_3Na]^+$ 167.0679 (M+Na$^+$), found: 167.0678.

IR (selected absorbances): 2959, 2933, 2873 (C-H alkyl), 1786 (C=O) cm^{-1}.

1,2-Decylene carbonate (CC5)

Yield: 0.272 g (colourless liquid, 82%).

¹H NMR (400 MHz): δ$_H$(CDCl₃) 4.72-4.65 (1H, m, OCH), 4.51 (1H, t, J = 8.0 Hz, OCH₂), 4.06 (1H, t, J = 8.0 Hz, OCH₂), 1.84-1.62 (2H, m, CH₂), 1.48-1.26 (12H, m, 6×CH₂), 0.87 (3H, t, J = 8.0 Hz, CH₃) ppm.

¹³C NMR (100 MHz): δ$_c$(CDCl₃) 155.0 (C=O), 77.0 (OCH), 69.4 (OCH₂), 33.8 (CH₂), 31.7 (CH₂), 29.2 (CH₂), 29.1 (CH₂), 29.0 (CH₂), 24.3 (CH₂), 22.6 (CH₂), 14.0 (CH₃) ppm.

Mass Spec ESI: Calc: [C₁₁H₂₁O₃]⁺ 201.1485 (M+H⁺), found: 201.1487.

Mass Spec ESI: Calc: [C₁₁H₂₀O₃Na]⁺ 223.1305 (M+Na⁺), found: 223.1308.

IR (selected absorbances): 2924, 2855 (C-H alkyl), 1794 (C=O), 1551 (C-O) cm⁻¹.

3-Chloropropylene carbonate (CC6)

Yield: 0.176 g (white solid, 78%).

¹H NMR (400 MHz): δ$_H$(CDCl₃) 4.98-4.92 (1H, m, OCH), 4.59 (1H, t, J = 8.0 Hz, OCH₂), 4.41 (1H, t, J = 8.0 Hz, OCH₂), 3.79-3.71 (2H, m, CH₂Cl) ppm.

¹³C NMR (100 MHz): δ$_c$(CDCl₃) 154.0 (C=O), 74.2 (OCH), 67.0 (OCH₂), 43.7 (CH₂Cl) ppm.

Mass Spec ESI: Calc: [C₄H₅³⁵ClO₃Na]⁺ 158.9819 (M+Na⁺), found: 158.9815.

IR (selected absorbances): 2966, 2925 (C-H alkyl), 1780 (C=O), 663 (C-Cl) cm⁻¹.

Melting point: 67-69 °C, literature: 68-69 °C.[105]

Glycerol carbonate (CC7)

Yield: 0.141 g (colourless liquid, 72%).

¹H NMR (400 MHz): δ$_H$(CDCl₃) 4.85-4.77 (1H, m, CH), 4.53 (1H, t, J = 8.3 Hz, OCH₂), 4.45 (1H, dd, J = 9.3, 5.8 Hz, OCH₂), 4.00 (1H, ddd, J = 12.7, 5.7, 3.1 Hz, C*H*OH), 3.68 (1H, ddd, J = 9.3, 7.6, 4.1 Hz, C*H*OH); 2.01 (1H, dd, J = 7.0, 5.7 Hz, CHO*H*) ppm.

^{13}C NMR (100 MHz): δ$_c$(CDCl$_3$) 155.1 (C=O), 76.4 (OCH), 65.7 (OCH$_2$), 61.7 (CH$_2$OH) ppm.

Mass Spec ESI: Calc: [C$_8$H$_{15}$O$_6$]$^+$ 207.0863 (M+EtOAc$^+$), found: 207.0865.

IR (selected absorbances): 3385 (O-H), 2899 (C-H alkyl), 1795 (C=O) cm^{-1}.

3-Phenoxypropylene carbonate (CC8):

Yield: 0.229 g (white solid, 71%).

^{1}H NMR (400 MHz): δ$_H$(CDCl$_3$) 7.31 (2H, t, *J* = 8.0 Hz, ArH), 7.02 (1H, t, *J* = 8.0 Hz, ArH), 6.91 (2H, d, *J* = 8.0 Hz, ArH), 5.06-5.00 (1H, m, OCH), 4.64-4.52 (2H, m, OCH$_2$), 4.24 (1H, dd, *J* = 11.0, 4.0 Hz, CH$_2$), 4.15 (1H, dd, *J* = 11.0, 4.0 Hz, CH$_2$) ppm.

^{13}C NMR (100 MHz): δ$_c$(CDCl$_3$) 157.7 (C=O), 154.6 (ArC), 129.7 (ArC), 122.0 (ArC), 114.6 (ArC), 74.1 (OCH), 66.8 (OCH$_2$), 66.2 (CH$_2$) ppm.

Mass Spec ESI: Calc: [C$_{10}$H$_{10}$O$_4$Na]$^+$ 217.0471 (M+Na$^+$), found: 217.0474.

IR (selected absorbances): 2924 (C-H alkyl), 1788 (C=O), 1598 (C-O carbonyl) cm^{-1}.

Melting point: 97-98 °C, literature: 100-102 °C.[87]

4-Chlorostyrene carbonate (CC9):

Yield: 0.299 g (white solid, 91%).

^{1}H NMR (400 MHz): δ$_H$(CDCl$_3$) 7.35 (2H, d, *J* = 8.0 Hz, ArH), 7.24 (2H, d, *J* = 8.0 Hz, ArH), 5.59 (1H, t, *J* = 8.0 Hz, CH), 4.73 (1H, t, *J* = 8.0 Hz, CH$_2$), 4.23 (1H, t, *J* = 8.0 Hz, CH$_2$) ppm.

^{13}C NMR (100 MHz): δ$_c$(CDCl$_3$) 154.5 (C=O), 135.8 (ArC), 134.2 (ArC), 129.5 (ArC), 127.2 (ArC), 77.2 (OCH), 71.0 (OCH$_2$) ppm.

Mass Spec ESI: Calc: [C$_9$H$_7$^{35}ClO$_3$Na]$^+$ 220.9976 (M+Na$^+$), found: 220.9975.

IR (selected absorbances): 2964, 2912, 2342 (C-H alkyl), 1789 (C=O) cm^{-1}.

Melting point: 66-68 °C, literature: 67-69 °C.[105]

4-Bromostyrene carbonate (CC10):

Yield: 0.357 g (white solid, 89%).

^{1}H NMR (400 MHz): δ_H(CDCl$_3$) 7.59 (2H, d, J = 8.0 Hz, ArH), 7.24 (2H, d, J = 8.0 Hz, ArH), 5.64 (1H, t, J = 8.0 Hz, CH), 4.80 (1H, t, J = 8.0 Hz, CH$_2$), 4.30 (1H, t, J = 8.0 Hz, CH$_2$) ppm.

^{13}C NMR (100 MHz): δ_c(CDCl$_3$) 154.5 (C=O), 134.8 (ArC), 132.5 (ArC), 127.4 (ArC), 123.9 (ArC), 77.2 (CH), 70.9 (CH$_2$) ppm.

Mass Spec ESI: Calc: [C$_9$H$_7$^{79}BrO$_3$Na]$^+$ 264.9471 (M+Na$^+$). Found: 264.9470.

IR (selected absorbances): 2963, 2910 (C-H alkyl), 1786 (C=O) cm^{-1}.

Melting point: 72-73 °C, literature: 72-75 °C.[84]

2.4.14 Synthesis of 3,4-diphenyloxazolidin-2-one (OX1A) and 3,5-diphenyloxazolidin-2-one (OX1B)[129]
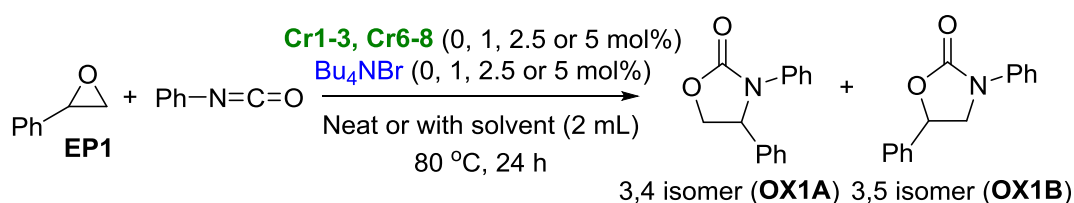
Styrene oxide **EP1** (0.1050 g, 0.87 mmol) and phenyl isocyanate (0.1041 g, 0.87 mmol) and were added to a mixture of catalyst **Cr1-3**, **Cr6-8** (0.0, 1.0, 2.5 or 5.0 mol%; 0.0, 0.0087, 0.022 or 0.044 mmol) and co-catalyst (0.0, 1.0, 2.5 or 5.0 mol%; 0.0, 0.0087, 0.022 or 0.044 mmol) in solvent (2 mL) or neat conditions. The reaction mixture was then heated to 80 °C for 24 h under reflux. Conversions were measured by ^{1}H NMR, by comparing the integral values of the unreacted epoxide, 3,4 isomer **OX1A** and 3,5 isomer **OX1B** peak of the reaction mixture when summed up to 100%. Isomer ratios were measured by ^{1}H NMR

after 24 h by comparing the ratio integrals of a 3,4 isomer **OX1A** and 3,5 isomer **OX1B** peak in the reaction mixture. After cooling to room temperature, the reaction mixture was concentrated in vacuo and then purified by column chromatography using a gradient elution of petroleum ether:ethyl acetate (5:1) then petroleum ether:ethyl acetate (3:1). The spectroscopic data for both isomers **OX1A** and **OX1B** prepared by using catalysts **Cr1-Cr3**, **Cr6-8** were consistent with those reported in the literature.[129,133]

Yield: 3,4-Diphenyloxazolidin-2-one **OX1A**, 0.1136 g (white solid, 54%); 3,5-diphenyloxazolidin-2-one **OX1B**, 0.0918 g (white solid, 44%); total yield 0.2054 g (98%). The highest total yield obtained is reported.

3,4-Diphenyloxazolidin-2-one (OX1A)

^{1}H NMR (400 MHz): δ_H(CDCl$_3$) 7.36-7.19 (9H, m, ArH), 7.02 (1H, t, J = 7.4 Hz, ArH), 5.34, (1H, dd, J = 8.7 Hz, 6.0 Hz, CHN), 4.71, (1H, t, J = 8.7 Hz, CH$_2$O), 4.14 (1H, dd, J = 8.6 Hz, 6.0 Hz, CH$_2$O) ppm.

^{13}C NMR (100 MHz): δ_c(CDCl$_3$) 156.0 (C=O), 138.1 (ArC), 136.9 (ArC), 129.3 (ArC), 128.9 (ArC), 128.8 (ArC), 126.2 (ArC), 124.6 (ArC), 120.8 (ArC), 69.8 (C-O), 60.6 (C-N) ppm.

Mass Spec ESI: Calc: [C$_{15}$H$_{14}$NO$_2$]$^+$ 240.1019 (M+H$^+$), found: 240.1008.

Mass Spec ESI: Calc: [C$_{15}$H$_{13}$NO$_2$Na]$^+$ 262.0838 (M+Na$^+$), found: 262.0847.

IR (selected absorbances): 2911 (C-H alkyl), 1745 (C=O), 1500 (C=C aromatic), 1209 (C-O), 1124 (C-N) cm^{-1}.

Melting point: 75.7-76.4 °C, literature: 76-78 °C.[133]

3,5-Diphenyloxazolidin-2-one (OX1B)

1H NMR (400 MHz): δ_H(CDCl$_3$) 7.56 (2H, d, J = 7.8 Hz, ArH), 7-46-7.35 (7H, m, ArH), 7.15 (1H, t, J = 7.4 Hz, ArH), 5.64, (1H, dd, J = 8.6 Hz, 7.6 Hz, CHO), 4.38, (1H, t, J = 8.8 Hz, CH$_2$N), 3.96 (1H, dd, J = 8.9 Hz, 7.6 Hz, CHO) ppm.

13C NMR (100 MHz): δ_c(CDCl$_3$) 154.6 (C=O), 138.0 (ArC), 138.0 (ArC), 129.0 (ArC), 128.9 (ArC), 125.6 (ArC), 124.1 (ArC), 118.2 (ArC), 73.9 (C-O), 52.5 (C-N) ppm.

Mass Spec ESI: Calc: [C$_{15}$H$_{14}$NO$_2$]$^+$ 240.1019 (M+H$^+$), found: 240.1024.

Mass Spec ESI: Calc: [C$_{15}$H$_{13}$NO$_2$Na]$^+$ 262.0838 (M+Na$^+$), found: 262.0840.

IR (selected absorbances): 2924 (C-H alkyl), 1745 (C=O), 1501 (C=C aromatic), 1210 (C-O), 1137 (C-N) cm^{-1}.

Melting point: 78.5-79.4 °C, literature: 79-82 °C.[133]

Chapter 3: A Novel Mixed Anode Approach for Electrochemical CO_2 Sequestration and Mineralisation Under Near Ambient Conditions

3.1 Introduction

3.1.1 Carbon (Dioxide) Capture and Storage (CCS)

Carbon Dioxide Utilisation is not the only methodology with the potential to decrease global CO_2 emissions. Carbon (dioxide) Capture and Storage (CCS) is another technique that can be used to diminish CO_2 levels. Carbon capture and storage is *"a process consisting of the separation of CO_2 from industrial and energy-related sources, transport to a storage location and long-term isolation from the atmosphere"*.[26] Carbon capture and storage is a multiple step process which proceeds via three main stages (Scheme 29):[27]

1) Capture: CO_2 is captured, and thus separated, from waste gases or other CO_2 gas sources,

2) Transport: The captured CO_2 is compressed and then transported (if required) to a suitable storage site, and

3) Storage: Carbon dioxide is permanently trapped, or sequestrated, via numerous methods, including transporting to deep underground rock formations.[159]

The first industrialised CCS project was started in 1972 at a natural gas processing plant in Texas, USA. Since then CCS has been implemented across the globe. As a result, more than 100 million tonnes of CO_2 has been trapped permanently since 1972.[160] Although CCS can be utilised on a global scale and make a significant impact in reducing CO_2 emissions it has only been partially implemented across the globe due to some drawbacks (*vide infra*).
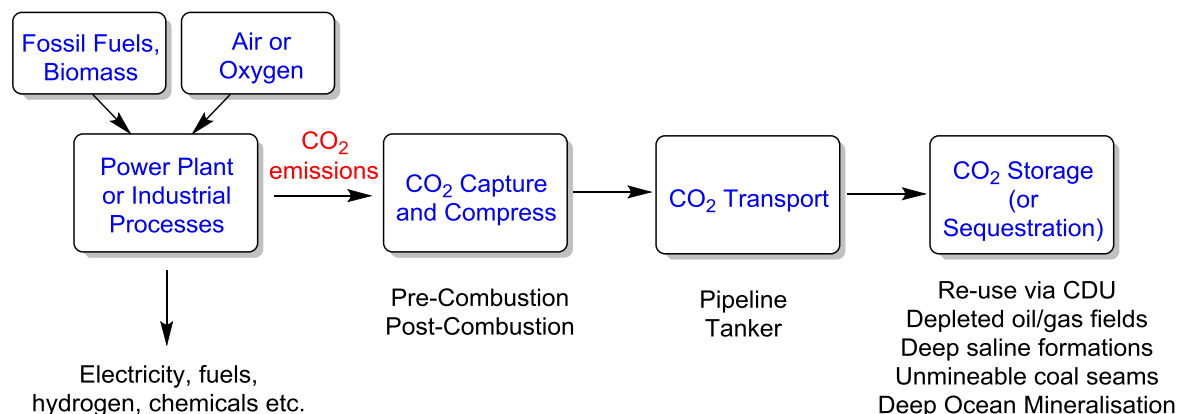
Scheme 29: The process of CCS methodology.[161,162]

3.1.2 The Disadvantages of CCS

The expensive and unfavourable economics of adding CCS, to current industrial processes, has hindered worldwide implementation. In a review by Rubin in 2015, it was highlighted that CCS can add an extra cost of approx. £50-£120 ($63-$150) per megawatt-hour (MWh) of energy used.[163,164] For example, implementing CCS in cement manufacturing would increase production costs by 68-105%.[164]

Funding towards future implementation and creation of CCS methodology is also limited, due to poor public perception of CCS.[14,165] In 2009, plans to implement a "German carbon capture plan" in Germany were halted due to public outcry, and in November 2015, the UK government withdrew £1 billion of funding to develop CCS further in the UK.[160,162,164] From 2007–2010, $30 billion (approx. £17 billion) was pledged to fund 35 large-scale global CCS projects. By early 2017, less than $3 billion (10%) of this globally pledged funding has been invested and only 7 of the planned CCS projects have reached the operation or construction stage.[164]

CCS is still an "infancy" technology compared to the well-established field of CDU, hence its small-scale global implementation and poor favourability. There are currently 15 large-scale global projects devoted to CCS, which in 2014 captured approx. 4-5 million tonnes of CO_2.[14,164,165] In comparison, CDU utilised 200 million tonnes of CO_2. When compared to the total CO_2 emissions in 2014 (32,000 million tonnes), CDU utilised 0.63%

of potential CO_2 emissions whereas CCS only captured 0.016%.[33] Carbon capture and storage is therefore not perceived by all as a long-term solution for reducing CO_2 emissions, perceived by some to be "wasteful" compared to CDU and is often given the analogy of "*sweeping dirt under the rug*".[35,159]

3.1.3 The Benefits of CCS and its Importance in Diminishing CO_2 Emissions

Despite the drawbacks associated with implementing CCS technology on an industrial scale, it is vital for reducing global CO_2 emissions. For example, CCS can decrease CO_2 emissions from a coal-fired power plant from 800 g of CO_2 per kWh to 100 g of CO_2 per kWh, if 90% of CO_2 emissions are captured and stored.[164] In 2015, the International Energy Agency (IEA) predicted that global CO_2 storage sites could store approx. 1680 gigatonnes of CO_2, with 94 gigatonnes of storage capacity in Europe alone, and only approx. 7% of these sites must be used by 2050 to significantly contribute to CO_2 reduction targets (Figure 28).[165] No other methodology offers the same scale or capacity for reducing CO_2 emissions, yet the majority of these sites are yet to be used. The Intergovernmental Panel on Climate Change (IPCC) declared in 2014 that the costs of decreasing CO_2 emissions, to stop a 2 °C increase in global temperature, would also increase by 138% without CCS.[160] Global use of CCS must therefore increase dramatically in the future.

Although CDU is often seen as the more favourable method to diminish CO_2 emissions compared to CCS, CDU alone is not enough to hinder the growth in global CO_2 emissions. In 2011, global CO_2 emissions reached 100 gigatonnes per year, but the maximum consumption possible for CDU via chemical and industrial processes was only 1 gigatonne per year.[166] There is therefore an ever-growing paradigm shift towards investigating not only CDU processes but also CCS, to try and bridge the ever expanding gap between increasing CO_2 emissions and captured (or utilised) CO_2 levels.
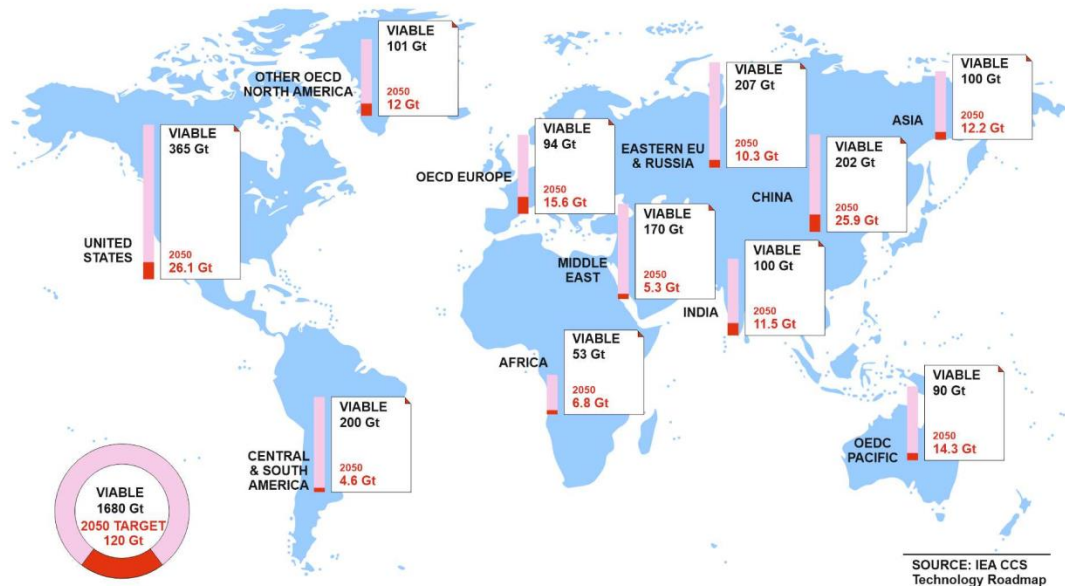
Figure 28: Predicted global storage capacity of CO_2 at CCS storage sites around the world in 2015.[165] Image was produced by Alisa Doroshenko.

It has been stated that "*CCS is the only technology that can achieve deep reductions in CO_2 emissions from high-emitting industries*".[160] This is because some industrial methods cannot be entirely decarbonised. For example, in 2012 cement production accounted for 5% of global CO_2 emissions. Half of this CO_2 was generated from the calcination of limestone, an inherent and unavoidable chemical process.[167] Bio-ethanol production and natural gas processing also inherently produce CO_2.[160,164] The implementation of CCS will therefore be required in the future.

Total decarbonisation of electricity generation and hence energy supplies, by eliminating the necessity for fossil fuels, such as coal, oil and natural gas, is also not an achievable, immediate solution to reducing CO_2 emissions. For example, approx. 2,400 new coal power stations are planned worldwide by 2030.[160] Full scale implementation of alternative and renewable energy resources, such as solar, wind and tidal, is also not a short-term solution.[160] Carbon capture and storage "*remains the only technology solution capable of delivering significant emissions reductions from the use of fossil fuels in power generation and industrial processes*".[164] In order to decrease CO_2 emissions sufficiently in the short term, the adaption of CCS to current industrial methods such as coal-fired power

137

generation must occur. However, current CCS methodology is lacking in worldwide implementation and requires further development to achieve current CO_2 reduction targets.

3.1.4 Current CCS Methodology

Carbon (Dioxide) Capture

The current state-of-the-art CO_2 capture method employed industrially is absorption via amine scrubbing, using the amine monoethanolamine (MEA, Figure 29).[168]
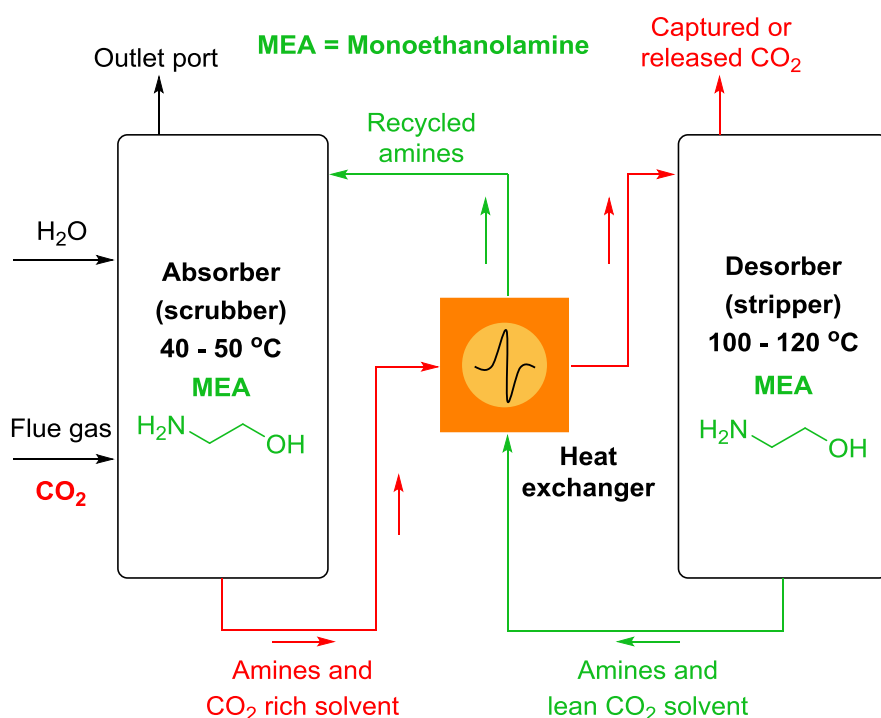
Figure 29: Simplified diagram of industrial CO_2 capture via amine scrubbing.[169,170]

Bottoms invented this technique in 1930 and it is capable of separating dilute levels of CO_2 from flue gas (gases emitted from an industrial burner or combustion chamber containing 7-14% CO_2).[27,168] The CO_2 mixture is bubbled into an aqueous amine solution, which traps CO_2 in solution as carbamate. The carbamate solution is then heated at $100–120$ °C in the presence of water vapour followed by condensation. This strips the carbamate solution, releasing the captured and purified CO_2, and regenerating the amine. The CO_2 can then be stored or used as desired (Scheme 30).[28,168,171] Amine scrubbing captures up to 75-90% of CO_2 from flue gas, and can supply 99% pure CO_2 gas.[172] On an industrial scale the energy

requirements of using amine scrubbing (with 30% w/w MEA) is 4215 kJ per kg of CO_2 or 186 kJ mol^{-1} (CO_2).[173]
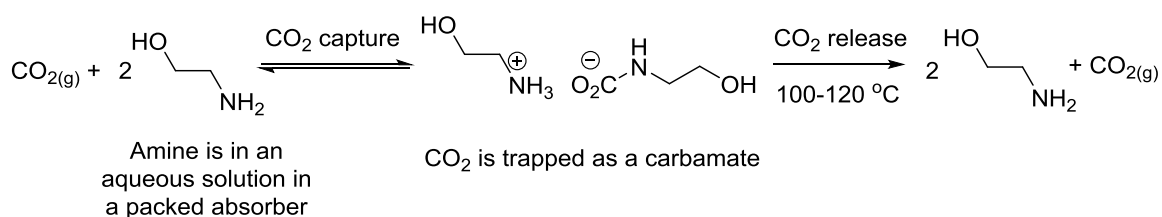
Scheme 30: Chemical process of CO_2 capture via amine scrubbing.[159,168]

Problems however exist with this technique. Amine scrubbing is ineffective at removing extremely dilute levels of gaseous CO_2 (<7% CO_2). The most favourable amine to use is monoethanolamine (MEA), which is an extremely toxic and unsustainable reagent. Over repeated use MEA degrades, due to the high temperature regeneration step and amine oxidation over time. The capital and operating costs entailed with CCS via amine scrubbing are therefore high, partly due to the energy requirements of the regeneration step and the need to refresh the amine over time. Flue gas must also be purified prior to CO_2 capture, because SO_x and NO_x gases in flue gas can destroy the amine, which further increases the costs of this process.[168,174]

Alternative Techniques

Numerous CO_2 capture techniques have been developed besides amine scrubbing, to try to overcome issues such as high operating costs and poor sustainability. The number of alternative CCS techniques in the literature is vast, and can be split into five techniques; CO_2 absorption (capture via a liquid sorbent), CO_2 adsorption (capture via a solid sorbent), cryogenics (freezing CO_2), membrane separation and using microbial or algal systems (Figure 30).[161] Many of these alternative methods however are less effective than amine scrubbing, in terms of CO_2 capture efficiency, and are not currently economically viable. Creating a cheaper and alternative CO_2 capture methodology is therefore still a major problem and hindrance to global implementation.
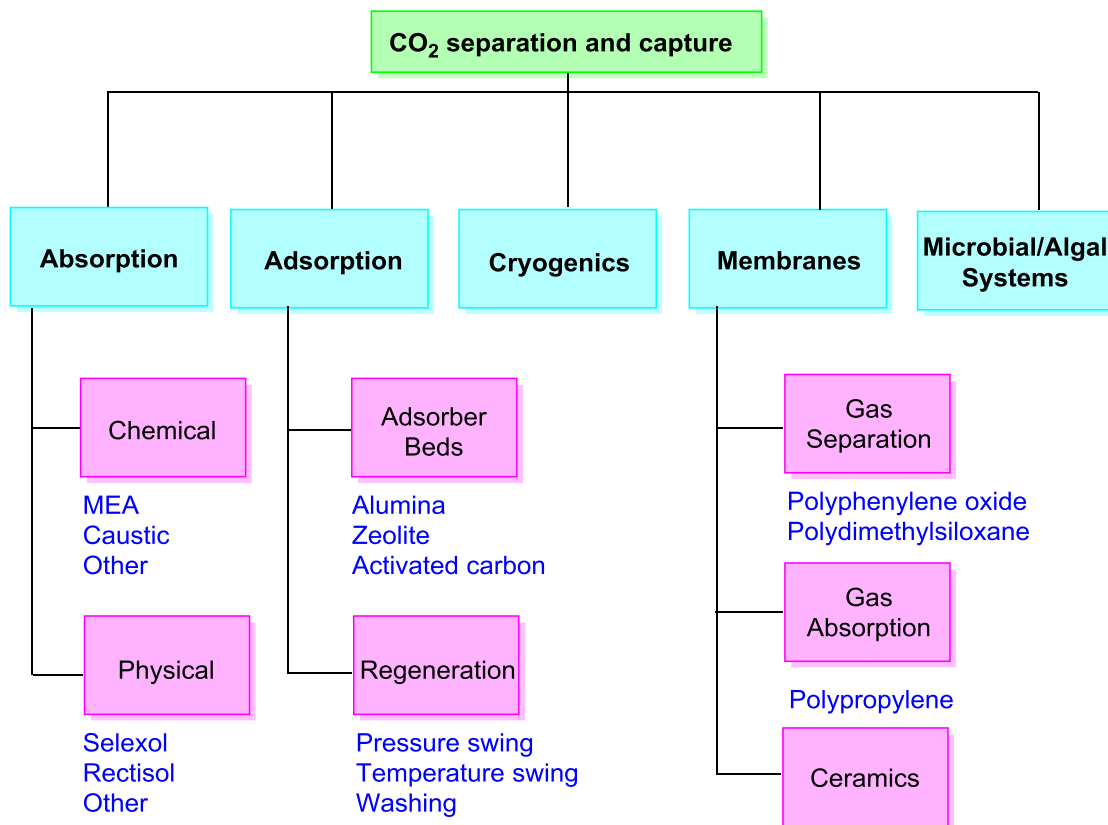
Figure 30: Different CO_2 capture methodologies reported in the literature.[161,172]

Carbon (Dioxide) Storage

Not only is CO_2 capture important, but its long-term storage post-CO_2 capture. The main storage or sequestration methods currently employed include geologic and ocean (or seabed) storage, Enhanced Oil Recovery (EOR) and mineralisation (aka mineral carbonation or CO_2 mineral sequestration).[27,175]

Geologic sites provide large-scale CO_2 storage, but have the potential risk of CO_2 leakage from fractures caused via geomechanical deformation, and therefore need constant monitoring.[23,162] In 2013, only three geologic storage sites were operating worldwide, Sleipner in Norway, Weyburn in Canada and Salah in Algeria, each capable of trapping >1 megatonne of CO_2 per year. The number of other suitable sites worldwide is however limited, therefore geologic storage is restricted in future global implementation.[23,27]

Ocean and seabed carbon sequestration offers extensive storage capacity for CO_2, with predictions that it could sequester approx. 90% of anthropogenic CO_2 emissions in the future. This process however will take thousands of years due to slow reaction kinetics and

mixing time of gases into the ocean, therefore it is not a short-term solution.[176] Ocean sequestration of CO_2 will also affect the ocean ecosystem, due to increasing the acidity of seawater.[177-179] The transportation of CO_2 via pipelines or tankers into the ocean, or seabed, is also problematic.[175]

Enhanced oil recovery is when CO_2 is pumped underground directly into oil reserves, thereby pumping oil from deep underground towards the Earth's surface whilst simultaneously storing CO_2 underground. The energy requirements for EOR however are extremely high, and it is not the most economically viable method of obtaining oil. The capability of performing EOR is also only viable in certain countries, such as the USA and China, and is therefore restricted in global implementation.[180]

One method growing in popularity worldwide is the mineralisation of CO_2. Carbon dioxide mineralisation is a natural process, when the weathering of silicate rocks, such as serpentine, olivine and wollastonite, leads to the formation of alkaline carbonates (Scheme 31). Chemical or industrial mineralisation is when CO_2 is reacted with alkaline-earth oxides, usually calcium oxide or magnesium oxides, to form alkaline carbonates.[181]

$$Mg_3Si_2O_5(OH)_4(s) + 3CO_2(g) \longrightarrow 3MgCO_3(s) + 2SiO_2(s) + 2H_2O(l)$$
Serpentine

$$MgSiO_3(s) + CO_2(g) \longrightarrow MgCO_3(s) + SiO_2(s)$$
Olivine

$$CaSiO_3(s) + CO_2(g) \longrightarrow CaCO_3(s) + SiO_2(s)$$
Wollastonite
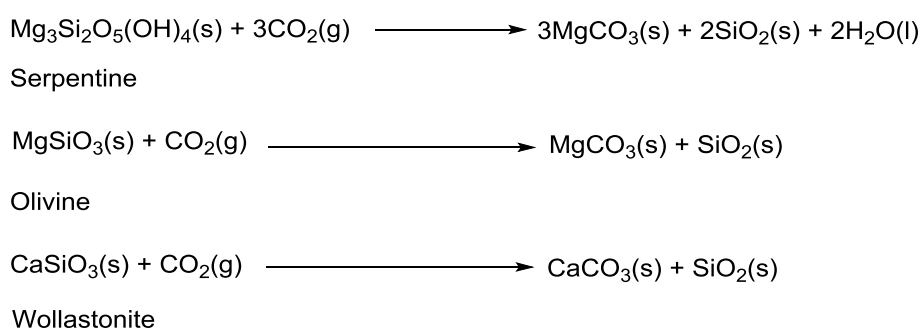
Scheme 31: Natural mineralisation of CO_2 with earth minerals to form stable alkaline carbonates.[181]

Mineralisation is often perceived as the most feasible global CO_2 storage method, as mineral carbonates provide the longest possible storage time, and highest carbon storage capacity, for CO_2 compared to any other methods (Figure 31).[182] In 2013, atmospheric levels of CO_2 were equivalent to 800 gigatonnes of carbon, whereas 39,000,000 gigatonnes
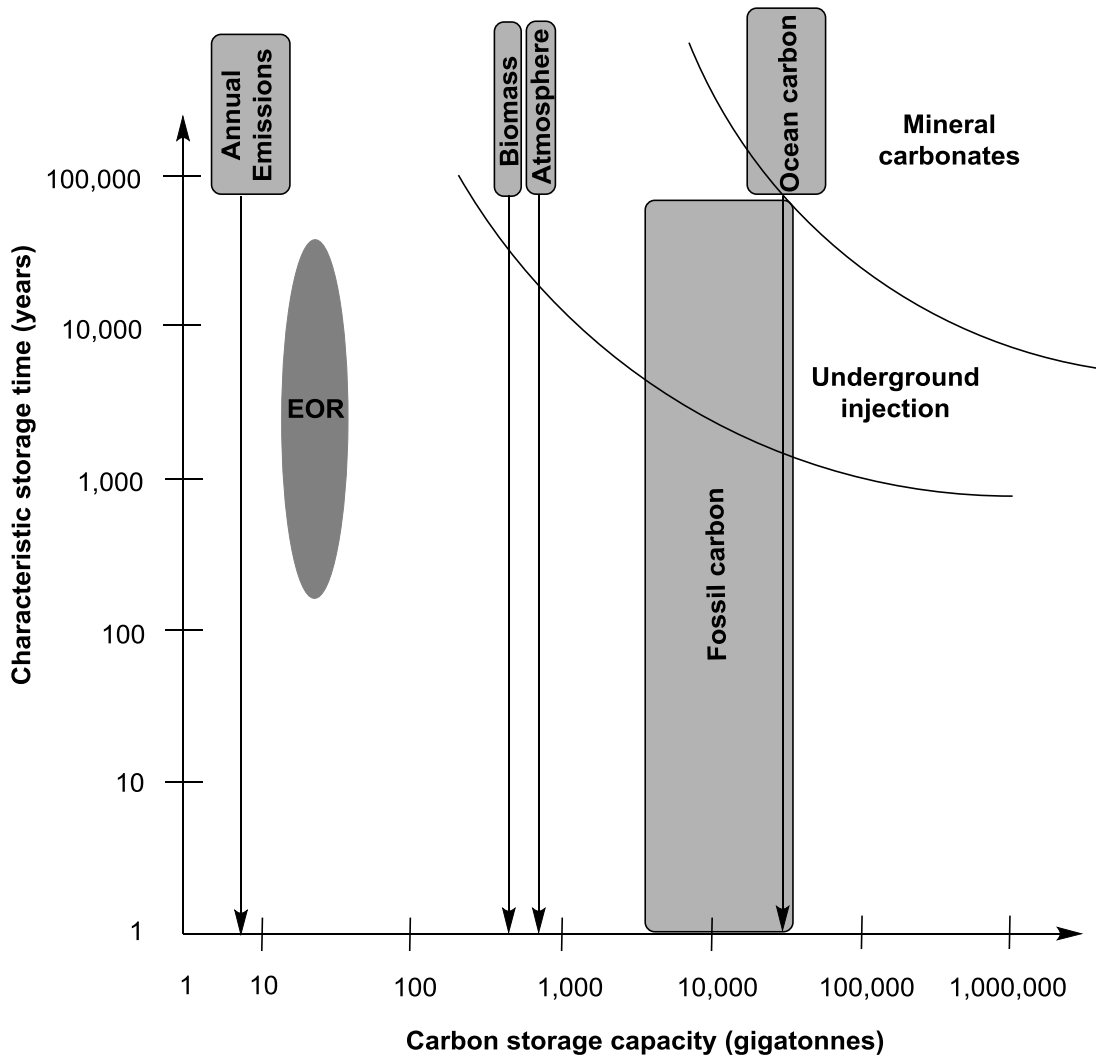
Figure 31: Estimated carbon storage capacities and storage times for CO_2 sources and CO_2 storage methods in 2006.[182]

of carbon were trapped in the Earth's crust in carbonate rocks, such as marble, limestone and chalk. The total carbon in the Earth's atmosphere was therefore <1% of the total carbon in the Earth's crust, further illustrating its extensive capacity to store CO_2.[175,183]

Mineralisation can be employed worldwide, due to the high availability and abundance of minerals such as serpentine, olivine and wollastonite.[175,181,183] Industrial alkaline waste, such as steelmaking slag, cement waste and industrial brines, can also be recycled and used for mineralisation due to their high concentration of calcium and magnesium cations.[181,183-185] Mineralisation can also convert "waste" CO_2 into high value products, such as precipitated calcium carbonate ($CaCO_3$, PCC), thus demonstrating that CCS does not necessarily have to dump CO_2 as waste.[181]

Carbon dioxide mineralisation however has some limitations. Mineralisation is an exothermic process, for example the formation of olivine, serpentine and wollastonite releases 89, 64 and 90 kJ of heat per mol of CO_2 respectively (Scheme 31). This suggests that no overall energy input is required for mineralisation to occur.[181] However, the kinetics of natural CO_2 sequestration or dissolution dictate that this process occurs naturally over a long time scale (years).[186,187] Carbon dioxide mineralisation therefore requires harsh conditions, such as high temperatures and pressures, to occur over a realistic timescale when employed industrially.[188] Current industrial mineralisation methods therefore have undesirable extensive energy requirements, expensive costs and often require complex setups.[181,182,188]

3.1.5 The Requirement for Cost-effective and Sustainable CCS

In order for CCS to contribute successfully towards reaching global CO_2 reduction targets, it is predicted that CCS must capture 17% of CO_2 current emission levels and 7 gigatonnes of CO_2 must be captured every year by 2050.[35] This is an ambitious task, one that cannot be fulfilled with currently employed CCS methodology.

As highlighted in "3.1.4 Current CCS Methodology", the major issues preventing global CCS implementation, and growth of alternative technologies, are high energy penalties and thus expensive costs.[168,172] This was emphasised by Rubin in 2012, who stated that "*major drawbacks of current capture processes are their high cost per unit of power produced*".[161] In 2017, Verhelst *et al.* also emphasised using renewable and sustainable energy to perform CCS or CDU will be vital in the future.[159] The development of cheaper CCS methodology, driven by sustainable and renewable energy, is therefore essential.

After considering the current situation of CCS methodology, we became interested in this field and wanted to investigate alternative and novel methodology, that could capture CO_2 with a low energy penalty, and therefore low cost, and use renewable energy. In Verhelst's review, it was suggested that renewable energy sources, such as higher temperatures,

chemical compounds or "*electrons from electricity*", should be used to perform CCS.[159] We therefore decided to investigate using electricity to perform CCS, the energy source intrinsic to the field of electrochemistry.

3.1.6 Electrochemistry and CCS

Electrochemistry is "*the branch of chemistry concerned with the interrelation of electrical and chemical effects*".[189] Electrochemistry therefore uses electricity, which can be generated from renewable energy, such as solar, geothermal, wind and tidal energy,[190] all of which provide low-carbon electricity. In the UK in 2011, electricity derived from solar energy emitted 88 g of CO_2 per kWh, whereas electricity from the combustion of coal energy emitted 786 g of CO_2 per kWh.[191] We therefore envisioned that developing an electrochemical method which could provide an economically viable and green alternative CCS method was a possibility.

The use of electrochemistry to decrease CO_2 emissions is not a novel concept, as electrochemistry has been researched in CDU, via CO_2 reduction, and CCS, via CO_2 capture or mineralisation.[35] Electrochemical CO_2 reduction is when CO_2 gains electrons (is reduced) and the carbon is consequently transformed into lower oxidation state hydrocarbons such as formaldehyde, methanol and methane.[33] The field of CO_2 reduction research is vast and this process has not only been achieved via electrochemistry, but also using chemical, photochemical and enzymatic methods.[28,192] The reduction of CO_2 is not simple, and the intrinsic thermodynamic stability of the carbon-oxygen bonds in CO_2 dictates that homogenous or heterogeneous catalysts are required to achieve low energy CO_2 reduction. A multitude of different reduction products are often formed, hence product selectivity is also problematic with CO_2 reduction.[193,194] As electrochemical CO_2 reduction is a CDU based technology, this methodology will not be discussed further. The two areas of CCS based electrochemistry research that were of interest were electrochemically driven CO_2 capture and electrochemically driven CO_2 mineralisation.

3.1.7 Electrochemically Driven CO_2 Capture

The concept of electrochemically driven CO_2 capture has been known since the 1980s, when Winnick *et al.* developed a high temperature molten carbonate fuel cell (MCFC) for manned spacecraft, which could capture dilute levels of CO_2 (Figure 32).[27,195]

(a)

$H_2 \rightarrow$

$CO_2 + H_2 \longrightarrow CO + H_2O$
$CO_3^{2-} + H_2 \longrightarrow CO_2 + H_2O + 2e^-$

$\rightarrow H_2 + H_2O + CO + CO_2$

Porous Electrodes

$CO_2\text{-Air} \rightarrow$

$CO_2 + 0.5O_2 + 2e^- \longrightarrow CO_3^{2-}$

$\rightarrow CO_2\text{-Air}$

(b)

$CO_2\text{-Air} \rightarrow$

$CO_2 + 0.5O_2 + 2e^- \longrightarrow CO_3^{2-}$

$\rightarrow CO_2\text{-Air}$

Porous Electrodes

$N_2 \rightarrow$

$CO_3^{2-} \longrightarrow CO_2 + 0.5O_2 + 2e^-$

$\rightarrow CO_2 + N_2$
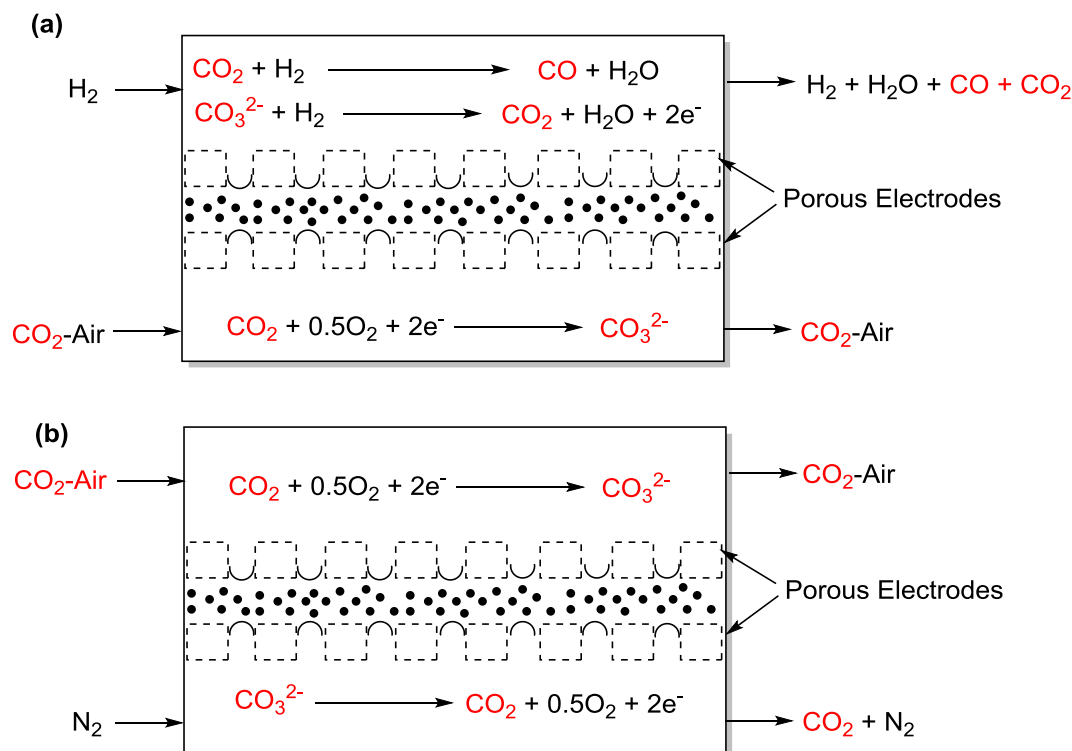
Figure 32: One of Winnick's MCFC used for CO_2 capture in (a) H_2 mode and (b) N_2 mode.[195]

Carbon dioxide capture efficiencies of up to 60% were reported with Winnick's method but required high temperatures of 650-700 °C to operate sufficiently. The energy and cost penalty of using this cell to promote CCS on a large, industrial scale would therefore be too extensive.[161,196] This technique also does not permanently trap CO_2 or create a pure CO_2 gas stream. Nevertheless, Winnick's research sparked interest in developing electrochemically driven CCS methodology. Some of the most notable examples in the literature are discussed further in this introduction.

Since Winnick's original MCFC design, more MCFCs have been developed for CO_2 capture. The majority of MCFCs reported in the literature have poorer CO_2 capture efficiencies compared to amine scrubbing (40-60% compared to 75-90%).[27,195-197] MCFCs also contain toxic and corrosive molten carbonates, which are extremely difficult to handle,

require high operating temperatures and cause electrolyte degradation over time. Solid phase membrane based fuel cells have been researched as an alternative to MCFCs, but are currently too expensive to employ industrially, also due to high temperature requirements and expensive operating costs.[27,174,196,197]

Another electrochemical method that has been researched for CO_2 capture is electrodialysis, which is the separation of ions in a liquid, aided by the application of an electric field to ion selective membranes. By using ion selective membranes, different compartments of an electrochemical cell can be pH controlled, and thus the capture of CO_2 can be achieved using a "pH swing" based system (Figure 33).[161,190,198,199]
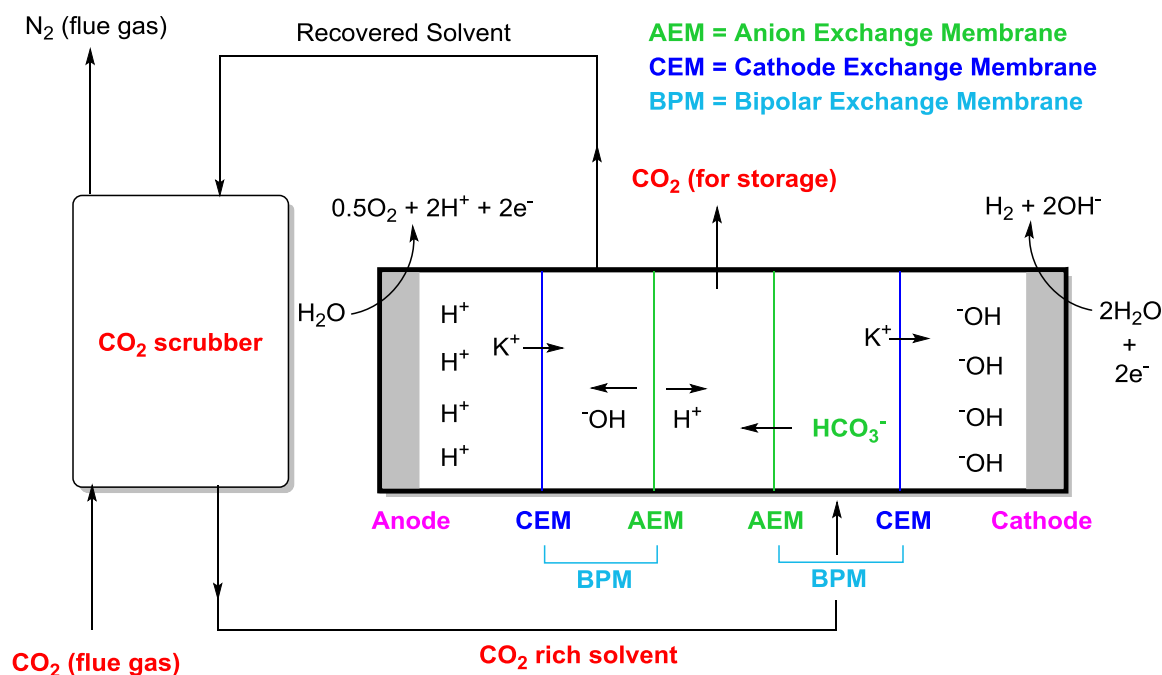
Figure 33: General schematic of CCS via electrodialysis.[161]

An interesting example of using electrodialysis for CO_2 capture was reported by Eisaman et al. in 2011. Eisaman investigated using BiPolar Membrane ElectroDialysis (BPMED) to promote CO_2 capture by electrochemically forming sodium and potassium hydroxide solutions. These caustic solutions would form bicarbonate or carbonate anions when gaseous CO_2 was bubbled through, which are then transported through bipolar membranes (BPMs, ion exchange membranes (IEMs) with a cathode exchange membrane (CEM) and anion exchange membrane (AEM) placed together).[200] The bicarbonate or carbonate

anions are then transferred into an acidic solution of phosphoric acid (H_3PO_4) and potassium dihydrogen phosphate (KH_2PO_4), as the increase in acidity releases CO_2 gas. This flow based method was capable of capturing CO_2 from concentrated CO_2 gas,[190,198,199] and required 100 kJ per mol^{-1} of CO_2 under optimum conditions,[190] This method is extremely effective but requires a complex setup, which ultimately hinders industrialisation of this process,[198,199] does not permanently store CO_2 and is not economically viable compared to amine scrubbing.[198,199,201,202] In general, electrodialysis and BPMED based methods often require pure CO_2 and therefore a CO_2 gas scrubber in the experimental setup (Figure 33). Therefore, unless this methodology can be improved to capture dilute levels of CO_2, future industrial implementation is unlikely.

Electrolysis, which is chemical decomposition achieved by passing an electric current through a liquid or electrolyte, can also perform CO_2 capture and is also based on the "pH swing" concept. Electrolysis, unlike electrodialysis, can produce valuable gases such as H_2 and O_2, therefore providing extra economic value to the capture process. However, the energy costs of utilising electrolysis for CO_2 capture are expensive due to the substantial energy requirements for water electrolysis.[161,203]

In 2010, Pennline *et al.* illustrated a novel electrochemical cell that could capture and separate CO_2 gas at lower temperatures compared to other electrochemical methods.[174] The cell contained polymer based nickel and platinum electrodes, supported on carbon paper, with an AEM between the electrodes. It was hypothesised that oxygen reduction at the cathode occurred upon application of a current to the cell, thus forming hydroxide anions which react with CO_2 gas to form bicarbonate anions. These anions then transport through the AEM towards the anode to become oxidised and thus release CO_2 gas. This specifically designed cell could capture CO_2 at temperatures lower than 400 °C, whereas similar electrochemical methods, such as MCFCs, require higher temperatures. As a consequence, the energy requirement for CO_2 capture was only 77 kJ mol^{-1} CO_2 under optimum

conditions. This cell however is incapable of permanently trapping CO_2 and was only tested with a 1:1 mixture of $CO_2:O_2$. This technique therefore cannot currently replace amine scrubbing, despite its energy efficiency.

In 2014, Stern *et al.* developed a combined electrochemical and amine based method for CO_2 capture called Electrochemically-Mediated Amine Regeneration (EMAR), which combines the CO_2 adsorption capability of the amine ethylene diamine (EDA) and copper oxidation to perform CO_2 capture (Scheme 32).[204,205]
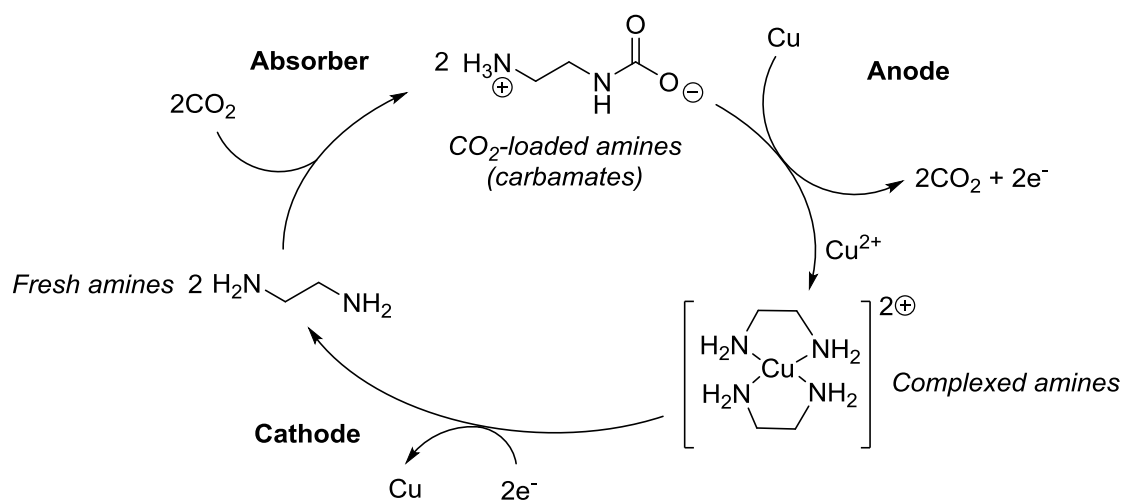
Scheme 32: The EMAR process.[204,205]

In EMAR, CO_2 is absorbed by EDA, and then desorbed from the amine by cupric ion displacement, facilitated by the oxidation of a copper anode, i.e. $Cu \rightarrow Cu^{2+} + 2e^-$, thus releasing pure CO_2. The copper amine complex is then electrochemically regenerated by electroplating the cupric ions onto a copper cathode, i.e. $Cu^{2+} + 2e^- \rightarrow Cu$, thus creating fresh amines to repeat the cycle (Scheme 32). This methodology can effectively trap CO_2 at ambient temperature with a low energy requirement of 100 kJ mol^{-1} (CO_2).[204,205] Electrochemically-mediated amine regeneration is an innovative and efficient technique but intrinsically requires toxic amines, only operates effectively with purified CO_2 gas and is ineffective for dilute levels of CO_2. Therefore this method is not currently as effective as amine scrubbing.

Capacitive deionisation is a well-known phenomenon that is utilised in industrial water and seawater purification technology. By applying a voltage across two electrodes, the ions of opposite charge to that on the surface are attracted to each electrode (Figure 34).[206,207]
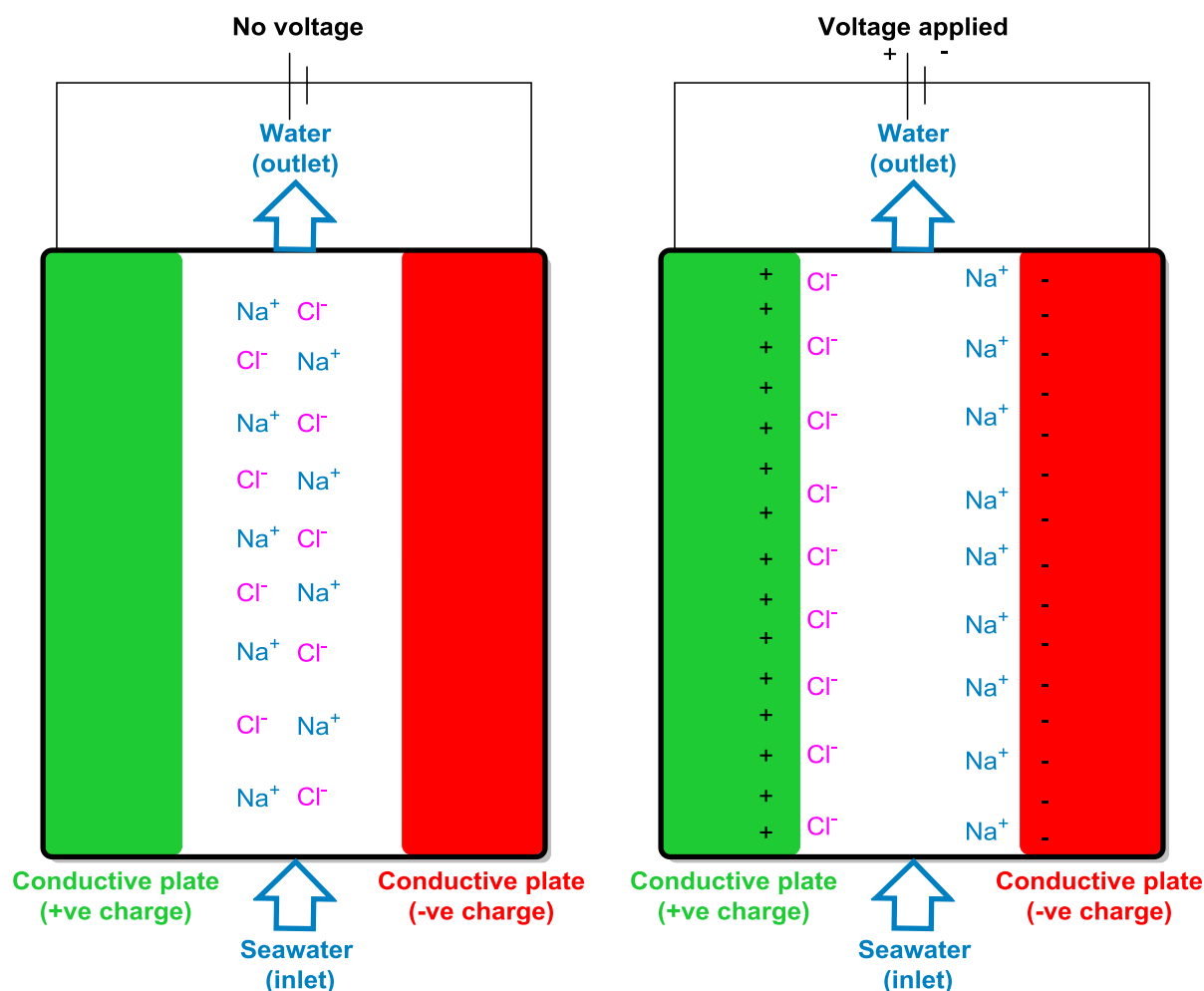
Figure 34: Schematic representation of capacitive deionisation.[206,207]

The ability of an electrode surface to store an electrical charge is expressed mathematically as $\Delta Q = C \times \Delta V$, where C is capacitance (in Farad or F), Q is charge stored (in coulombs or C), and V is voltage.[208] As well as water purification applications, capacitors are used as electronic components, because they are capable of storing an electric charge and then delivering the stored charge on demand as an electric current. A supercapacitor (Figure 35) is defined as a capacitor that possesses higher energy densities, and therefore specific energies (5-10 Wh kg^{-1} or 18-36 kJ kg^{-1}), than conventional capacitors (<0.1 Wh kg^{-1} or 0.36 kJ kg^{-1}),[209,210] where energy density and specific density are the amount of energy stored in a given system per unit volume and per unit mass, respectively.

149
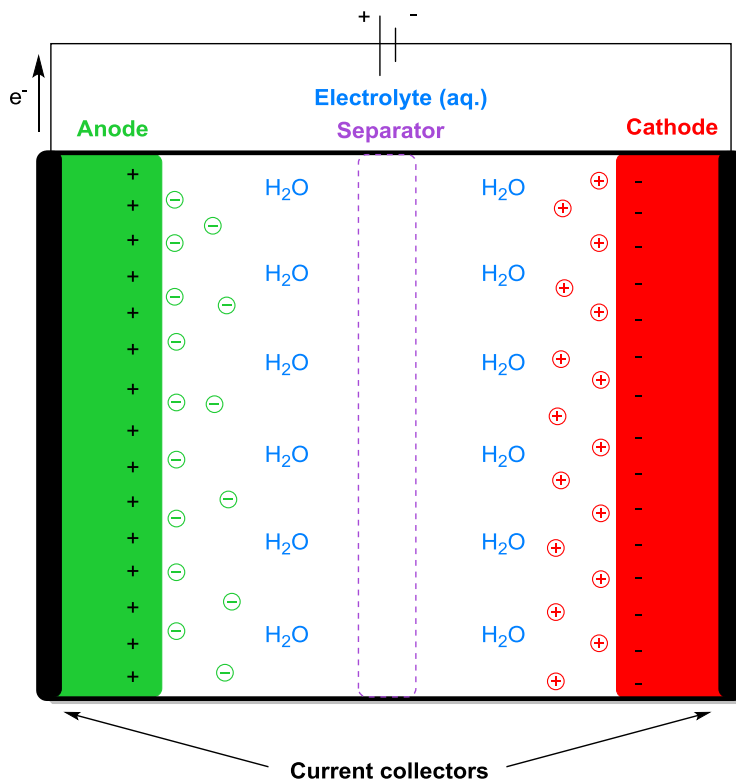
Figure 35: Schematic representation of a supercapacitor.[211]

A report by Landskron *et al.* in 2014 illustrated how capacitive technology could be extended to carbon capture applications. By using porous carbon based electrodes as both the anode and cathode, they promoted the sequestration of dilute levels of CO_2 into an aqueous solution of 1 M NaCl in a sealed electrode cell (Figure 36).[212] This method is coined "supercapacitive swing absorption" (SSA), as charging the electrodes creates the formation of an Electrical Double Layer (EDL, Figure 36), which subsequently causes a gas pressure drop in the headspace of the cell. Switching off the voltage induces a gas pressure rise, indicating reversible CO_2 adsorption, and thus CO_2 capture, is achieved at the electrodes.

Not only did this method illustrate how simple methodology could be adapted to electrochemically sequester CO_2, it also showed the potential to use simple non-metal based electrodes for CO_2 capture. Carbon based electrodes have favourable electrode characteristics, due to their chemical and physical properties of high conductivity, surface-area range, temperature stability, low costs and ability to be processed and compacted as desired.[213] Using carbon based electrodes for CO_2 capture, as
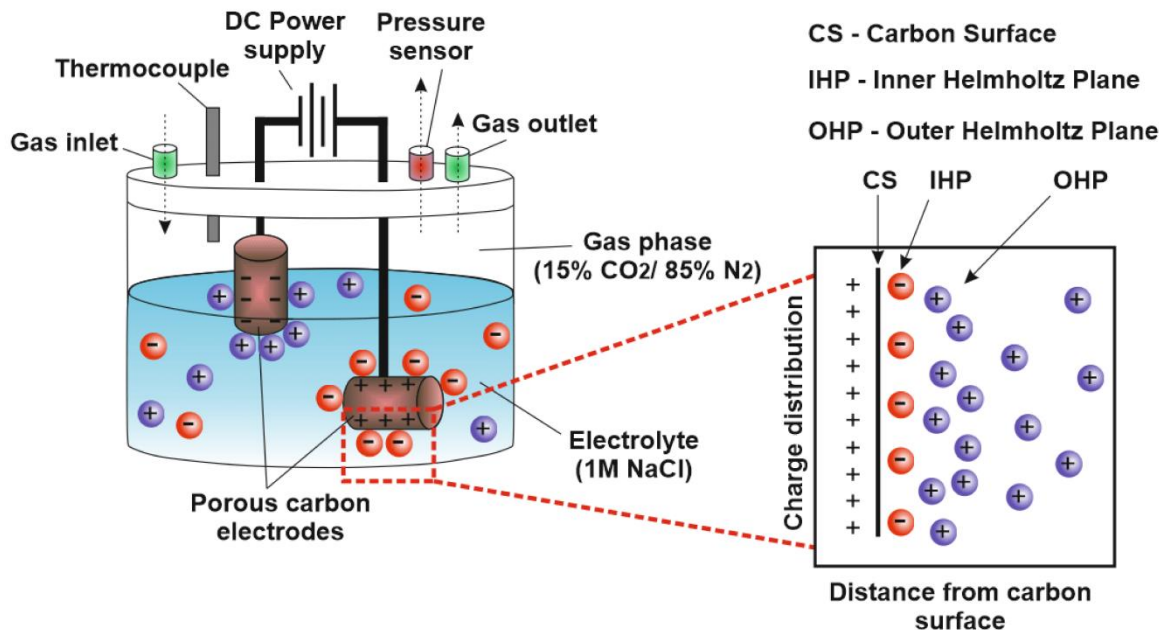
Figure 36: The experimental setup reported in the supercapacitive swing adsorption of CO_2 by Landskron with a representative structure of the electrical double layer (EDL) forming on the carbon electrodes.[212] Image was produced by Alisa Doroshenko.

illustrated by Landskron, twinned with the non-toxic NaCl electrolyte, could therefore provide a simple and sustainable alternative CO_2 capture technique, without the need for expensive membranes such as IEMs.[214-216] This system however was only studied to a basic level, as pH levels were not monitored. Carbon dioxide capture via this supercapacitive swing adsorption method is also not permanent, as once the current flow was stopped the captured CO_2 was released. This was also a sealed system, and therefore unsuitable for downstream application for a constant CO_2 producing industrial plant.

Landskron *et al*. therefore further developed their method in 2017 with the development of a gas-flow SSA module.[217] This module contained a similar setup to coin type supercapacitors[218] (Figure 35), with the implementation of gas-flow channels and a gas diffusion layer, similar to those used in fuel cells (Figure 37). These components were used together to ensure gases (such as CO_2) could be separated from a permanent gas-flow and diffuse between the electrodes and graphite plates, whilst a constant electrical contact between the electrodes and current collectors was maintained.[219] In principle, this would improve the charge-discharge kinetics of the cell, and thus adsorption-desorption capability

Black = Current Collector   Grey = Graphite Plates   Purple = Gas Diffusion Layer
Green = Anode   Blue = Separator containing Electrolyte   Red = Cathode
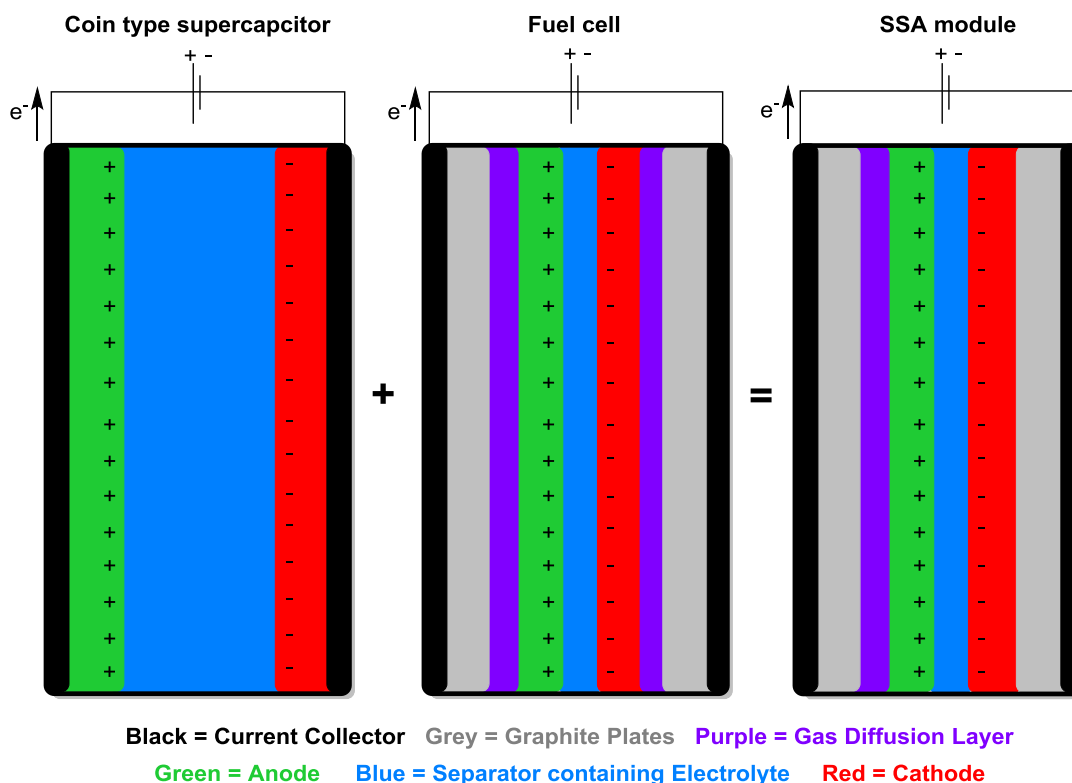
Figure 37: Design process of the supercapacitive swing adsorption (SSA) module, with schematic (not-to-scale) representations of a coin type supercapacitor, fuel cell and SSA module.[211]

for CO_2 capture, due to a large contact area between the gas and electrodes. The development of the SSA module was successful, as the charge-discharge kinetics improved, taking only 30 mins to reach full sorption compared to 8 h in the original module (Figure 36). This cell could also perform low energy CO_2 capture in a flow-based system with an energy consumption of only 57 kJ mol^{-1} CO_2. This module nonetheless is still at the prototype stage.[217]

3.1.8 Electrochemically Driven CO_2 Mineralisation

The sequestration of CO_2 into aqueous solutions to perform CO_2 mineralisation is not a novel concept.[177,220-222] For example, in 2005 Druckenmiller *et al.* illustrated that aqueous NaCl could be used to sequester CO_2 and consequently form carbonate salts. High temperatures and pressures of 75-150 °C and 40-100 bar of CO_2 were required for effective CO_2 capture and storage over a realistic timescale.[186] Some research has therefore been devoted towards investigating electrochemically driven CO_2 mineralisation, to investigate if CO_2 sequestration and mineralisation can be performed using less strenuous, or even

near ambient, conditions.[177] As of early 2017, this field of science has not been thoroughly researched. For example, a search for "*electrochemical carbon dioxide mineralisation*" on Web of Science[TM] in January 2017, without fine-tuning the search, produced approx. 80 results, whereas a similar search for "*electrochemical carbon dioxide reduction*" obtained approx. 2,800 results. From these 80 results, there are a few notable examples.

In 2012, Gilliam *et al.* and Calera Corporation developed an electrochemical method that performed CO_2 mineralisation using aqueous NaCl by electrochemically converting CO_2 into carbonates.[223-225] The electrochemical cell uses IEMs to perform hydrogen oxidation at the anode and water reduction at the cathode. Protons then react with chloride ions to produce HCl at the anode, and hydroxide ions react with sodium ions to form NaOH at the cathode (Step 1, Figure 38).
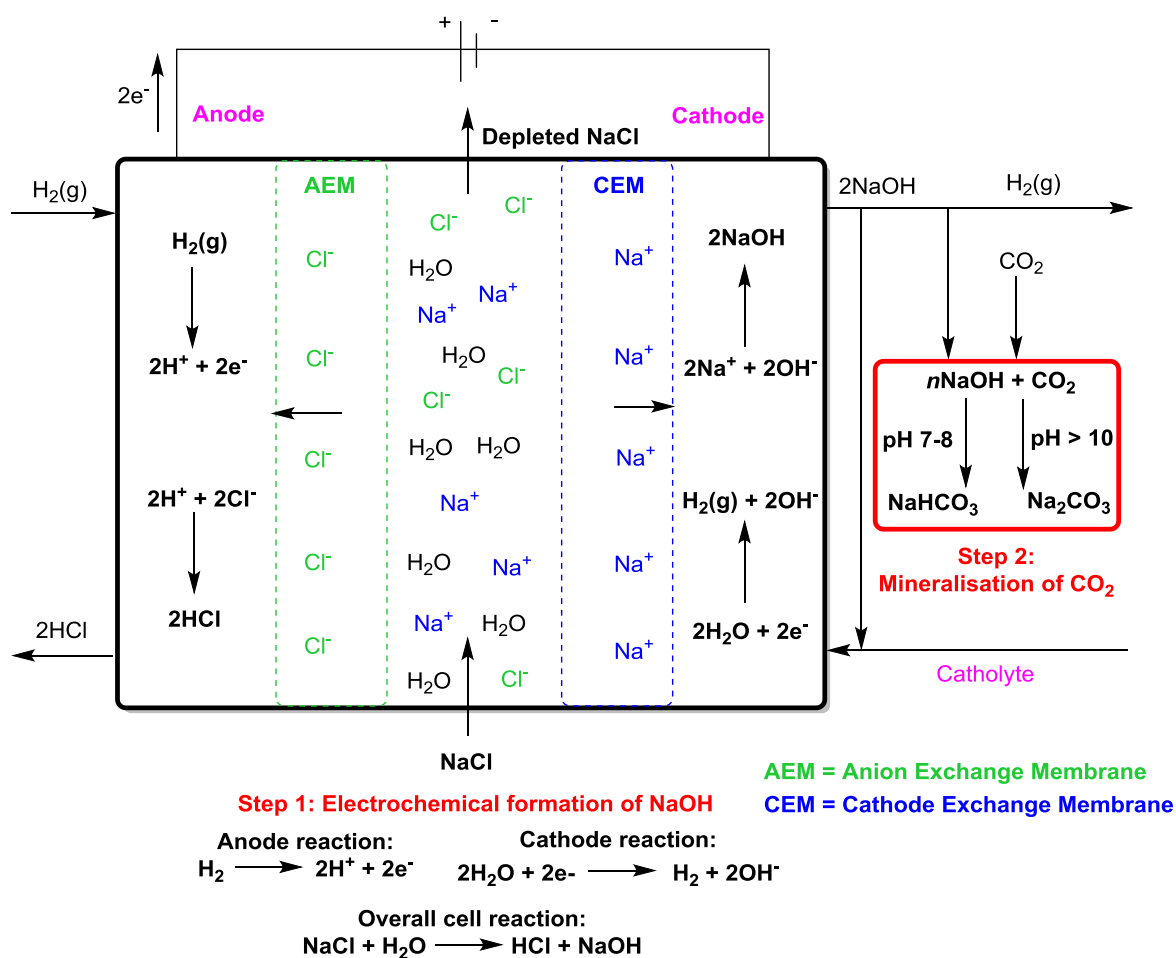
Figure 38: Electrochemical method designed by Gilliam and Calera Corporation for CO_2 capture and mineralisation via NaOH production.[226]

Electrochemically formed NaOH then reacts with gaseous CO_2 to produce sodium bicarbonate or carbonate, depending on solution pH (Step 2, Figure 38).[226] Gilliam and Calera Corporation's continuous-flow setup has been further developed into a more compact design by Mehmood *et al.*, with an optimised energy requirement of 676 kJ mol^{-1} (NaOH) for carbon capture.[226,227]

This methodology provides a simplistic approach to CO_2 mineralisation but has some drawbacks. This technique requires pure H_2 gas to operate, which is an extremely flammable gas, has only been tested with pure CO_2, and also uses expensive membranes. This, twinned with the energy penalty associated with forming aqueous NaOH,[188] increases the cost of this method dramatically and hinders any future industrialisation. Nevertheless, this process illustrated how simple and non-toxic electrolytes can be used to electrochemically mineralise CO_2 under near ambient conditions.

In 2010 a similar but simpler technology was patented by Skyonic Corporation. In this method, the electrolysis of aqueous NaCl was utilised to form aqueous NaOH. Flue gas levels (10-16%) of CO_2 were then flowed through the caustic solution to promote the formation of sodium carbonate.[228] This further illustrated the capability to perform electrochemically driven CO_2 sequestration and mineralisation, using the simple and non-toxic electrolyte NaCl. No further studies into this technique however have been performed, and the technology has not been industrialised, suggesting scale-up and implementation of this technique is not straightforward.

In 2015, He *et al.* illustrated the potential to perform electrochemical CO_2 capture and mineralisation simultaneously using sustainable materials. He demonstrated that membrane electrolysis combined with simulated hard water (water with concentrated levels of calcium and magnesium cations) could electrochemically form carbonates, by bubbling pure CO_2 through the cell whilst applying a current flow between the anode and cathode.[229] The anode region used HCl (or NaCl) as the anolyte and a Pt/C covered hydrogen gas

diffusion anode. The cathode region used hard seawater as the catholyte and nickel foam as the cathode. By using the anode region to selectively remove chloride anions from the hard water, and the cathode region to form hydroxide anions, CO_2 is sequestered whilst $Mg(OH)_2$ is formed simultaneously. Magnesium hydroxide would then react with CO_2 to form magnesium bicarbonate. The hard water is then recycled so that the remaining calcium cations react with CO_2 to form calcium carbonate (Figure 39).

Step 1: Magnesium hydroxide formation
Step 2: CO_2 mineralisation as magnesium bicarbonate
Step 3: CO_2 mineralisation as calcium carbonate
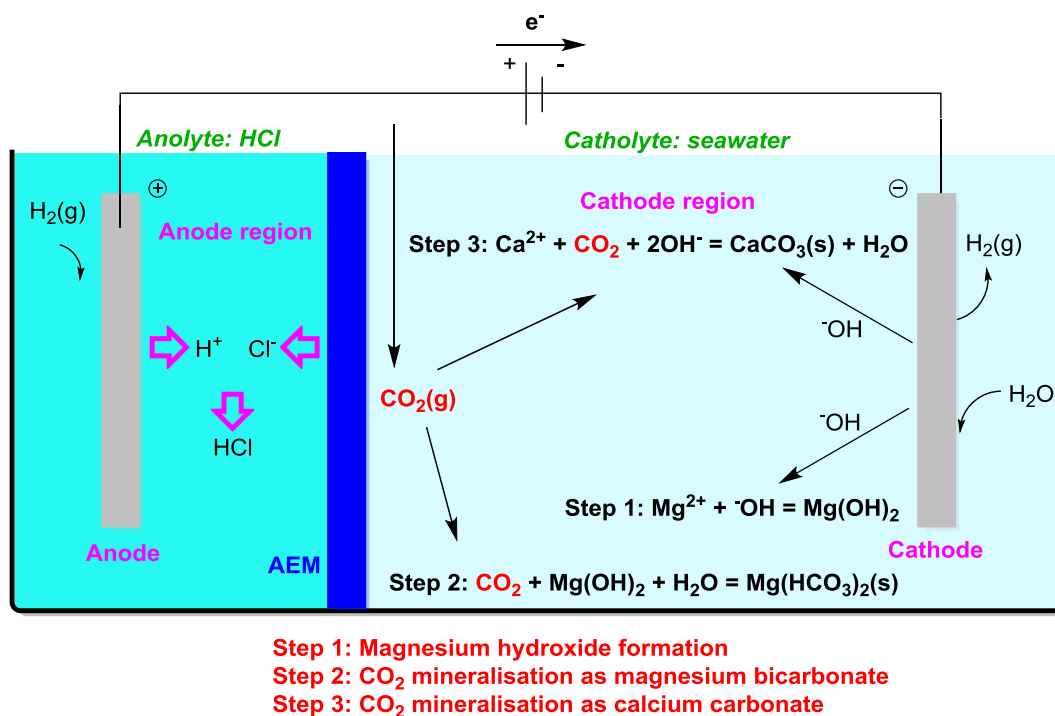
Figure 39: He's electrochemical cell used to capture and store CO_2 in the form of magnesium bicarbonate and calcium carbonate in simulated hard seawater.[229]

This process however is far from ideal. The methodology requires a pure stream of CO_2 and has not yet been tested with dilute levels of CO_2.[229] The energy required to perform this process on a large scale (using 1000 m^3 of simulate hard seawater) was predicted to be 5676 kWh, which is equivalent to 20.43 x 10^9 J and therefore 193 kJ mol^{-1} of CO_2 (due to capturing 4.66 tonnes of CO_2 via mineralisation). This cost to capture CO_2 is therefore not extensive, but is nonetheless a hypothesised cost. The use of an AEM would increase the operational costs dramatically, therefore it is likely that this process is currently too expensive to implement on an industrial scale, despite the predicted cheap cost. Nevertheless this method illustrated that a simple electrochemical setup can perform CO_2

capture and mineralisation simultaneously at near ambient conditions and use seawater as the electrolyte.

3.1.9 Summary and Project Aims

Carbon capture and storage is capable of capturing substantial levels of gaseous CO_2 on a global scale, but is often hindered by poor public perception, substantial energy requirements, which create expensive operating and capital costs, and poor sustainability. A realistic scenario for a global reduction in CO_2 emissions however dictates that CCS must be implemented worldwide. The development of economically viable and sustainable CCS methodology is therefore extremely important. Creating innovative methodology which could not only remove dilute levels of CO_2 but also permanently trap it in a secure manner is highly desired.

Electrochemistry can be used as a sustainable and environmentally friendly alternative for CO_2 capture as well as CO_2 mineralisation. Electrochemically driven CO_2 capture however often requires complicated setups, expensive equipment (such as membranes), harsh conditions and is not currently economically viable. Many of these methods are therefore too expensive to implement industrially and are still no match to the state-of-the-art methodology; amine scrubbing. Electrochemically driven CO_2 mineralisation offers an intriguing prospect for promoting permanent CO_2 storage using sustainable energy, but is still in the early stages of research. Current methods also have issues such as substantial energy requirements, expensive equipment and often require pure CO_2. Nonetheless, Gilliam and Landskron *et al.* have illustrated that CO_2 capture is possible with simple electrochemical designs and that electrochemistry can promote CO_2 mineralisation respectively.[212,224] The creation of an electrochemically driven CCS technique which is simple, sustainable and economically viable, with the capability of long-term CO_2 storage, is yet to be achieved. We became interested with this challenge, and therefore decided to investigate this area of research further. Could a more sustainable and cheaper alternative

electrochemical method for capturing dilute levels of CO_2 be developed, with the potential to also permanently trap CO_2?

The aims of this project were therefore to investigate and develop a novel and simplistic electrochemical method capable of CO_2 capture without the use of expensive membranes, using aqueous NaCl as the electrolyte, and a similar concept of supercapacitive charging of carbon based electrodes as presented by Landskron. If the capture of CO_2 is successful, a study into the electrochemical process required for CO_2 capture will be performed, to develop a detailed understanding of the process. Further developing this methodology to permanently trap or store CO_2 was also of interest. The energy requirements and thus costs associated with this carbon capture will be evaluated, to determine if this methodology could provide a cheaper alternative for CCS compared to current state-of-the-art methods (Section 3.2, Part 1: Performing Electrochemical CO_2 Sequestration and Mineralisation). In the interest of sustainability, the ability to use renewable energy sources and resources, such as solar power and seawater, to perform sustainable and economic CO_2 capture will also be investigated (Section 3.4, Part 2: Promoting Cost-effective and Sustainable Electrochemical CO_2 Capture and Mineralisation).

3.2 Results and Discussion Part 1: Performing Electrochemical CO_2 Sequestration and Mineralisation

3.2.1 Preliminary Results Obtained Prior to this Project

Prior to the start of this project, initial studies had been performed by an undergraduate summer project student, Abigail Burstein, to investigate the ability of a newly constructed graphite-aluminium mixed anode, and platinum cathode electrochemical cell containing 1 M aqueous NaCl electrolyte (Figure 40-Figure 42, described further in experimental) to perform CO_2 capture upon application of an electrical current (Figure 43). Unless otherwise stated, all experiments shown in this chapter were conducted with solution
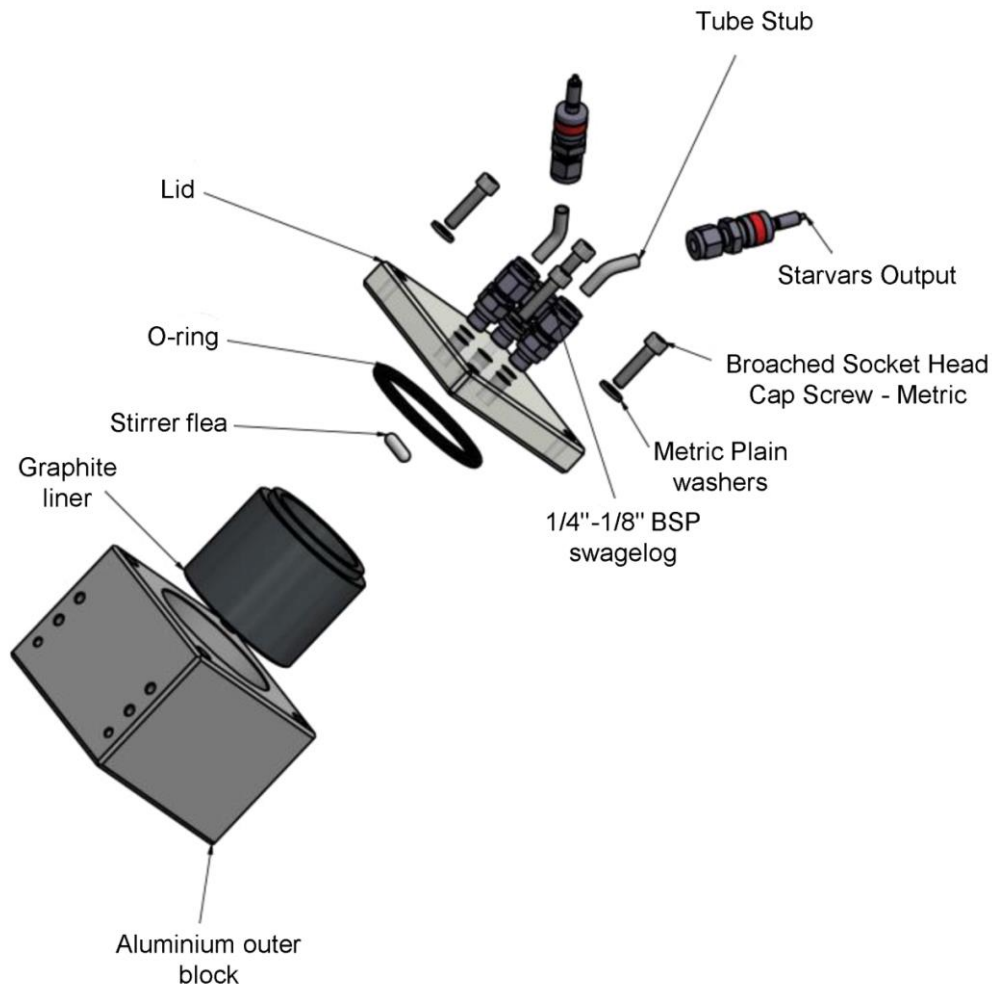
Figure 40: The graphite-aluminium anode cell and its components.
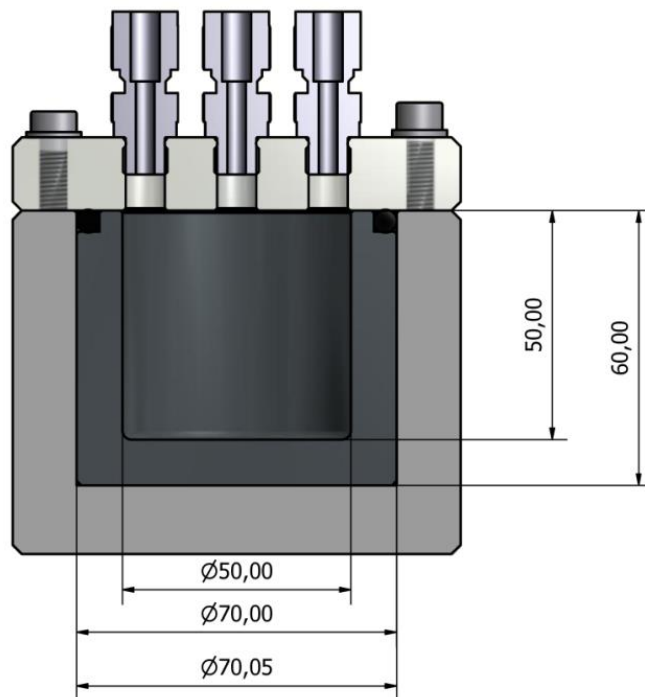
Figure 41: Inside view and dimensions of graphite-aluminium anode cell, with diameter lengths

(Ø) in mm.
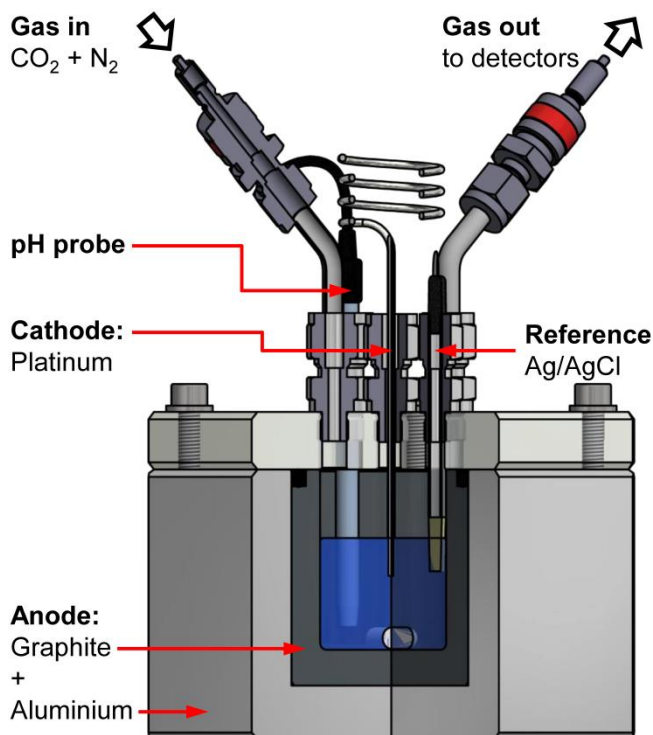
Figure 42: Schematic of the graphite-aluminium anode cell and cell components used in a standard experiment, with a cross-section view of the inside of the cell.

agitation from a magnetic stirrer bar (10 x 4 mm) at an average temperature of 34 °C (see experimental for further details). The main findings from this work were that CO_2 levels decreased with the application of a current, but only exit gas CO_2 levels and the anode electrode potentials were measured. No investigations into the levels of carbon (or CO_2) captured, or the intrinsic electrochemical mechanisms were undertaken. One intriguing observation was that the potential of the graphite-aluminium anode (the working electrode) during positive current steps dropped dramatically, observed due to the development of cracks inside the graphite "liner" portion of the electrochemical cell (compare Figure 43c and Figure 43f). Solid precipitation also occurred.

My work on this project therefore commenced with the hypothesis that the cracks enabled the electrolyte to interact with the aluminium casing, which then potentially acted as a sacrificial anode.[230] This thereby changed the anodic process, creating a lower potential and could account for solid precipitation. The use of a sacrificial aluminium anode for carbon capture was reported in 2016 by Al Sadat *et al.*,[231] but to the best of our knowledge
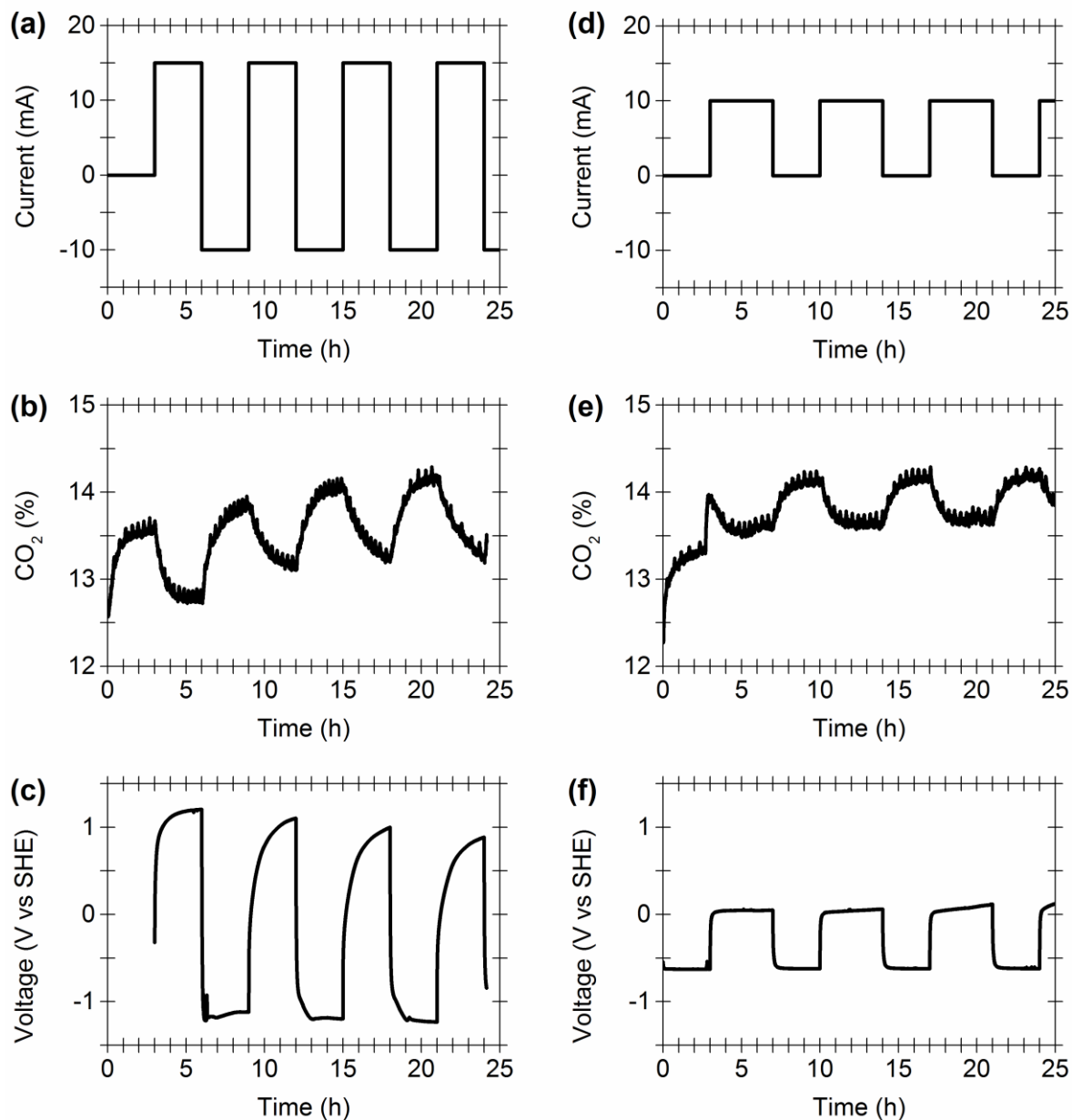
Figure 43: Preliminary experiments performed in the graphite-aluminium anode cell as the graphite liner went from "uncracked" (a-c) to "cracked" (d-f). (a) and (d) Programmed current-time steps; (b) and (e) Carbon dioxide content in the exit gas stream; (c) and (f) Resultant changes to the electrochemical potential of the graphite-aluminium mixed anode. Other reaction conditions: a continuous gas flow of 2.0 mL min^{-1} CO_2 (14.3%) and 12.0 mL min^{-1} air, and 60 mL of 1 M NaCl.

a dual graphite-aluminium anode has never been tested in CO_2 capture. The first aim of this project was to further explore this hypothesis, by investigating the ability of a graphite-only anode cell and aluminium-only anode cell to perform CO_2 capture (see experimental

for full details on electrochemical cell designs). It was anticipated that the separate studies for individual anode cells would enable a deeper understanding of the overall electrochemical process occurring in the graphite-aluminium mixed anode cell.

3.2.2 Probing the Electrochemical Process: Changing Components of the Mixed Anode Cell

Standard Reaction Conditions

In a typical experiment, a gas of 5% CO_2, in a CO_2/N_2 gas mixture, was flowed continuously through the cell containing a constantly stirred 1 M NaCl electrolyte. The first 7 h were an "equilibration period" to purge the cell with the CO_2/N_2 gas mixture, ensure gaseous CO_2 levels stabilised at 5% and saturate the electrolyte with CO_2. No electrochemical current was applied during this time. The voltages reported during this period therefore reflect "open circuit" values. All electrode voltages were measured as V vs Ag/AgCl and then converted to, and reported as, <u>V vs SHE</u> (see experimental).[232] Calculated electrode voltages are reported as <u>V vs SHE</u>. After 7 h, a 10 mA current was applied. In order to sustain this current, the anode potential increased and the cathode potential decreased. The current was applied for 24 h, and then turned off (31 h into the experiment), followed by another 7 h "equilibration period". These programmed current steps were used in order to compare the ability of each cell to capture CO_2 over 24 h. Carbon dioxide levels in the exit gas stream were monitored throughout to investigate whether CO_2 capture was electrochemically driven. The potential of the anode (graphite, aluminium or graphite-aluminium) and platinum cathode were monitored relative to a reference electrode, to give the cell potential, E_{Cell}. The pH of the solution was measured to aid mechanistic interpretations. The quantification of millimolar levels of carbon (equivalent to molar levels of CO_2) captured in the electrolyte and solid are discussed later.

Carbon Dioxide Capture with a Graphite-only Anode Cell

Carbon dioxide sequestration was possible with a graphite-only anode cell but CO_2 absorption is low, with the amount of CO_2 in the exit gas stream returning to input levels approx. 5 h into the 24 h 10 mA current-time step (Figure 44).
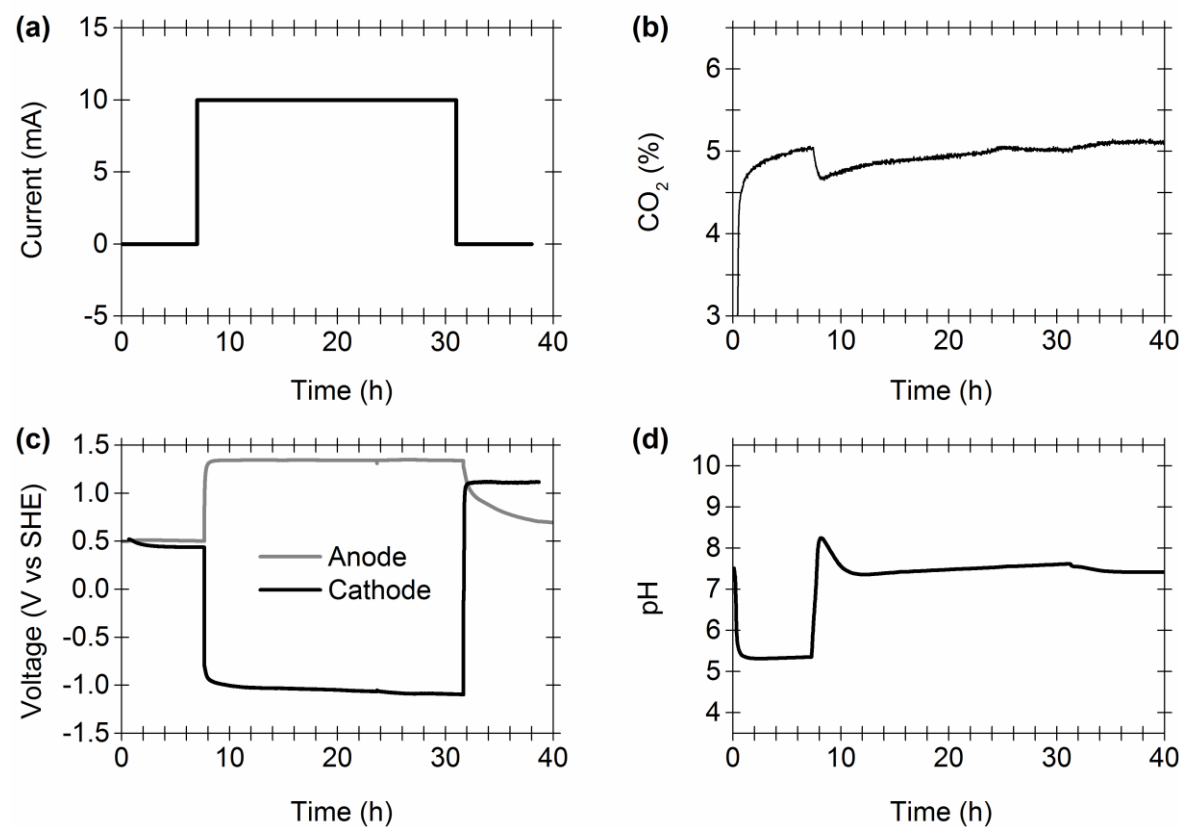
Figure 44: Carbon dioxide capture with 1 M NaCl in the graphite-only anode cell. (a) Programmed current-time steps; (b) Carbon dioxide content in the exit gas stream; (c) Resultant changes to the electrochemical potential of the anode (grey line) and cathode (black line); (d) Corresponding changes in solution pH. Other reaction conditions: a continuous gas flow of 0.7 mL min^{-1} CO_2 (5%) and 13.3 mL min^{-1} N_2, and 60 mL of 1 M NaCl.

Compared to the "cracked" graphite-aluminium anode cell, the graphite-only cell reached a notably higher potential (+1.34 V, Figure 44c, compared to +0.05 V, Figure 43f).[233] This supports the hypothesis that the drop in anodic potential reported in the "cracked" graphite-aluminium anode cell was indeed a consequence of the electrolyte interacting with the aluminium casing.

Upon application of the 10 mA current, for the first hour the pH level of the electrolyte rises from approx. pH 5 to pH 8 (Figure 44d). In order to explain this steep increase in pH, it is deduced that the cathode reaction is consuming protons ($2H^+ + 2e^- \rightarrow H_{2(g)}$) while the much slower, proton-neutral process of Electrical Double Layer (EDL) formation occurs at the large surface area graphite anode. This hypothesis is supported by the potential of the platinum cathode, which is approx. -1.1 V during the 10 mA current step (Figure 44c). Hydrogen formation would therefore be thermodynamically favourable since the redox potential for the $2H^+/H_2$ couple is approx. -0.49 V under the experimental conditions (calculated using the Nernst Equation, pH 8, and assuming a H_2 partial pressure of 1 bar at the cathode).[189,234-236]

Following the rise in solution pH, the pH decreases to approx. 7.4 in the following 4 h. This pH drop is attributed to the absorption of gaseous CO_2 into the alkaline solution, with the formation of bicarbonate acting to lower the pH via the well-known process $CO_{2(g)} + OH^-_{(aq)} \rightarrow HCO_3^-{}_{(aq)}$. Carbon dioxide absorption levels off simultaneously as the pH also reaches a steady value. The eventual equilibration in solution pH during the 10 mA step indicates that eventually both electrode processes involve the same proton to electron ratios. This supports the notion that following electrocapacitive charging (EDL formation) at the anode, the electrode starts to catalyse water oxidation, with an expected high overpotential of 0.59 V (anode potential equilibrates to +1.35 V while $E(O_2/H_2O)$ is estimated as +0.76 V under experimental conditions using the Nernst equation and assuming a O_2 partial pressure of 1 bar at the anode).[189,234-236]

Carbon Quantification in the Electrolyte

Post-CO_2 capture, bulk analysis of the electrolyte was performed to identify and quantify the amount of carbon (and therefore CO_2) captured. By employing Vogel's titration method,[237] bicarbonate was identified as the solvated carbon species (at 1.4 mmol) and carbonate levels were negligible (see experimental for more details). All molar values

reported for carbon detected in solution post-CO_2 capture correspond to the <u>total</u> amount of carbon captured in the <u>total</u> volume of electrolyte. This was to be expected, considering the final solution pH was approx. 7 (Figure 44d, Scheme 33)[186,238,239] and the phase diagram for carbonate speciation (Figure 45),[240,241] as carbonate species are only expected to be formed at extremely alkaline pH levels (>10). No solid was formed in this cell during this experiment.

$$CO_2 + H_2O \rightleftharpoons H_2CO_3 \text{ (carbonic acid)} \qquad pH < 6.5$$

$$H_2CO_3 \rightleftharpoons HCO_3^- + H^+ \text{ (bicarbonate anions)} \qquad 6.5 < pH < 10.5$$

$$HCO_3^- \rightleftharpoons CO_3^{2-} + H^+ \text{ (carbonate anions)} \qquad pH > 10.5$$
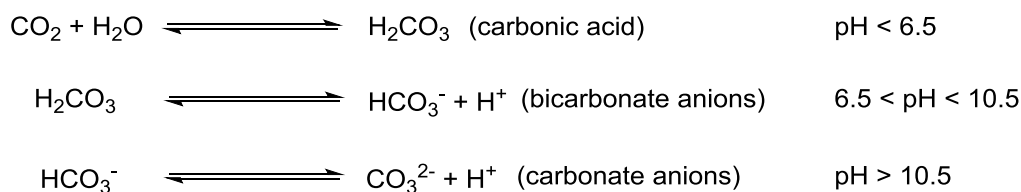
Scheme 33: Carbon dioxide speciation in aqueous solution at different pH levels.[186,238,239]
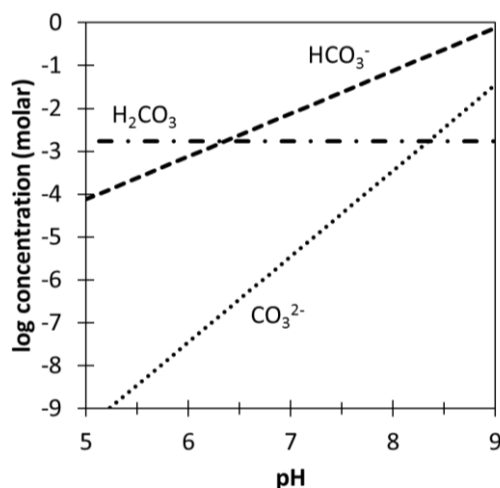
Figure 45: Phase diagram depicting carbonate speciation as a function of pH for an aqueous solution in equilibrium with an atmosphere of 5% CO_2.[240,241]

Carbon Dioxide Capture with an Aluminium-only Anode Cell

When an aluminium only was used as the anode, CO_2 capture was effectively non-existent (Figure 46). As in the graphite-only anode cell, the platinum cathode potential in the aluminium-only anode experiment was again approx. -1.1 V, indicating the cathodic process was the same in both cells. In contrast, the anode potential (-0.54 V) was much lower (Figure 46c) and correspondingly the pH profile of the experiment was also different, since during the 10 mA current step the pH gradually increased from 5.5 to 7.3 (Figure 46d). The electrode potentials were similar in the absence and presence of CO_2,
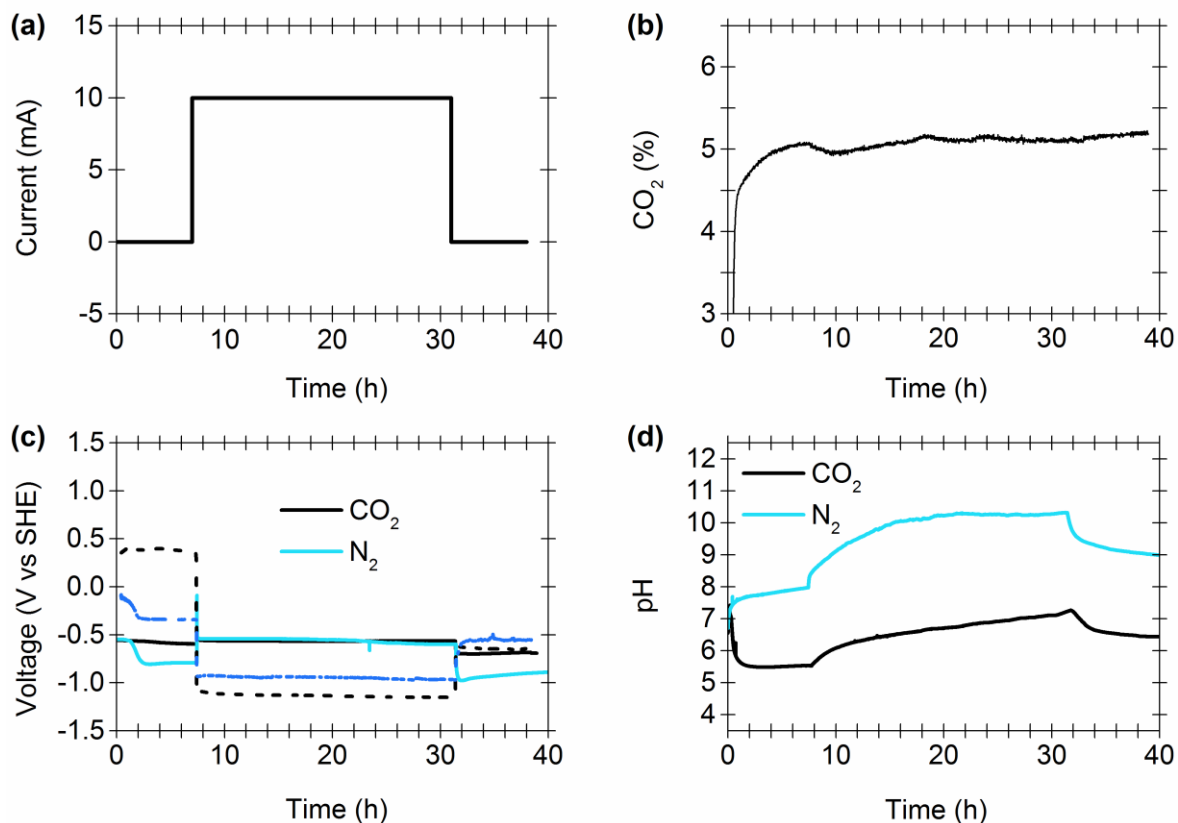
Figure 46: Carbon dioxide capture with 1 M NaCl in the aluminium-only anode cell. (a) Programmed current-time steps; (b) Carbon dioxide content in the exit gas stream; (c) Resultant changes to the electrochemical potential of the anode (black line, CO_2; light blue, N_2) and cathode (black line, CO_2; dark blue, N_2); (d) Corresponding changes in solution pH (black line, CO_2; light blue, N_2). Other reaction conditions: a continuous gas flow of 0.7 mL min^{-1} CO_2 (5%) and 13.3 mL min^{-1} N_2, or 14.0 mL min^{-1} N_2, and 180 mL of 1 M NaCl.

indicating that the same anodic and cathodic processes were occurring. The solution pH was higher in the presence of N_2 only and in the absence of CO_2 (approx. pH 9-10 vs pH 6-7 respectively, Figure 46d), which illustrated that the CO_2/N_2 mixture acts as a pH buffer.

Precipitation of a white solid occurred during this experiment (0.54 g). Consideration of the Pourbaix diagram of aluminium (Figure 47), the anode voltage and solution pH suggest that $Al(H_2O)_3(OH)_{3(s)}$ or $Al(OH)_3.3H_2O_{(s)}$, (simplified to $Al(OH)_{3(s)}$), is being formed.[230,242] The proposed anode process is therefore aluminium oxidation, $Al_{(s)} + 6H_2O_{(l)} \rightarrow Al(H_2O)_3(OH)_{3(s)} + 3e^- + 3H^+$, which can also be expressed as $Al_{(s)} + 3H_2O_{(l)} \rightarrow Al(OH)_{3(s)} + 3e^- + 3H^+$.[230,243] The potential for the $Al/Al(OH)_3$ couple is approx. -2.02 V under the

experimental conditions (at pH 8). The hypothesis that $Al(OH)_3(s)$ is formed in the aluminium-only anode cell is further supported by the fact that in a control experiment, in which a 10 mA current was applied for 24 h across the aluminium-only anode cell under an N_2 only atmosphere, rather than a CO_2/N_2 mixture, a solid still formed (0.27 g), with solid analysis suggesting the formation of $Al(OH)_{3(s)}$ only (see 4.2 Appendix 2, Section 4.2.1, Figure A1-Figure A4, for electrochemical data for this run only and solid analysis).
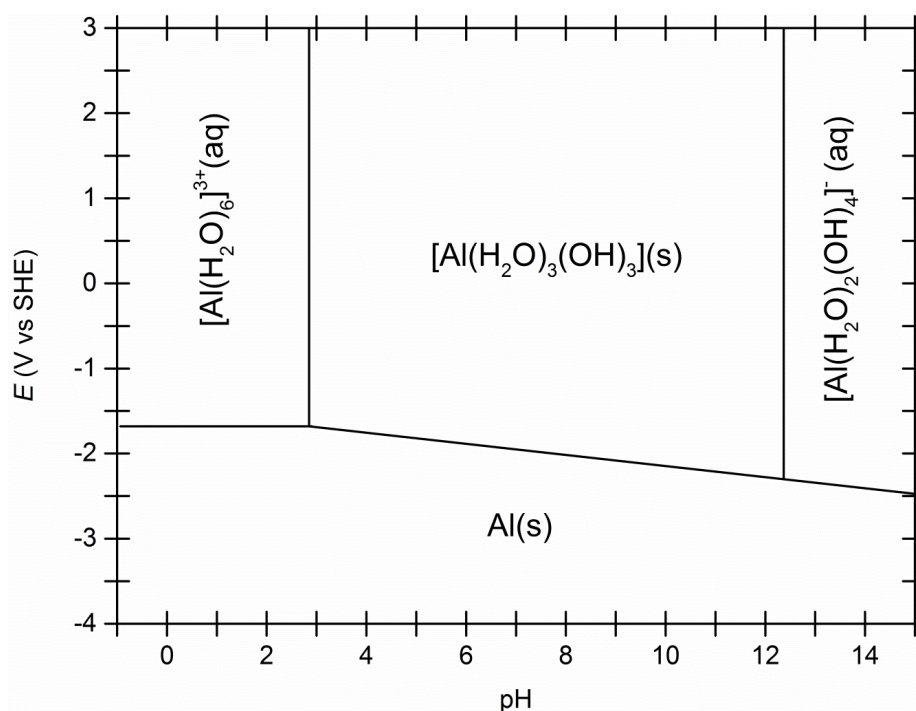
Figure 47: Pourbaix plot for aluminium at different voltages and pH levels. The small regions of $Al(H_2O)_5(OH)^{2+}_{(aq)}$ and $Al(H_2O)_4(OH)_2^{+}_{(aq)}$ have been omitted for simplicity.[230,242,243]

Carbon Quantification in the Electrolyte and Solid

As expected from the high CO_2 content of the exit gas from the aluminium-only anode electrochemical cell, analysis of the electrolyte isolated post-CO_2 capture detected negligible levels of bicarbonate, indicating that no CO_2 was sequestered in solution.[186,238-240] By employing a TGA-IR quantification method, the amount of carbon (and therefore CO_2) trapped in the solid could be quantified (see experimental for details). The level of carbon trapped in the solid is also extremely low (0.3 mmol) as could be expected. All molar values reported for carbon detected in the solid isolated post-CO_2 capture correspond to the <u>total</u> amount of carbon captured in the <u>total</u> mass of solid

collected. In the case of when N_2 only was flowed through the cell, carbon levels were even lower (0.018 mmol). This further supported the hypothesis that $Al(OH)_{3(s)}$ was formed in the aluminium-only anode cell as a result of current application, which would consequently absorb CO_2 if it was present.

3.2.3 Carbon Dioxide Capture with a Graphite-Aluminium Mixed Anode Cell

Having proven that the graphite- and aluminium-only anode cells do not permit low power CO_2 sequestration and mineralisation, the next aim of the project was to study a purposefully designed graphite-aluminium mixed-material anode for CO_2 capture.

Optimising Anode Construction

The effect on CO_2 capture and anodic potentials of drilling different sized holes into the graphite liner was investigated (Figure 48). These experiments were conducted by applying a 10 mA current for "on" period of 3 h and then turning "off" for a period of 3 h, over the course of 18 h (Figure 48a). Initially, eight holes with a width of 1 mm, depth of 13.18 mm and total surface area of 6.3 mm^2 were drilled into the graphite liner (Figure 48a-d). Carbon dioxide sequestration occurred during the programmed current-time steps (Figure 48b) with a simultaneous rise in pH levels (Figure 48c) but no solid formation occurred. High average anode voltages (1.04 V) were also reached during the CO_2 capture step (Figure 48a-e), which with an average cathode voltage at -1.17 V leads to an E_{Cell} value of 2.21 V, equivalent to a high energy input (716 J) over the total 9 h "on" period of the 10 mA current.

To increase the contact between the electrolyte and aluminium, the same eight holes were extended to a width of 3.2 mm, with the same depth, yielding a total surface area of 64 mm^2. This new electrochemical cell was then subjected to the same reaction conditions (Figure 48e-h). The pH level again became basic, with simultaneous CO_2 sequestration,
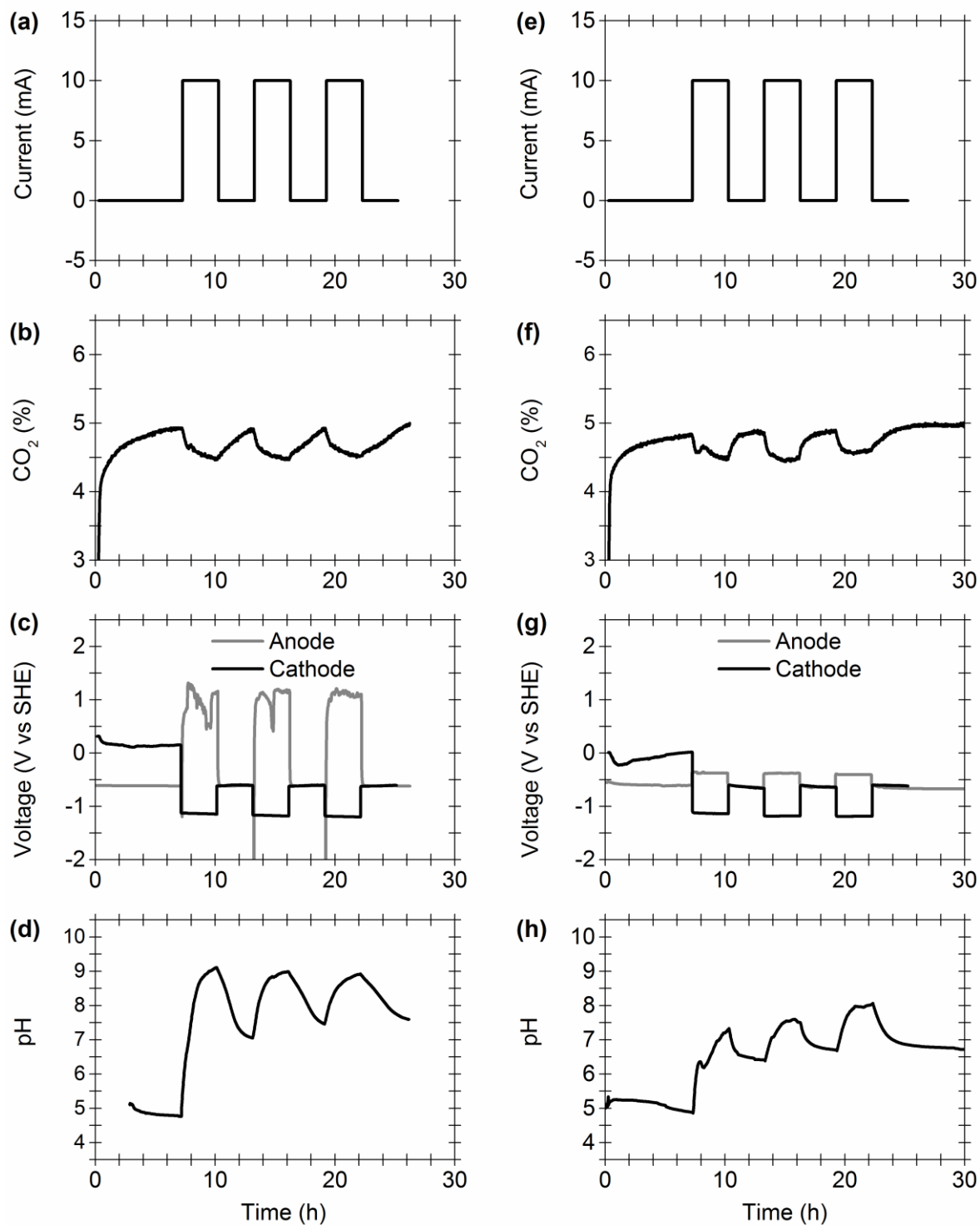
Figure 48: Comparing electrode potentials vs hole size in the graphite-aluminium anode cell. (a-d) Data collected with 8 x 1 mm holes in the graphite; (e-h) Data collected with 8 x 3.2 mm holes in the graphite. (a) and (e) Programmed current-time steps; (b) and (f) Carbon dioxide content in the exit gas stream; (c) and (g) Resultant changes to the electrochemical potential of the anode (grey line) and cathode (black line); (d) and (h) Corresponding changes in solution pH. Other reaction conditions: a continuous gas flow of 0.7 mL min^{-1} CO_2 (5%) and 13.3 mL min^{-1} N_2, and 60 mL of 1 M NaCl.

and a similar average cathodic voltage (-1.16 V), but a much lower anodic voltage (-0.53 V) was observed (Figure 48g). This corresponds to a decreased E_{Cell} value of 0.63 V, during the 9 h "on" period of the 10 mA current, meaning that relative to the cell with the smaller holes; only 28% of the energy (204 J) was required. A solid precipitate only formed in the cell with the larger holes. These tests proved that a mixed anode component could be used to promote CO_2 sequestration with simultaneous solid precipitation and low energy requirements, when the interaction between the electrolyte and aluminium was controlled. The graphite-aluminium anode cell with the 3.2 mm holes was therefore used in all further studies, and this setup is henceforth described as the "graphite-aluminium anode cell".

Carbon Dioxide Levels, Anode and Cathode Voltages and pH Levels

After constructing the graphite-aluminium anode cell with the desired sized holes in the graphite liner, its ability to capture CO_2 was further investigated using the same 24 h style experiments performed with the graphite- and aluminium-only anode cells (Figure 49).

Throughout the 10 mA current application time, the percentage of CO_2 in the exit gas stream was on average 0.34% lower than the level of CO_2 in the inlet gas (5%), indicating constant CO_2 uptake (Figure 49b). The anode and cathode reach potentials of -0.32 V and -1.13 V respectively, during the current application and CO_2 sequestration period (Figure 49c). The electrode potentials were similar in the presence of N_2 only and 5% CO_2, indicating the same anodic and cathodic processes were occurring and suggested that CO_2 was not taking part in any redox reactions. The gas outlet of the cell however was not analysed for products such as CO or formaldehyde, therefore this hypothesis is unconfirmed. The processes occurring at the electrodes are discussed further in "The Cathodic and Anodic Process".
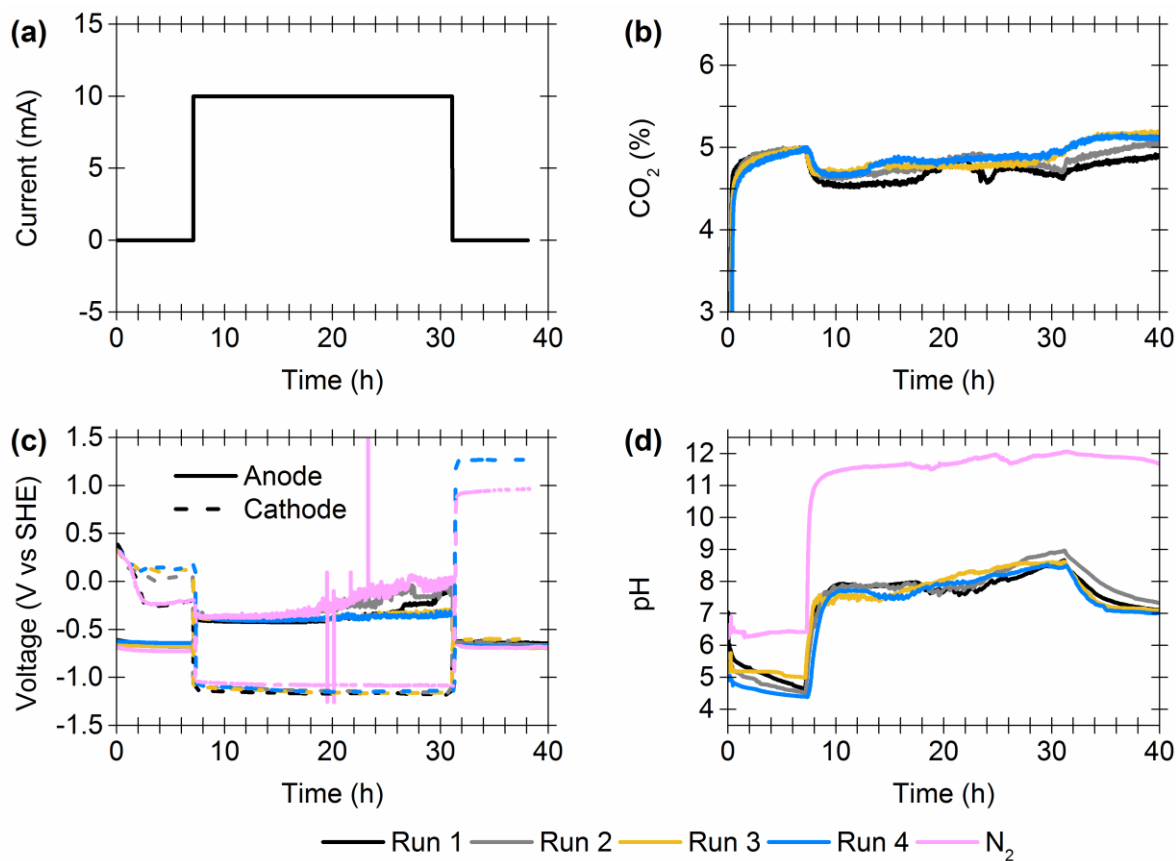
Figure 49: Overlay of repeat CO_2 capture experiments with 1 M NaCl in the graphite-aluminium anode cell. (a) Programmed current-time steps; (b) Carbon dioxide content in the exit gas stream; (c) Resultant changes to the electrochemical potential of the anode (solid line) and cathode (dashed line); (d) Corresponding changes in solution pH. Other reaction conditions: a continuous gas flow of 0.7 mL min^{-1} CO_2 (5%) and 13.3 mL min^{-1} N_2, or 14.0 mL min^{-1} N_2, and 60 mL of 1 M NaCl.

The pH of the 1 M NaCl electrolyte was approx. 6-7 before the CO_2 gas mixture was flowed through the cell. At the start of the experiment, during the 7 h gas equilibration step, the electrolyte becomes acidic with a pH of approx. 4.5-5.5 (Figure 49d) indicating carbonic acid formation (Scheme 33 and Figure 45).[186,238-240] Upon application of the 10 mA current, the pH level of the electrolyte rises to 8-9 in less than 3 h, and remains at this level during the remaining time at 10 mA. At this pH, CO_2 will dissolve as bicarbonate (Scheme 33 and Figure 45).[186,238-240] In the absence of CO_2 and presence of N_2 only (see 4.2 Appendix 2, Section 4.2.2, Figure A5 for electrochemical data), the solution pH was higher (approx. pH 11-12 vs pH 8-9 respectively), again illustrating that the CO_2/N_2 mixture acts as a pH buffer. Only a 0.14% change in CO_2 levels were detected in control

experiments where 5% CO_2 was flowed through the graphite-aluminium anode cell for over 40 h in the absence of current (Figure 50), confirming that all reported drops in CO_2 levels in the mixed anode cell are electrochemically driven.
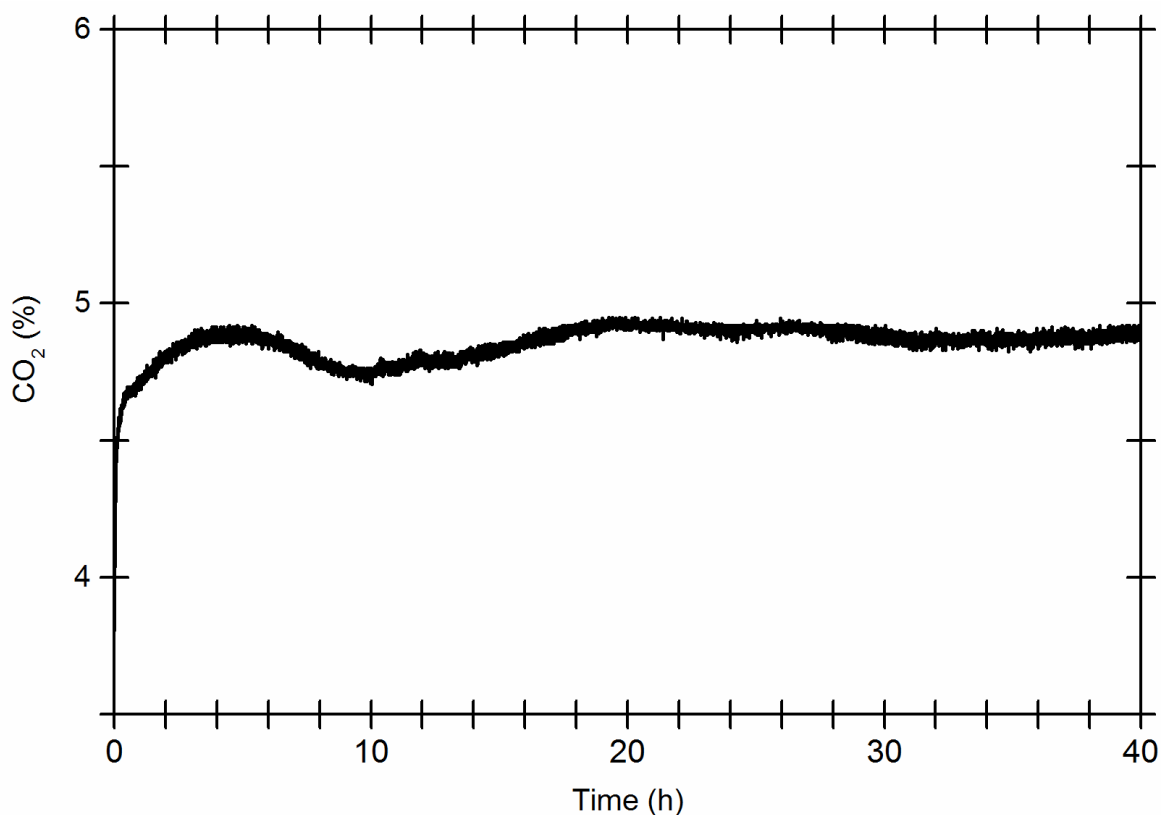
Figure 50: Monitoring CO_2 levels flowing through the graphite-aluminium anode cell in the absence of a 10 mA current flow from the anode to the cathode. Other reaction conditions: a continuous gas flow of 0.7 mL min^{-1} CO_2 (5%) and 13.3 mL min^{-1} N_2, and 60 mL of 1 M NaCl.

When the current flow was stopped after 24 h, the CO_2 level rose and stabilised at 5%, again demonstrating CO_2 fixation is electrochemically driven (Figure 49b). Simultaneously, the anode and cathode voltages return to "open circuit" values which are different to those at the start of the experiment, indicating changes to solution composition or the electrode surfaces. Concurrently, pH levels decreased from approx. 8-9 to 7.5. The analysis and quantification of the carbonate phase trapped in the electrolyte with this cell is discussed further in "3.2.10 Carbon Quantification and Analysis of Electrolyte". A solid was formed at the end of the reaction, and its analysis is discussed further in "3.2.4 Carbon Dioxide Mineralisation".

The Cathodic and Anodic Process

The Cathodic Process

During the 10 mA step, the potential of the platinum cathode (-1.13 V) would be sufficient to drive platinum-catalysed H_2 ($2H^+ + 2e^- \rightarrow H_{2(g)}$) production at a pH of 8 (-0.49 V as determined earlier).[189,234-236] In order to prove that this occurs, replicate experiments in the graphite-aluminium anode cell were performed with an in-line H_2-GC monitoring the gas outlet, and on average 0.142% H_2 was detected in the outlet gas (Figure 51). In order to calculate the faradaic efficiency for H_2 production, the moles of H_2 produced must be compared to the total numbers of electrons available during the electrochemical experiment. Using Faraday's constant (96485 C mol^{-1}), a current flow at 10 mA (0.01 A or 0.01 C s^{-1}) over 24 hours is equivalent to 8.95 mmol of electrons. Therefore the maximum amount of H_2 would be 4.48 mmol. By using the ideal gas law, $pV = nRT$, the average percentage of H_2 reported from the outlet cell (0.142%) in a gas flow of 14 mL min^{-1} over 24 h, can be converted into a molar value (1.14 mmol), assuming a pressure of 1 atm at 34 C (307 K) and using a gas constant value of 0.082 L atm K^{-1} mol^{-1}. The moles of H_2 detected compared to the total moles which could be produced electrochemically is therefore equivalent to a Faradaic efficiency of 25%.[189] This Faradaic efficiency was lower than that reported for cobalt-, tungsten-, platinum- or microbe-catalysed H_2 formation.[244-246] As the cell is not optimised for H_2 formation, for example no gas membranes were placed around the platinum cathode, these low efficiencies are unsurprising.

When aluminium metal is exposed to an alkaline solution, hydroxide anions can remove the stable aluminium oxide (Al_2O_3) layer from the aluminium surface, thus exposing aluminium to water and enabling spontaneous hydrogen formation to occur: $2Al_{(s)} + 6H_2O_{(l)} \rightarrow 2Al(OH)_{3(s)} + 3H_{2(g)}$, or $2Al_{(s)} + 3H_2O_{(l)} \rightarrow Al_2O_{3(s)} + 3H_{2(g)}$.[247,248] To ensure the
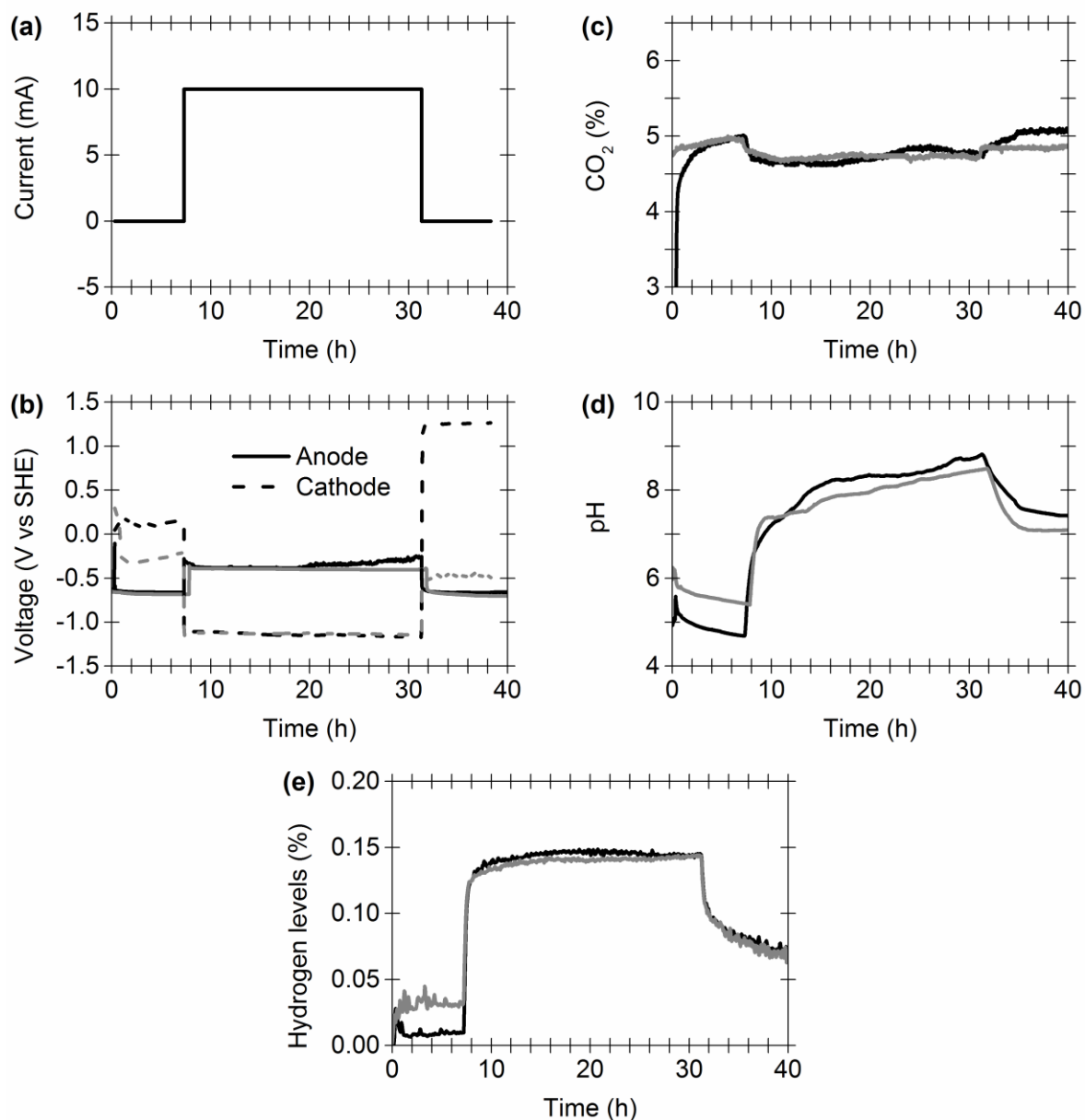
Figure 51: Overlay of repeat experiments with hydrogen detection. (a) Programmed current-time steps; (b) Carbon dioxide content in the exit gas stream; (c) Resultant changes to the electrochemical potential of the anode (solid line) and cathode (dashed line); (d) Corresponding changes in solution pH; (e) Hydrogen levels. Other reaction conditions: a continuous gas flow of 0.7 mL min^{-1} CO_2 (5%) and 13.3 mL min^{-1} N_2, and 60 mL of 1 M NaCl.

reported H_2 levels in the graphite-aluminium cell were due to the platinum cathodic process only, identical experiments were performed in a graphite-only anode cell. Hydrogen levels were similar in both cells, with 0.12% of H_2 reported in the graphite-only anode cell (Figure 52), confirming that H_2 formation is primarily due to the platinum cathodic process.
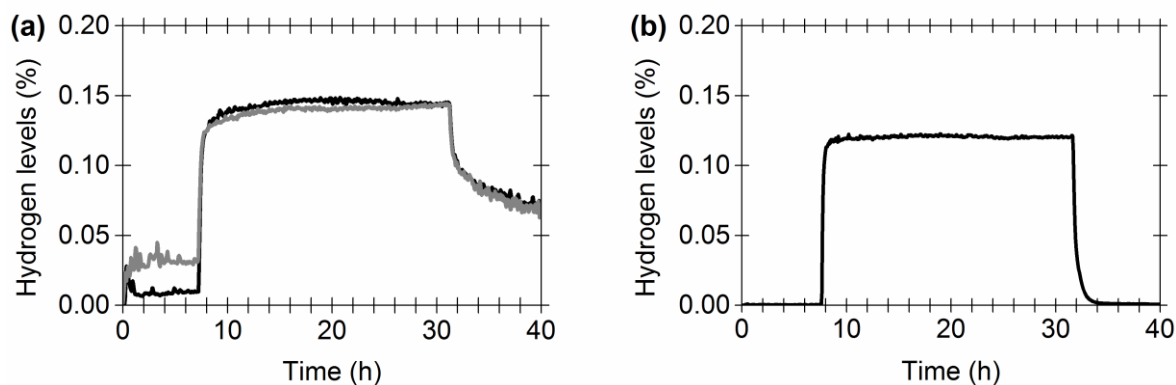
Figure 52: Hydrogen levels reported using (a) the graphite-aluminium anode cell and (b) graphite-only anode cell.

The Anodic Process

Experiments were conducted in which the anodic (and cathodic) potentials were monitored on a second timescale instead of every minute, in order to analyse the charging capabilities of different anodes (Figure 53). The equilibrium voltage for the aluminium-only anode was achieved in a couple of seconds, as expected for an electrode with a low charging capacity. In contrast, the graphite-only anode required approx. 200 s to reach a constant potential, illustrating its potential capacitive charging properties. The mixed anode showed a carbon charging process, which occurred over approx. 5 s. This suggests that combining the graphite and aluminium anode enables low power CO_2 capture because a mixture of EDL formation and aluminium oxidation ($Al_{(s)} + 3H_2O_{(l)} \rightarrow Al(OH)_{3(s)} + 3e^- + 3H^+$) occurs at the mixed-material anode, offset by H_2 formation at the cathode.[230,235]

During the 10 mA step, the potential of the anode (-0.32 V) in the graphite-aluminium cell would be sufficient to drive aluminium oxidation ($Al_{(s)} + 3H_2O_{(l)} \rightarrow Al(OH)_{3(s)} + 3e^- + 3H^+$) at a pH of 8 (-2.02 V as determined earlier). Aluminium oxidation is further supported by analysis of the precipitate formed in the electrochemical CO_2-capture experiments (as discussed further in "3.2.5 Analysis of Electrochemical Formed Solids").

In terms of the faradaic efficiency for aluminium oxidation, the maximum amount of aluminium that the solid contain would be 2.98 mmol of Al (during the 24 h experiments in the graphite-aluminium anode cell). Considering the solid formed in the cell contains on
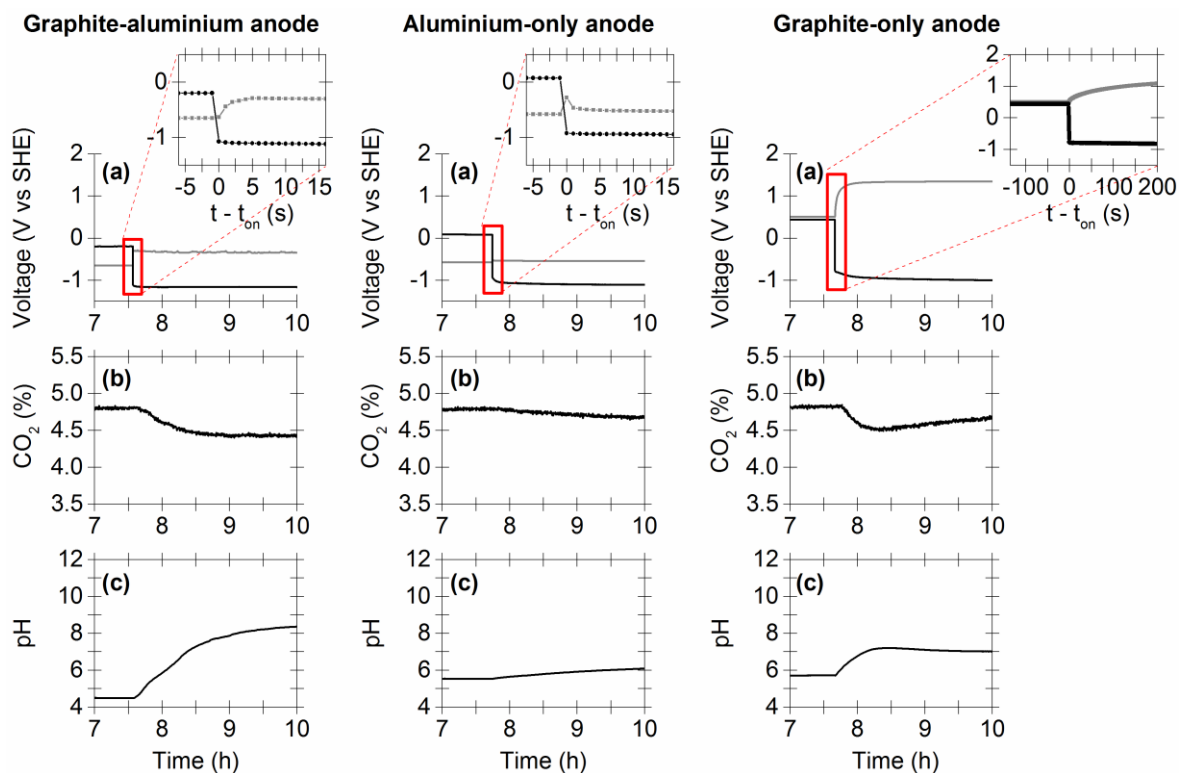
Figure 53: Comparing changes in reaction variables with different anodes in the electrochemical cell following current application. (a) Anode (grey line) and cathode (black line) voltages before and after a 10 mA current was applied. Inset shows zoomed in region around the time (t) when the current is applied (the exact time the current is applied is t_{on} set as zero); (b) Carbon dioxide content in the exit gas stream; (c) Changes in solution pH. Other reaction conditions: a continuous gas flow of 0.7 mL min^{-1} CO$_2$ (5%) and 13.3 mL min^{-1} N$_2$, and 1 M NaCl.

average 3.9 ± 0.4 mmol of aluminium, the Faradaic efficiency of aluminium oxidation is over 100% (approx. 131%). This high percentage may be due to corrosion of the aluminium oxide layer, facilitated by pitting attack from chloride anions in the 1 M NaCl aqueous solution,[249,250] thus creating a greater concentration of Al^{3+} cations available for the electrochemical process. The faradaic efficiencies for H$_2$ (25%) and aluminium oxidation (>100%) do not match. This may be due to potentially some of the H$_2$ forming in the cell not reaching the outlet port of the cell (the detection of other gas based products being released from the cell was not performed), and the corrosion of the aluminium oxide layer as discussed previously.

Temperature Monitoring

To ensure changes in CO_2 levels were only electrochemically driven, temperature monitoring of the same four experiments in Figure 49 was performed (Figure 54).
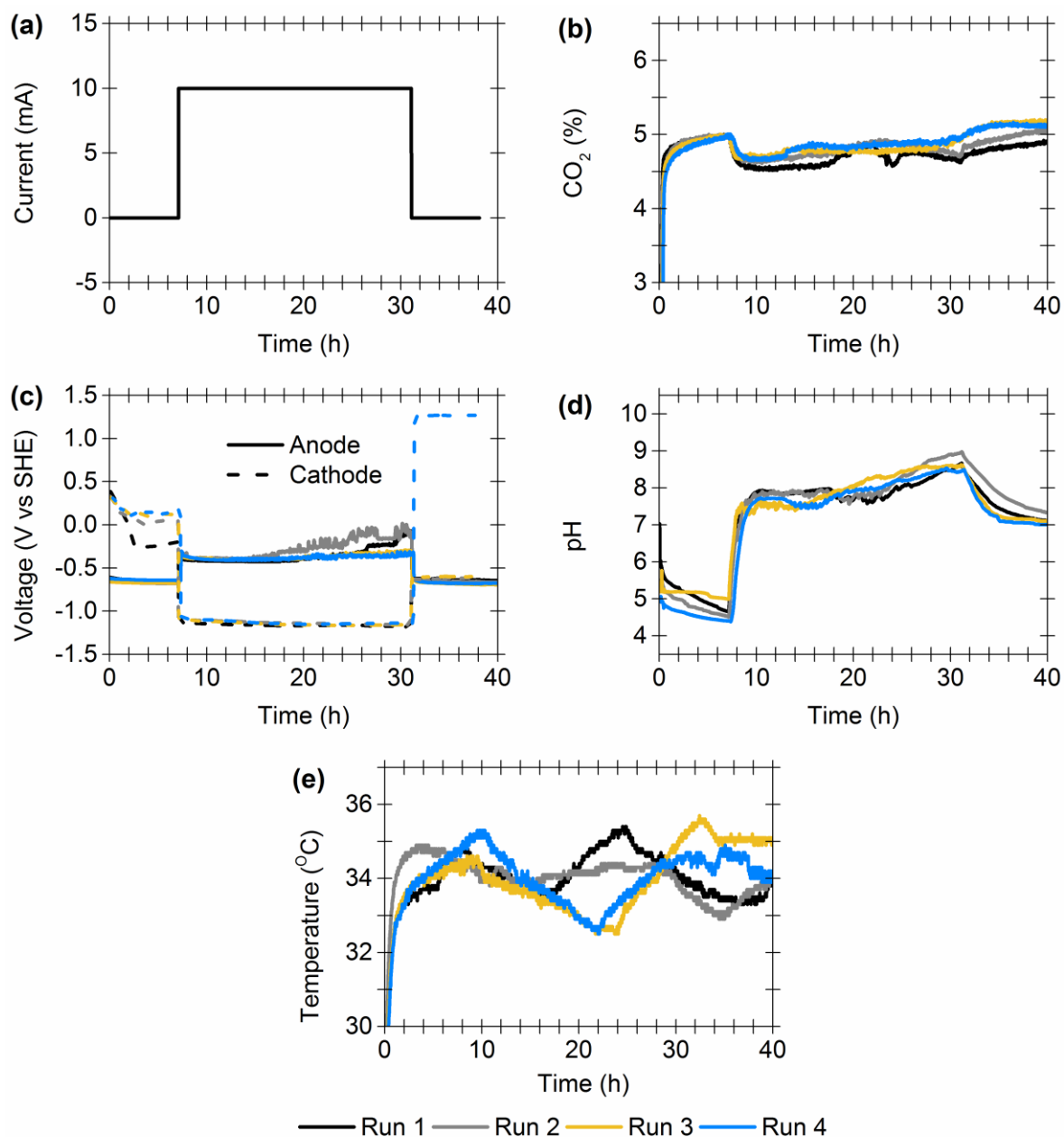
Figure 54: Monitoring temperature effects on CO_2 capture in the graphite-aluminium anode cell. (a) Programmed current-time steps; (b) Carbon dioxide content in the exit gas stream; (c) Resultant changes to the electrochemical potential of the anode (solid line) and cathode (dashed line); (d) Corresponding changes in solution pH; (e) Temperature of the magnetic stirrer hotplate and graphite-aluminium anode cell. Other reaction conditions: a continuous gas flow of 0.7 mL min^{-1} CO_2 (5%) and 13.3 mL min^{-1} N_2, and 60 mL of 1 M NaCl.

During standard experiments, the temperature of the magnetic stirrer hotplate, and consequently the cell, measured between 32-35 °C with an average temperature of 34 °C (Figure 54e). Changes in temperature and CO_2 levels over the 40 h experiment were unrelated, therefore slight temperature fluctuations (within 4 °C) do not cause or influence CO_2 capture. The effect of increasing temperature is explored more significantly in "3.4 Part 2: Promoting Cost-effective and Sustainable Electrochemical CO_2 Capture and Mineralisation, Changing Temperature".

3.2.4 Carbon Dioxide Mineralisation

The nature of the insoluble precipitate, or electrochemically formed solid, obtained post-CO_2 capture using the graphite-aluminium anode cell was initially unknown. This solid arose from electrochemically driven CO_2 sequestration since it was not generated in control experiments when 1) no current was applied, and 5% CO_2 was flowed through the cell for 38 h, or 2) when a CO_2-free (100% N_2) gas feed was used and a 10 mA current was applied to the cell for 24 h. Four new and separate experiments were therefore performed with the intention of isolating the solid formed post-CO_2 capture in the graphite-aluminium anode cell (Figure 55). The four solids formed from each test were then collected and analysed to determine their composition, and whether captured CO_2 was intrinsic to the structure ("3.2.5 Analysis of Electrochemically Formed Solids"). On average. 0.58 ± 0.08 g of solid were collected after the experiment for these four experiments. Quantification of elements in the solid is discussed in Section 3.2.5.

3.2.5 Analysis of Electrochemically Formed Solids

Analysis of Carbonate and Aluminium Environment(s)

FT-IR (DRIFT) spectroscopy indicated that a carbonate environment is present in the precipitate isolated post-CO_2 capture in the graphite-aluminium anode cell, but not as sodium bicarbonate or sodium carbonate (Figure 56). Interestingly, two peaks are present in the carbonyl stretch region at 1513 and 1407 cm^{-1} (Figure 56b, black line), indicative of
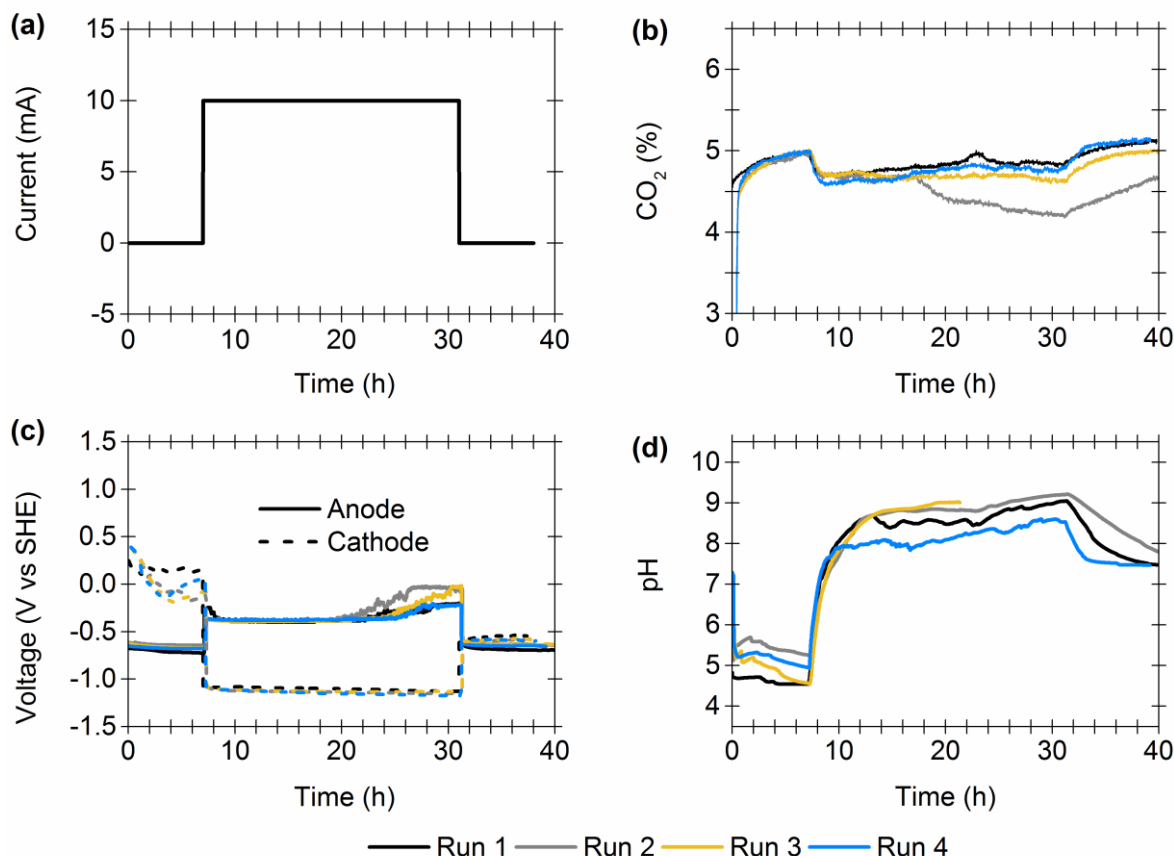
Figure 55: Overlay of repeat CO_2 capture experiments with 1 M NaCl in the graphite-aluminium anode cell. (a) Programmed current-time steps; (b) Carbon dioxide content in the exit gas stream; (c) Resultant changes to the electrochemical potential of the anode (solid line) and cathode (dashed line); (d) Corresponding changes in solution pH, instrument error gave rise to the premature end in data recording for Run 3. Other reaction conditions: a continuous gas flow of 0.7 mL min^{-1} CO_2 (5%) and 13.3 mL min^{-1} N_2, and 60 mL of 1 M NaCl.
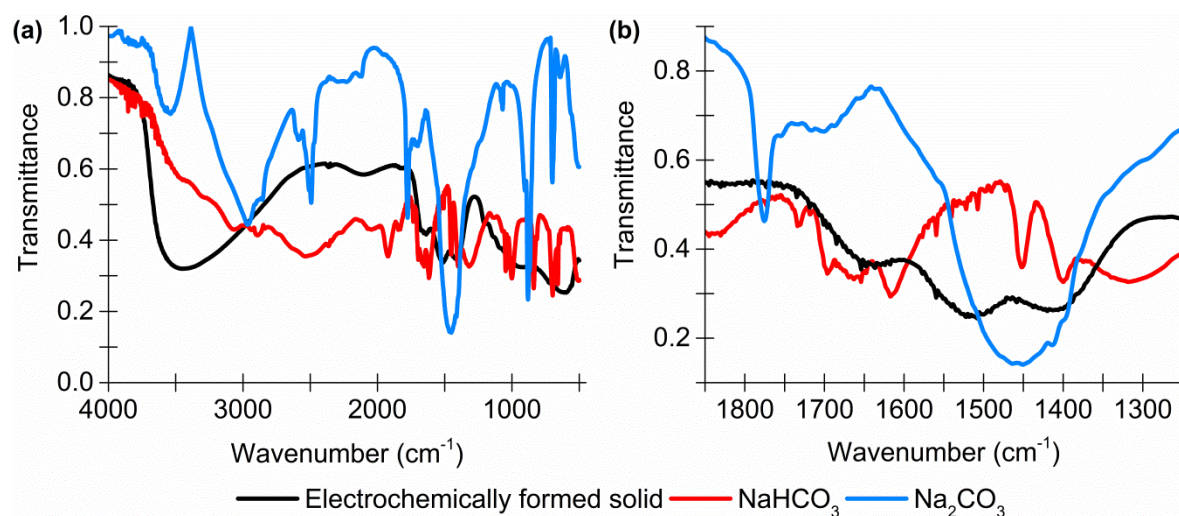
Figure 56: Comparing FT-IR (DRIFT) analysis of electrochemically formed solid (black line) with the spectra of $NaHCO_3$ (red line) and Na_2CO_3 (blue line). (a) Full spectrum; (b) Carbonyl stretch region.

a split v_3 carbonate peak. This split pattern was previously reported by Serna *et al.* whilst synthesising aluminium hydroxycarbonates. Serna synthesised these carbonates by instigating the precipitation of an aluminium based species, by titrating aqueous aluminium nitrate into an aqueous solution of sodium carbonate (Na_2CO_3) at pH 9.15.[251,252] This could explain the broad stretch from 910-580 cm^{-1}, which is in the Al-O stretch region.[253,254] The only other distinguishable peaks are a broad O-H stretch and O-H bend at 3450 cm^{-1} and 1640 cm^{-1} respectively.[255] When the electrochemically formed solid is also compared to carbonate free aluminium compounds $Al(OH)_3$ and $NaAlO_2$, as well as commercial basic aluminium carbonate, (BAC, or basic $Al_2(CO_3)_3$), only the carbonyl region of basic $Al_2(CO_3)_3$ is similar (Figure 57 and Table 14). Overall, FT-IR (DRIFT) analysis suggested the electrochemically formed solid is potentially an aluminium hydroxycarbonate based material.
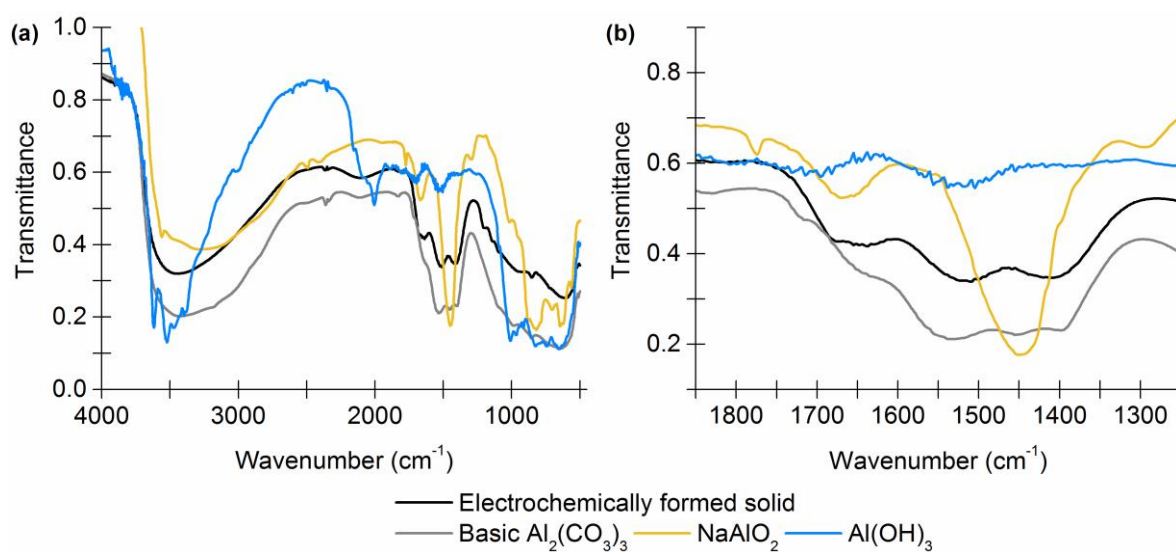
Figure 57: Comparing FT-IR (DRIFT) analysis of electrochemically formed solid (black line) with the spectra of commercial basic $Al_2(CO_3)_3$ (grey line), $NaAlO_2$ (yellow line) and $Al(OH)_3$ (blue line). (a) Full spectrum; (b) Carbonyl stretch region.

The results obtained from solid state $^{13}C\{^1H\}$ MAS and CPMAS NMR analysis supported the conclusions obtained from FT-IR (DRIFT) analysis, as a carbonate environment was detected. Please note, <u>all</u> solid state NMR analysis, experiments and data/figures were performed and provided by Dr Pedro M. Aguiar whilst at the University of York.

Table 14: Comparison of carbonate peaks reported for the electrochemically formed solid and the aluminium hydroxycarbonate species synthesised by Serna *et al*. detected via IR.[251,252]

Reference	Carbonate peak / cm^{-1}		
Serna *et al.*, 1978[251]	1650 (v_2 bend for water)	1520 (splitting of the v_3 carbonate vibration)	1415 (splitting of the v_3 carbonate vibration)
This work	1643 (v_2 bend for water)	1513 (splitting of the v_3 carbonate vibration)	1407 (splitting of the v_3 carbonate vibration)

The observed ^{13}C chemical shifts for standard carbonates are consistent with previous observations for carbonate and bicarbonate systems;[256] carbonate moieties possess chemical shifts of 168-172 ppm, whereas the bicarbonates moieties are more shielded with chemical shifts of ca. 165 ppm (Table 15 and Figure 58).

Table 15: ^{13}C{^{1}H} MAS NMR isotropic shifts observed for carbonate standards and an electrochemically formed precipitate (CO_2 capture solid). Basic $Al_2(CO_3)_3$ refers to basic aluminium carbonate.

Sample	δ_{iso} / ppm
$NaHCO_3$	164.8 ± 2
Na_2CO_3, signal 1	170.9 ± 2
Na_2CO_3, signal 2	170.7 ± 2
$Na_2CO_3 \cdot H_2O$	172.3 ± 2
$Na_2CO_3 \cdot 10H_2O$	169.0 ± 2
$Na_3H(CO_3)_2 \cdot 2H_2O$	167.8 ± 2
Basic $Al_2(CO_3)_3$, signal 1	164.3
Basic $Al_2(CO_3)_3$, signal 2	162.4
CO_2 capture solid	163 ± 1
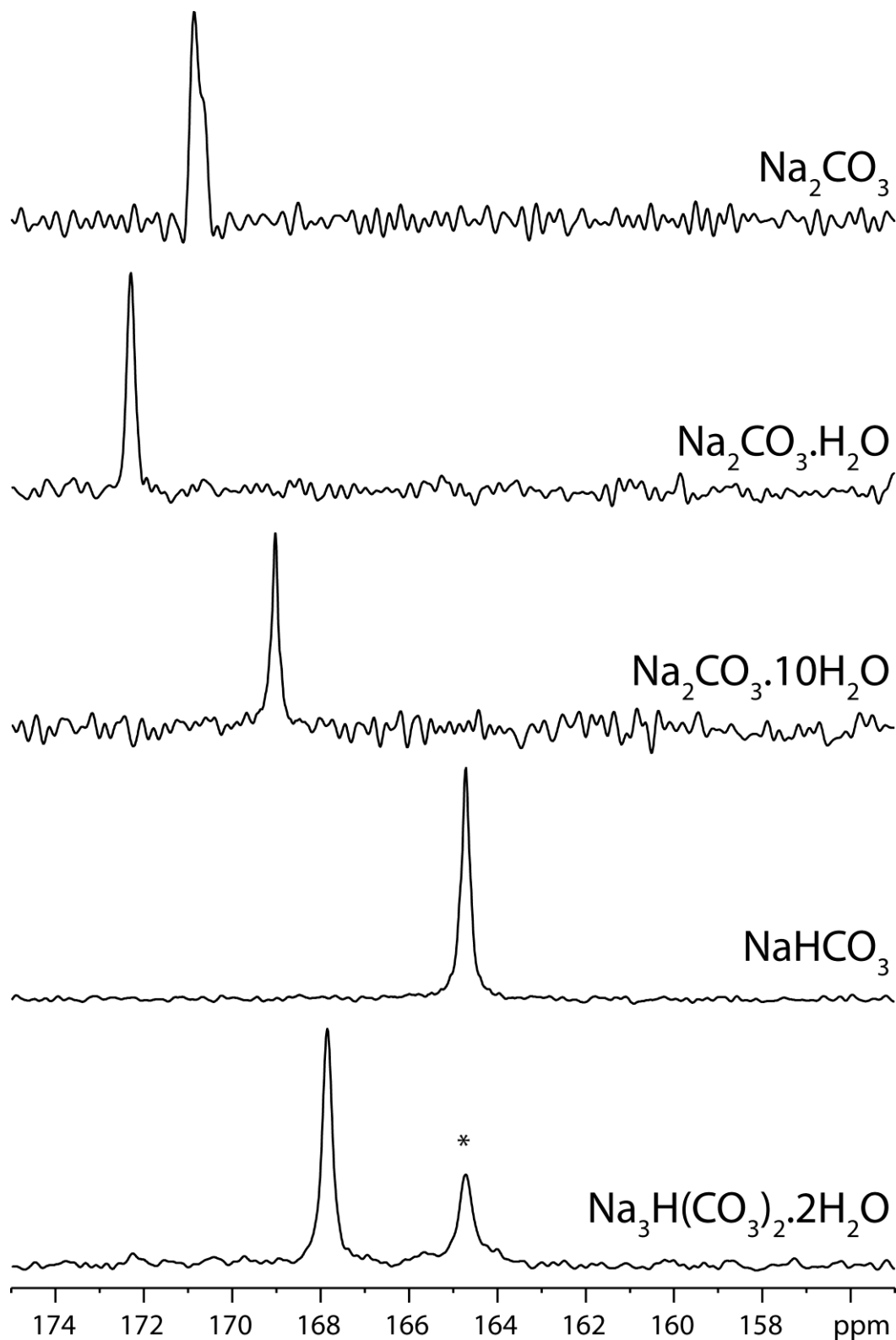
Figure 58: $^{13}C\{^1H\}$ MAS (Na_2CO_3) and $^{13}C\{^1H\}$ CPMAS spectra of sodium carbonate and bicarbonate standards. An asterisk marks the presence of a signal arising from a sodium bicarbonate impurity in the sodium sesquicarbonate sample.

Electrochemically formed precipitates, generated in 24 h, 10 mA carbon capture experiments, yielded broad signals, indicative of disorder with isotropic chemical shifts of

162-164 ppm (Figure 59), consistent with bicarbonate.[256] ^{13}C{^{1}H} Bloch-decay (single-pulse) experiments on the sodium precipitates revealed no additional signals to those observed under cross-polarisation.
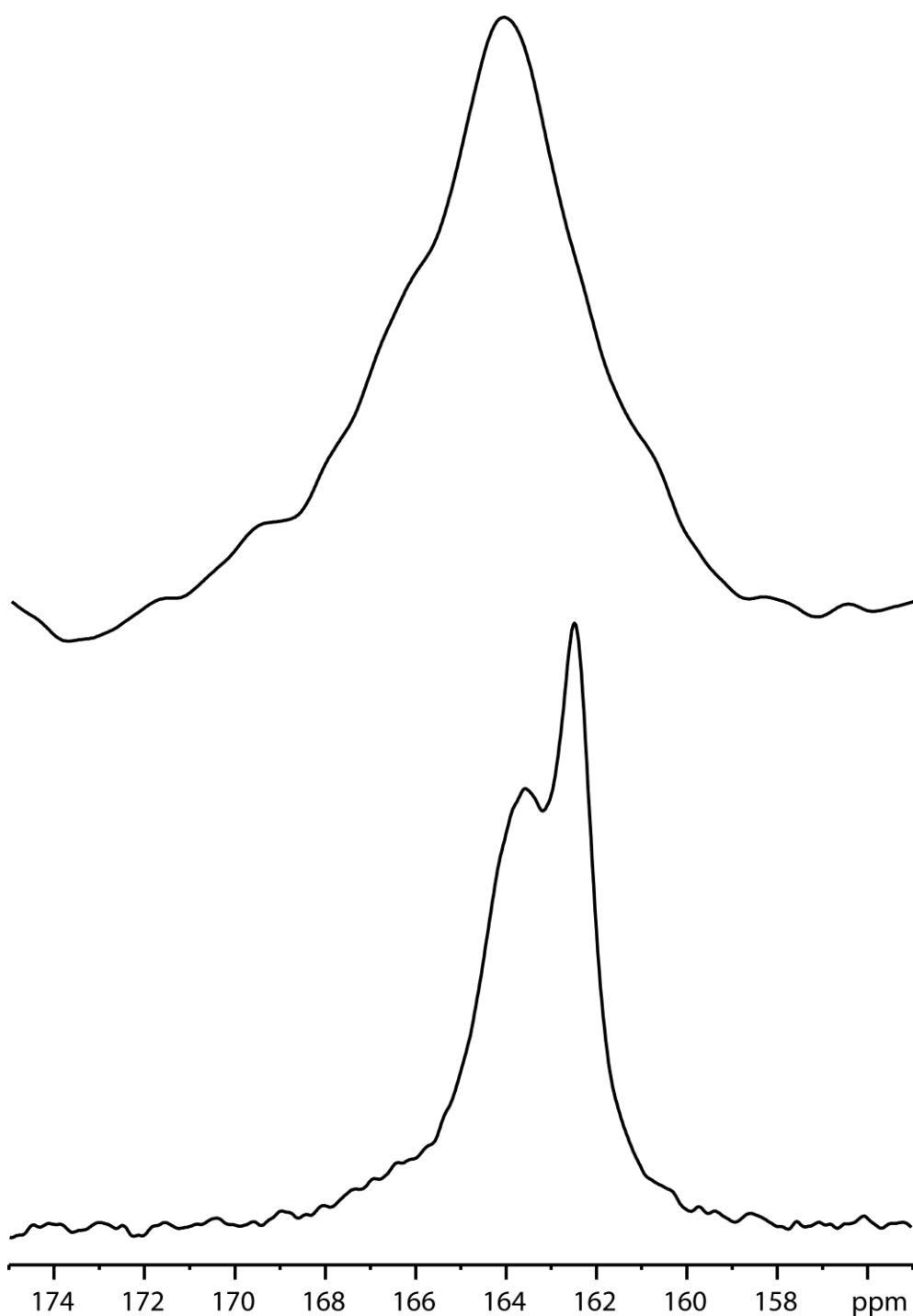
Figure 59: ^{13}C{^{1}H} CPMAS spectra (top and bottom) obtained for two precipitates generated in 24 h, 10 mA carbon capture experiments with 1 M NaCl in the graphite-aluminium anode cell. The observed isotropic shifts of 162-164 ppm are typical of solids acquired from various electrochemical runs.

FT-IR (DRIFT) analysis illustrated that aluminium is a major component of the electrochemically formed precipitates. Solid state ^{27}Al MAS NMR of electrochemically formed precipitates revealed that it is predominantly six-coordinated aluminium (^{VI}Al) with small amounts (<8% total) of five- and four-coordinated aluminium sites (^{V}Al and ^{IV}Al, Figure 60). No distinct second-order lineshape features are observable in the MAS spectra and a significant tailing of the signal to the more shielded region of the spectrum is indicative of a composite signal resulting from sites possessing a distribution of quadrupole coupling constants. The ^{27}Al 3-Quantum Magic-Angle Spinning (3QMAS) spectrum (Figure 61) confirms the assignment of the signals at ca. 30 and 60 ppm as arising from ^{V}Al and ^{IV}Al sites and reveals that all three sites have similar quadrupole parameters, P_Q ~ 3.6 ± 0.5 MHz.
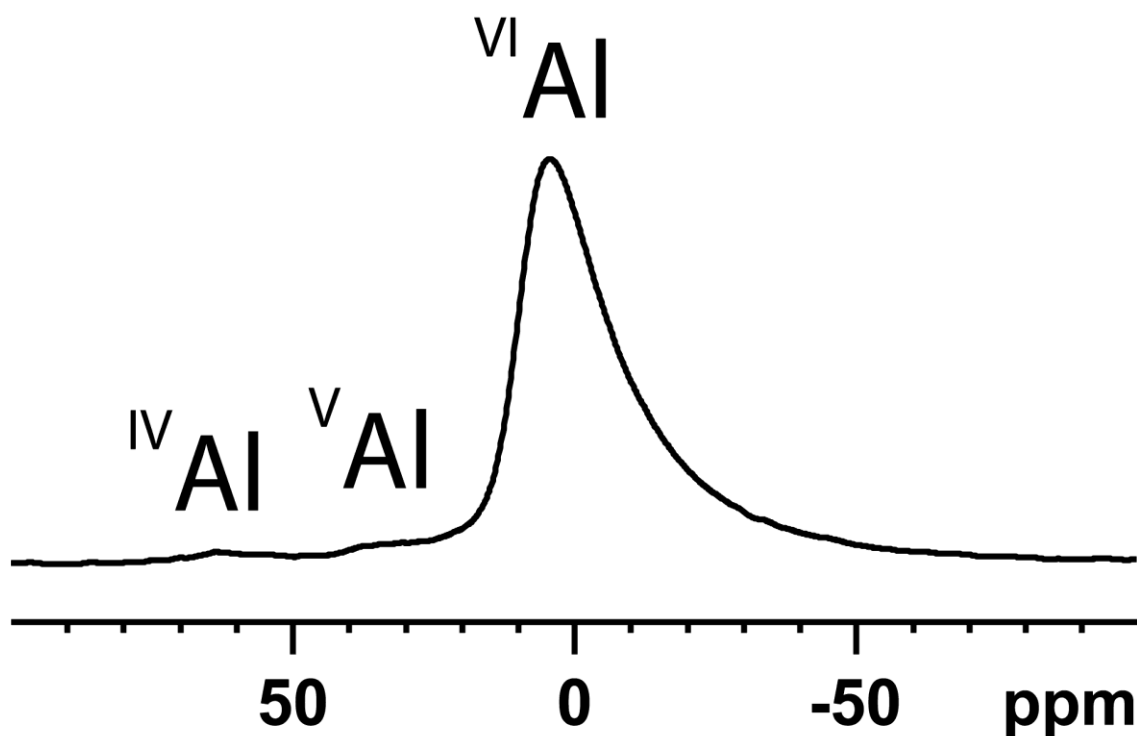
Figure 60: ^{27}Al MAS spectrum of an electrochemically formed precipitate generated in a 24 h, 10 mA carbon capture experiment with 1 M NaCl in the graphite-aluminium anode cell.
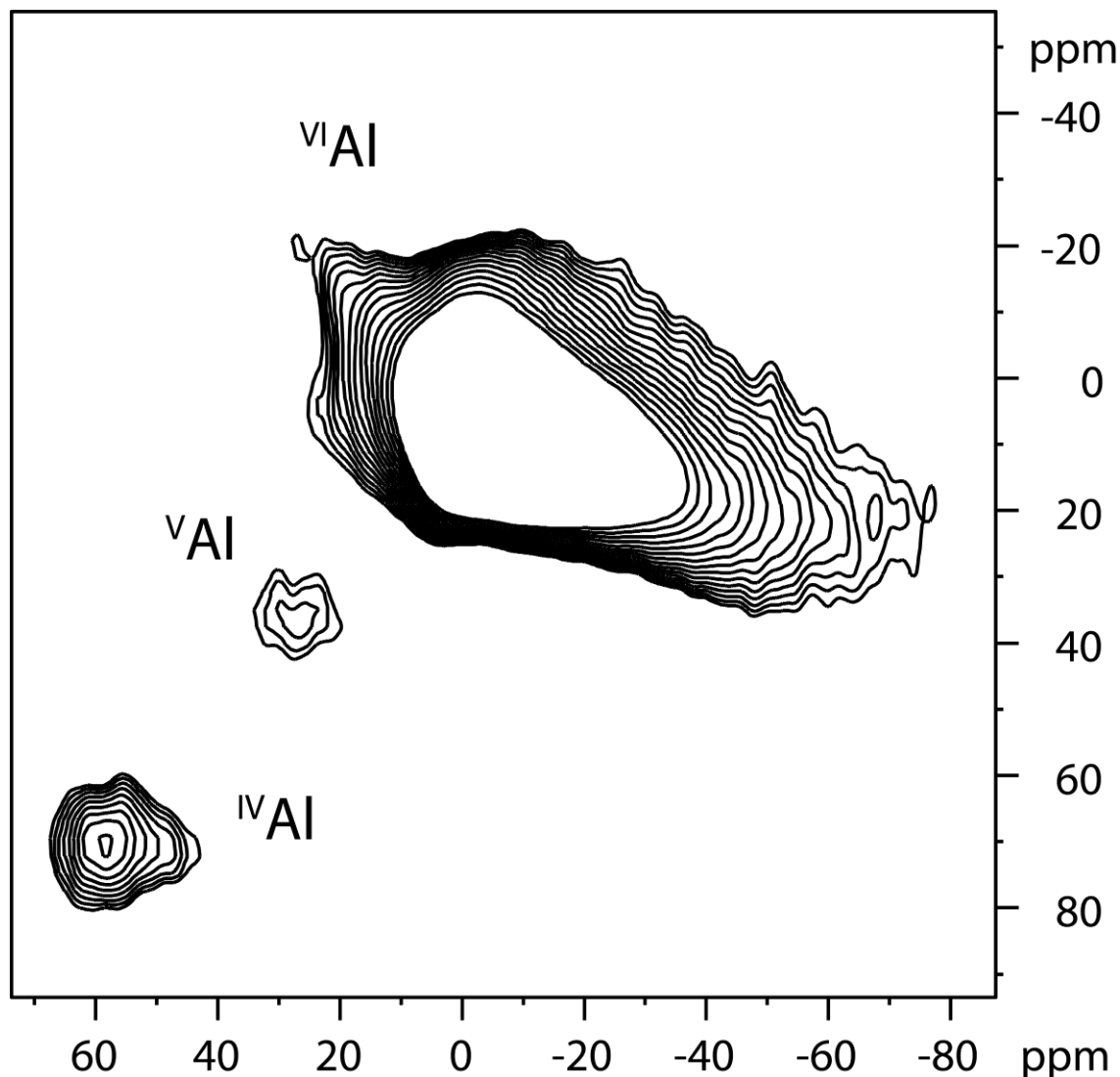
Figure 61: ^{27}Al 3QMAS spectrum of an electrochemically formed precipitate generated in a 24 h, 10 mA carbon capture experiment with 1 M NaCl in the graphite-aluminium anode cell.

When commercial basic $Al_2(CO_3)_3$ (Alfa Aesar) was analysed via solid state NMR, $^{13}C\{^1H\}$ CPMAS NMR revealed two signals at 164.3 and 162.4 ppm (Figure 62, top spectrum). The ^{27}Al MAS NMR revealed the primary aluminium species is six-coordinated aluminium (^{VI}Al) with small amounts of four (^{IV}Al) and five-coordinated aluminium (^{V}Al) sites (Figure 62, bottom spectrum). No signal is observed in the ^{23}Na MAS NMR (data not shown). Hence, a similar but not identical aluminium and carbonate environment to the electrochemically formed solid is present.
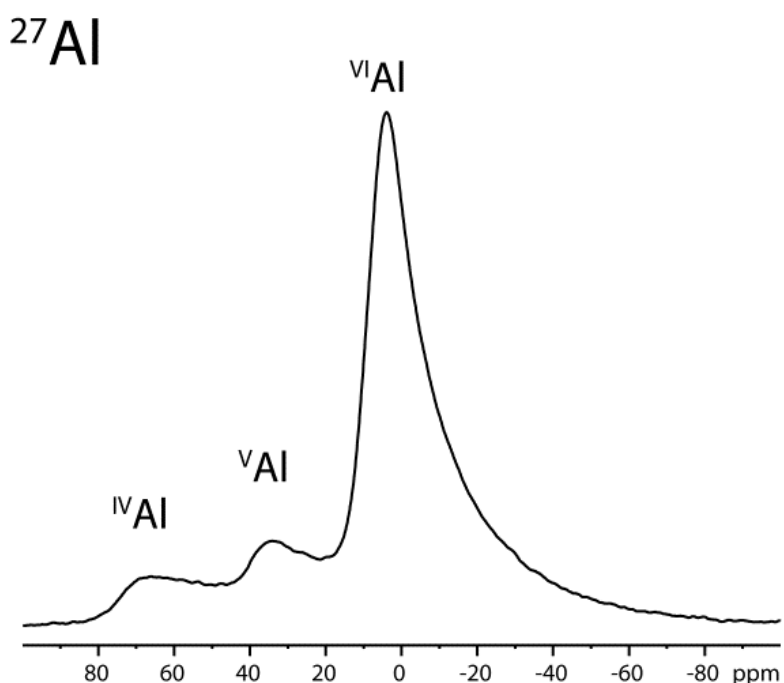
Figure 62: $^{13}C\{^{1}H\}$ CPMAS and ^{27}Al MAS NMR spectra of a commercial basic aluminium carbonate.

TGA-IR analysis of bicarbonate and carbonate standards indicated that bicarbonates release CO_2 gas at temperatures <200 °C, whereas carbonates release CO_2 gas at temperatures >800 °C (Figure 63). The electrochemically formed samples show a mass loss of 30-35% at 150-200 °C with the concurrent loss of CO_2 gas and water (black line, Figure 64). This is indicative of a bicarbonate environment rather than a carbonate environment (red and blue lines, Figure 64).
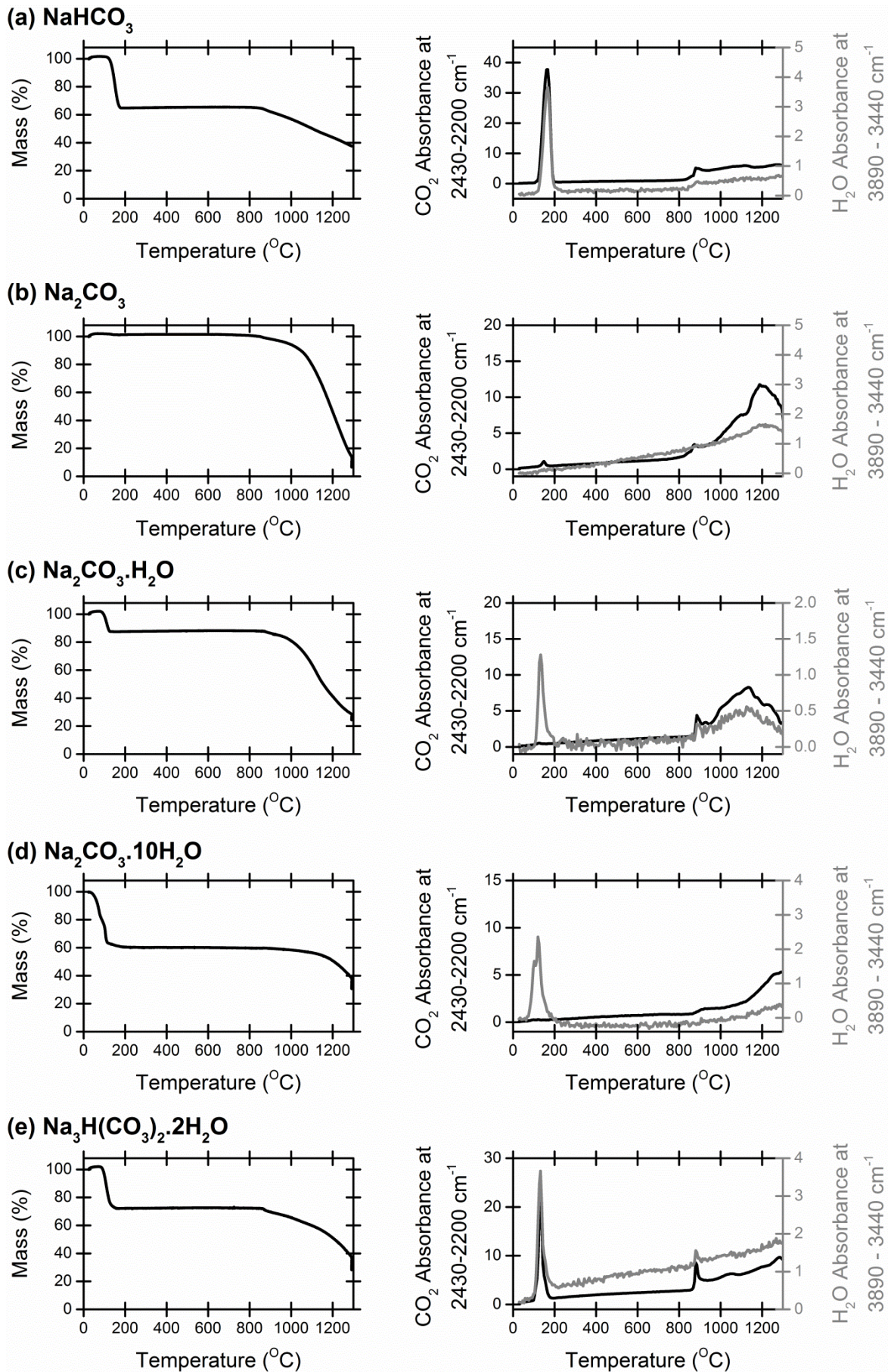
Figure 63: TGA-IR analysis of sodium bicarbonate and different sodium carbonate standards.
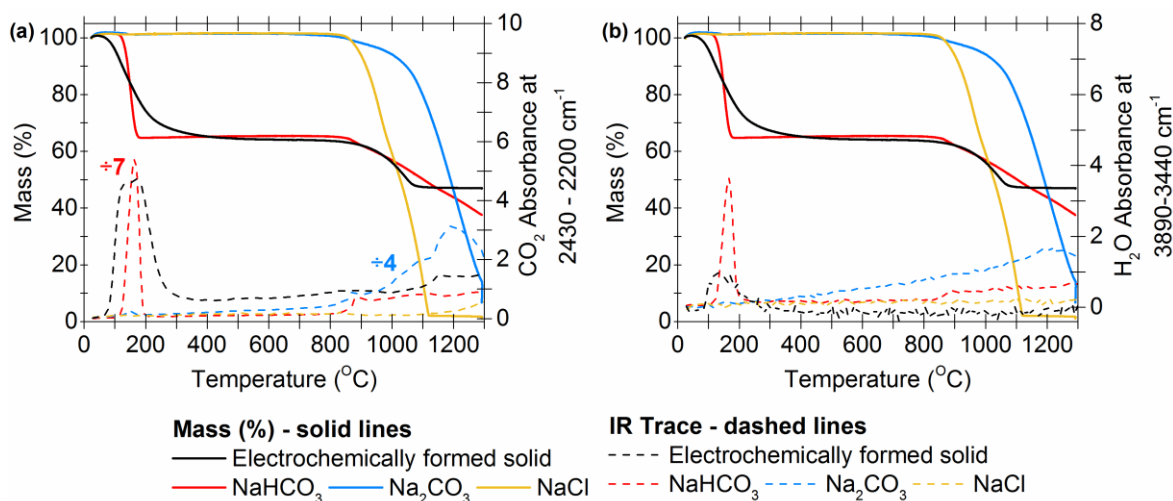
Figure 64: Comparing TGA-IR analysis and consequent (a) CO_2 IR spectra and (b) H_2O IR spectra of an electrochemically formed solid, carbonate standards and NaCl.

A mass loss of 15% is detected from 800 °C without the release of CO_2 (black line, Figure 64), and occurs at a similar temperature to when NaCl decomposes (yellow line, Figure 64), as NaCl has a melting point of 800-801 °C and boiling point of 950-1150 °C.[257] This suggests this mass loss at 800 °C is due to isolating NaCl from the electrolyte along with an aluminium hydroxycarbonate based species. A mass loss of 100% did not occur at 1250 °C, indicating components of the solid are stable at this temperature. The temperature of decomposition is also similar to the profile of commercial basic $Al_2(CO_3)_3$ (Figure 65), which suggested that an aluminium oxide based environment is also present.

The presence of an aluminium oxide was supported by powder XRD, because analysis of the retained solid post-TGA-IR analysis shows the diffraction pattern of corundum (α-Al_2O_3) which is formed in the thermal transition of $Al(OH)_{3(s)}$ when exposed to temperatures >1000 °C (Figure 66 and Figure 67 respectively).[258] The rising baseline also indicated the presence of a secondary unidentifiable amorphous phase, which was hypothesised to be an aluminium based specie(s). Overall, the solid analysis suggested that an aluminium phase consisting of aluminium hydroxycarbonate and aluminium oxide is present in the solid.
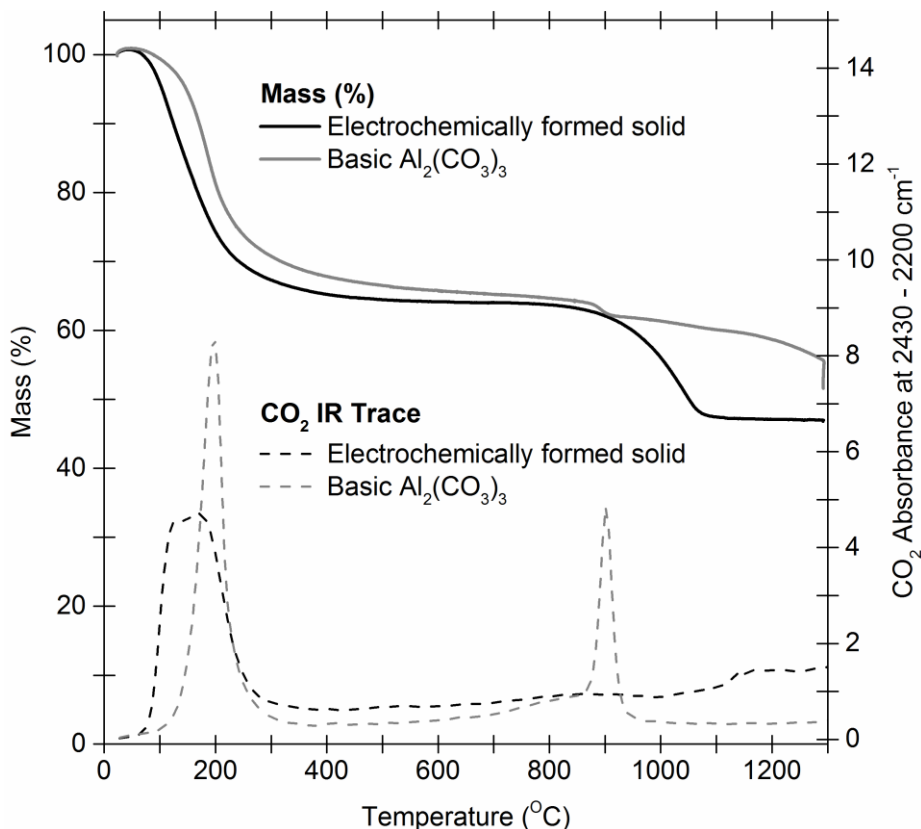
Figure 65: Comparing TGA-IR analysis and consequent CO_2 IR spectra of an electrochemically formed solid and commercial basic $Al_2(CO_3)_3$. A secondary loss of CO_2 at 900 °C is hypothesised to be traces of $NaHCO_3$ or Na_2CO_3 which may have been used to synthesise basic $Al_2(CO_3)_3$.[259,260]
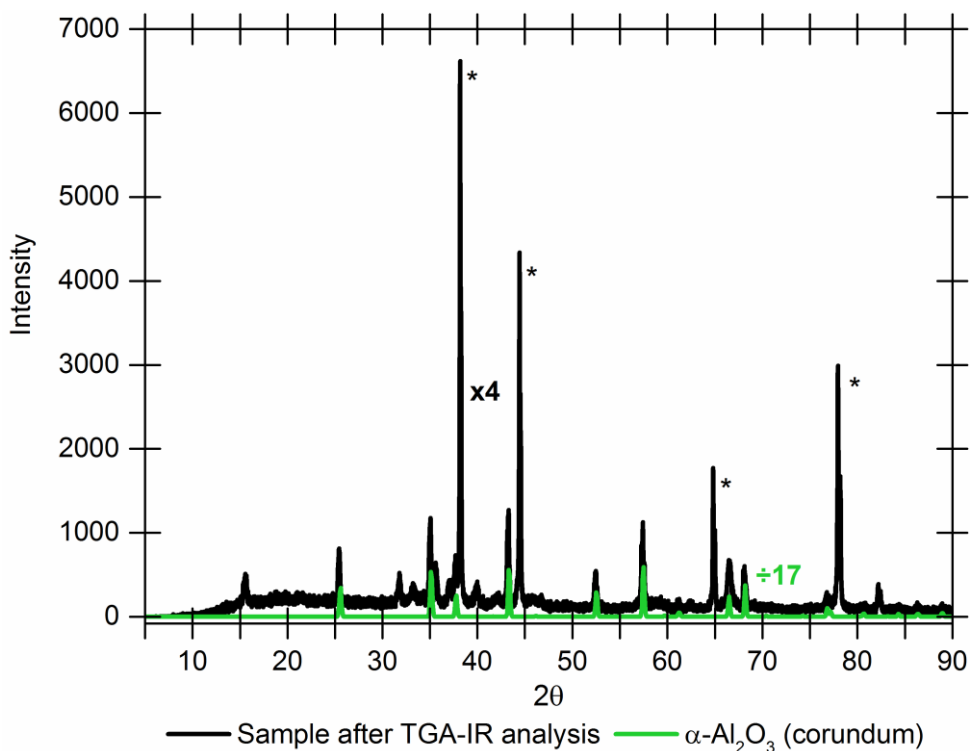
Figure 66: Powder XRD analysis of electrochemically formed solid post-TGA-IR analysis (black line) and corundum (green line); * metal plate (Al) sample holder.[258]
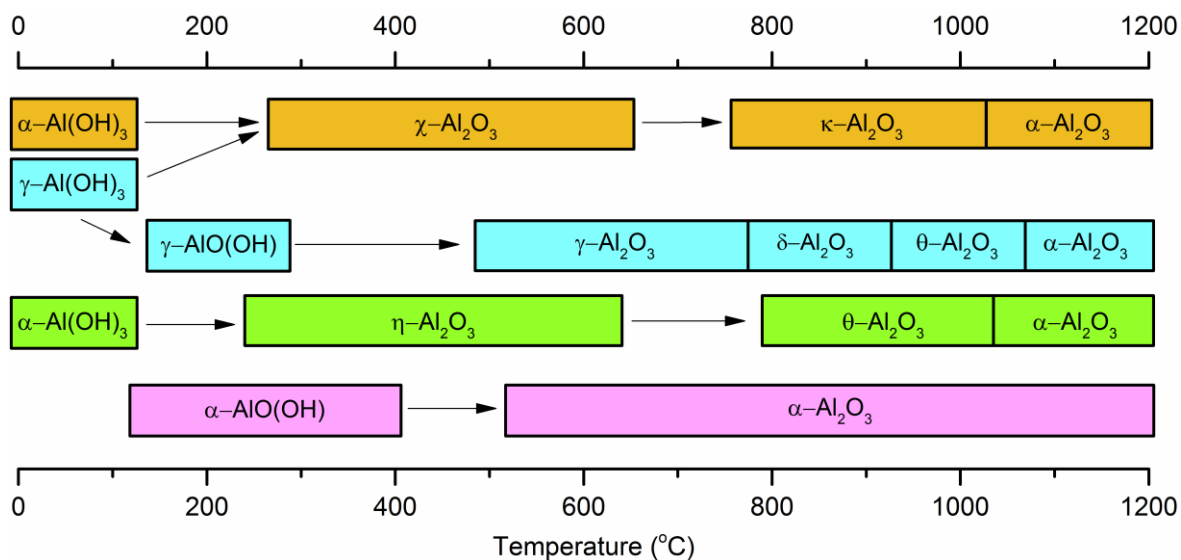
Figure 67: Transformation of aluminium hydroxides to aluminium oxides.[261]

Analysis of Sodium Environment(s)

Solid state ^{23}Na MAS NMR analysis was performed to see if only sodium from NaCl was present. The NMR spectrum shows a sharp signal centred about 7 ppm and a second broader signal centred about -9.5 ppm (Figure 68) suggestive of two different Na environments.
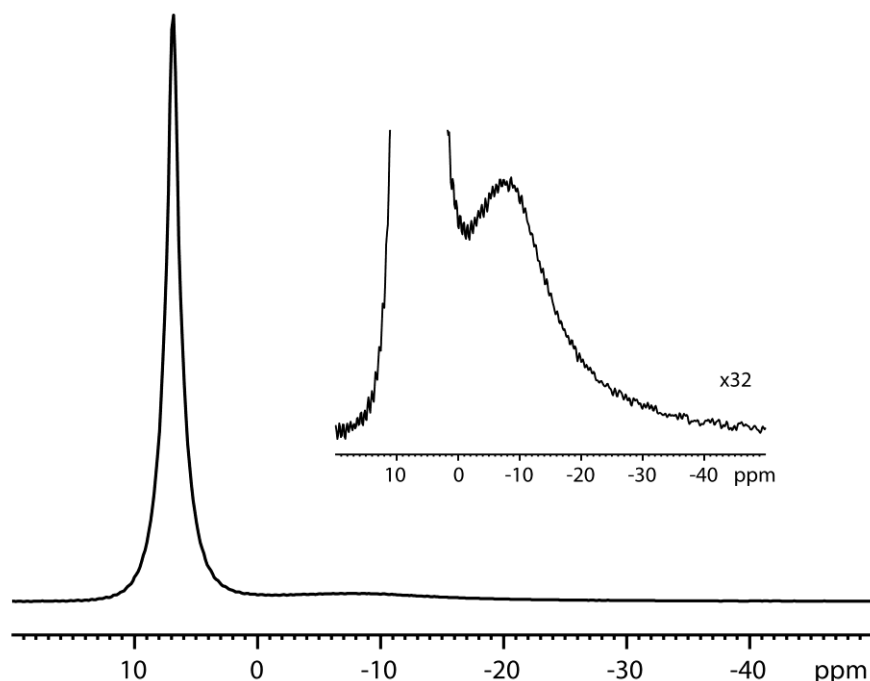
Figure 68: ^{23}Na MAS spectra of an electrochemically formed precipitate generated in a 24 h, 10 mA carbon capture experiment with 1 M NaCl in the graphite-aluminium anode cell. An inset of the spectrum (x32) shows the carbonate component more clearly. The amount of NaCl (δ = 7 ppm) co-precipitating varied from sample to sample.

Comparison to published data allows assignment of the signal at 7 ppm to NaCl[262] and was the major sodium species detected. A secondary minor sodium environment indicative of a disordered bicarbonate environment was also detected. From a comparison of experimental data from a series of standards (Figure 69-Figure 73 and Table 16), the lack of distinct discontinuities in the precipitate data compared to the well-ordered crystalline samples is indicative of structural disorder about the sodium site(s). This is evidenced by the 2D lineshape of the carbonate signal in the ^{23}Na (3QMAS) spectrum (Figure 73).
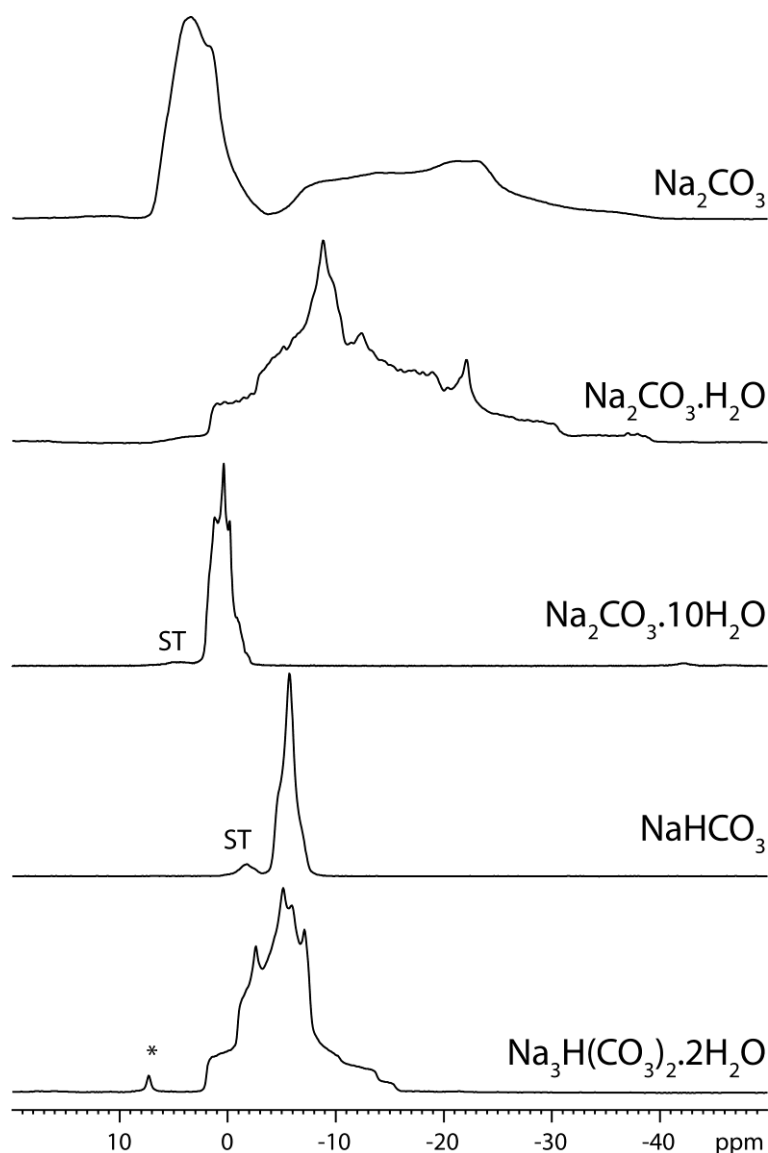
Figure 69: ^{23}Na MAS NMR spectra of a series of sodium carbonate standards. Signals arising from the satellite transitions (ST) are marked where visible. A small amount of NaCl in the sesquicarbonate sample is marked by an asterisk. ^{23}Na 3QMAS also reveals a small amount (ca. 10% based on fits of the MAS lineshape) of sodium bicarbonate in the sesquicarbonate sample, which was also observed in the ^{13}C{^{1}H} MAS spectrum of this sample.
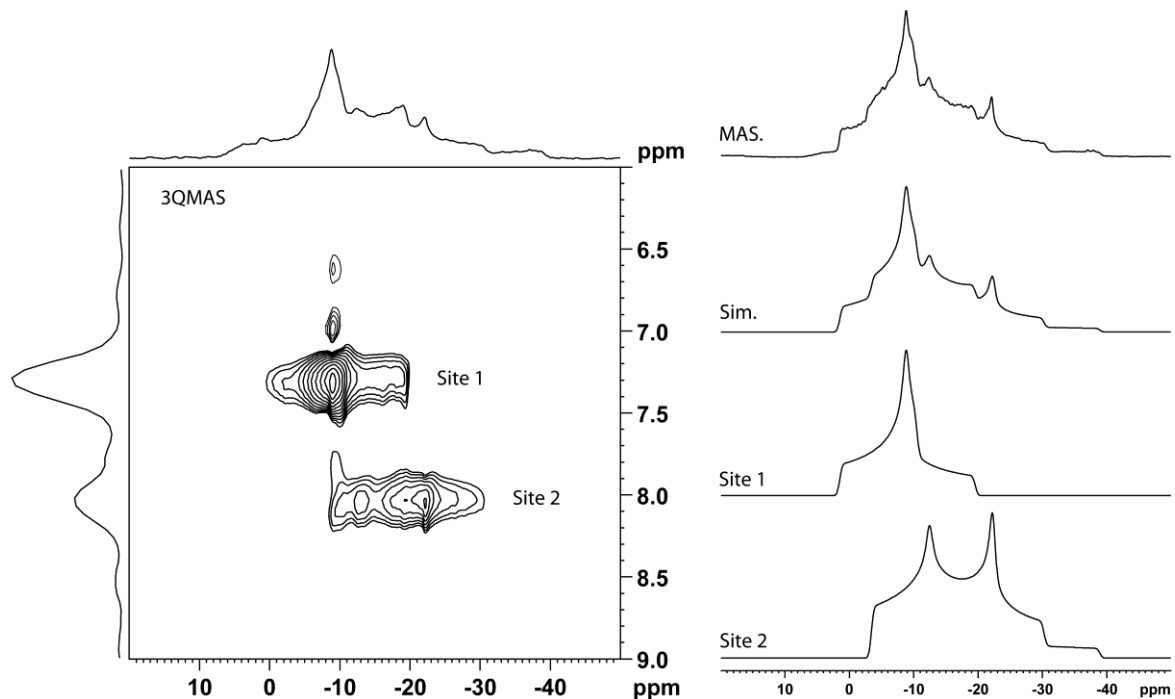
Figure 70: ^{23}Na 3QMAS spectrum (left) of $Na_2CO_3.H_2O$ showing resolution of the two overlapping signals along with ^{23}Na MAS and simulation of the lineshape taking into account the two signals (right).
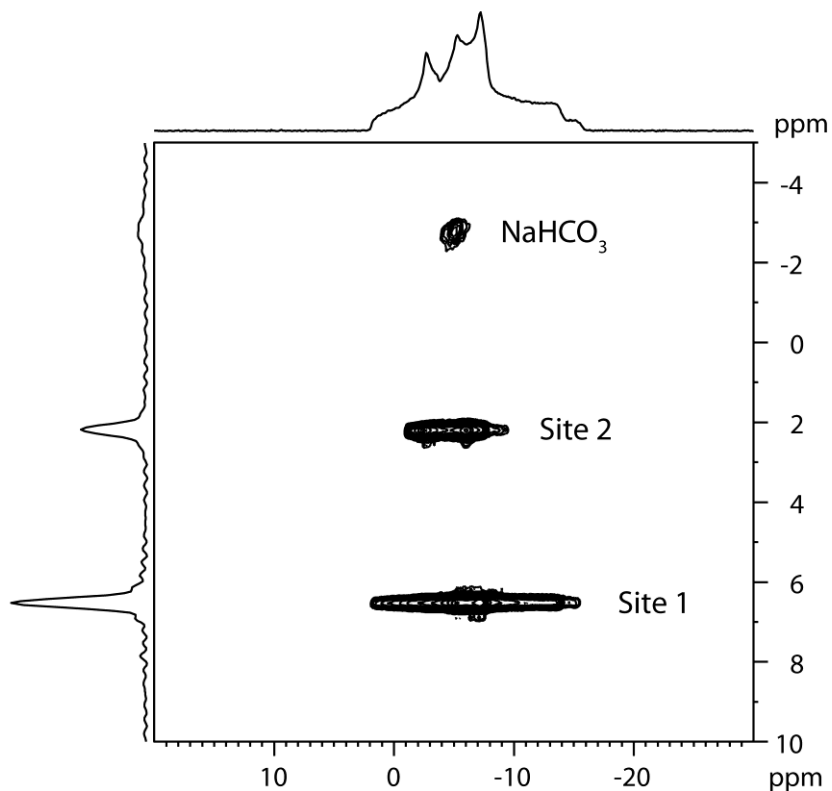
Figure 71: ^{23}Na 3QMAS spectrum of $Na_3H(CO_3)_2.2H_2O$ showing resolution of the two crystallographically distinct sites[263] along with sodium bicarbonate impurity.
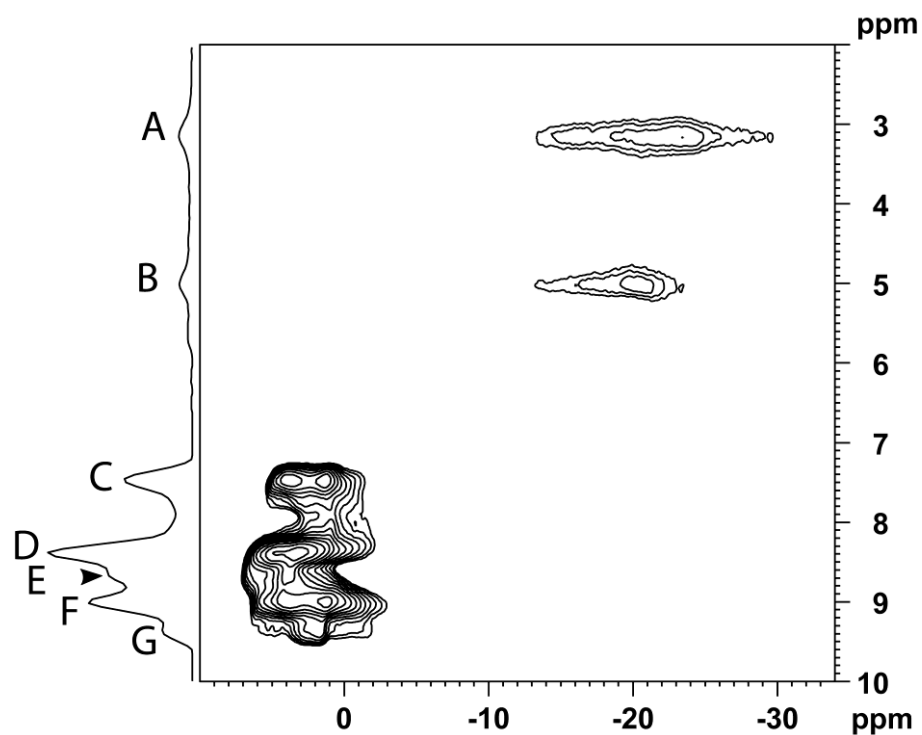
Figure 72: ^{23}Na 3QMAS spectrum of Na_2CO_3. A series of signals could be resolved due to the large number of unique sites present in the incommensurately modulated structure of sodium carbonate.[264]
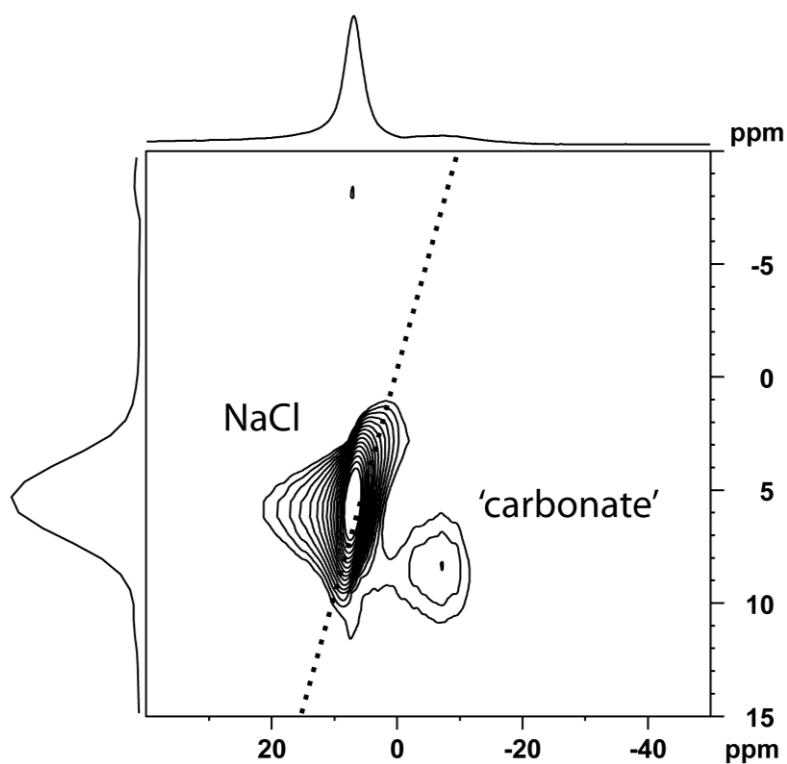
Figure 73: ^{23}Na 3QMAS spectra of an electrochemically formed precipitate with differing amounts of NaCl. The slope of the dashed line corresponds to the chemical shift contribution to the position in the 'isotropic' (vertical) dimension. Elongation along this slope indicates a distribution of isotropic chemical shifts.[265]

Table 16: ^{23}Na NMR parameters for sodium carbonate standards and an electrochemically formed precipitate solid (labelled as CO_2 capture solid).

Sample	δ_{iso} / ppm	C_Q / MHz	η	P_Q / MHz
$NaHCO_3$	-4.3 ± 1	0.68 ± 1	0.95 ± 5	0.88
$Na_2CO_3 \cdot H_2O$[a], site 1	1.5	1.80	1	2.4
$Na_2CO_3 \cdot H_2O$[a], site 2	-1.8	2.54	0.44	2.7
$Na_2CO_3 \cdot 10H_2O$[a], site 1	2.2	0.77	0.48	0.80
$Na_2CO_3 \cdot 10H_2O$[a], site 1	1.85	0.81	0.65	0.87
$Na_3H(CO_3)_2 \cdot 2H_2O$[a], site 1	2.0	1.70	0.75	1.90
$Na_3H(CO_3)_2 \cdot 2H_2O$[a], site 2	-0.2	1.33	0.26	1.39
Na_2CO_3[a,b], signal A	-6.2 ± 5	-	-	2.7 ± 3
Na_2CO_3[a,b], signal B	-4.5 ± 5	-	-	2.7 ± 3
Na_2CO_3[a,b], signal C-G	5.6-6.9	-	-	1.2-1.4
CO_2 capture solid[a]	1 ± 2	-	-	1.5 ± 4

a) Parameters extracted from ^{23}Na 3QMAS experiments (Figure 70-Figure 73).

b) The structure of Na_2CO_3 is incommensurately modulated (aperiodic) resulting in signals representing the distribution of sodium environments. Thus even 'resolved' signals belong to a distribution of sites in the crystal. No attempt has been made herein to ascribe the observed signals to the sites within the crystal.

Overall, this suggested that both an aluminium hydroxycarbonate material and a separate sodium bicarbonate environment were isolated, or that one aluminium and sodium carbonate based species was being formed. Identifying which of these two scenarios is occurring was not possible via solid state NMR.

Any Crystalline Phase(s)?

To determine if any crystalline compounds were present in the isolated solids, powder XRD analysis was employed (Figure 74). The only crystalline material detectable is NaCl, which could be expected due to isolating the solid from aqueous 1 M NaCl. Interestingly, the baseline of the spectrum is not flat and contains a slight rise, indicating that there is a
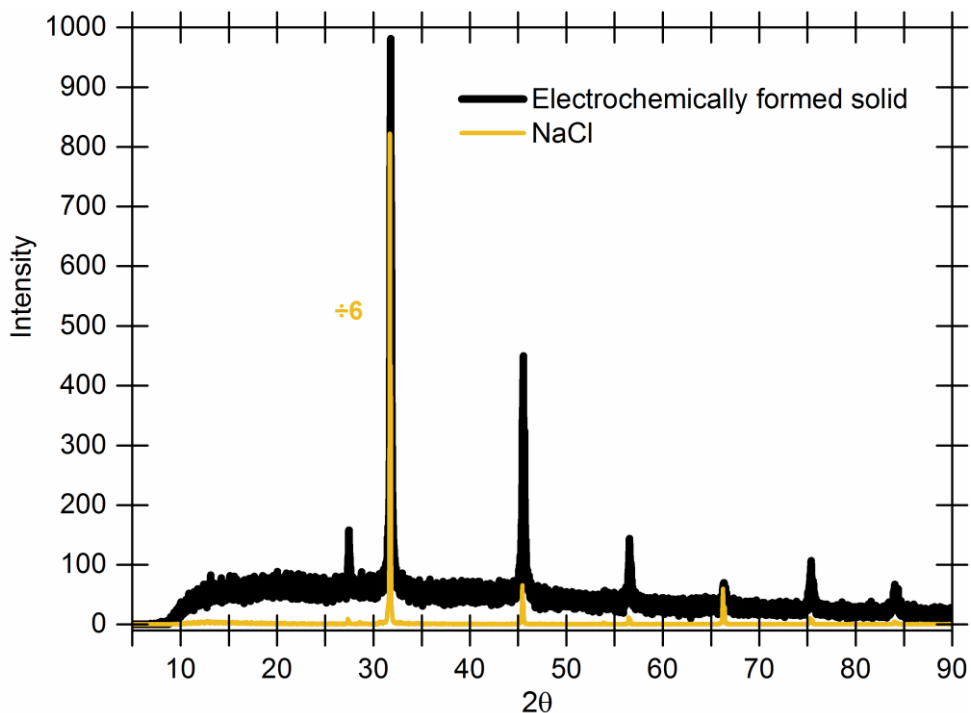
Figure 74: Powder XRD analysis of electrochemically formed solid compared to NaCl.

secondary amorphous species. Research into carbonate containing bauxite, a mineral containing hydrous aluminium oxides, has indicated that the presence of CO_2, as carbonate, can hinder the crystallisation of $Al(OH)_3$ in bauxite.[266] It is therefore probable that the secondary amorphous species is due to the aluminium hydroxycarbonate species, as detected by FT-IR (DRIFT), solid state $^{13}C\{^1H\}$ CPMAS, solid state ^{27}Al MAS NMR and TGA-IR analysis.

Element Quantification

After identifying some of the major elements present in the electrochemically formed solids, ICP-MS analysis was performed to quantify sodium and aluminium, and TGA-IR analysis was used to quantify carbon via a calibrated TGA-IR method (see section 3.7). These results show the average molar ratios of C:Al and Na:Al are 1:4 ± 1.6 and 1:7 ± 3.6 respectively, which is inconsistent with the formation of a homogenous phase (Table 17). All errors quoted for solid analysis (and for any values in this chapter) are standard deviation values. This analysis suggested that the electrochemically formed solids are a heterogeneous mixture of different chemical species, as indicated by other solid analysis techniques.

Table 17: Quantification of the major elements in the electrochemically formed solids post-CO_2 capture in the graphite-aluminium anode cell.[a]

1 M Electrolyte	Solid mass / g	C / mmol[b]	Na / mmol[c]	Al / mmol[c]
NaCl, Run 1[d]	0.62	0.6 ± 0.1	7.2 ± 0.2	4.1 ± 0.4
NaCl, Run 2[d]	0.63	1.0 ± 0.2	6.2 ± 0.2	3.9 ± 0.2
NaCl, Run 3[d]	0.46	1.0 ± 0.1	3.4 ± 0.2	3.3 ± 0.3
NaCl, Run 4[d]	0.60	1.1 ± 0.1	8.4 ± 0.5	4.1 ± 0.4
Average	0.58 ± 0.08	0.9 ± 0.2	6.3 ± 2.1	3.9 ± 0.4

a) All molar values reported for carbon, sodium and aluminium detected in the solid post-CO_2 capture correspond to the <u>total</u> amount of carbon, sodium and aluminium in the <u>total</u> mass of solid collected respectively.
b) Quantified via TGA-IR analysis.
c) Quantified via ICP-MS analysis.
d) The four runs correspond to the four experiments in Figure 55.

3.2.6 Surface Analysis: Is NaCl the Only Crystalline Material?

Bulk solid analysis demonstrated that a heterogeneous mixture of an amorphous aluminium hydroxycarbonate and crystalline NaCl is isolated post-CO_2 capture in the graphite-aluminium anode cell. A disordered separate sodium bicarbonate species was also detected, however it was unclear whether this was a separate species or part of an aluminium hydroxycarbonate based species. Therefore, to determine if any crystalline $NaHCO_3$, which was undetectable via powder XRD, is present, Raman and SEM-EDX analysis was performed.

Raman Analysis

Raman analysis shows a broad amorphous structure, with peaks at 1093 cm^{-1} and at 1566 cm^{-1} indicative of a carbonate based environment[267] and amorphous carbon respectively[268] (Figure 75). Numerous points of the sample produced identical results, indicating this material is dispersed throughout. No indication of crystalline $NaHCO_3$ formation was detected, suggesting that if crystalline $NaHCO_3$ is present, it may be nano-crystalline.
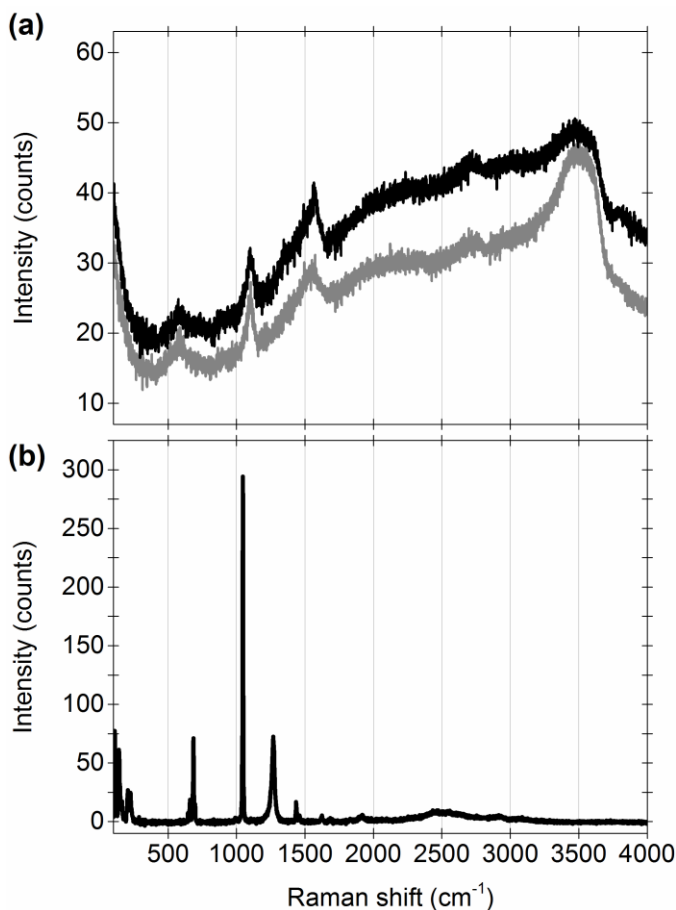
Figure 75: Raman analysis of (a) two different regions and hence spectra of an electrochemically formed solid, and (b) $NaHCO_3$ for comparison.

SEM-EDX Analysis

When the precipitate was analysed via SEM imaging, an amorphous bulk morphology is detected (Figure 76). A few crystallites were detected, varying in size from 0.8-1.3 µm (Figure 76b). When analysed via EDX analysis, these crystallites are identified as NaCl, supporting powder XRD analysis. The non-crystalline bulk of the material contains aluminium and oxygen as the major elements (Table 18), supporting the formation of an aluminium oxide material. Elemental ratios vary throughout the sample, consistent with a heterogeneous mixture. All elemental ratios obtained from SEM-EDX analysis are stated in a 1:XX manner, with the LHS element quoted in the ratio set as 1.
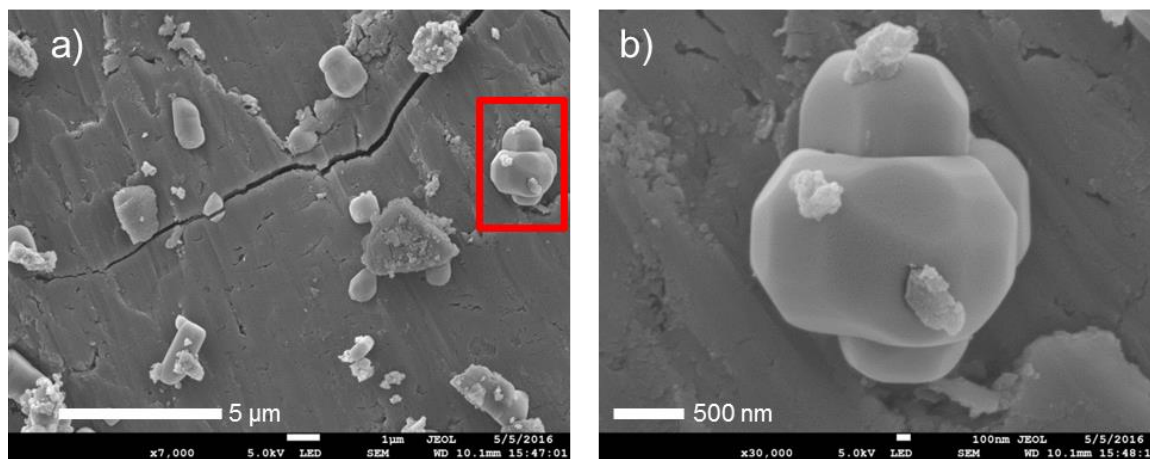
Figure 76: SEM analysis of electrochemically formed solid. (a) Shows small crystallites and largely non-crystalline bulk, (b) a closer view of the crystal highlighted in the red square of panel a.

Table 18: SEM-EDX analysis of electrochemically formed solid.

Run	Al:Na ratio[a]	Al:C ratio[a]	Al:O ratio[a]	Na:Cl ratio[a]
Run 1[b,c]	75.75 ± 43.81	N/A	1.75 ± 0.75	1.23 ± 0.74
Run 2[b,d]	1.35 ± 0.86	1.86 ± 2.42	4.22 ± 1.59	0.80 ± 0.23

a) Values are stated in a 1:XX manner, with the LHS element quoted in the ratio set as 1.
b) In each run, a different viewpoint of the sample was chosen and eight points along a diagonal line were analysed. The average values obtained from these eight runs are quoted.
c) Analysis of small crystallite (Figure 76b, shown in the red square panel of Figure 76a).
d) Analysis of large non-crystalline bulk (Figure 76a).

A low abundance of carbon is however detected which was puzzling. Analysis of $NaHCO_3$ and Na_2CO_3 for comparison also detected low carbon levels, with all elemental ratios quoting unexpected values (Table 19).

Table 19: EDX analysis of standard $NaHCO_3$ and Na_2CO_3.

Standard	Na:O ratio[a]	Na:C ratio[a]	O:C ratio[a]
$NaHCO_3$, run 1[b]	1.38 ± 0.11	0.03 ± 0.04	0.02 ± 0.03
$NaHCO_3$, run 2[b]	1.41 ± 0.15	0.06 ± 0.12	0.04 ± 0.01
Na_2CO_3, run 1[b]	0.83 ± 0.12	0.01 ± 0.02	0.01 ± 0.01
Na_2CO_3, run 2[b]	0.85 ± 0.12	0.01 ± 0.01	0.01 ± 0.01

a) Values are stated in a 1:XX manner, with the LHS element quoted in the ratio set as 1.
b) In each run, a different viewpoint of the sample was chosen and eight points along a diagonal line were analysed. The average values obtained from these eight runs are quoted.

This therefore suggested that quantification of carbon, and elemental ratios, via SEM-EDX was not entirely reliable. It was therefore concluded that $NaHCO_3$ is either not isolated in the heterogeneous amorphous solid or is an extremely minor component.

3.2.7 Further Analysis of the Amorphous, Insoluble Material

After detailed analysis of the precipitates, the evidence suggested that the solid was a heterogeneous mixture of NaCl, aluminium oxide and an aluminium (and potentially sodium based) hydroxycarbonate material. The amorphous nature of the insoluble material creates difficulties in assigning a more exact chemical structure, so attempts were made to further purify the carbon-containing component via cold and hot water washes (Scheme 34).
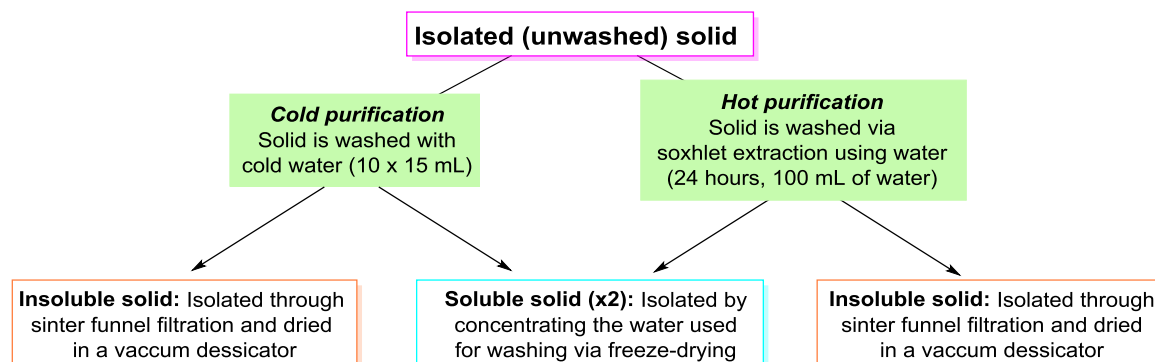
Scheme 34: Water washes employed to further investigate the electrochemically formed solids.

After performing a cold water wash of an electrochemically formed solid, an amorphous disordered phase is still isolated, as shown by the rising baseline in the powder XRD spectrum (Figure 77). This solid is similar, but not identical, to commercial basic $Al_2(CO_3)_3$. No traces of NaCl were detected, indicating that NaCl had been removed. A drop in captured CO_2 levels was also indicated by TGA-IR analysis. This could be expected due to the hydrolysis of carbonate in the presence of water. When washed with hot water, NaCl and the carbonate phase were removed from the precipitate, and the aluminium oxide phase transitioned to crystalline boehmite, γ-AlO(OH), with an amorphous phase still detected, as shown by powder XRD[269-271] and Raman analysis[272]
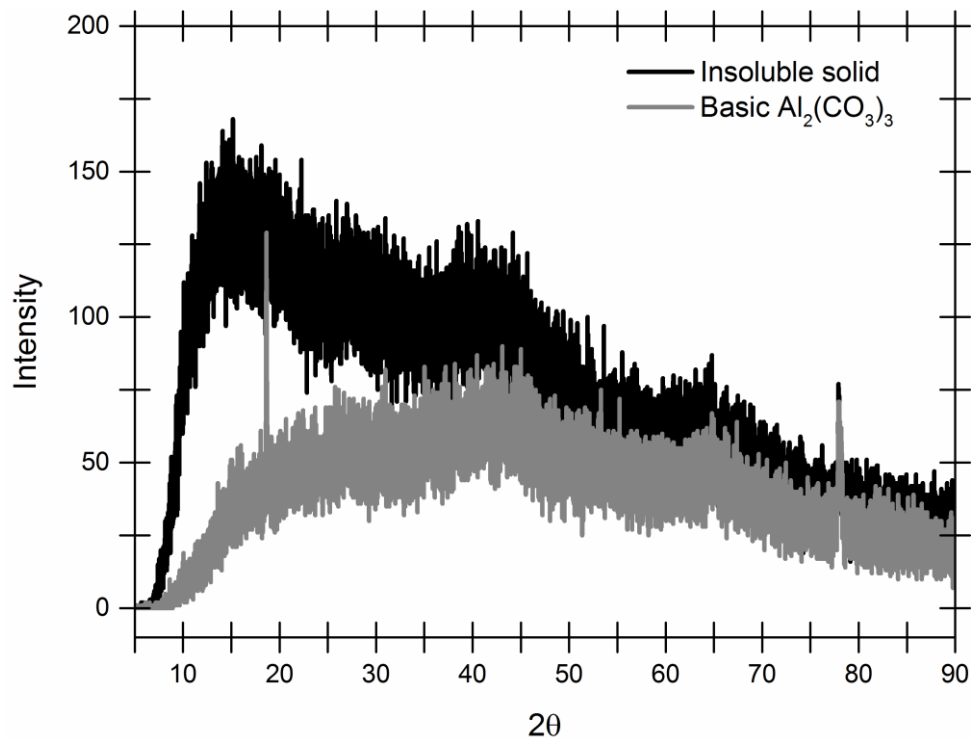
Figure 77: Powder XRD analysis of electrochemically formed solid after a cold water wash (black line) and commercial basic $Al_2(CO_3)_3$ (grey line).

(Figure 78 and Figure 79 respectively). This could be expected due to the thermal transition of $Al(OH)_{3(s)}$ when exposed to 100 °C (Figure 67).
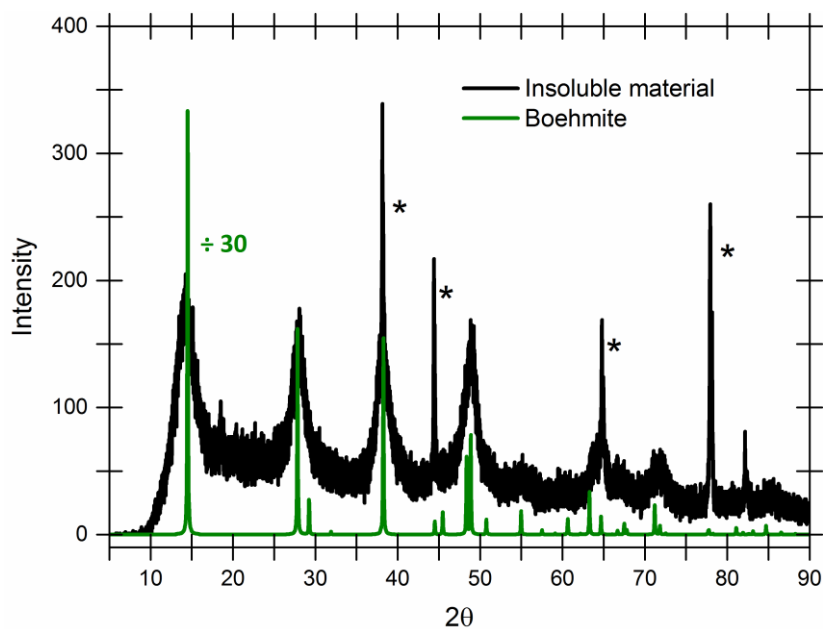
Figure 78: Powder XRD analysis of electrochemically formed solid after a hot water wash (black line) and boehmite (green line);[269-271] * signal from metal (Al) sample holder.
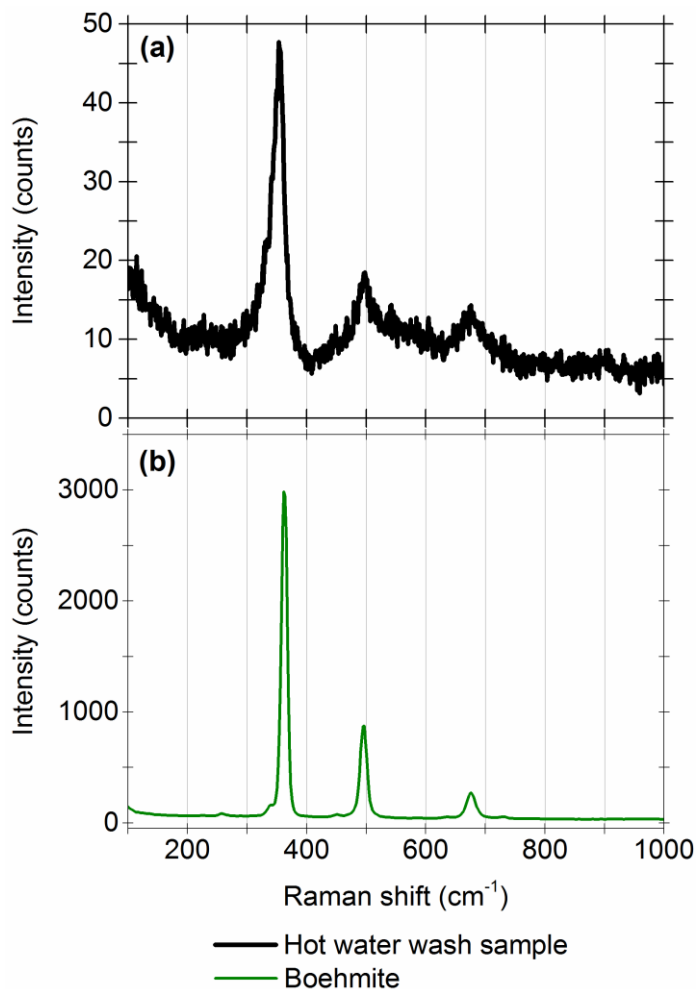
Figure 79: Raman analysis of a) solid isolated following a hot water wash and b) boehmite.[272]

The formation of boehmite at approx. 100 °C could be expected considering the phase transitions of aluminium oxide (Figure 67) and supported the powder XRD detection of corundum in the solid isolated after heating up to 1300 °C (Figure 66). This change in chemical composition of the aluminium species is further supported by SEM analysis, as the samples change from a smooth amorphous structure to a pore based structure (Figure 80). EDX analysis shows a decrease in the Al:O ratio, which can be expected in the transformation of $Al(OH)_3$ to γ-AlO(OH), as well as the removal of NaCl (Table 20).
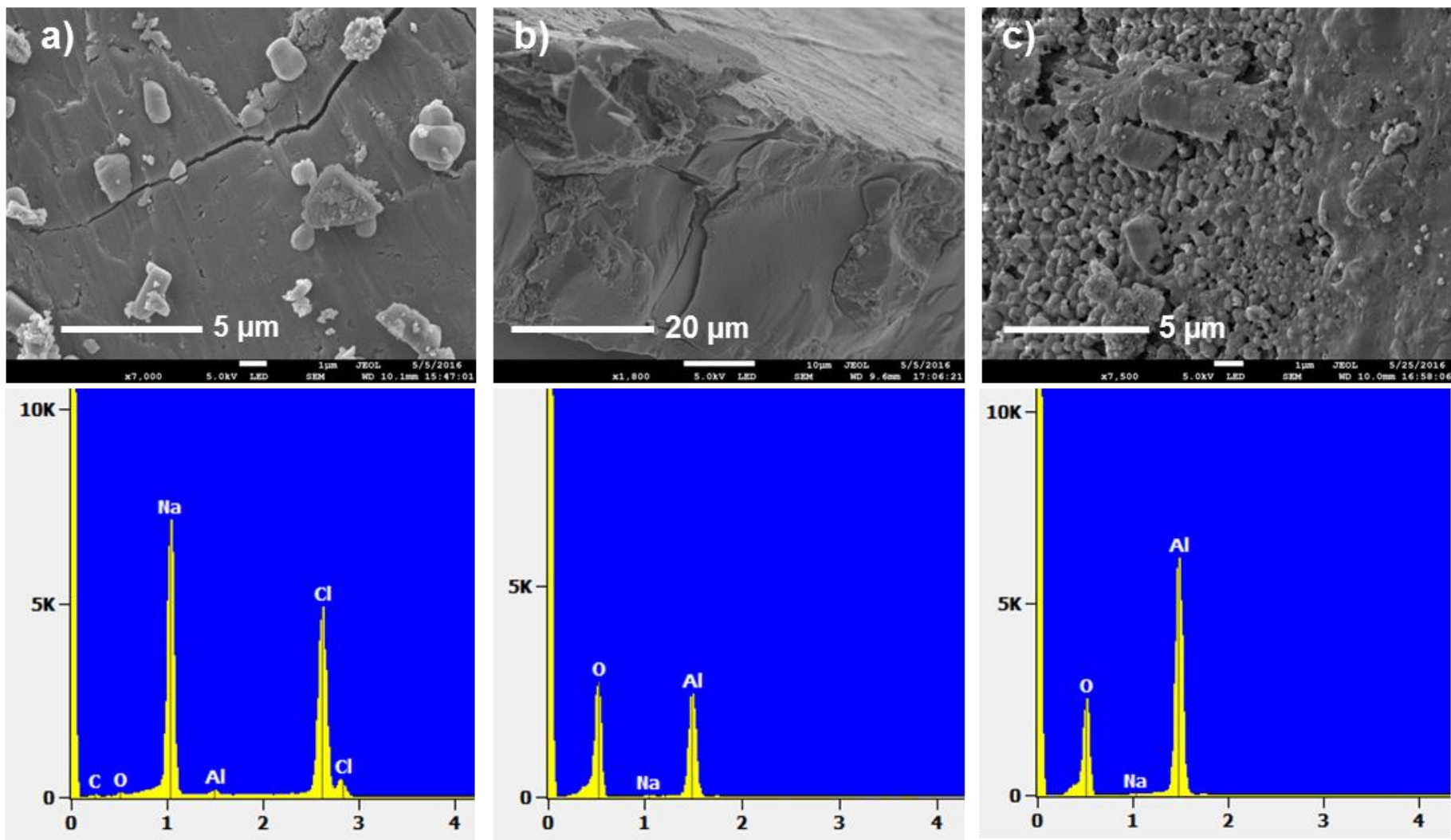
Figure 80: SEM imaging and EDX analysis of the a) unwashed, b) cold water washed and c) hot water washed samples with representative EDX spectra.

Table 20: SEM-EDX analysis of unwashed, cold and hot water washed samples.

Sample	Al:Na ratio[a]	Al:C ratio[a]	Al:O ratio[a]	Na:Cl ratio[a]
Unwashed, run 1[b]	75.75 ± 43.81	N/A	1.75 ± 0.75	1.23 ± 0.74
Unwashed, run 2[b]	1.35 ± 0.86	1.86 ± 2.42	4.22 ± 1.59	0.80 ± 0.23
Cold wash, run 1[b]	0.02 ± 0.005	0.15 ± 0.14	2.10 ± 0.58	N/A
Cold wash, run 2[b]	0.02 ± 0.003	0.02 ± 0.25	1.93 ± 0.32	N/A
Hot wash, run 1[b]	0.002 ± 0.001	N/A	1.25 ± 0.18	N/A
Hot wash, run 2[b]	0.02 ± 0.001	N/A	1.26 ± 0.23	N/A

a) Values are stated in a 1:XX manner, with the LHS element quoted in the ratio set as 1.
b) In each run, a different viewpoint of the sample was chosen and eight points along a diagonal line were analysed. The average values obtained from these eight runs are quoted.

3.2.8 Does Changing the Electrolyte Affect Mineralisation?

In order to investigate whether 1 M NaCl was the only electrolyte capable of performing CO_2 mineralisation in the graphite-aluminium anode cell, experiments were conducted using 1 M aqueous LiCl and 1 M aqueous CsCl as the electrolyte. These tests also gave constant CO_2 uptake and mineralisation during a 10 mA current-time period of 24 h, with similar electrode potentials and pH levels to those reported when using 1 M NaCl as electrolyte (Figure 81).

Using 1 M LiCl led to the unique case of a crystalline Layered Double Hydroxide (LDH) being formed. This was highlighted by powder XRD analysis, which detected a species similar to the structure of LDHs such as $LiAl_2(OH)_6Cl.H_2O$ or $LiAl_2(OH)_6Cl$ (Figure 82), changes in the FT-IR (DRIFT) spectrum (Figure 83) and the release of CO_2 at a higher temperature of approx. 275 °C (Figure 84). Using 1 M CsCl formed a heterogeneous mixture of crystalline CsCl and a secondary amorphous phase, in a similar manner to using 1 M NaCl as the electrolyte (Figure 85).

LDHs are crystalline anionic clays, composed of metal hydroxide sheets with metal cations coordinated to hydroxide ions in an octahedral geometry. Due to the combination of di-
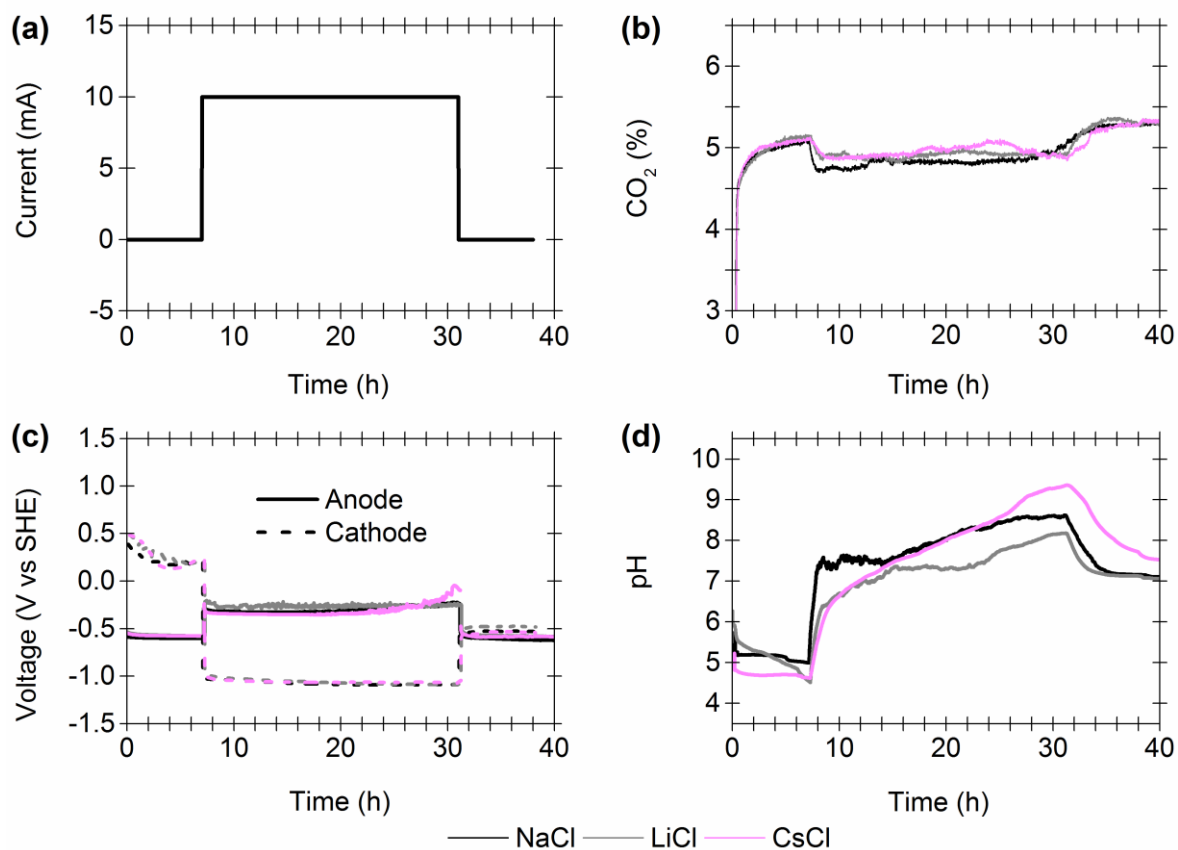
Figure 81: Effects of changing electrolyte in the graphite-aluminium anode cell. (a) Programmed current-time steps; (b) Carbon dioxide content in the exit gas stream; (c) Resultant changes to the electrochemical potential of the graphite-aluminium anode (solid line) and platinum cathode (dashed line); (d) Corresponding changes in solution pH. Other reaction conditions: a continuous gas flow of 0.7 mL min^{-1} CO$_2$ (5%) and 13.3 mL min^{-1} N$_2$, 60 mL of 1 M electrolyte.

and trivalent metal cations, or mono- and trivalent metal cations, in the structure, the positive charge is balanced by anions located between the metal cations in the interlayer region. LDHs therefore have the general structure of $[M^{z+}_{1-x}M^{3+}_{x}(OH)_2]^{m+}A^{n-}_{m/n} \cdot yH_2O$, where M^{2+} and M^{3+} are di- and trivalent metal cations respectively and A^{n-} is the interlayer anion.[273] In the majority of cases, z = 2, and the LDHs consist of divalent metal cations, such as magnesium and zinc, and trivalent cations, such as aluminium and chromium etc.[274-276] There is one unique case when z = 1, and in this example, lithium is the monovalent cation and only aluminium can be the trivalent metal cation. Lithium LDHs therefore have a general structure of $[LiAl_2(OH)_6]^+A^- \cdot H_2O$.[276] As lithium is the only
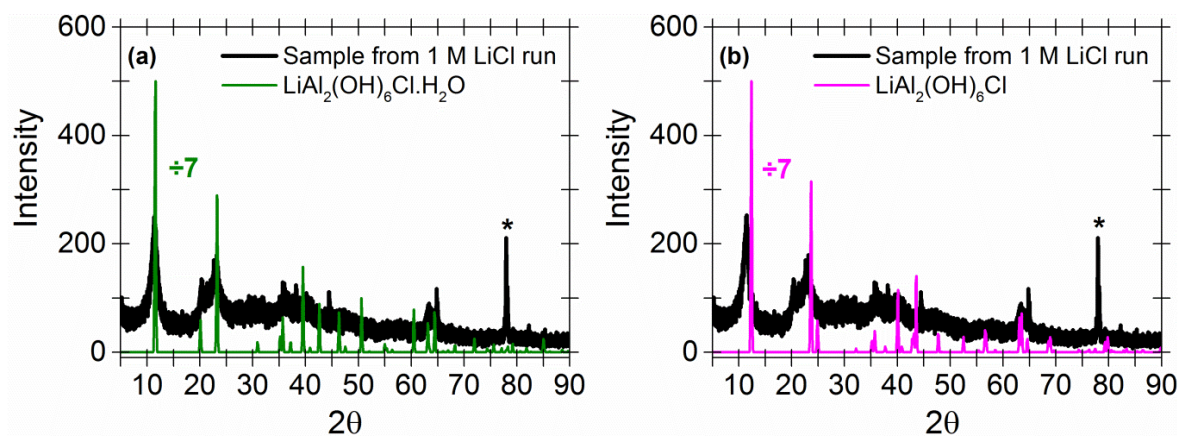
Figure 82: Comparing powder XRD spectra of electrochemically formed solid using 1 M LiCl (black line) with (a) $LiAl_2(OH)_6Cl.H_2O$ (grey line) and (b) $LiAl_2(OH)_6Cl$ (grey line) sample data;[277,278] * metal plate (Al) sample holder.
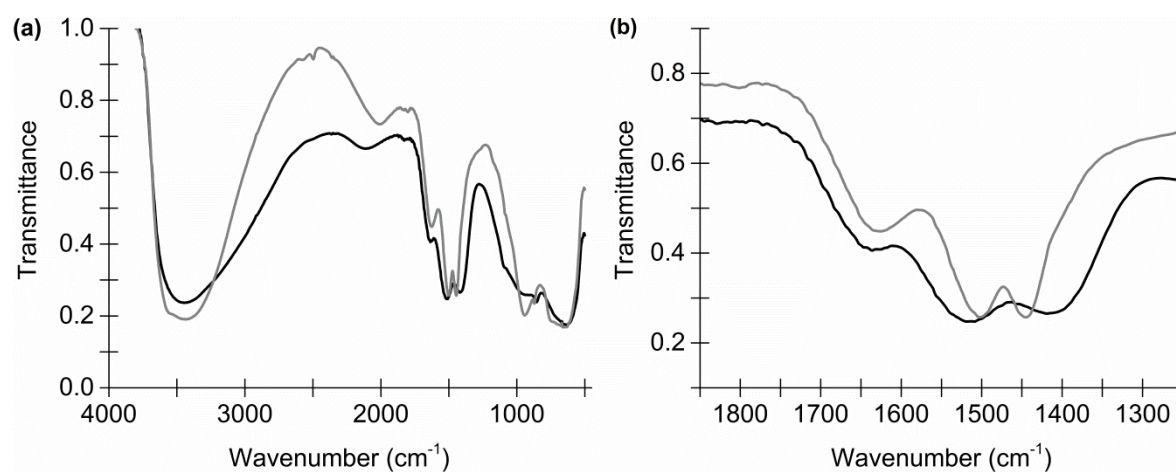
Figure 83: Comparing FT-IR (DRIFT) analysis of electrochemically formed solid using 1 M NaCl (black line) and 1 M LiCl (grey line). (a) Full spectrum; (b) Carbonyl stretch region.

monovalent metal that can form LDHs, this explains why no LDH based structure was reported when using NaCl or CsCl.[274-276,279] Lithium based LDHs have been reported to capture CO_2 as carbonate anions (CO_3^{2-}) in the interlayer region.[276,280-283] This could explain why a different CO_2 environment is detected via FT-IR analysis (Figure 83) and TGA-IR analysis (Figure 84).[276,280-282] LDH formation was supported further by solid state MAS NMR analysis, which detected environments consistent with a LDH structure (Figure 86). No ^{13}C signal is observed under conditions of cross-polarization. However a single-pulse spectrum reveals a signal at 169.5 ppm. Based on the shift and its absence under cross-polarization conditions this is assigned as belonging to a CO_3^{2-} moiety. A single ^7Li
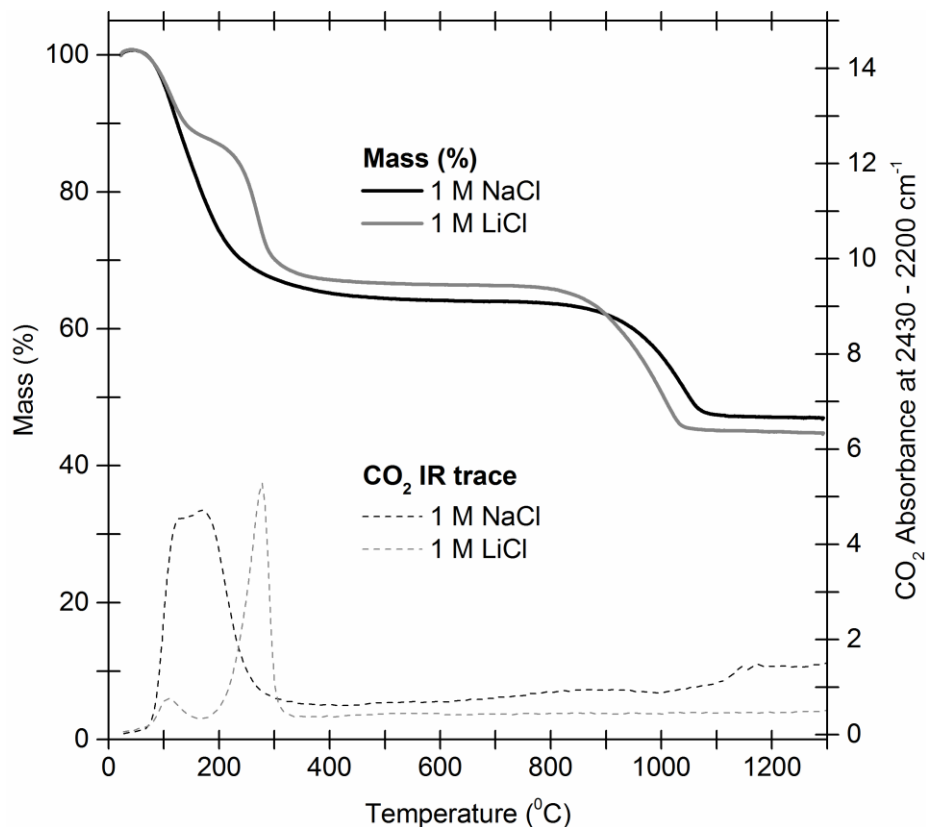
Figure 84: Comparing TGA-IR analysis of electrochemically formed solid using 1 M NaCl (black line) and 1 M LiCl (grey line) in the graphite-aluminium anode cell.
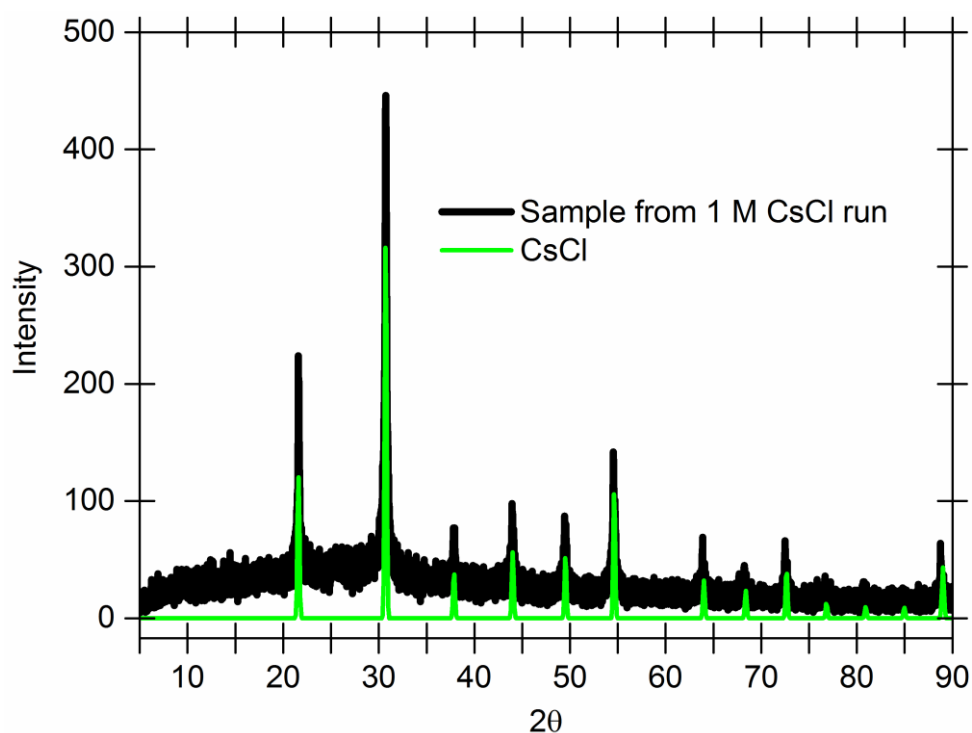
Figure 85: Powder XRD analysis of electrochemically formed solid using 1 M CsCl in the graphite-aluminium cell and CsCl.[278,284]

signal at 0 ppm is observed. The small chemical shift range of lithium in diamagnetic solids does not permit accurate estimate of the coordination number.[285] A single [27]Al signal centred about 7.8 ppm consistent with six-coordinate aluminium is observed. Both of these signals are consistent with the results observed for a related lithium layered double hydroxide.[275]
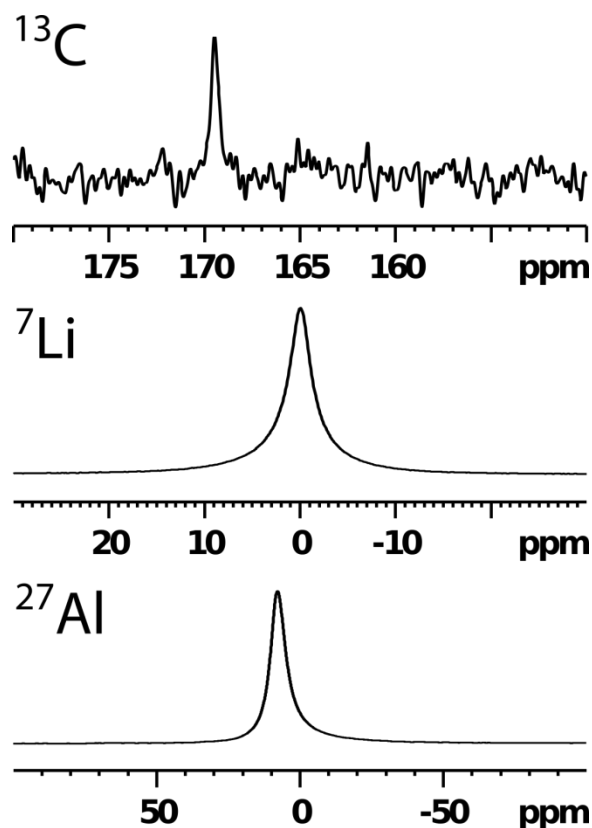
Figure 86: [13]C{[1]H} single-pulse, [7]Li and [27]Al MAS spectra of the electrochemically formed precipitate generated in a 24 h, 10 mA carbon capture experiment with 1 M LiCl in the graphite-aluminium anode cell.

Elemental analysis highlighted that the C:Al and C:Na ratios for the electrochemically formed solids changed slightly with electrolyte (Table 21). The C:Al ratio increased for the LiCl formed sample (1:6 vs 1:4), potentially due to the formation of a LDH, and was similar for the CsCl formed sample (1:4). This suggested that a similar aluminium and carbonate species was formed as in the standard NaCl experiments (Figure 55). The variance in C:Na ratios again suggested that a heterogeneous mixture was formed in each

case. The C:Na ratio was higher than expected for the CsCl experiment, and was potentially due to Na contamination.

Table 21: Quantification of carbon, sodium and aluminium in the solid formed post-CO_2 capture in the graphite-aluminium anode cell with 1 M LiCl and 1 M CsCl.[a]

1 M Electrolyte	Solid mass / g	C / mmol[b]	Na / mmol[c]	Al / mmol[c]
LiCl	0.34	0.4 ± 0.01	1.6 ± 0.1	2.3 ± 0.1
CsCl	0.96	0.8 ± 0.1	5.4 ± 0.1	3.4 ± 0.2

a) All molar values reported for carbon, sodium and aluminium detected in the solid post-CO_2 capture correspond to the <u>total</u> amount of carbon, sodium and aluminium in the <u>total</u> mass of solid collected respectively.
b) Quantified via TGA-IR analysis.
c) Quantified via ICP-MS analysis.

3.2.9 Solid Analysis Summary

All solid analysis indicated that an amorphous heterogeneous mixture is electrochemically formed as a consequence of CO_2 capture and mineralisation in the graphite-aluminium anode cell. The solids consist of amorphous aluminium hydroxycarbonate, aluminium hydroxide in the form of $Al(OH)_3$, and crystalline NaCl. It is hypothesised that the aluminium hydroxycarbonate species isolated is an amorphous form of the crystalline mineral Dawsonite ($NaAlCO_3(OH)_2$). Elemental quantification of the main species present suggests that $[Al(OH)_3]_3[NaAlCO_3(OH)_2]_1[NaCl]_{2-7}$ is isolated from the four experiments shown in Figure 55. Changing the electrolyte did not hinder CO_2 mineralisation, with 1 M LiCl leading to the novel synthesis of a LDH as part of the heterogeneous mixture. Carbon is trapped in the electrochemically formed solids as a result of CO_2 mineralisation, with carbon levels in the 0.4-1.1 mmol range (Table 22). When comparing the level of carbon captured using different electrolytes, the trend of carbon levels captured were NaCl ≈ CsCl > LiCl (Table 22). Carbon capture with 1 M LiCl and CsCl was only performed once, therefore the reproducibility and accuracy of these results are unknown.

Table 22: Quantification of carbon, sodium and aluminium in the solid formed post-CO_2 capture in the graphite-aluminium anode cell with 1 M NaCl, 1 M LiCl and 1 M CsCl.[a]

1 M Electrolyte	Solid mass / g	C / mmol[b]	Na / mmol[c]	Al / mmol[c]
NaCl, Run 1[d]	0.62	0.6 ± 0.1	7.2 ± 0.2	4.1 ± 0.4
NaCl, Run 2[d]	0.63	1.0 ± 0.2	6.2 ± 0.2	3.9 ± 0.2
NaCl, Run 3[d]	0.46	1.0 ± 0.1	3.4 ± 0.2	3.3 ± 0.3
NaCl, Run 4[d]	0.60	1.1 ± 0.1	8.4 ± 0.5	4.1 ± 0.4
NaCl average	0.58 ± 0.08	0.9 ± 0.2	6.3 ± 2.1	3.9 ± 0.4
LiCl	0.34	0.4 ± 0.01	1.6 ± 0.1	2.3 ± 0.1
CsCl	0.96	0.8 ± 0.1	5.4 ± 0.1	3.4 ± 0.2

a) All molar values reported for carbon, sodium and aluminium detected in the solid post-CO_2 capture correspond to the <u>total</u> amount of carbon, sodium and aluminium in the <u>total</u> mass of solid collected respectively.
b) Quantified via TGA-IR analysis.
c) Quantified via ICP-MS analysis.
d) The four runs correspond to the four experiments in Figure 55.

3.2.10 Carbon Quantification and Analysis of Electrolyte

After investigating the solid formed as a consequence of CO_2 mineralisation, research into analysing, and quantifying, the carbon levels in the electrolyte was performed, to determine the total level of carbon captured overall (in the solid and electrolyte) for each experiment. Carbon quantification was performed via titration methods (see "3.7 Methods and Experimental" for further details). The electrolyte isolated post-CO_2 capture, using 1 M NaCl in the graphite-aluminium anode cell (Figure 55), contains on average 1.9 mmol of carbon in the form of bicarbonate (Table 23). All errors quoted are standard deviation values. Similar carbon levels as bicarbonate were captured using CsCl (1.7 mmol), but lower levels were present in the case of LiCl (0.8 mmol). This could be due to the formation of an LDH affecting the ability of CO_2 to sequester into the electrolyte. No carbonate was detected as expected.

Table 23: Carbon levels in the electrolyte post-CO_2 capture in the graphite-aluminium anode cell.[a]

1 M Electrolyte	C / mmol[b]
NaCl, Run 1[c]	1.3 ± 0.1
NaCl, Run 2[c]	1.7 ± 0.1
NaCl, Run 3[c]	1.9 ± 0.1
NaCl, Run 4[c]	2.6 ± 0.1
NaCl average	1.9 ± 0.5
LiCl	0.8 ± 0.1
CsCl	1.7 ± 0.1

a) All molar values reported for carbon detected in solution post-CO_2 capture correspond to the <u>total</u> amount of carbon in the <u>total</u> volume of electrolyte.
b) Quantified via titration of electrolyte.
c) The four runs correspond to the four experiments in Figure 55.

To further prove bicarbonate was forming as a result of CO_2 capture, an electrolyte post-CO_2 capture was concentrated via freeze-drying to afford a white solid. Analysis of this solid via powder XRD showed it contained NaCl as a crystalline phase. TGA-IR analysis showed a bicarbonate environment is present, with a small mass loss of CO_2 occurring at approx. 110 °C, similar to $NaHCO_3$ (Figure 87). FT-IR (DRIFT) analysis showed the sample contains a near identical IR spectrum to $NaHCO_3$ (Figure 88). Sodium bicarbonate is therefore formed in the electrolyte during electrochemically driven CO_2 capture.

3.2.11 Energetics and Cost of CO_2 Capture

An important consideration was the energy required to drive CO_2 sequestration and mineralisation, as an ideal CCS process would have low energy requirements and thus low costs (Table 24). During CO_2 capture with 1 M NaCl in the graphite-aluminium anode cell, the average voltage of the platinum cathode was -1.13 V and the average graphite anode potential was -0.32 V, hence equating an average E_{Cell} value of 0.81 V. The electrical
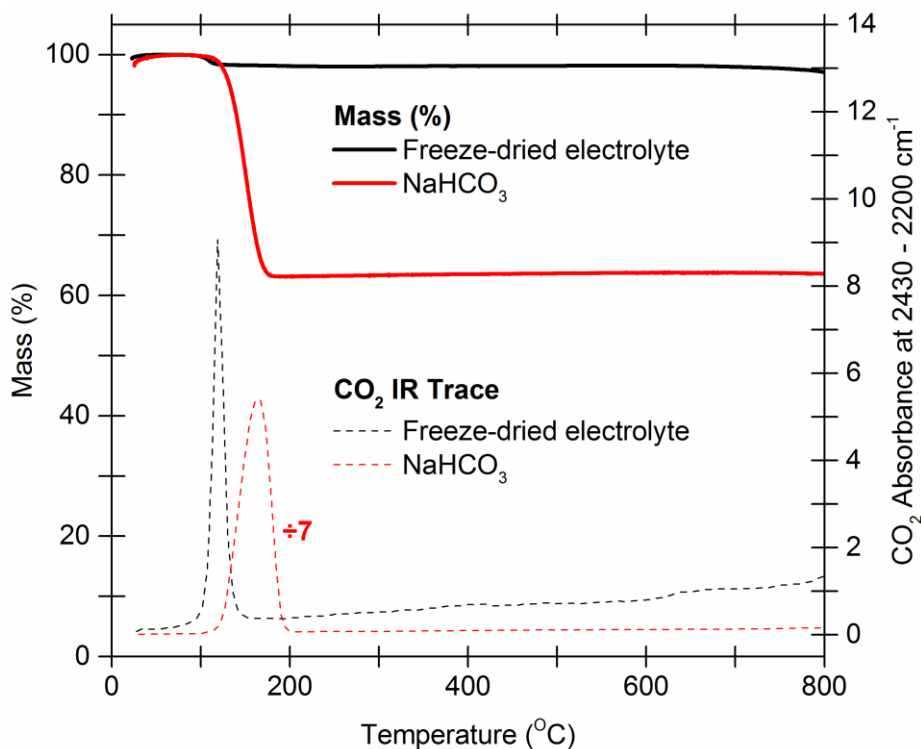
Figure 87: Comparing TGA-IR analysis of freeze-dried electrolyte post-CO_2 capture in the graphite-aluminium anode cell with 1 M NaCl (black line) and $NaHCO_3$ (red line).
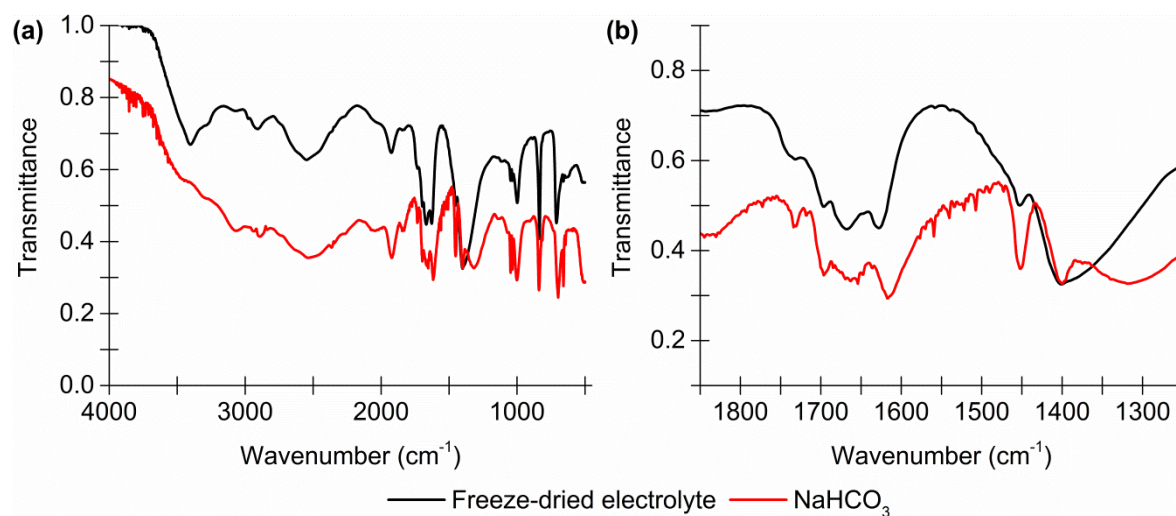
Figure 88: Comparing FT-IR (DRIFT) analysis of the freeze-dried electrolyte post-CO_2 capture in the graphite-aluminium anode cell (black line) with the spectra of $NaHCO_3$ (red line). (a) Full spectrum; (b) Carbonyl stretch region.

power (in W) was determined by Power = Voltage x Current (P = VI), therefore during the 24 h uptake period 8.1 mW of power was required, equivalent to 700 J. Considering, on average, a total of 2.8 ± 0.7 mmol of CO_2 was captured in the solid and electrolyte post-CO_2 capture, this translated to an average energy requirement of 250 kJ mol^{-1} (CO_2).

Table 24: Comparing energy requirements for carbon capture using 1 M NaCl, LiCl and CsCl and in the graphite-aluminium anode cell.

1 M Electrolyte	E_{Cell} [a] / V	E_{Cell} energy[b] / J	C total[c] / mmol	Energy of C capture[d] / kJ mol^{-1}
NaCl, Run 1[e]	0.76	657	1.9 ± 0.1	346
NaCl, Run 2[e]	0.87	753	2.7 ± 0.2	279
NaCl, Run 3[e]	0.80	693	2.9 ± 0.1	239
NaCl, Run 4[e]	0.81	696	3.7 ± 0.1	188
NaCl, average	0.81 ± 0.05	700 ± 40	2.8 ± 0.7	250
LiCl	0.80	695	1.2 ± 0.1	579
CsCl	0.72	618	2.5 ± 0.2	247

a) Difference between the graphite-aluminium anode and platinum cathode voltage.
b) The E_{Cell} value is converted into watts (watt = voltage x current). Watts are equivalent to J s^{-1}, therefore J s^{-1} x time of current application is equivalent to joules.
c) Combination of the total carbon captured in the total volume and mass of solution and solid respectively.
d) (E_{Cell}/1000) ÷ (C total/1000).
e) The four runs correspond to the four experiments in Figure 55.

Using 1 M LiCl and 1 M CsCl in the cell did affect carbon capture levels, as LiCl was more expensive to use and CsCl led to similar energy requirements compared to 1 M NaCl (Table 24). When comparing the total levels of carbon captured using different anodes, the mixed anode cell also captured the most carbon, and therefore had the lowest energy requirements for carbon, or CO_2, capture, no matter which electrolyte was used (Table 25).

Compared to current carbon capture and mineralisation methods, this new electrochemical method was fairly expensive (Table 26). Assuming that there is a linear relationship between E_{Cell} values and the total carbon captured, the costs of capturing a tonne of CO_2 using electricity would be US$267-618 (£219-507), using NaCl in the graphite-aluminium anode cell.[26,286] This is more expensive than currently employed methods, such as industrial mineralisation (Table 26). This methodology would therefore need to be improved and more cost-effective for large-scale carbon capture.

Table 25: Energy requirements for CO_2 capture using different anodes and NaCl.

Anode	E_{Cell}[a] / V	E_{Cell} energy[b] / J	C total[c] / mmol	Energy of C capture[d] / kJ mol^{-1}
Graphite anode	2.39	2065	1.4 ± 0.1[e]	1475
Aluminium anode	0.58	501	0.3 ± 0.02[f]	1670
Graphite-aluminium anode	0.81	700	2.8 ± 0.7[g]	250

a) Difference between the anode and platinum cathode voltage.
b) The E_{Cell} value is converted into watts (watt = voltage (V) x current (A)). Watts are equivalent to J s^{-1}, therefore J s^{-1} x time of current application is equivalent to joules.
c) Combination of the total carbon captured in the total volume and mass of solution and solid respectively.
d) (E_{Cell}/1000) ÷ (C total/1000).
e) Carbon captured in the electrolyte. No solid was formed.
f) Carbon captured in the electrochemically formed solid. No carbon was detected in the electrolyte.
g) Average C value obtained from the four experiments in Figure 55.

Table 26: Energy costs of CO_2 sequestration and mineralisation with 1 M NaCl in the graphite-aluminium anode cell.[26,286]

CCS system[a]	Cost range[b,c] / US\$ tCO$_2^{-1}$
Geological storage	0.5-8
Ocean storage	5-30
Capture from hydrogen or ammonia production	5-55
Capture from a coal- or gas-fired power plant	15-75
Mineralisation	50-100
This methodology	267-618[d,e]

a) Cost of CCS systems in 2005.
b) Costs have not been scaled according to inflation.
c) A conversion factor of £1 equals US\$1.22 was used. This was the average conversion for British pounds to American dollars over the year 2016 by 9th November 2016.
d) The energy required to capture a tonne of carbon in joules was converted to kWh (1 J = 2.78 x 10^{-7} kWh). Using the average cost of electricity in the UK between March 2015-2016,[286] which was 13.86 p per kWh, this energy value was then converted into a cost in £ and then US\$.
e) Range of results obtained from using NaCl, LiCl and CsCl as the electrolyte in the graphite-aluminium anode cell.

This novel electrochemical cell enables carbon capture as bicarbonate in solution and as a hydroxycarbonate species in a solid. It can however be argued that the only true carbon capture method is via mineralisation, as the solid in the carbon will remain under fairly stable conditions (unless heated over 100 °C as shown by TGA-IR analysis). The carbon

trapped in solution however is pH dependent, and therefore could be lost, or slowly evaporate over time. The extraction of the bicarbonate in solution as a solid, via freeze-drying or solvent evaporation, would undoubtedly add extra costs to the process and could even be perceived as wasteful in terms of energy. Dismissing the carbon captured in solution leads to less cost-effective carbon capture, for example the average carbon captured via mineralisation during the 24 h experiments (Figure 55) at 0.9 ± 0.2 mmol would require over three times more energy, 778 kJ mol^{-1} (CO_2) compared to 250 kJ mol^{-1} (CO_2), if the carbon captured in solution is not considered. The capture for carbon as bicarbonate solution however is vital to ensuring that carbon is mineralised in the first place, as a consequence of the electrochemical processes that occur in the graphite-aluminium mixed anode cell. Without CO_2 sequestration solid formation would not occur, hence all energetic calculations take carbon in solution and in the solid into account.

Another aspect to consider is how much hydrogen formation could offset the total cost of carbon capture. Hydrogen can be used as an alternative fuel, and therefore the enthalpy of combustion for hydrogen ($2H_{2(g)} + O_{2(g)} = 2H_2O_{(l)}$) at 286 kJ mol^{-1} means that 326 J of energy is saved by producing hydrogen using the graphite-aluminium anode cell (considering the cell on average produces 0.14% of H_2). The energetic costs of running the electrochemical cell is 700 J, when a 10 mA (0.01 A) current is applied for 24 h and a difference of 0.81 V is measured between the electrodes. When hydrogen combustion is considered, the energetic requirement decreases to 374 J. Considering the cell on average captures 2.8 ± 0.7 mmol of carbon, this would equate to only 134 kJ mol^{-1} (CO_2) compared to 250 kJ mol^{-1} (CO_2). Hydrogen formation therefore can decrease the costs of carbon capture by approx. 46%. It is also worth noting that if the cell was maximised to achieve 100% Faradaic efficiency of H_2 formation was achieved, the enthalpy of combustion would equate to 1280 J of energy, and therefore the energetic requirements to power the

cell would became negative (-580 kJ mol^{-1} of CO_2) and change the process from endothermic to exothermic.

3.2.12 The Electrochemical Process and Mechanism

The detection of hydrogen suggests that the cathodic process is hydrogen formation (Equation 1, Figure 89). The formation of a solid and consideration of the Pourbaix diagram for aluminium (Figure 47) suggests that the anodic process is aluminium oxidation (Equation 2, Figure 89). The net cell reaction can therefore be expressed as $2Al + 6H_2O \rightarrow 3H_2 + 2Al(OH)_3$ (Equation 3, Figure 89).

$$2H^+ + 2e^- \rightleftharpoons H_{2(g)} \qquad (1)$$

$$Al + 3H_2O \rightleftharpoons Al(OH)_3 + 3H^+ + 3e^- \quad (2)$$

$$2Al + 6H_2O \rightleftharpoons 3H_2 + 2Al(OH)_3 \qquad (3)$$
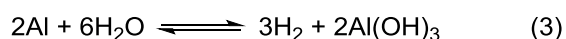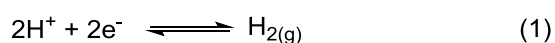
Figure 89: The cathodic and anodic process, and net reaction, occurring in the graphite-aluminium anode electrochemical cell.

By using the Nernst Equation, the electrode potential for hydrogen formation under experimental conditions is -0.49 V (at 1 bar, pH 8 and 34 °C).[234,235] The electrode potential for aluminium oxidation under experimental conditions can also be calculated as -2.02 V at pH 8.[243] The overall cell potential for this reaction is therefore +1.53 V. The positive potential also dictates that this reaction is spontaneous. The E_{Cell} value (and experimental potential of the mixed anode) both indicate that $Al(OH)_{3(s)}$ or $Al(H_2O)_3(OH)_{3(s)}$ formation is plausible, in accordance with the Pourbaix diagram (Figure 47).[230,243]

After analysing the solid formed, the anodic and cathodic process, and the carbon species present in the electrolyte, post-CO_2 capture, an electrochemical mechanism was proposed. The graphite-only anode operates via a non-Faradaic process, with the formation of an EDL, whereas the aluminium-only anode simply led to the corrosion of aluminium.[230] It appears that the unique mixed anode material was required for low-power CO_2 sequestration and mineralisation. We attribute the low power, continual CO_2 uptake demonstrated by the graphite-aluminium anode cell to the combined anode processes of

both EDL formation and aluminium oxidation. Upon initially applying the 10 mA current it was assumed that the pH-neutral anodic charging process was balanced by the immediate catalysis of proton reduction at the platinum cathode, so that overall an increase in solution pH was observed. This in turn led to an increase in the concentration of bicarbonate in solution.[186,238,239] Since the ratio of electrons to protons in the aluminium oxidation reaction equals that of the platinum-catalysed H_2 production reaction, the pH ultimately stabilizes between 8 and 9. Aluminium oxidation then commences at the anode, creating a low anode potential and generating aluminium hydroxide, a material which has previously been shown to adsorb CO_2, thus yielding a heterogeneous mixture of amorphous aluminium hydroxycarbonate,[252] aluminium hydroxide and crystalline NaCl (with a composition of $[Al(OH)_3]_3[NaAlCO_3(OH)_2]_1[NaCl]_{2-7}$). Hence the creation of the mixed anode cell creates a temporal separation of the two anodic processes, thus enabling CO_2 sequestration and mineralisation to occur. An electrochemical mechanism occurring when using 1 M NaCl in the graphite-aluminium anode cell was therefore proposed (Figure 90).
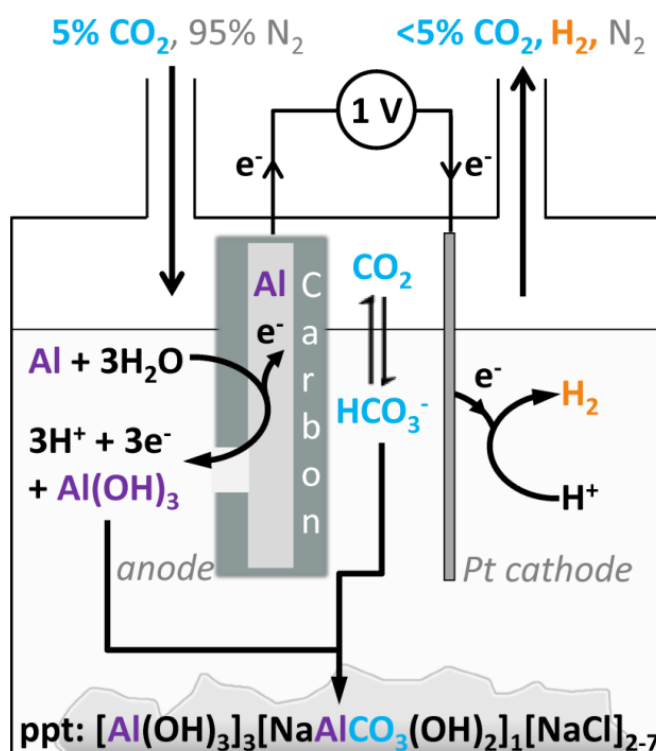
Figure 90: Proposed electrochemical process leading to CO_2 sequestration and mineralisation with 1 M NaCl in the graphite-aluminium anode cell.

3.2.13 Data Summary

A summary of the key results obtained by promoting electrochemical CO_2 capture with 1 M NaCl in the mixed anode cell, and analysis of the solid as a result of CO_2 mineralisation, are summarised in 4.2 Appendix 2, Section 4.2.3. An overall data summary is illustrated in Figure A6. Elemental analysis of the electrochemically formed solids obtained with different electrolytes, as well as levels of carbon captured in the electrolyte and solid, are summarised in Table A7. The energy requirements for carbon capture with different anodes in the electrochemical cell and electrolytes are summarised in Table A8.

3.3 Conclusion

The mixed graphite-aluminium anode, used as a novel electrochemical component, offers a unique CO_2 capture technology, that enables a temporal separation of the anode and cathode processes and in turn CO_2 sequestration and mineralisation with simultaneous H_2 production. The graphite was vital for EDL formation whilst the sacrificial aluminium anode enabled low power CO_2 mineralisation via aluminium oxidation. The absence of graphite or aluminium created an inefficient CO_2 capture method and high power process, respectively. The solid formed as a consequence of CO_2 mineralisation is an amorphous heterogeneous mixture of aluminium hydroxycarbonate, aluminium oxide and crystalline NaCl, with an proposed average composition of $[Al(OH)_3]_3[NaAlCO_3(OH)_2]_1[NaCl]_{2-7}$. Using 1 M LiCl leads to the unique case of LDH formation. The energy required for capturing carbon varied with different anodes and electrolytes, with the lowest energy range reported as 247-250 kJ mol^{-1} (CO_2). Sodium chloride is table salt, and therefore this electrolyte may be more beneficial to use than LiCl and CsCl, due to its greater global availability.

In order for this novel cell to have any potential as a future CCS method, the energy required to capture the amount of aluminium in the electrochemically formed solid, as a result of CO_2 mineralisation, must be lower than the energy required to recycle the same

amount of aluminium. In this method, the average amount of aluminium captured in the mineralised solid (using 1 M NaCl in the graphite-aluminium cell with a 10 mA current over 24 h) is 3.9 mmol of aluminium (4.2 Appendix, Section 4.2.3, Table A7). The average amount of carbon captured under the same conditions is 2.8 mmol of CO_2 (4.2 Appendix, Section 4.2.3, Table A8). Therefore, 3.9 mmol of aluminium is required to capture 2.8 mmol of CO_2, at an energetic cost of 700 J and 250 kJ mol^{-1} of CO_2 (4.2 Appendix, Section 4.2.3, Table A8). If the electrochemical method used a tonne of aluminium, this would correspond to 6.7 GJ of energy to capture 1.2 tonnes of CO_2, if CO_2 capture increases linearly with energy input. Recycling aluminium requires 10 GJ of energy per tonne of aluminium.[287,288] Thus, our electrochemical CO_2 mineralisation method requires 33% less energy than conventional aluminium recycling and has the added benefit of capturing CO_2.

Amine scrubbing is currently the state-of-the-art CCS method, and requires 4215 kJ of energy to capture 1 kg of CO_2 (with 30% w/w MEA).[173] Our method (using 1 M NaCl in the graphite-aluminium anode cell with a 10 mA current over 24 h) would require 5681 kJ to capture 1 kg of CO_2. This methodology is therefore currently not as energy effective as MEA, but can hopefully be improved further in the future.

At this method's current capability, the amount of CO_2 captured over a 24 h period, would only equate to 3.5 x 10^{-14} % of the total global carbon available in the atmosphere today.[14] Considering that CO_2 emissions are a huge problem, and that 0.095 Gt of CO_2 were emitted every day in 2015, this low number is not surprising.[159] In 2014, all of the CO_2 used for chemical production only accounted for, or removed, 0.63% of total CO_2 emissions in the same year.[14,33] Aiming for this method to be the sole "magic answer" for capturing and reducing global CO_2 emissions is therefore unrealistic. Improving this method and using it with other techniques, to make it part of the overall solution towards reducing CO_2 emissions, however could be worthwhile.

3.4 Results and Discussion Part 2: Promoting Cost-effective and Sustainable Electrochemical CO_2 Capture and Mineralisation

As discussed in "3.2 Part 1: Performing Electrochemical CO_2 Sequestration and Mineralisation", it was established that a novel graphite-aluminium anode cell could perform low power CO_2 sequestration and mineralisation, and an amorphous heterogeneous solid composed of amorphous aluminium hydroxycarbonate, aluminium hydroxide and crystalline NaCl was formed. Hydrogen was also formed as a valuable by-product. At this stage, this electrochemical CCS technique could be considered fairly "green", as it can function with environmentally friendly and innocuous chemicals, such as table salt (NaCl), and produces non-toxic by-products. This methodology already satisfies some Green Chemistry prinicples,[31] such as the use of "*innocuous*" solvents, it can be "*conducted at near ambient temperature and pressure*" and "*generates substances which possess little or no toxicity to human health and the environment.*" Further research into obeying the principle of "*energy requirements……..should be minimised*" was still a must.

In the initial studies, this methodology required substantial energy for CO_2 capture (247-579 kJ mol^{-1} of CO_2) and was therefore fairly expensive compared to other CCS methodology (US$267-618 per tonne of CO_2 respectively). This was a consequence of capturing low levels of carbon (1.2-2.8 mmol) and using electricity, which is an expensive form of energy. From 2005 to 2014, the cost of using electricity in industry increased by approx. 154%, from £37 to £94 per MWh of electricity.[289] Electricity is not currently a carbon neutral energy source,[191,290] as in 2015, 61% and 75% of electricity used by Organisation for Economic Cooperation and Development (OCED) member and non-member countries came from the combustion of fossil fuels and bio-fuels.[289] The decarbonisation of electricity will increase in the future, with the UK aiming to decarbonise electricity extensively by 2050,[290] but current methods of electricity generation cannot be ignored. With this in-mind, a few research aims were set in an

attempt to further improve the cost-efficiency and sustainability of this electrochemical method. 1) Change reaction variables to see if similar levels, or more, carbon can be captured with less energy and therefore at a lower cost; 2) study the ability to use renewable energy to drive CO_2 capture and 3) investigate if this methodology could work with sustainable reagents and with similar energy requirements.

Although different electrolytes and anode cells had been evaluated for CO_2 sequestration and mineralisation, the effect of changing reaction conditions on carbon capture, such as current, reaction time and reaction temperature, remained unexplored. The outcomes from these studies are considered in "3.4.1 Changing Reaction Conditions". Although the majority of electricity is generated by fossil fuel combustion, electricity can be generated using renewable energy sources such as wind, tidal and solar energy. It was hypothesised that using solar-derived electricity could perform CO_2 mineralisation with a low carbon footprint, therefore experiments powered with a solar panel were performed. Using an aqueous solution of 1 M NaCl can be seen as a concentrated and simplified mimic of seawater,[291] therefore could natural seawater be used as the electrolyte? The aluminium block was vital for low power CO_2 mineralisation. Aluminium is one of the most sustainable elements in the world today and is the most abundant metal in the Earth's crust, accounting for around 8% of Earth's core mass.[5] Aluminium is also one of the most recycled elements, and in 2013, 46% of global aluminium production came from 24 million tonnes of recycled aluminium.[292] The ability to use recycled, or "waste", aluminium as a replacement for the aluminium block and still promote CO_2 mineralisation was therefore investigated. The combination of seawater and "waste" aluminium for simultaneous for CO_2 capture and mineralisation was also explored. All of these variables were examined further in "3.4.2 Improving Sustainability with Renewable Energy and Sustainable Materials". The energetics and cost as a result of changing reaction conditions and using sustainable materials, as well as solid analysis, is detailed in "3.4.3 Carbon Dioxide Mineralisation" and "3.4.4 Energetics and Costs".

3.4.1 Changing Reaction Conditions

Changing Temperature

Low-grade, or "waste", heat (30-250 °C) is often produced by large-scale industrial processes, and thus can be freely available to utilise in power stations and chemical processing plants. The prospective of using low-grade heat to drive this electrochemical methodology was intriguing and could be a possibility in future industrialisation. Under standard conditions the temperature of the cell would measure between 32-35 °C and reach an average temperature of 34 °C after 1 h. An experiment was conducted with the cell heated consistently at 60 °C, to see if 1) this would affect the carbon capture capability of the cell and 2) change the electrode potentials and therefore the energy cost of the process (Figure 91).

Carbon dioxide sequestration and mineralisation was still possible at 60 °C and in terms of reaction variables, such as changes in CO_2 levels, anodic voltages and pH levels, no major differences were seen (Figure 91). However, the platinum cathode potential (Figure 91c) was higher than typically reported at 32-35 °C (-0.94 V vs -1.13 V). The cathodic voltage was still capable of H_2 formation with an overpotential of 0.41 V (equilibrium cathode potential is -0.94 V and $E(2H^+/H_2)$ estimated as -0.53 V under experimental conditions using the Nernst equation and 1 bar of H_2).[189,234-236] Increasing the temperature therefore did not change the intrinsic electrochemical mechanism, and could lower the E_{Cell} value required for electrochemical CO_2 capture. Lower levels of carbon are, however, trapped in the electrolyte and solid post-CO_2 capture (1.8 mmol, Table 27) as CO_2 solubility decreases in water at higher temperatures.[293,294] This process with an E_{Cell} value of 0.52 V constituted an energy requirement of 453 J for the electrochemical process, and 252 kJ mol^{-1} (CO_2) for carbon capture. Higher temperatures therefore offer no energetic benefits to electrochemical carbon capture. FT-IR (DRIFT) analysis demonstrated that a similar solid was isolated regardless of temperature (Figure 92).
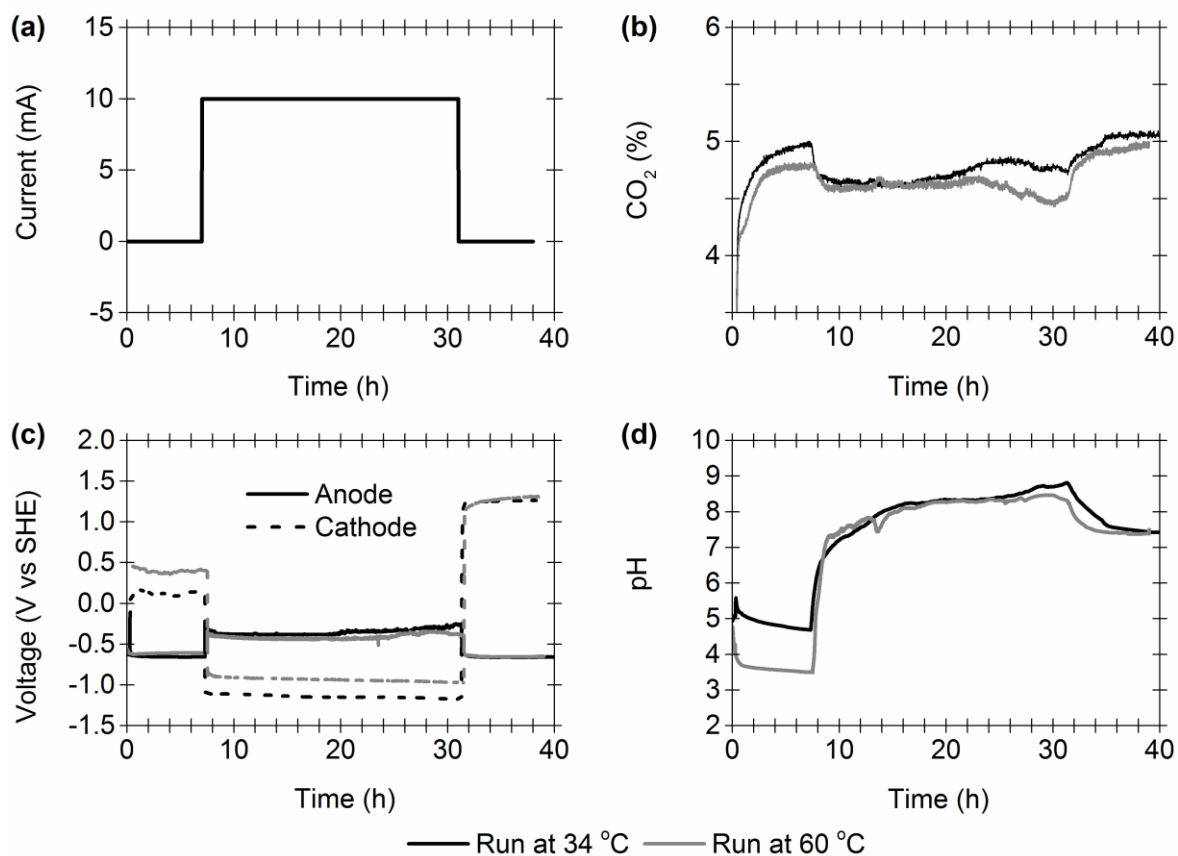
Figure 91: Effect of changing temperature on the electrochemical CCS process. (a) Programmed current-time steps; (b) Carbon dioxide content in the exit gas stream; (c) Resultant changes to the electrochemical potential of the anode (solid line) and cathode (dashed line); (d) Corresponding changes in solution pH. Other reaction conditions: a continuous gas flow of 0.7 mL min^{-1} CO$_2$ (5%) and 13.3 mL min^{-1} N$_2$, 60 mL of 1 M NaCl.

Table 27: Effect of temperature on carbon levels trapped in the electrolyte and isolated precipitate post-CO$_2$ capture with 1 M NaCl in the graphite-aluminium anode cell.[a]

Temperature[b] / °C	Solid mass / g	C in solid[c] / mmol	C in solution[d] / mmol	C total[e] / mmol
34	$0.58 \pm 0.08^{\text{f}}$	$0.9 \pm 0.2^{\text{f}}$	$1.9 \pm 0.5^{\text{f}}$	2.8 ± 0.7
60	0.39	0.3 ± 0.01	1.5 ± 0.1	1.8 ± 0.1

a) All molar values reported for carbon detected in the solid and solution post-CO$_2$ capture correspond to the total amount of carbon in the total volume of electrolyte and total mass of solid, respectively.
b) Average temperature of stirrer hotplate on which the graphite-aluminium anode cell was placed.
c) Quantified via TGA-IR analysis.
d) Quantified via titration of electrolyte.
e) Combination of carbon in solution and solid.
f) Average values obtained from the four 24 h current-time experiments in Figure 55.
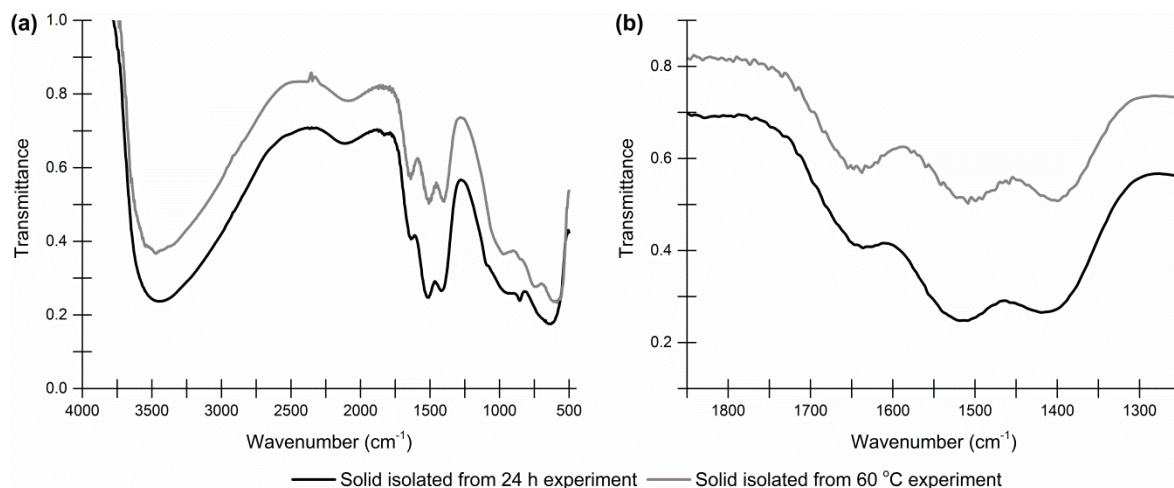
Figure 92: FT-IR (DRIFT) analysis of electrochemically formed solids, when applying a 10 mA current for 24 h and 36 h, with 1 M NaCl in the graphite-aluminium anode cell. (a) Full spectrum; (b) Carbonyl stretch region.

Changing Current: Current Setting

In "3.2 Part 1: Performing Electrochemical CO_2 Sequestration and Mineralisation", only a 10 mA current flow from the anode to the cathode was tested in this electrochemical process. It was therefore unknown if a higher or lower current could perform more efficient CO_2 capture. This was investigated by applying 5 h bursts of 5 mA, 10 mA and 15 mA respectively to the graphite-aluminium anode cell, whilst 10.7% CO_2 was flowing through the cell, with 5 h "off" periods between each current step (Figure 93).

Changing the current setting highlighted that using more powerful currents led to greater changes in CO_2 levels, as a 5, 10 and 15 mA current led to a 0.15%, 0.41% and 0.53% change in CO_2 levels respectively. A 15 mA current may cause a greater drop in CO_2 levels but at an increased energetic cost; as Ohm's law dictates that current is proportional to voltage, (voltage = current x resistance) and the power law equation states that power increases with current or voltage (P = VI).[295] The 10 mA current already employed in standard experiments was deemed suitable to use for future experiments, as this would create a greater change in CO_2 levels compared to a 5 mA current and require less energy than a 15 mA current.
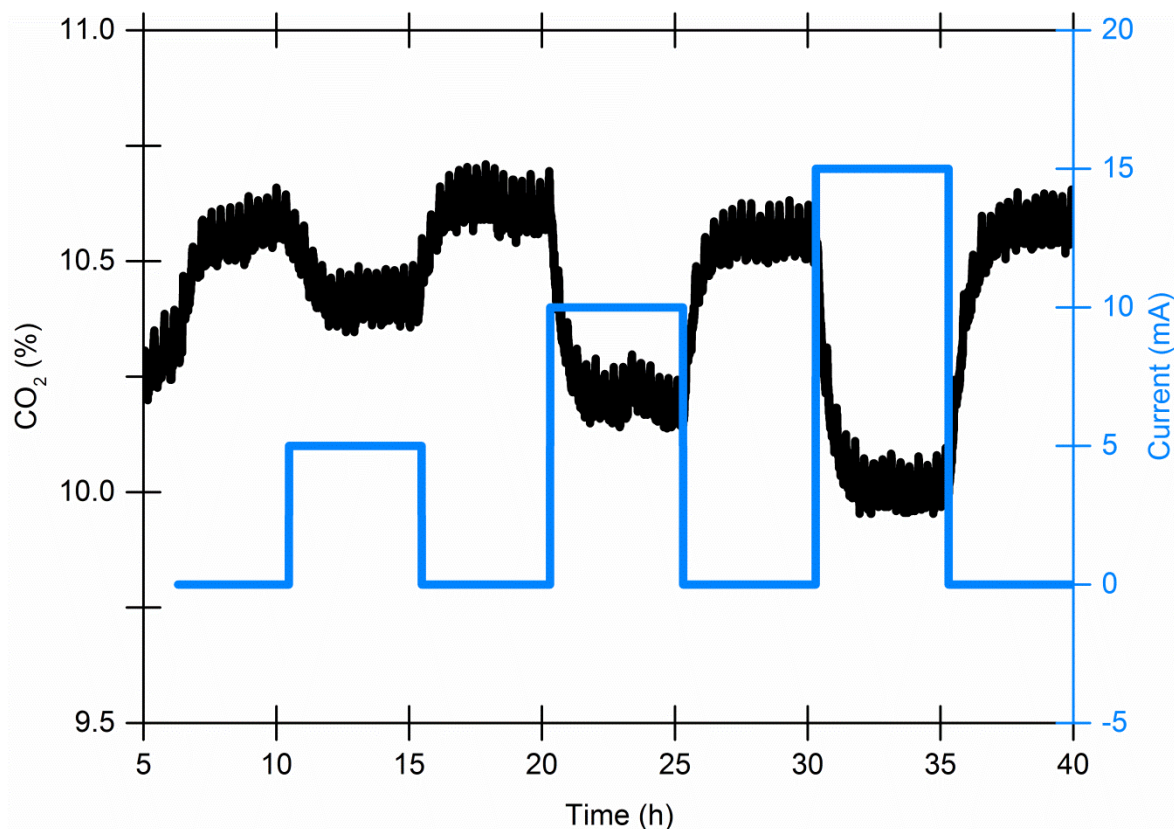
Figure 93: Investigating changes in CO_2 levels (black line) when flowing a current of 5, 10 and 15 mA (blue line) through the graphite-aluminium anode cell. Other reaction conditions: a continuous gas flow of 1.5 mL min^{-1} CO_2 (10.7%) and 12.5 mL min^{-1} N_2, and 60 mL of 1 M NaCl.

Changing Current: Length of Current Step

In standard experiments performed in "3.2 Part 1: Performing Electrochemical CO_2 Sequestration and Mineralisation", the 10 mA current was always applied over a 24 h period. It was therefore unknown whether increasing or decreasing the current-time period would improve or worsen carbon capture. Three separate experiments were therefore performed in which a 10 mA current was applied for 36 h (Figure 94). All reaction variables, such as CO_2 levels (Figure 94b), anodic and cathodic potentials (Figure 94c), pH levels (Figure 94d), and therefore the electrochemical mechanism, remained unchanged compared to the 24 h current-time experiments (Figure 49 and Figure 55) and were reproducible. Increasing the length of current-time step had some advantageous outcomes, as the total level of carbon captured via sequestration and mineralisation increased (4.7 mmol, Table 28) indicating that a 24 and 36 h current-time period did not reach the
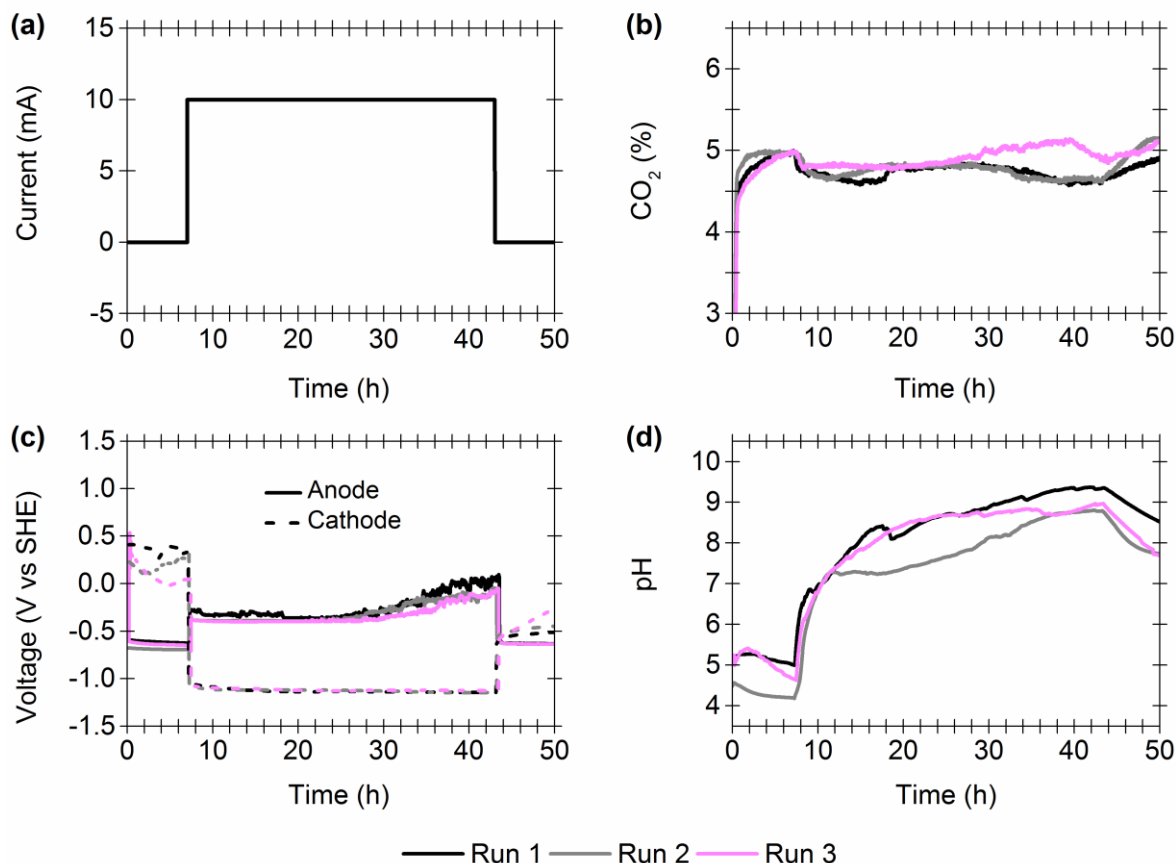
Figure 94: Overlay of repeat CO_2 capture experiments with 1 M NaCl in the graphite-aluminium anode cell with a 10 mA current flow applied over 36 h. (a) Programmed current-time steps; (b) Carbon dioxide content in the exit gas stream; (c) Resultant changes to the electrochemical potential of the anode (solid line) and cathode (dashed line); (d) Corresponding changes in solution pH. Other reaction conditions: a continuous gas flow of 0.7 mL min^{-1} CO_2 (5%) and 13.3 mL min^{-1} N_2, and 60 mL of 1 M NaCl.

carbon capture limits of this methodology. Overall the energy required to perform carbon capture (Table 29) was similar to applying a current for 24 h (231 vs 250 kJ mol^{-1} of CO_2), indicating that increasing the length of the current-time step could capture more carbon without higher capture costs. No major differences also occurred in the C:Al and C:Na ratios of the solids, and obtained similar FT-IR (DRIFT) spectra, indicating that the same solid was isolated (Figure 95).

Table 28: Carbon captured by varying the duration of the 10 mA current-time step.[a]

Electrolyte	Solid mass / g	Na in solid[b] / mmol	Al in solid[b] / mmol	C in solid[c] / mmol	C in solution[d] / mmol	C total[e] / mmol
NaCl, Run 1[f]	0.87	10.3 ± 0.2	5.5 ± 0.4	1.6 ± 0.1	2.9 ± 0.1	4.5 ± 0.1
NaCl, Run 2[f]	0.57	6.3 ± 0.2	5.3 ± 0.2	0.6 ± 0.02	4.2 ± 0.1	4.8 ± 0.1
NaCl, Run 3[f]	0.78	8.3 ± 0.2	6.2 ± 0.3	0.9 ± 0.1	3.9 ± 0.1	4.8 ± 0.1
NaCl, 36 h average	0.74 ± 0.15	8.3 ± 2.0	5.7 ± 0.5	1.0 ± 0.2	3.7 ± 0.7	4.7 ± 0.2
NaCl, 24 h Average[g]	0.58 ± 0.08	6.3 ± 2.1	3.9 ± 0.4	0.9 ± 0.2	1.9 ± 0.5	2.8 ± 0.8

a) All molar values reported for sodium, aluminium and carbon detected in the solid and carbon in the solution post-CO_2 capture, correspond to the total moles of sodium aluminium and carbon in the total mass of solid and the total amount of carbon in the total volume of electrolyte, respectively.
b) Quantified via ICP-MS analysis.
c) Quantified via TGA-IR analysis.
d) Quantified via titration of electrolyte.
e) Combination of carbon in solution and solid.
f) The three runs correspond to the 36 h current-time experiments in Figure 94.
g) Average results obtained from the four 24 h current-time experiments in Figure 55.

Table 29: Energy requirements for carbon capture when varying the duration of the 10 mA current-time step.

Electrolyte	E_{Cell}[a] / V	E_{Cell} energy[b] / J	C total[c] / mmol	Energy of C capture[d] / kJ mol^{-1}
NaCl, Run 1[e]	0.89	1151	4.5 ± 0.1	256
NaCl, Run 2[e]	0.83	1076	4.8 ± 0.1	224
NaCl, Run 3[e]	0.80	1033	4.8 ± 0.1	215
NaCl, 36 h average	0.84 ± 0.05	1087 ± 60	4.7 ± 0.2	231
NaCl, 24 h average[f]	0.81 ± 0.05	700 ± 40	2.8 ± 0.7	250

a) Difference between the graphite-aluminium anode and platinum cathode voltage.
b) The E_{Cell} value is converted into watts (watt = voltage x current). Watts are equivalent to J s^{-1}, therefore J s^{-1} x time of current application is equivalent to joules.
c) Combination of carbon in solution and solid.
d) (E_{Cell}/1000) ÷ (C total/1000).
e) The three runs correspond to the 36 h current-time experiments in Figure 94.
f) Average results obtained from the four 24 h current-time experiments in Figure 55.
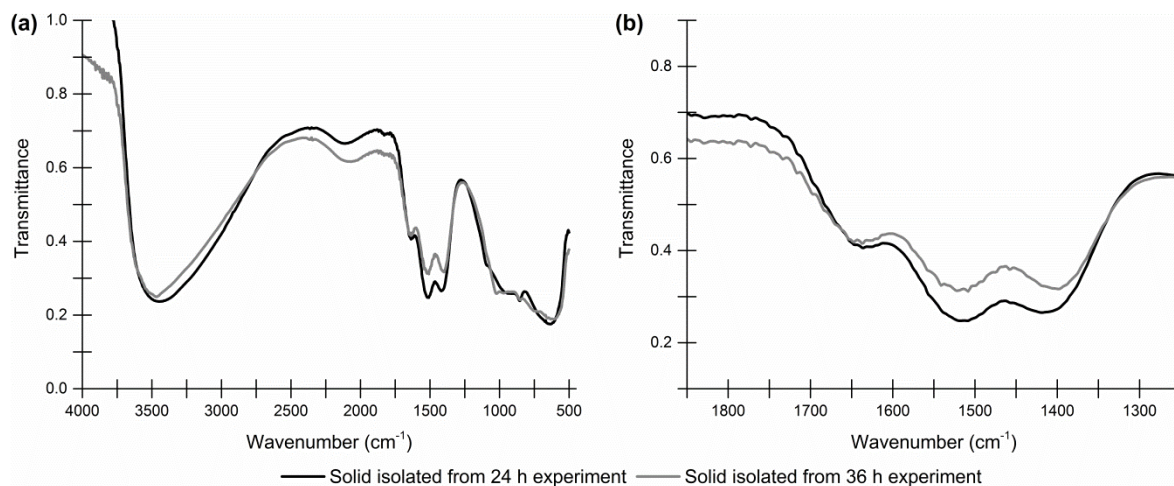
Figure 95: FT-IR (DRIFT) analysis of electrochemically formed solids, when applying a 10 mA current for 24 h and 36 h, with 1 M NaCl in the graphite-aluminium anode cell. (a) Full spectrum; (b) Carbonyl stretch region.

3.4.2 Improving Sustainability with Renewable Energy and Sustainable Materials

Using Renewable Energy: Solar Energy vs Electrical Energy

The energetic cost required to capture CO_2 (231-250 kJ mol^{-1} of CO_2 with NaCl in the graphite-aluminium anode cell) must be reduced for this method to have any future prospects as an industrial CCS method. As electricity will be a major cost contributor, the concept of using solar energy, and therefore carbon neutral, cheaper and renewable energy, to drive this process was explored. To investigate whether solar light could power CO_2 capture, a solar panel (14 cm tall and 10 cm wide, MC-SP0.8-NF-GCS, 800 mW, maximum voltage; 3.85 V, maximum current; 0.21 A) was used instead of the potentiostat and connected directly to the electrodes in the electrochemical cell (Figure 96). The solar panel was placed at a 30-32° N by NE angle in front of a window during the late autumn of 2016. Our methodology is capable of being solar powered, with CO_2 capture and release occurring concurrently with the rise and fall of sun levels (Figure 96), with similar changes in CO_2 levels (0.35-0.4%) during the daylight periods (Figure 96a), compared to when
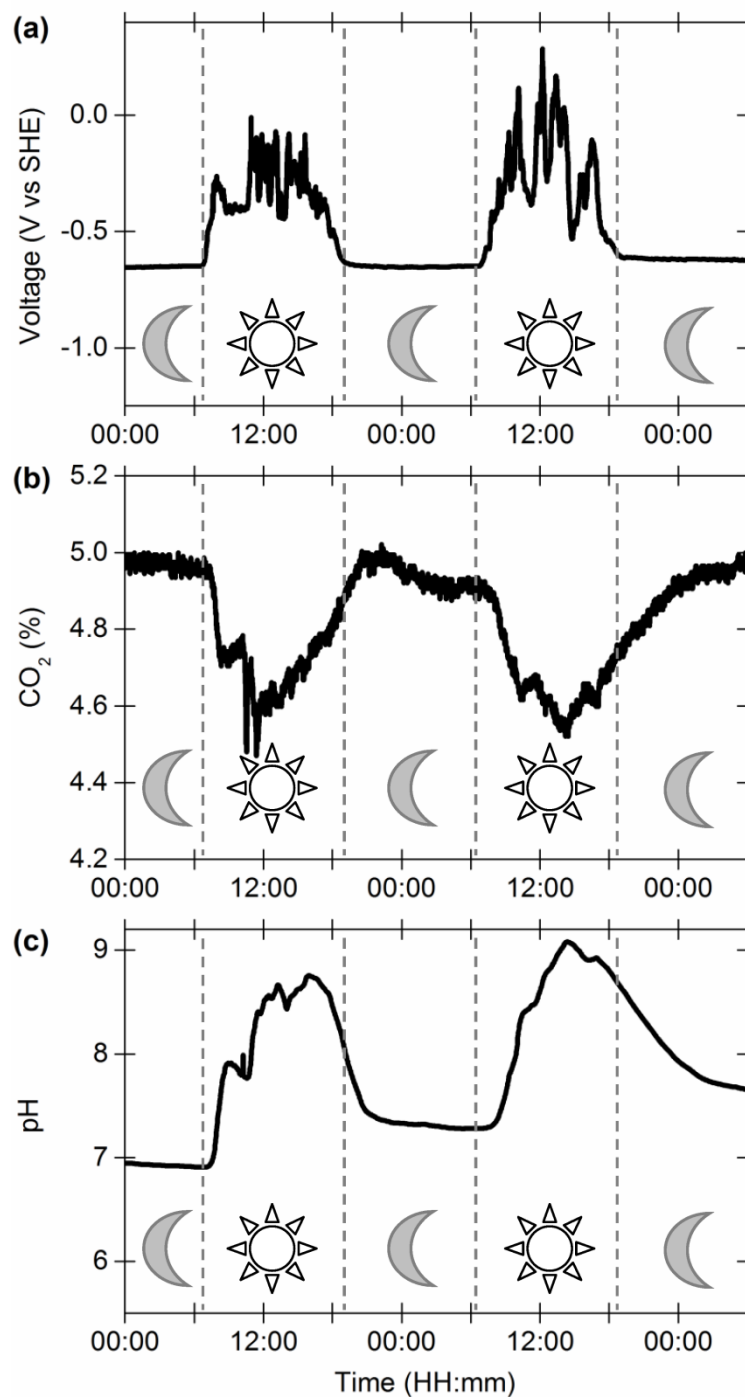
Figure 96: Solar powered electrochemical capture in the graphite-aluminium anode cell. (a) Potential of the graphite-aluminium anode; (b) Carbon dioxide levels in the outlet gas stream of the cell; (c) Corresponding solution pH. Other reaction conditions: a continuous gas flow of 0.7 mL min^{-1} CO_2 (5%) and 13.3 mL min^{-1} N_2, and 60 mL of 1 M NaCl. Experiment was conducted over 4.5 days, and exposed to 48 h of sunlight. The experiment was run from 00 49 am 29th September until 08.54 am 3rd October 2016. Solar noon was at 12.54 pm each day.

mains electricity was used (0.34%). The average anodic voltage reported during the two daylight periods was -0.30 V and -0.19 V respectively (Figure 96b). This indicated that similar anode potentials could be reached with sunlight compared to mains electricity (-0.32 V).

In this preliminary experiment, the cathode and solar panel voltage were unmonitored, and it was assumed that the voltage of the cathode remained unchanged. pH levels again reached basic levels of 8-9 concurrently with CO_2 capture (Figure 96c), suggesting bicarbonate formation was occurring and that the electrochemical mechanism remained the same. The levels of carbon captured (Table 30) in the electrolyte and solid (2.2 mmol) are comparable to those captured using mains electricity (2.8 mmol).

Table 30: Comparing carbon capture with mains and solar powered electricity.[a]

Electrolyte	Solid mass / g	Cell (anode)	C in solid[b] / mmol	C in solution[c] / mmol	C total[d] / mmol
1 M NaCl	0.58 ± 0.08[e]	Graphite-aluminium	0.9 ± 0.2[e]	1.9 ± 0.5[e]	2.8 ± 0.7
1 M NaCl	0.39	Graphite-aluminium (solar panel)	0.3 ± 0.07[f]	1.9 ± 0.1[f]	2.2 ± 0.1

a) All molar values reported for carbon detected in the solid and solution post-CO_2 capture correspond to the total amount of carbon in the total volume of electrolyte and total mass of solid, respectively.
b) Quantified via TGA-IR analysis.
c) Quantified via titration of electrolyte.
d) Combination of carbon in solution and solid.
e) Average values obtained from the four 24 h current-time experiments in Figure 55.
f) Carbon levels were scaled to account for 24 h of sunlight for a fair comparison.

A potential downside to using solar energy is the variability and unreliability of weather forecasts, illustrated by the non-uniform CO_2 levels, electrode potentials and pH variations with synchronous alterations in sunlight intensity during the experiment (Figure 96). Sunlight availability is also irregular, changes seasonally and is different across the globe, due to variations in global weather systems. Nevertheless, this experiment illustrated that the reliance of this method on mains electricity, and the costs associated with mains electricity, can potentially be eliminated. This electrochemical process can also be powered with renewable energy and thus have a low carbon footprint.

Using Sustainable Materials: "Waste" Aluminium as the Anode

Aluminium "waste" in the form of aluminium foil (approx. 3-4 g) along with 1 M NaCl as the electrolyte could be used for CO_2 sequestration and mineralisation (Figure 97).
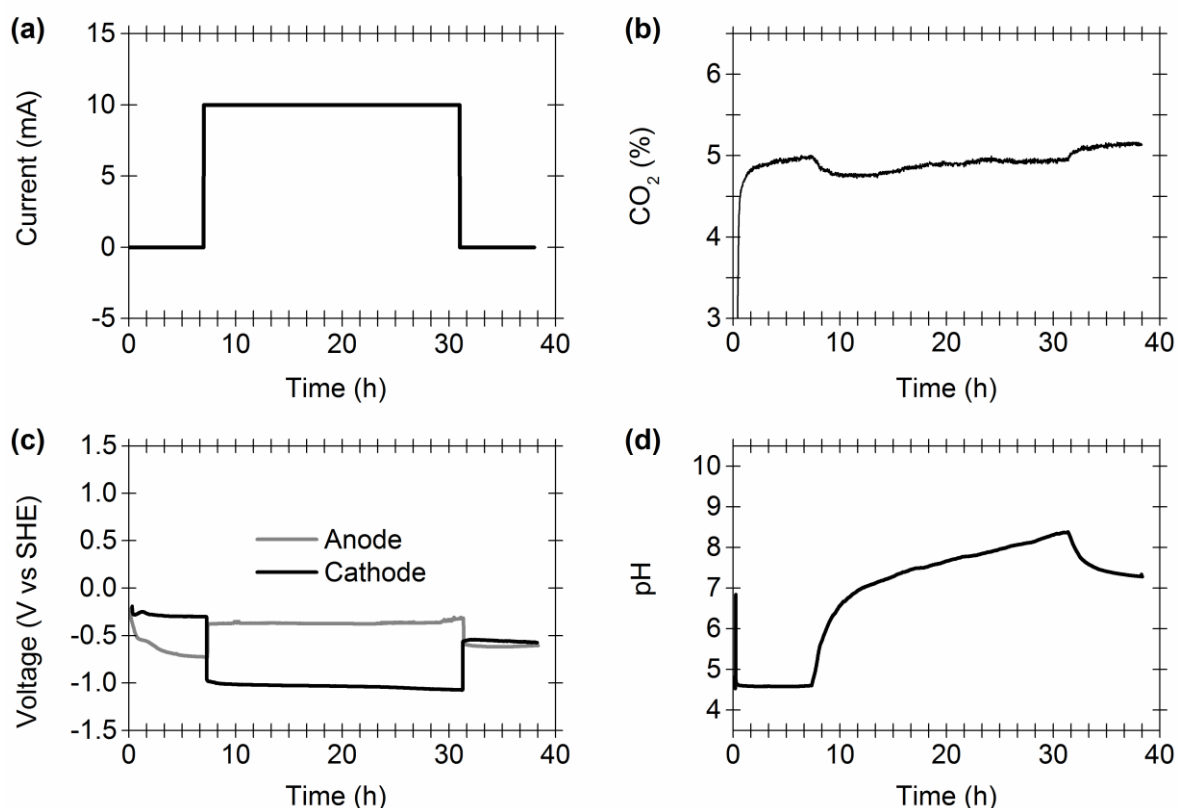
Figure 97: Promoting CO_2 capture with "waste" aluminium and 1 M NaCl in the graphite-aluminium anode cell. (a) Programmed current-time steps; (b) Carbon dioxide content in the exit gas stream; (c) Resultant changes to the electrochemical potential of the anode (grey line) and cathode (black line); (d) Corresponding changes in solution pH. Other reaction conditions: a continuous gas flow of 0.7 mL min^{-1} CO_2 (5%) and 13.3 mL min^{-1} N_2, and 60 mL of 1 M NaCl.

The aluminium had to be wrapped round the back of the graphite so that it was between the graphite liner and plastic casing. Placing aluminium directly in the electrolyte and on the inside of the graphite liner, without establishing an electrical connection to the aluminium directly, led to non-existent CO_2 capture, similar to when the aluminium-only anode cell was used (Figure 46). Changing the anode aluminium source did not affect the electrochemical mechanism, and CO_2 levels (Figure 97b), electrode potentials (Figure 97c) and pH levels (Figure 97d) were similar to those reported with 1 M NaCl in the graphite-aluminium anode cell (Figure 49 and Figure 55). Analysis of the electrolyte and solid

revealed that similar levels of carbon are mineralised but less is sequestrated in solution, and thus captured less carbon overall (1.5 mmol, Table 31). Therefore this is a less efficient CO_2 capture setup. This may be due to the difficulty of establishing a smooth coverage of "waste" aluminium foil around the graphite liner, leading to a weak electrical connection.

Table 31: Comparison of carbon levels captured with the graphite-aluminium anode and aluminium "waste" as the anode source.[a]

Electrolyte	Solid mass / g	Cell (anode)	C in solid[b] / mmol	C in solution[c] / mmol	C total[d] / mmol
1 M NaCl	0.58 ± 0.08^e	Graphite-aluminium	0.9 ± 0.2^e	1.9 ± 0.5^e	2.8 ± 0.7
1 M NaCl	0.61	"Waste" aluminium	1.1 ± 0.1	0.4 ± 0.01	1.5 ± 0.1

a) All molar values reported for carbon detected in the solid and solution post-CO_2 capture correspond to the total amount of carbon in the total volume of electrolyte and total mass of solid, respectively.
b) Quantified via TGA-IR analysis.
c) Quantified via titration of electrolyte.
d) Combination of carbon in solution and solid.
e) Average values obtained from the four 24 h current-time experiments in Figure 55.

Using Sustainable Materials: Seawater as the Electrolyte

Seawater obtained from Whitby, North Yorkshire was found to be a suitable electrolyte for CO_2 sequestration and mineralisation (Figure 98), with all reaction indicators similar to those reported when using 1 M NaCl in the graphite-aluminium anode cell. The total level of carbon captured is similar to when 1 M NaCl is used in the graphite-aluminium anode cell, but was slightly lower (2.0 mmol, Table 32). This novel cell can therefore use the sustainable, and non-geographically limited or politically hindered, resource of seawater, and thus be performed at numerous worldwide locations. One interesting difference was that a higher anodic potential was required when using seawater (-0.03 V) compared to 1 M NaCl (-0.32 V). It was hypothesised that there was a correlation between E_{Cell} and the salinity (i.e. concentration of dissolved salts) of the seawater collected from Whitby which had a salinity of approx. 0.20 M NaCl (see "3.7 Methods and Experimental" for more details). This is discussed further in "3.4.4 Energetics and Costs, Salinity vs E_{Cell}".
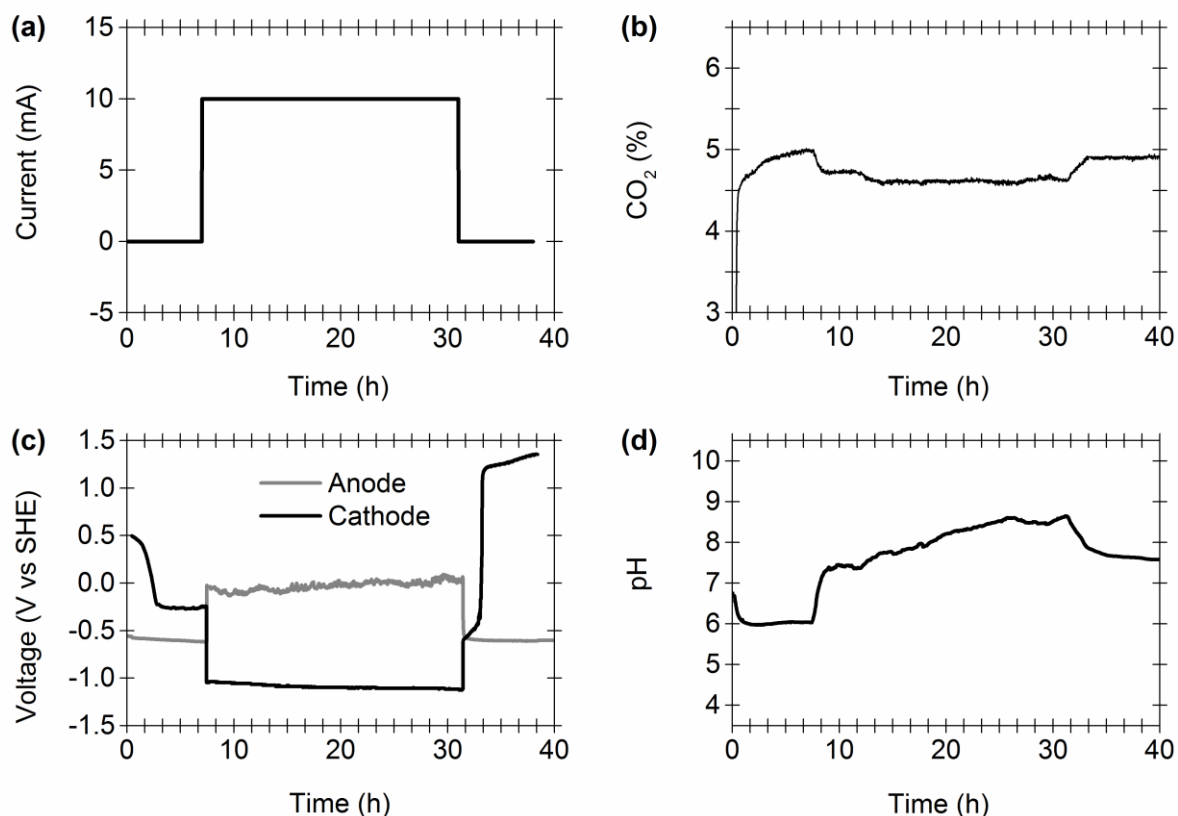
Figure 98: Promoting CO_2 capture with seawater in the graphite-aluminium anode cell. (a) Programmed current-time steps; (b) Carbon dioxide content in the exit gas stream; (c) Resultant changes to the electrochemical potential of the anode (grey line) and cathode (black line); (d) Corresponding changes in solution pH. Other reaction conditions: a continuous gas flow of 0.7 mL min^{-1} CO_2 (5%) and 13.3 mL min^{-1} N_2, and 60 mL of seawater.

Table 32: Comparison of carbon levels captured with seawater and 1 M NaCl as the electrolyte.[a]

Electrolyte	Solid mass / g	Cell (anode)	C in solid[b] / mmol	C in solution[c] / mmol	C total[d] / mmol
1 M NaCl	0.58 ± 0.08[e]	Graphite-aluminium	0.9 ± 0.2[e]	1.9 ± 0.5[e]	2.8 ± 0.7
Seawater	0.42	Graphite-aluminium	0.6 ± 0.02	1.4 ± 0.1	2.0 ± 0.1

a) All molar values reported for carbon detected in the solid and solution post-CO_2 capture correspond to the total amount of carbon in the total volume of electrolyte and total mass of solid, respectively.
b) Quantified via TGA-IR analysis.
c) Quantified via titration of electrolyte.
d) Combination of carbon in solution and solid.
e) Average values obtained from the four 24 h current-time experiments in Figure 55.

Using Sustainable Materials: Seawater and "Waste" Aluminium Combined

With both seawater and "waste" aluminium used simultaneously, CO_2 capture and mineralisation is also possible (Figure 99). Due to numerous instrument errors when attempting these experiments, the data presented in Figure 99 comes from replicated experiments.
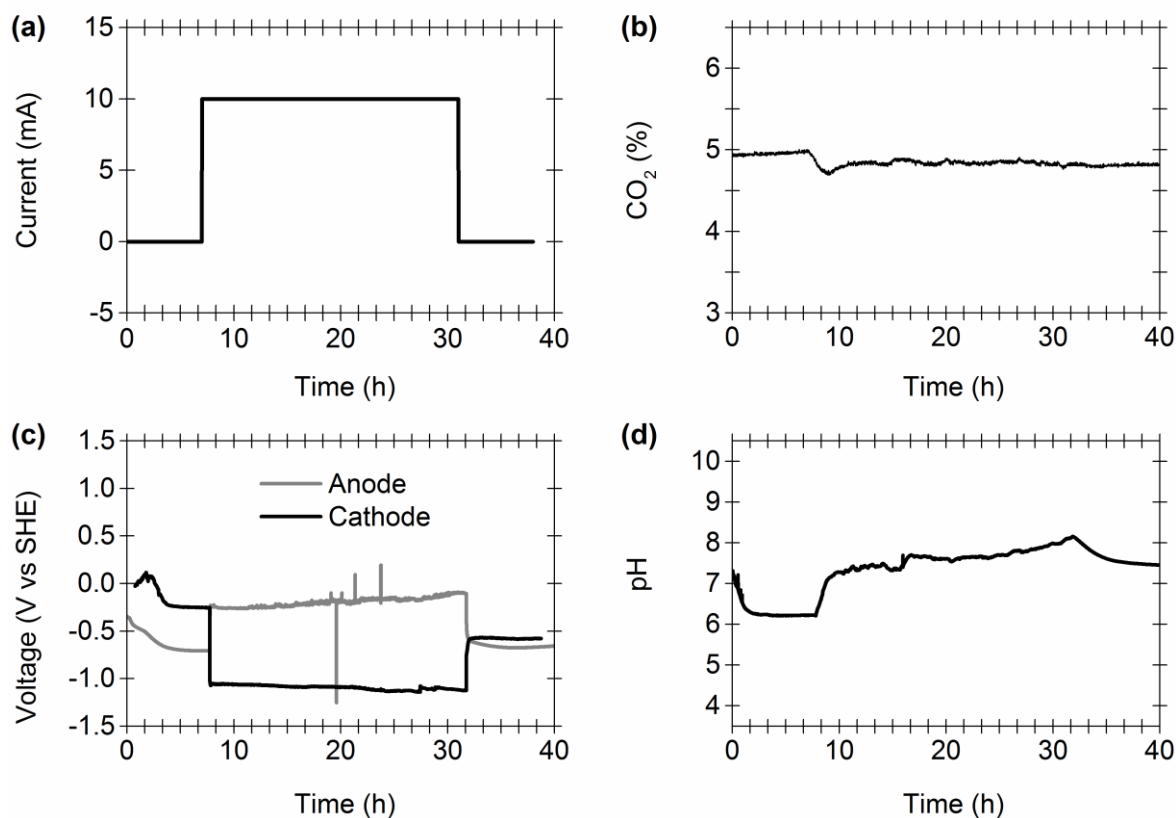
Figure 99: Promoting CO_2 capture with seawater and "waste" aluminium. (a) Programmed current-time steps; (b) Carbon dioxide content in the exit gas stream; (c) Resultant changes to the electrochemical potential of the anode (grey line) and cathode (black line); (d) Corresponding changes in solution pH. Other reaction conditions: a continuous gas flow of 0.7 mL min^{-1} CO_2 (5%) and 13.3 mL min^{-1} N_2, and 90 mL of seawater.

The highest total level of carbon captured from these experiments however is extremely low compared to the standard setup (0.5 vs 2.8 mmol), capturing only 18% of the usual carbon levels (Table 33). This may be due to the electrolyte pH not reaching the same basic levels reported with 1 M NaCl (pH >8, Figure 99d), thus hindering CO_2 sequestration and mineralisation. The low result is also not surprising considering the small drop in CO_2 levels reported (Figure 99b).

Table 33: Comparison of carbon levels captured when using seawater and "waste" aluminium combined, to using 1 M NaCl in the graphite-aluminium anode cell.[a]

Electrolyte	Solid mass / g	Cell (anode)	C in solid[b] / mmol	C in solution[c] / mmol	C total[d] / mmol
1 M NaCl	0.58 ± 0.08[e]	Graphite-aluminium	0.9 ± 0.2[e]	1.9 ± 0.5[e]	2.8 ± 0.7
Seawater	0.36	"Waste" aluminium	0.2 ± 0.01	0.3 ± 0.01	0.5 ± 0.01

a) All molar values reported for carbon detected in the solid and solution post-CO_2 capture correspond to the total amount of carbon in the total volume of electrolyte and total mass of solid, respectively.
b) Quantified via TGA-IR analysis.
c) Quantified via titration of electrolyte.
d) Combination of carbon in solution and solid.
e) Average values obtained from the four 24 h current-time experiments in Figure 55.

The combination of low salinity seawater and weak electrical connection between the graphite liner and aluminium foil were hypothesised to cause poor CO_2 capture. To investigate if any carbon was trapped in the traverses of the crumpled aluminium following reaction completion, the "waste" aluminium was washed with water and concentrated via freeze-drying. The white solid obtained was then analysed to determine if any carbon or carbonate was present. TGA-IR analysis and powder XRD analysis however detected no carbonate based material and only detected NaCl.

3.4.3 Carbon Dioxide Mineralisation

For each trialled reaction setup in Section 3.4, mineralisation occurred as a consequence of CO_2 capture. The precipitates isolated from each setup are identical to each other, as highlighted by FT-IR (DRIFT) and TGA-IR analysis (Figure 100 and Figure 101 respectively). This suggests that the mechanism for CO_2 mineralisation remained the same using different electrolytes and aluminium sources for the anode.
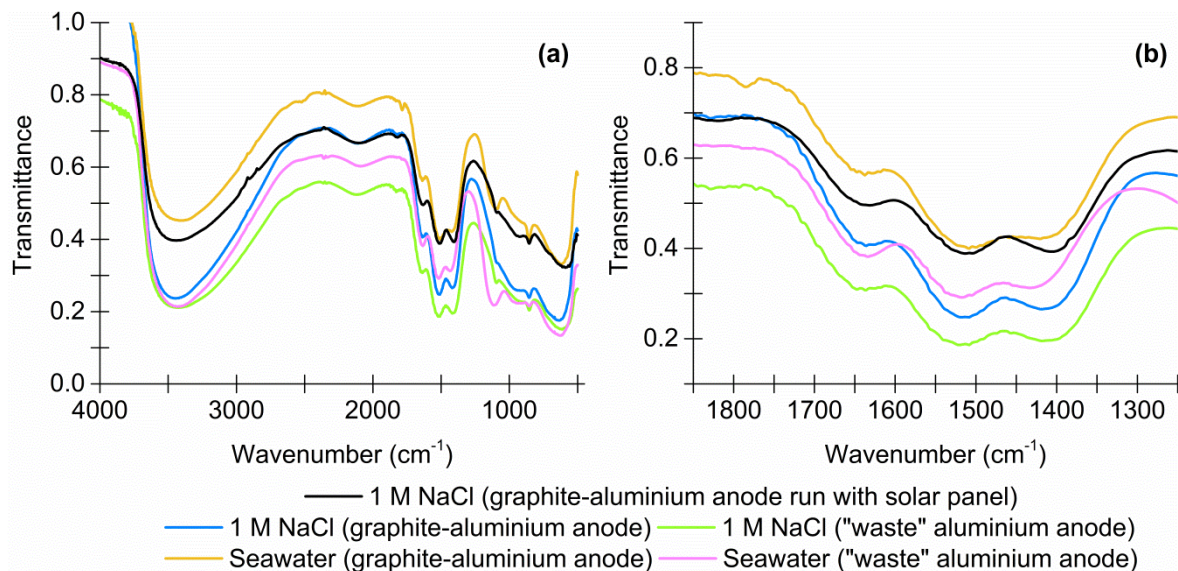
Figure 100: FT-IR (DRIFT) analysis of solid precipitates formed using solar energy, 1 M NaCl in the graphite-aluminium anode cell, 1 M NaCl and "waste" aluminium, seawater in the graphite-aluminium anode cell and seawater with "waste" aluminium. (a) Full spectrum; (b) Carbonyl stretch region.
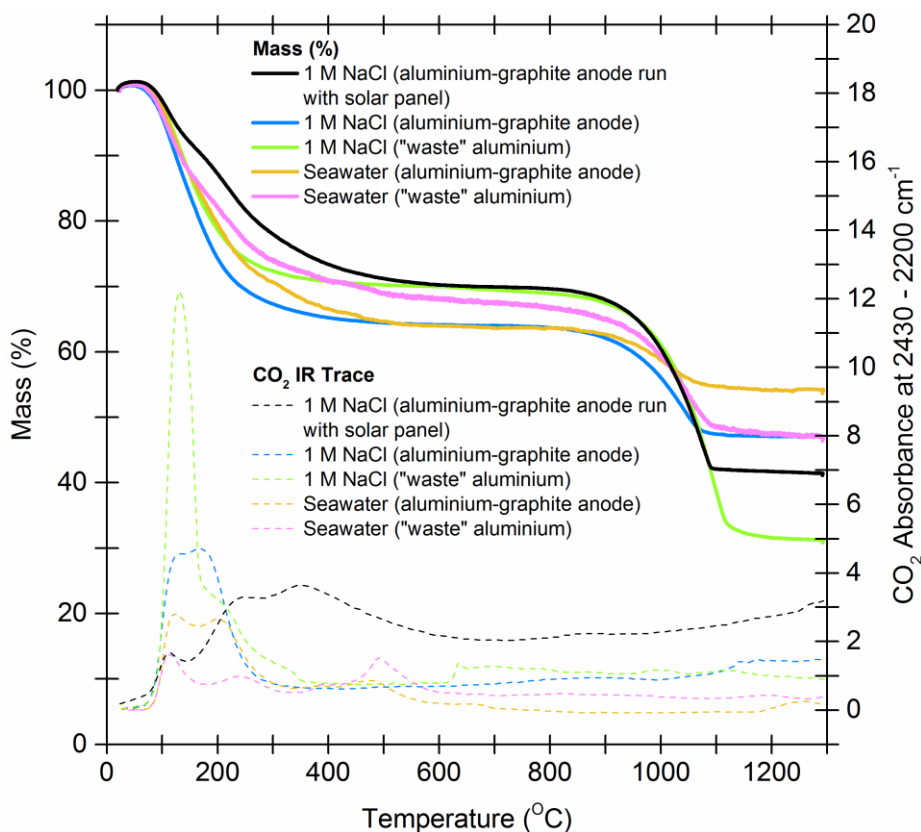
Figure 101: TGA-IR analysis of solid precipitates formed using solar energy, 1 M NaCl in the graphite-aluminium anode cell, 1 M NaCl and "waste" aluminium, seawater in the graphite-aluminium anode cell and seawater with "waste" aluminium.

3.4.4 Energetics and Costs

The most efficient electrochemical setup, in terms of carbon capture and energy, was using 1 M NaCl in the graphite-aluminium anode cell with a 10 mA current-time step over 36 h. (Table 34).

Table 34: Comparison of E_{Cell} and energy required for carbon capture with different energy sources, electrolytes and anode material.

Electrolyte	Cell (anode)	E_{Cell}[a] / V	E_{Cell} energy[b] / J	C total[c] / mmol	Energy of C capture[d] / kJ mol^{-1}
1 M NaCl	Graphite-aluminium	0.81[e]	700[e]	2.8 ± 0.7[e]	250
1 M NaCl	Graphite-aluminium[f]	0.52	453	1.8 ± 0.1	252
1 M NaCl	Graphite-aluminium	0.84[g]	1087[g]	4.7 ± 0.2[g]	231
1 M NaCl	Graphite-aluminium (solar panel)	0.83-0.94	718-813	2.2 ± 0.1	326-369
1 M NaCl	"Waste" aluminium	0.67	579	1.5 ± 0.1	386
Seawater	Graphite-aluminium	1.06	917	2.0 ± 0.1	459
Seawater	"Waste" aluminium	0.86	743	0.5 ± 0.01	1486

a) Difference between the anode and platinum cathode voltage.
b) The E_{Cell} value is converted into watts (watt = voltage x current). Watts are equivalent to J s^{-1}, therefore J s^{-1} x time of current application is equivalent to joules.
c) Combination of carbon in solution and solid.
d) (E_{Cell}/1000) ÷ (C total/1000).
e) Average values obtained from the four 24 h current-time experiments in Figure 55.
f) Temperature of stirrer hotplate, on which the graphite-aluminium block was placed, was set to 60 °C.
g) Average values obtained from the three 36 h current-time experiments in Figure 94.

Increasing the reaction temperature had similar energy requirements for carbon capture compared to standard reaction conditions. The energetic cost of using the solar cell was greater than using mains electricity, on the assumption that H_2 formation still occurred at the cathode and at a similar potential reported during standard experiments (-1.13 V). The

energy of carbon capture from this experiment is quoted as a range due to the variance in E_{Cell} values during different sunlight periods. The energy requirements for carbon capture when using seawater, "waste" aluminium or both combined were greater than the standard conditions of 1 M NaCl in the graphite-aluminium cell (Table 34).

Overall, changing reaction conditions and using renewable energy and sustainable materials unfortunately did not lower the cost of carbon capture, and was therefore more expensive than currently employed CCS methodology (Table 35). Using seawater and "waste" aluminium created the most expensive setup in terms of energy requirements (1310 J) and hence carbon capture (1486 kJ mol^{-1} of CO_2). It was hypothesised that the low salinity of the seawater (discussed further in "Salinity vs E_{Cell}"), and the weak electrical contact between the graphite liner and the "waste" aluminium, hindered carbon capture, hence explaining why this combination had the worst performance overall.

Table 35: Energy costs of CO_2 sequestration and mineralisation using different anodes and electrolytes.[26]

CCS system[a]	Cost range[b,c] / US\$ tCO_2^{-1}
Geological storage	0.5-8
Ocean storage	5-30
Capture from hydrogen or ammonia production	5-55
Capture from a coal- or gas-fired power plant	15-75
Range from experiments	246-1584[d]

a) Cost of CCS systems in 2005.
b) Costs have not been scaled according to inflation.
c) A conversion factor of £1 equals US\$1.22 was used. This was the average conversion for British pounds to American dollars over the year 2016 by 9th November 2016.
d) The energy required to capture a tonne of carbon in joules was converted to kWh (1 J = 2.78 x 10^{-7} kWh). Using the average cost of electricity in the UK between March 2015-2016,[286] which was 13.86 p per kWh, this energy value was then converted into a cost in £ and then US\$.
e) Range of results obtained using the different experimental setups in Section 3.4.

The combination of NaCl in the electrolyte and a basic pH means that sodium hydroxide formation is possible. Therefore, it could be argued that starting with a NaOH solution from the start may be more beneficial than creating the desired pH electrochemically.

Sodium hydroxide is a cheap chemical (£30 or US\$37 per kg, VWR international, 2017) and may therefore be more cost-effective than using water. Carbon dioxide capture with NaOH has been reported in the literature,[296-298] with Lowry claiming that it would cost only US\$127 tCO_2^{-1}),[296] which is cheaper compared to our method (US\$267 tCO_2^{-1}). Sodium hydroxide however creates a caustic solution, and may therefore be disadvantageous to use in this method, because it could react with the aluminium and thus perform undesired electrochemical processes.[299] The use of NaOH solutions also require high temperatures and thus expensive operating costs (the cost quoted by Lowry was from a theoretical model, not experimental data).[296] The regeneration and recycling of NaOH is also problematic. Using water or seawater in the cell from the start of the experiments may not be as cost-effective but may be worthwhile in terms of sustainability.

Salinity vs E_{Cell}

Intriguingly, a higher E_{Cell} value was required for CO_2 capture with seawater as the electrolyte, as a higher anodic potential was reported during electrochemical CO_2 capture (Figure 98). This was hypothesised to be due to the low salinity (0.2 M NaCl) of the collected seawater (see experimental for further details). To investigate this, CO_2 capture experiments were performed using different concentrations of NaCl, to determine if there was a correlation between salinity and the E_{Cell} required for carbon capture (Figure 102).

There was a correlation between salinity and E_{Cell}, as when the salinity (or NaCl concentration) of the electrolyte decreased, the difference between the anodic and cathodic voltage increased (Figure 102c). The E_{Cell} value required to perform capture carbon therefore also increased (Figure 103).[300,301] This was unsurprising, as a decrease in salinity, and thus ionic strength, will increase electrolyte resistance and hence the power required to perform CO_2 capture. Using saltier seawater from different geographical locations could therefore overcome this issue.
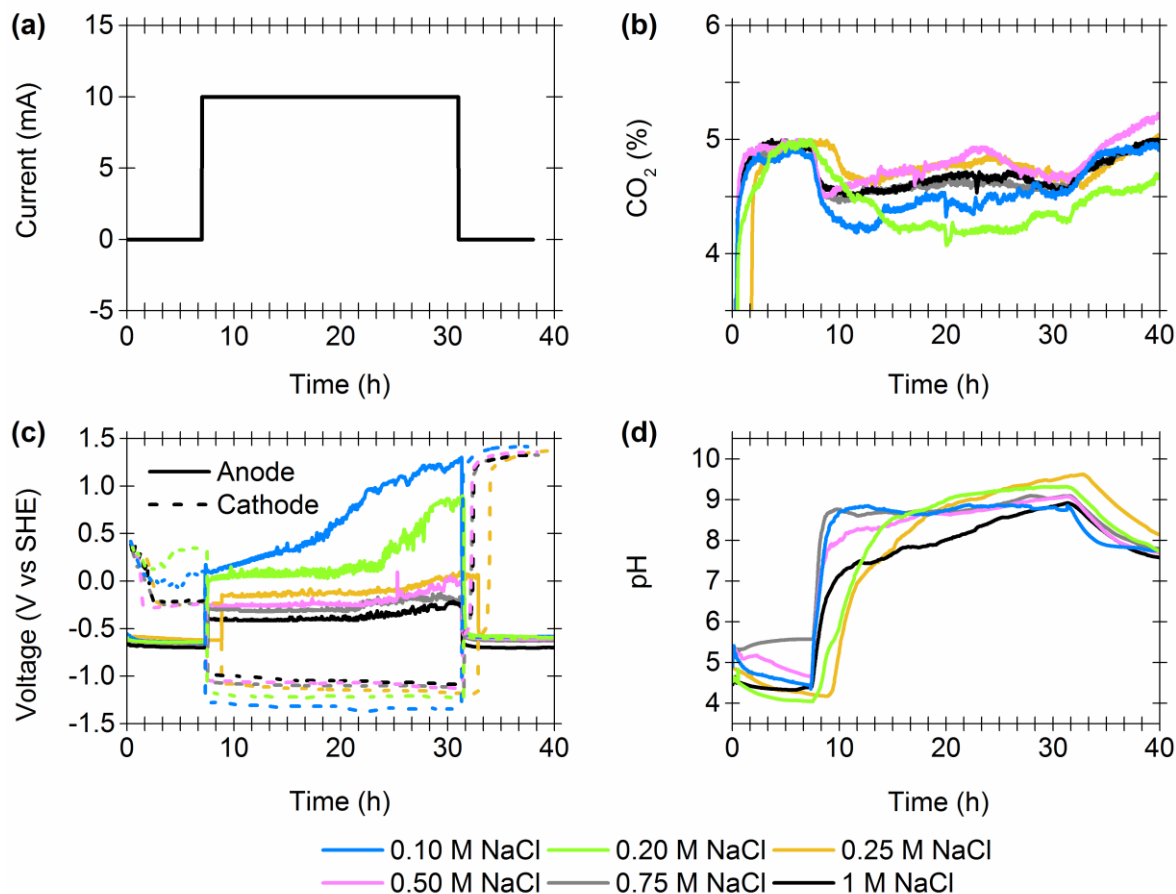
Figure 102: Investigating the effects of changing NaCl concentration on CO_2 sequestration and E_{Cell} in the graphite-aluminium anode cell. (a) Programmed current-time steps; (b) Carbon dioxide content in the exit gas stream; (c) Resultant changes to the electrochemical potential of the anode (solid line) and cathode (dashed line); (d) Corresponding changes in solution pH. Other experiment conditions: a continuous gas flow of 0.7 mL min^{-1} CO_2 (5%) and 13.3 mL min^{-1} N_2, and 60 mL of 1 M NaCl.

In an attempt to try and overcome the low salinity of the Whitby seawater, aliquots were concentrated *in vacuo* to increase salt concentration and to potentially improve CO_2 capture capability. Concentrating seawater however led to a pH buffering effect, as pH levels stayed neutral at pH 7 and carbon capture was non-existent. This suggested that other components in the seawater such as microbes were affecting CO_2 capture. Salty seawater must therefore be used in the electrochemical cell and cannot simply be concentrated.
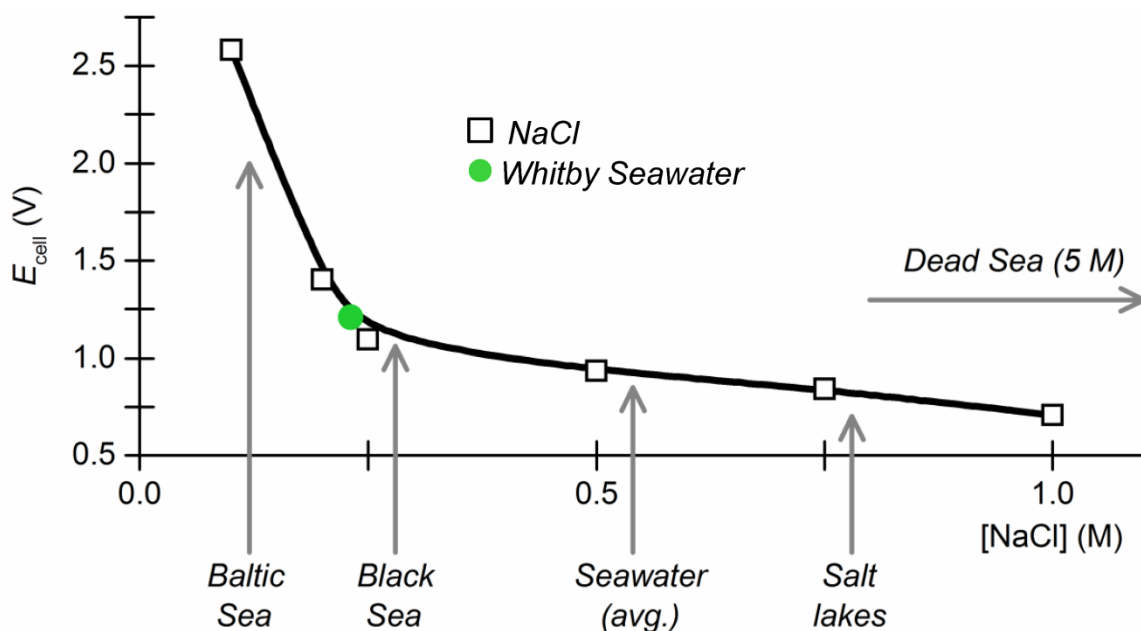
Figure 103: Difference between anode and cathode voltages, and thus E_{Cell}, as a function of NaCl concentration, with predictions for results that would be obtained using seawater samples from around the world. Solid lines are drawn as a guide to the eye.[300,301]

3.4.5 Data Summary

A summary of the electrochemical data obtained for this results and discussion part is shown in 4.2 Appendix 2, Section 4.2.4. An overall summary of results is shown by Figure A7. The correlation between NaCl concentration and E_{Cell} for different experiments is summarised in Figure A8. The carbon capture levels and consequent energy requirements for all trialled systems is summarised in Table A9 and Table A10.

3.5 Conclusion

This novel electrochemical cell is versatile and can work with numerous reaction conditions, such as high temperatures, different current strengths and longer current-time steps. This cell can also be solar-powered and use sustainable reagents. The standard reaction setup at near ambient conditions with the application of a 10 mA current over a 36 h period provided the least energy intensive, and therefore cheapest, system for carbon and CO_2 capture. Renewable energy in the form of carbon neutral solar energy can be used to perform CO_2 sequestration and mineralisation, with a similar energy requirement, and

therefore cost, to using mains electricity. Factors such as weather fluctuations during the year and different weather systems in different climates however cannot be ignored.

This methodology can be used with non-toxic, geographically available and sustainable materials, such as aqueous NaCl (table salt) or seawater as the electrolyte and "waste" aluminium as the anode. Improving the sustainability of this unique electrochemical CO_2 mineralisation method was possible but had a knock-on effect in terms of total carbon captured and consequently energy requirements and costs. Although sustainability is an important factor for future CCS methods, low carbon capture will hinder the industrialisation of this methodology. The potential for this methodology to be scaled up, and reach the same production level as CO_2 based feedstocks, is significant if the carbon capture ability is improved. In 2013, 24 million tonnes of aluminium was recycled,[288,292,302] which was similar to the total production of CO_2 based chemicals in 2014 (Table 36).[14,33] The scale of aluminium recycling therefore lies within the scale of chemicals produced using CO_2. If the carbon capture efficiency of this process, and the ability to use "waste" aluminium, was thus improved, the potential to scale-up to an industrial level is possible.

Table 36: Production scale of chemicals using CO_2 compared to aluminium recycling.[14,33,288,292,302]

Feedstock	Total production in 2014 / million tonnes
Urea	155
Methanol	50
Sodium Carbonate	50
Aluminium recycling	24[a]
Formaldehyde	21
DMC and DEC[b]	1
Formic acid	0.6

a) Total aluminium recycled in 2013.
b) Dimethyl carbonate and diethyl carbonate.

An important consideration of this methodology was if it creates a net removal of CO_2, because if the CO_2 emitted from the electrical energy required to perform CO_2 capture is greater than the level of CO_2 captured, true CCS is not occurring. The graphite-aluminium anode cell (using 1 M NaCl with a 10 mA current over 24 h) was capable of a net removal of CO_2, when the CO_2 emitted from the required electrical energy (700 J) from different UK mains electricity sources was taken into account (Table 37). The level of CO_2 removed is greater if solar powered electricity is used, therefore improving this methodology with solar energy would be extremely beneficial.

Table 37: Comparing total CO_2 emitted when performing electrochemical CO_2 capture using different sources of electricity in the UK.[191,290]

CO_2 emissions from mains electricity sources / g CO_2 per kWh	CO_2 emitted using 700 J of electrical energy[a,b]		Total CO_2 emitted / mmol[c]
	g	mmol	
500 (coal-fired power station with no CCS)	0.097	2.21	-0.59
200 (coal-fired power station with CCS)	0.039	0.88	-1.92
88 (solar power)	0.017	0.39	-2.41

a) 1 kWh is equal to 3.6×10^6 J or 3.6 MJ.
b) 700 J was the average energy required to perform CO_2 capture with 1 M NaCl in the graphite-aluminium cell, when a 10 mA current was applied for 24 h.
c) Millimoles of CO_2 emitted by 700 J of electrical energy – total mmol of CO_2 captured (2.8 mmol) with 1 M NaCl in the graphite-aluminium cell, when a 10 mA current was applied for 24 h.

This method could also create a net removal of CO_2 when scaled up to using a tonne of aluminium. In the worst case scenario, when all the energy required for electrochemical CO_2 mineralisation comes from a coal fuelled power station, 500 g of CO_2 would be produced for each kWh (or 3.6 MJ) of energy. Considering that 6.7 GJ of energy would be required to electrochemical capture CO_2 using a tonne of aluminium (using 1 M NaCl in the graphite-aluminium cell with a 10 mA current over 24 h),[287,288] using electricity from a coal fuelled power station would produce 0.9 tonnes of CO_2. Performing our electrochemical method on this scale would capture 1.2 tonnes of CO_2, thus this method would net consume 0.3 tonnes of CO_2 (per tonne of aluminium). If the percentage of

carbon neutral energy increases in the UK, and globally, the net CO_2 consumed could increase even more.

One unavoidable aspect of this methodology is the use of electricity, which is one of the largest sources of anthropogenic CO_2 emissions (Table 38).[303] The scale of CO_2 emissions from electricity far exceeds the capacity of any chemical process which might consume CO_2. Thus, for this methodology to have any chance of reducing CO_2 emissions, not only must the carbon capture ability of this method improve, but the global implementation of CCS and use of alternative, and low carbon footprint, energy sources, such as hydroelectric, wind, solar and tidal, must also increase. This will be an ambitious task but not impossible.

Table 38: Global anthropogenic emissions of CO_2 in 2008.[303]

Source	CO_2 emissions / million tonnes per year
Electricity production (coal)	14,200
Electricity production (gas)	6,320
Cement production	2,000
Iron and Steel production	1,000
Oil Refineries	850
Ethene production	260
Ammonia production	150
Natural gas production	50

3.6 Future Work

The mechanism leading to CO_2 capture and H_2 formation will be further investigated, to further prove or disprove the proposed mechanism, as many questions remain unanswered. One such question is does the graphite truly display capacitance-only behaviour in the

mixed anode cell. This could analysed and quantified with further cyclic voltammetry experiments. This would further indicate whether or not we have a true temporal separation of the anodic and cathodic process. Changing the mass quantity of aluminium required in the cell to find the limiting aluminium to carbon ratio to perform CO_2 mineralisation remains unanswered. Investigating reaction conditions further, such as percentage of CO_2 gas, electrolyte volume, and further temperature studies could be worthwhile. The limiting point at which this system can capture CO_2 in terms of time remains unexplored. Creating a flow based system for the electrolyte supply and gas flow could lead to a more efficient and self-standing methodology. Changing the metal cation of electrolyte has been performed, but could be investigated further, as well as changing the anion.

The ability to use the joint application of CO_2 mineralisation and sequestration with H_2 formation for the synthesis of C_1 products, for example formic acid, formaldehyde and methanol, would be an intriguing endeavour. One carbonate mineral that is extremely stable and thus offers near permanent CO_2 capture is calcite, or calcium carbonate ($CaCO_3$). Changing reaction variables so that more alkaline pH's could be reached and form this highly stable carbonate may be worthwhile investigating. Performing further tests to monitor the cathodic potential, and thus the E_{Cell} value, whilst using the solar panel to perform CO_2 capture is vital. Performing these experiments during the summer period, to compare results to those obtained over a winter period, would also be interesting.

Using metals as the cathode which are cheaper, environmentally friendly and more earth-abundant than platinum would be an interesting endeavour and could help offset future scale-up costs. The cost of creating an aluminium block (or outer) for the cell to then slowly passivate this into an aluminium hydroxycarbonate material also seems slightly counterintuitive. If this cell was to be further developed for CO_2 mineralisation, then developing a graphite anode doped with aluminium, or using graphite and aluminium as separate electrode rods may be intriguing to examine. Using this cell for an

electrochemical microbial based setup to utilise both features of CO_2 capture and H_2 formation to form C_1 based products would also be interesting.

3.7 Methods and Experimental

3.7.1 Cell Designs

Four electrochemical cells were designed by the mechanical workshops at the University of York's Chemistry Department, under the guidance of Chris Mortimer:

- One graphite-aluminium anode cell;

- Two graphite-only anode cells (one for standard experiments and one designed to use with "waste" aluminium); and

- One aluminium-only anode cell.

Graphite-Aluminium Anode Cell

The graphite-aluminium anode cell was used for majority of electrochemical CO_2 capture experiments (Figure 104 and Figure 105).
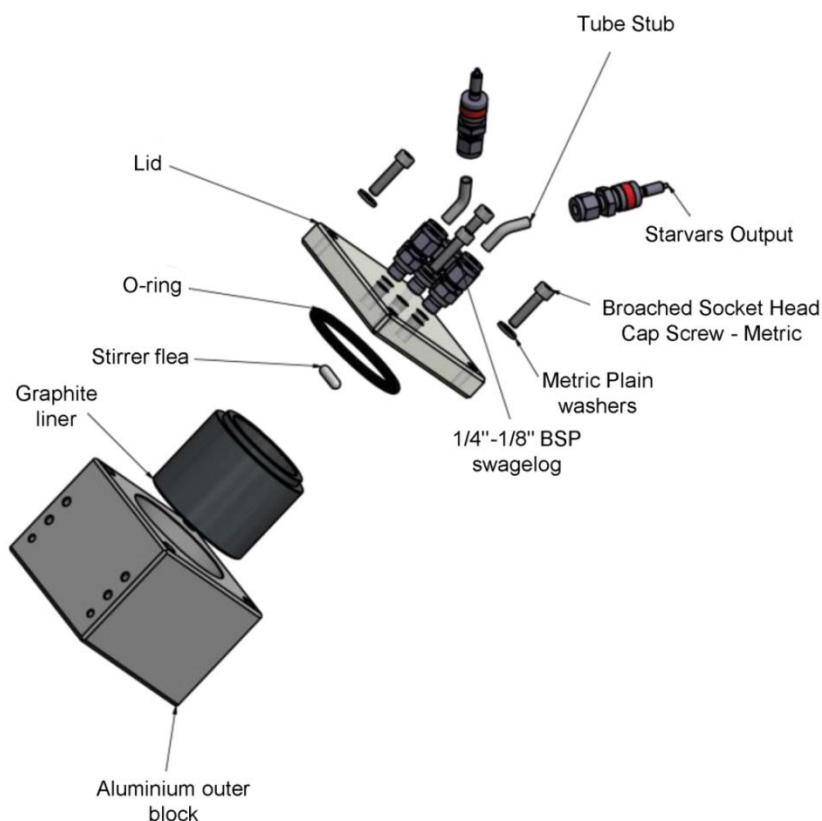
Figure 104: The graphite-aluminium anode cell and its components.
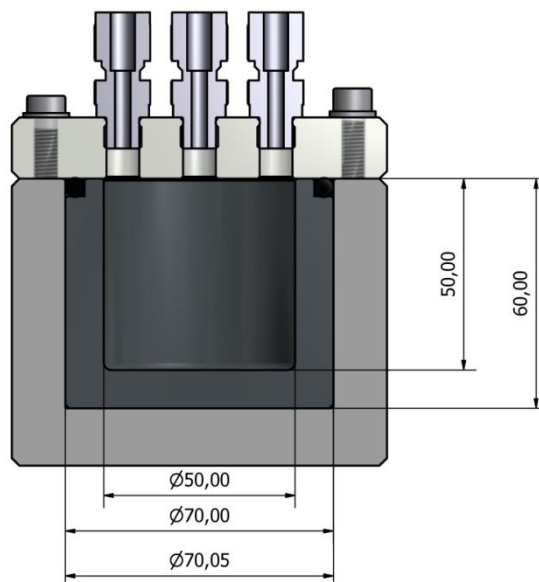
Figure 105: Inside view and dimensions of graphite-aluminium anode cell, with diameter lengths (Ø) in mm.

The beaker-shaped graphite electrode or liner (graphite supplied by OLMEC, grade MCCA 84) was 70.05 mm in diameter and 60 mm in depth. Holes were drilled in the graphite liner to enable the electrolyte to reach the aluminium outer block (8 holes, each 3.2 mm wide and 13.18 mm long, with a total surface area of 64 mm^2). The aluminium was supplied by Alaco (Grade 6082, Temper T6), with an aluminium content of 95-98%.

Graphite-Only Anode Cell (for Standard Experiments)

The graphite-only anode cell and a separate graphite liner were made to the same dimensions as the graphite-aluminium anode cell, except the aluminium outer block was replaced with plastic. An aluminium ring was placed on top of the graphite liner, to create an electrical connection between the cell and potentiostat, whilst ensuring only the carbon portion of the anode came into contact with the solution (Figure 106).

Graphite-Aluminium Anode Cell (for "Waste" Aluminium Experiments)

A graphite-only anode cell had the base of the plastic outer block, where the graphite liner sits, extended by 5 mm in depth, so that a sufficient amount of "waste" aluminium (aluminium foil) could be placed underneath the graphite liner. All other cell dimensions were kept the same.

245
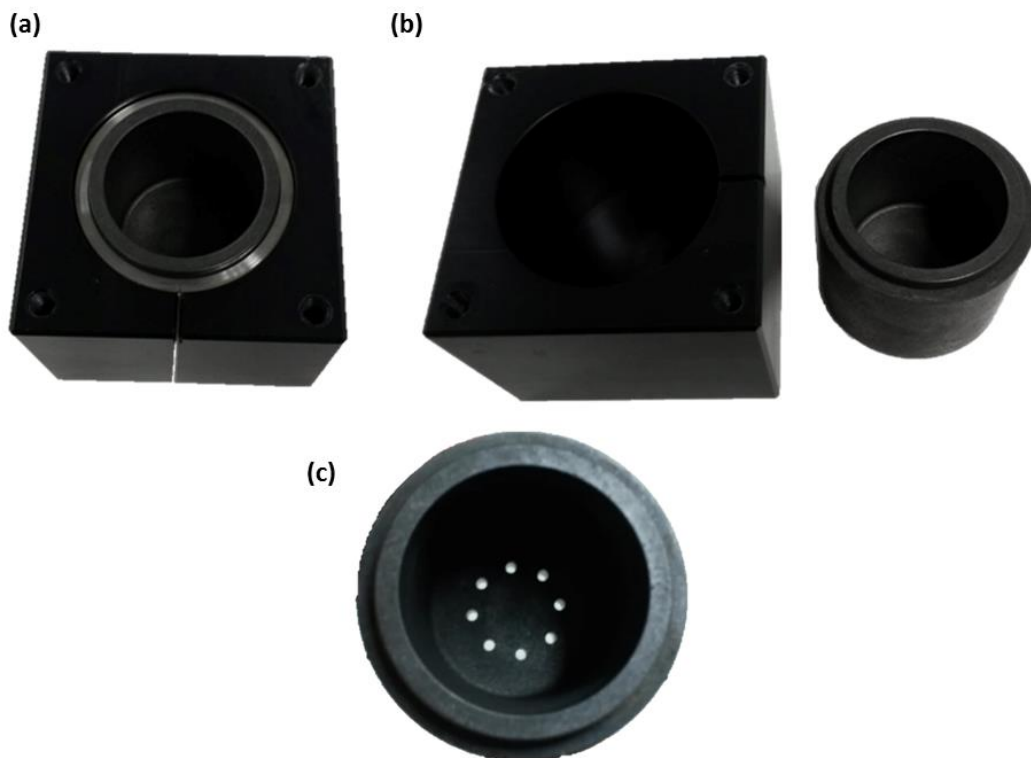
Figure 106: The graphite-only anode cell. (a) All components of the cell together. (b) Plastic casing (LHS) and graphite liner (RHS). (c) Graphite liner with 8 x 3.2 mm holes.

Aluminium-Only Anode Cell

An aluminium-only anode cell was created by removing the graphite liner from a graphite-aluminium cell. All other cell dimensions were kept the same.

3.7.2 Experimental Setup

Each cell used a specially designed Perspex® lid which sealed onto a recessed O-ring. This lid contained five ports, which were used to place a pH probe (Semi-micro epoxy gel BNC pH electrode, VWR International), platinum counter electrode (wire, 3.5 cm in length and 1.30 mm in diameter) and Ag/AgCl reference electrode (3 M NaCl, BASi, 7.5 cm in length, 6 mm in diameter) into the electrolyte. The final two ports were used as gas-tight inlet and outlet ports. Swagelok fittings and quick-connects were used to ensure an air tight seal at each port (Figure 107).
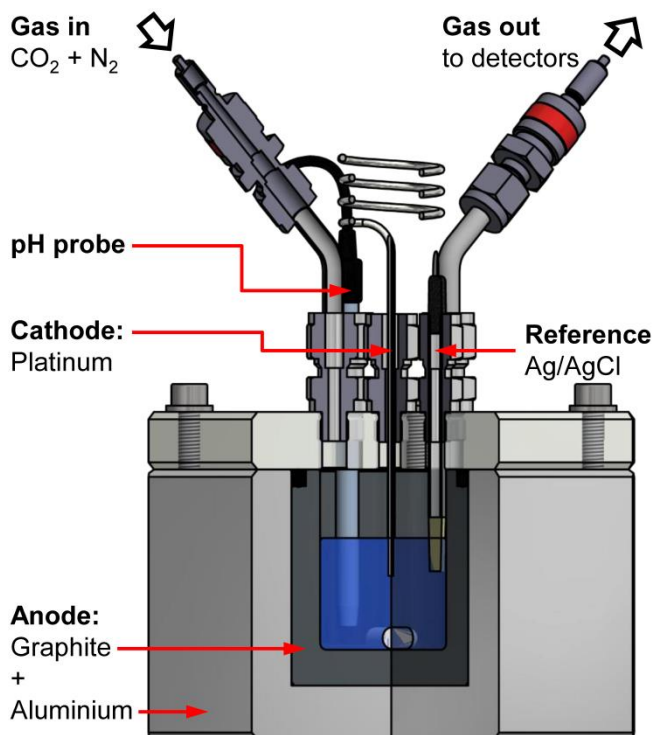
Figure 107: Schematic of the graphite-aluminium anode cell and cell components used in a standard experiment, with a cross-section view of the inside of the cell.

All electrolyte solutions were made using ultrapure water (Purite, ONDEO, average resistivity of 18 MΩ cm^{-1} at 25 °C). The suppliers for electrolyte salts (all of at least 99% purity) were: NaCl, VWR International (100%); LiCl, Santa Cruz Biotechnology (>99%) and CsCl, MP Biomedicals Europe (>99%). All experiments used 60 mL of electrolyte except when using the aluminium-only anode cell (180 mL) and for the seawater with "waste" aluminium tests (90 mL), to ensure the electrodes and monitoring equipment were placed in the electrolyte during the experiments. Approx. 3-4 g of aluminium foil was wrapped round the graphite liner when used as the "waste" aluminium source (Figure 108).

Regardless of the cell, a VoltaLab 50 potentiostat with VoltaMaster software was used to control current flow and to monitor the potential of the platinum counter electrode relative to the Ag/AgCl reference electrode. In addition, a digital voltmeter with USB data logging (PT-4000ZC, Digitec) was used to monitor the potential of the anode with respect to the Ag/AgCl reference electrode. All electrochemical potentials reported were corrected to vs

Figure 108: Aluminium foil wrapped around a graphite liner for "waste" aluminium anode electrochemical experiments.

the standard hydrogen electrode (SHE) as described in "Calibration of Ag/AgCl Reference Electrode". Further solution phase monitoring was provided by linking the pH probe to a second digital voltmeter with USB data logging. The pH probe was calibrated prior to each run as described in "pH Probe Calibration".

In each experiment, solution agitation was performed by placing the electrochemical cell on top of a magnetic stirrer hotplate (Stuart UC152, set to a speed setting of 4) and using a 10 x 4 mm magnetic stirrer bar. The magnetic stirrer hotplate, and electrochemical cell, reached temperatures of 32-35 °C after 1 h of operation with an average temperature of 34 °C during each run. To ensure that temperature fluctuations were within ± 0.1 °C a digital temperature probe, in contact with a third digital voltmeter with USB data logging, was used for some experiments. When performing experiments powered by light, a Multicomp solar panel (1.4 cm tall and 1 cm wide, MC-SP0.8-NF-GCS, 800mW, maximum voltage; 3.85 V, maximum current; 0.21 A) was used. The solar panel was placed in front of a window at a 30-32° N by NE angle.

Gas mass flow controllers (Aalborg, GC717, a 0-10 mL min^{-1} or 0-100 mL min^{-1}) were used to control the CO_2 (BOC, >99%) and N_2 (BOC, >99%) inlet gas flow rates respectively. A downstream CO_2 gas analyser was incorporated to measure the level of

CO_2 in the gas leaving the electrochemical cell (Quantek CO_2 analyser, model 906). A gas chromatography system adapted for H_2 detection was also used to monitor H_2 levels as described in "3.7.4 Quantifying Hydrogen Production".

3.7.3 Calibration of Equipment

Calibration of Ag/AgCl Reference Electrode

To quantify the conversion factor required to adjust the potentials measured with our Ag/AgCl reference electrode to vs SHE, three independent cyclic voltammetry (CV) measurements were performed. These measurements were conducted with N_2-purged 10 mM ferricyanide (K_3FeCN_6) in 0.1 M pH 7 phosphate buffer, the Ag/AgCl reference electrode used in the electrochemical CO_2 capture experiments, a glassy carbon working electrode (BASi) and a platinum counter electrode (wire), according to O'Reilly's method (Figure 109).[232] Analysis was performed with an EmStat[3] potentiostat and PSTrace4 software (PalmSens) yielding a conversion factor of V vs SHE = V vs Ag/AgCl + 0.194 V (Table 39).
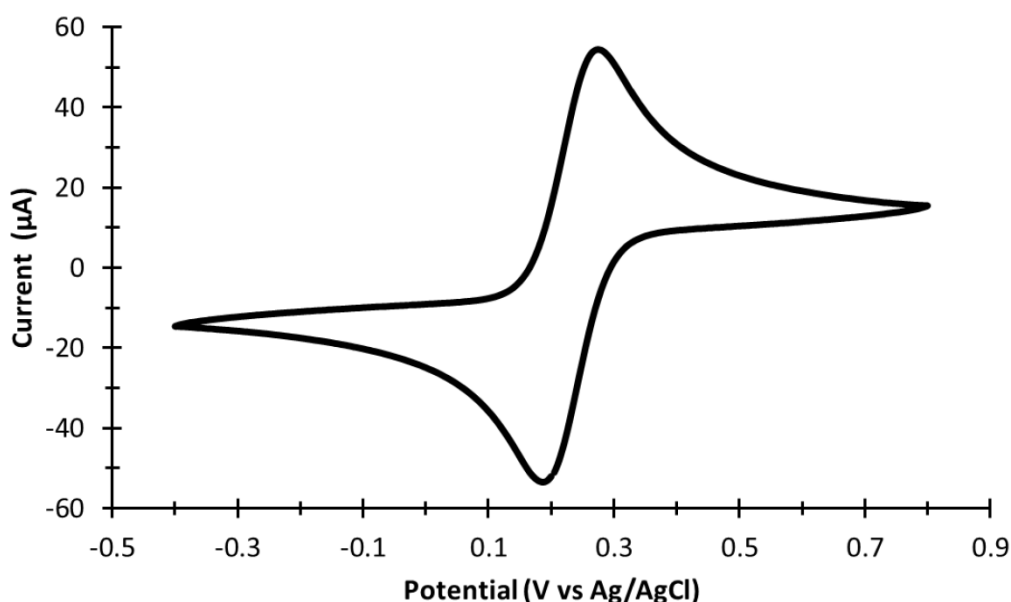
Figure 109: Example CV plot for the calibration of the Ag/AgCl reference electrode. Experimental conditions: starting potential; 0.2 V vs Ag/AgCl; maximum potential: 0.7 V vs Ag/AgCl; scan rate: 50 mV s^{-1}; current range: 1 mA to 1 nA; total number of scans: 8; equilibration time: 10 s.

Table 39: Calculating the Ag/AgCl reference electrode conversion factor.[232]

Run	$E_{p,a}$ (V vs Ag/AgCl)	$E_{p,c}$ (V vs Ag/AgCl)	$E_{1/2}$ (V vs Ag/AgCl)	Reported $E_{1/2}$ (V vs SHE)[232]	Conversion factor for V vs Ag/AgCl to V vs SHE (V)
1	0.275	0.185	0.230		
2	0.285	0.180	0.233	0.425	0.194
3	0.285	0.175	0.230		
		Average	**0.231 ± 0.0014**		

pH Probe Calibration

The pH probe was calibrated prior to each experiment (Figure 110) using four reference buffer solutions from Fisher Scientific, pH 4 (potassium acid phthalate), 7 (phosphate), 9.2 (borate) and 10 (potassium carbonate).
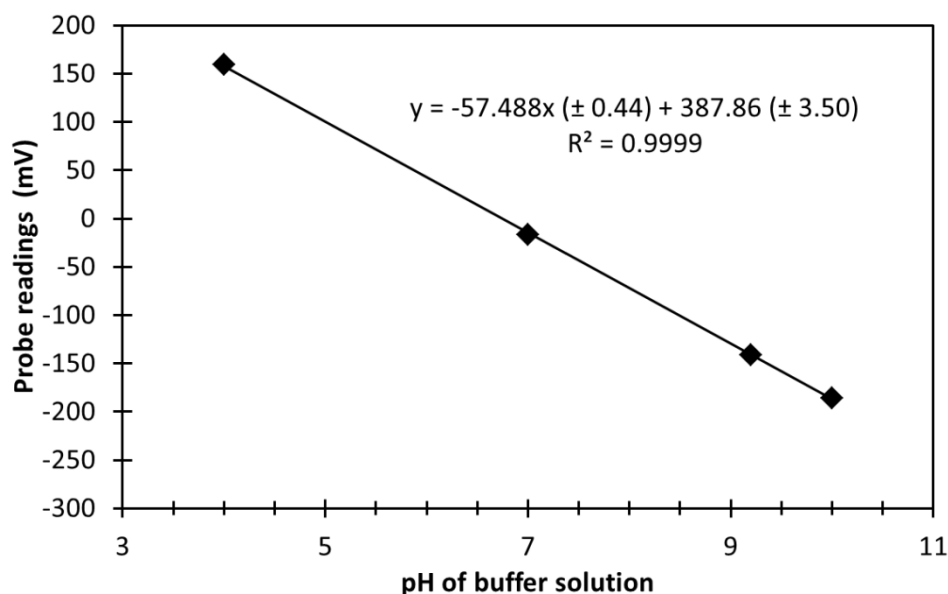
Figure 110: Example pH calibration curve.

3.7.4 Quantifying Hydrogen Production

The level of H_2 production was quantified using a commercial analyser utilising GC combined with an HgO reduction detector (Ametek TA3000R), designed to detect CO and H_2 gas. In operation, CO and H_2 are separated using the gas stream on the GC column and then detected via the reduction of mercuric oxide and the subsequent detection of mercury vapour by UV absorption.[304] In order to reduce the concentration to within the instrument

range; the outlet flow was diluted by a factor of approx. 500 in ultra-pure N_2 gas. The dilution flow rates were continuously monitored in order to correct the diluted instrument readings into H_2 concentrations in the original gas flow. Data from the H_2 detector was logged and analysed using DAQ factory software. Equipment setup, method design and data analysis was performed by Dr James Lee from the Wolfson Atmospheric Chemistry Laboratory (WACL) at the University of York.

3.7.5 Analysis of Electrochemically Formed Precipitates

Solid Precipitate Isolation

Any solid precipitate formed at the end of an electrochemical experiment was separated from the electrolyte via vacuum filtration, using a sinter funnel or filter paper (185 mm, Fischer-Scientific). The solid precipitate was then rinsed with acetone (3 x 40 mL) and left under vacuum for 15 min. The sample was then dried in a vacuum desiccator with P_2O_5 (Sigma-Aldrich, 98.5%) or KOH (Fischer-Scientific, 85.5%) until it reached constant mass.

Powder X-Ray Diffraction (XRD) Analysis

Powder XRD was performed using a Bruker D8 powder diffractometer equipped with a Cu source (K-α1; 1.54 Å, K-α2; 1.54 Å; K-β; 1.39 Å). A Position Sensitive Detector (PSD) Lynxeye detector in a Bragg-Brentano θ-2θ geometry was used and spectra were analysed using Bruker EVA software. Samples were ground to a fine powder and analysed over a 2θ = 5-90° angle with a 0.0066° step size, each averaged over 0.1 s per point for a total acquisition time of 23 min. Generator voltage and current were set to 40 kV and 40 mA respectively. All samples were analysed at room temperature. Reference data was obtained from the online Inorganic Crystal Structure Database (ICSD) when necessary.[277,278]

ThermoGravimetric Analysis-Infrared Spectroscopy (TGA-IR) Analysis

TGA-IR analysis was performed with a Netzsch 409 Simultaneous Thermo Analysis (STA) TGA twinned with a Bruker Equinox 55 FT-IR, which used Netzsch Proteus and

OPUS software respectively. This method measures how much solid samples decompose over a given temperature range and also identifies the released gas during the decomposition via in-line gas IR analysis. Samples were placed in alumina pre-burnt cups and analysed over the temperature range 25 °C to 1300 °C at a ramp rate of 10 °C min^{-1}, with the temperature held at 1300 °C for 15 min (with a total run time of approx. 142 min). The TGA was pre-vacuumed and purged with N_2 gas three times prior to use to ensure any CO_2 detected was from the sample. A N_2 flow rate of 100 mL min^{-1} was run through the Netzsch apparatus during each run. IR spectra were measured between 4000-550 cm^{-1}, with a resolution of 4 cm^{-1} and 64 scans per measurement. A background scan which took 128 scans per measurement was run prior to sample analysis. The FT-IR contained a Mercury Cadmium Telluride (MCT) detector that was cooled using liquid nitrogen prior to each run. The transfer line between the TGA and IR was kept at 200 °C to ensure nothing condensed in the transfer line.

Quantification of CO_2 Trapped in the Electrochemically Formed Solids

TGA-IR analysis of electrochemically formed solids led to the concurrent loss of water and CO_2. To relate the peak area of the CO_2 detected via IR analysis to a corresponding mass loss of CO_2 only, calcium carbonate was analysed ($CaCO_3$, Sigma-Aldrich, $\geq$99%), which releases only CO_2 when heated to 1300 °C. Three different starting masses of $CaCO_3$ were analysed by heating from 25 °C to 1300 °C at a ramp rate of 10 °C min^{-1} (Figure 111a). "Peak area" values were obtained by extracting the IR peak obtained for CO_2 (2200-2430 cm^{-1}) from the whole IR spectrum using OPUS, and then integrating this peak using Origin software (Figure 111b). An average mass loss of CO_2 to "peak area" ratio was obtained, and this average value was used in consequent calculations to determine the moles of CO_2 in the electrochemically formed solids (Table 40). Each electrochemically formed sample was run in triplicate and the average molar value obtained is quoted. All molar values reported for carbon detected in the solids isolated post-CO_2 capture correspond to the total amount of carbon captured in the total mass of solid collected.
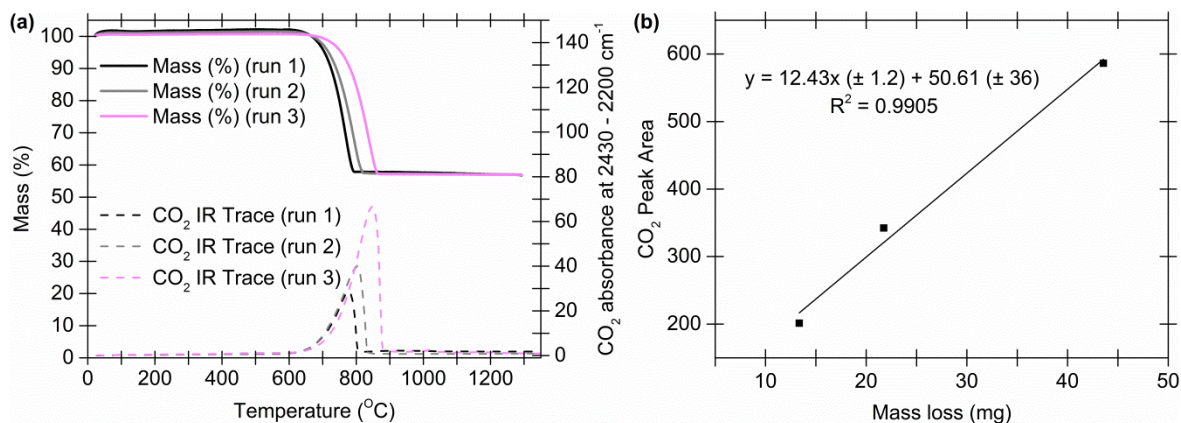
Figure 111: (a) TGA mass loss trace and corresponding CO_2 IR trace obtained for standard $CaCO_3$. (b) Resultant graph relating IR CO_2 peak area (from 2430-2200 cm^{-1}) to mass loss for $CaCO_3$.

Table 40: Calibration data for quantitative TGA-IR analysis.

$CaCO_3$ mass / mg	CO_2 mass loss / mg	CO_2 absorbance-time "peak area"	Mass loss:peak area ratio
30.2	13.4	201.2	0.0636
50.9	21.7	342.2	0.0743
99.9	43.6	586.2	0.0664
		Average	**0.0681 ± 0.0056**

DRIFT (Diffuse Reflectance Infrared Fourier Transform) Analysis

Samples were analysed with a Bruker Equinox 55 FT-IR via DRIFT methodology and Bruker OPUS software. Samples were mixed with freshly ground and oven-dried KBr (Fisher Scientific, spectroscopy grade) in a 1:10 mass ratio. IR spectra were measured between 4000-500 cm^{-1}, with a resolution of 4 cm^{-1} and 128 scans per measurement. A background scan which took 256 scans per measurement was run prior to sample analysis. The FT-IR contained a Mercury Cadmium Telluride (MCT) detector that was cooled using liquid nitrogen prior to each run.

Raman Analysis

Raman spectra were recorded using a 532 nm wavelength laser as the excitation source. A 50x magnification objective lens (0.5x numerical aperture) was used to focus the laser light on a spot size area of approx. 1.5-2 μm in diameter. The total acquisition time was 2 s per

scan over 130 repeated scans for each measurement. A 1650x200 pixels size CCD detector was used to generate Raman graphs. The spectral resolution was approx. 1.5 cm^{-1} per pixel. Analysis and data collection was performed by Konstantinos Chatzipanagis, with guidance from Dr Roland Kröger, from the University of York's Physics Department.

Scanning Electron Microscope-Energy Dispersive X-Ray Spectroscopy (SEM-EDX) Analysis

Solid samples were pelletised with a Specac 15-25 tonne Manual Hydraulic Press prior to analysis. The dried samples were mounted with double-sided carbon adhesive tape onto 12.5 mm diameter aluminium stubs to be examined by SEM-EDX at the York JEOL Nanocentre. To minimize charging for SEM imaging the samples were sputter coated for 5 min with platinum and palladium (15 nm) using a JEOL JFE-2300HR high resolution fine coater (JEOL, USA). An extreme-resolution analytical field emission scanning electron microscope (JEOL JSM-7800F, USA), operating at an acceleration voltage of 5 kV, was used for best resolution. For EDX analysis, a Noran EDX system with an Oxford INCA analyser was employed. The uncoated samples were investigated at an acceleration voltage of 15 kV using a 30 mm two light element Silicon-Lithium (SiLi) detector. Imaging, data collection and analysis was performed by Dr Zhan Wei Scullion, with guidance from Dr Roland Kröger, from the University of York's Physics Department.

Inductively Coupled-Plasma-Mass Spectrometry (ICP-MS)

Samples were digested in 5 mL of nitric acid (HNO_3, TraceSELECT® solvent grade, Sigma-Aldrich) and heated at 110 °C for 3 h. After cooling, the sample was dissolved in 100 mL of ultrapure water and diluted further if required. Samples were analysed with an Agilent 7700x ICP-MS spectrometer, using nickel sample and skimmer cones whilst under helium. Each sample was taken up for 60 s, stabilised for 40 s, and washed for 60 s (with 5% HCl for 30 s, and 2% HNO_3 for 30 s). Samples were run three times and the mean value of ppm or ppb for the desired element was used to determine the moles of the

element in the samples. Samples were run and analysed by Dr Helen Parker, Andrea Muñoz García or Dr María García Gallarreta from the Green Chemistry Centre of Excellence at the University of York, at the Biorenewables Development Centre (BDC) in the York Science Park. All molar values reported for aluminium and sodium detected in the solid isolated post-CO_2 capture correspond to the <u>total</u> amount of aluminium and sodium in the <u>total</u> mass of solid collected respectively.

Solid-state NMR methodology

All solid-state NMR experiments, along with sample analysis, were designed and conducted by Dr Pedro M. Aguiar, from the University of York's Chemistry Department. All solid-state NMR figures, tables and analyte information were also produced and provided by Dr Pedro M. Aguiar.

All solid-state NMR spectra were collected using a Bruker AvanceIII HD 400 spectrometer equipped with a 9.4 T widebore magnet and a 4 mm MAS probe. Spectra were acquired at a regulated temperature of ca. 298 K (accounting for heating from rotational friction) for most samples. In order to minimise decomposition, spectra of sodium carbonate decahydrate were acquired at ca. 278 K.

$^{13}C\{^1H\}$ Cross Polarisation Magic-Angle Spinning (CPMAS) experiments employed a 2 ms linearly-ramped contact pulse (^1H channel), spinning rates of 1.25 to 10 kHz, recycle delays of 1-60 s, spinal-64 heteronuclear decoupling (at $\nu_{rf} = 85$ kHz) and are a sum of 48-3000 co-added transients. For the crystalline model systems with long ^1H T1s a flip-back pulse was utilised to reduce the necessary recycle delay. $^{13}C\{^1H\}$ Bloch-decay experiments for anhydrous sodium carbonate (Na_2CO_3), sodium sesquicarbonate ($Na_3H(CO_3)_2 \cdot 2H_2O$) and electrochemically formed precipitates/samples were acquired using a 1.66 μs pulse (30-degree tip-angle) with recycle delays of 30-120 s. Chemical shifts are reported with respect to TMS, and were referenced using adamantane ($C_{10}H_{16}$, $\delta = 29.50$ and 38.55 ppm) as an external secondary reference.

^{23}Na{^{1}H} MAS experiments were acquired using a Bloch-decay sequence employing a 0.83 μs pulse (at ν_{rf} = 42 kHz), spinning rates of 5 to 14 kHz (10 kHz for most samples), optimized recycle delays of 1-5 s, spinal-64 heteronuclear decoupling (at ν_{rf} = 85 kHz) and are a sum of 64-512 co-added transients. Relative frequencies are reported with respect to 1 M NaCl, used as an external secondary reference.

^{23}Na and ^{23}Na{^{1}H} Multiple Quantum Magic-Angle Spinning (MQMAS) experiments were acquired using a z-filtered experiment with Fast Amplitude Modulated pulse train (2 loops) for the conversion step.[305] The hard pulses were 4.5 and 2.2 μs (ν_{rf} = 83 kHz) and the selective pulse was 9 μs (ν_{rf} = 14 kHz). Spectra were rotor-synchronised in the indirect dimension and acquired at spinning rates of 5-10 kHz, with recycle delays of 1-5 s, and spinal-64 heteronuclear decoupling (at ν_{rf} = 85 kHz). For crystalline samples sufficient increments were collected to cover 8-10 ms of evolution in T1, whereas for the electrochemically formed precipitates the signal decayed within 2 ms. All displayed MQMAS spectra have been processed including a shearing transformation, and the indirect dimension scaled following the C_{3b} convention.[306]

^{27}Al MAS experiments were acquired using a Bloch-decay sequence employing a 0.9 μs pulse (at ν_{rf} = 42 kHz), spinning rates of 10-14 kHz, optimized recycle delays of 2 s, and are a sum of 32-128 co-added transients. Relative frequencies are reported with respect to 1 M aluminium nitrate ($Al(NO_3)_3$), used as an external secondary reference.

^{7}Li MAS experiments were acquired using a Bloch-decay sequence employing a 0.8 μs pulse (at ν_{rf} = 50 kHz), spinning rates of 5-14 kHz, optimized recycle delays of 5 s and are a sum of 128 co-added transients. Relative frequencies are reported with respect to 1 M LiCl, used as an external secondary reference.

3.7.6 Electrolyte Isolation and Analysis Post-CO$_2$ Capture

After each electrochemical experiment, electrolytes were kept in Parafilm® sealed falcon tubes. Bulk analysis was performed according to Vogel's titration methods (*vide infra*).[237]

Titrations were performed with a 50 mL burette (± 0.05 mL) and all samples were stirred continuously during titration. A 1000-5000 µL automated pipette was used for volume measurements <5 mL. All titrations were run in triplicate, and the average titrant was used in subsequent calculations.

Titration Preparation and Standardisation

A 0.01 M sodium hydroxide (carbonate free) solution was made following Vogel's procedure,[237] by adding NaOH (25 g) to 25 mL of water. After leaving to settle, a 0.325 mL aliquot was then added to 500 mL of water. Phenolphthalein indicator was made by dissolving 1.25 g of phenolphthalein in 125 mL ethanol and 125 mL of water. A 1 M HCl solution was made by adding 42 mL of concentrated HCl (12 M, 37 %) to 500 mL of water, and further diluted by a factor of 10 to obtain 0.1 M HCl.

Standardisation of 0.1 M HCl and 0.01 M NaOH was performed using Vogel's methods.[237] Standardisation of 0.1 M HCl was performed with 0.1 M sodium carbonate. Pre-heated sodium carbonate (5.3 g) was dissolved in 500 mL of water, and then titrated with 0.1 M HCl and methyl orange-indigo carmine as an indicator. Methyl orange-indigo carmine was prepared by dissolving 0.25 g of methyl orange and 0.625 g of indigo carmine in 250 mL of water. Standardisation of 0.01 M NaOH was performed using 0.01 M HCl (made by diluting 0.1 M HCl by a factor of 10) and phenolphthalein as an indicator.

Bicarbonate, and CO$_2$, Quantification

This was performed according to Vogel's titration method.[237] A measured excess of 0.01 M NaOH was added to a known volume of electrolyte to convert all bicarbonate anions into carbonate anions. A few drops of phenolphthalein were then added to form a pink solution, followed by a slight excess of 10% BaCl$_2$ solution (58.7 g of BaCl$_2$ in 500 mL of water) to form BaCO$_3$. The analyte was then heated at 70 °C using a magnetic stirrer hotplate for 1 min. The solution was then taken off the heat and titrated immediately with 0.01 M HCl, until the indicator turned from pink to colourless. The added volume of

0.01 M HCl was used to determine the excess volume of NaOH added in the initial step, and thus the exact volume of NaOH that was required to convert all bicarbonate anions into carbonate anions. Hence the moles of bicarbonate and therefore CO_2 in the electrolyte were calculated. All molar values reported for carbon detected in solution post-CO_2 capture correspond to the <u>total</u> amount of carbon captured in the <u>total</u> volume of electrolyte.

Carbonate Quantification

To a measured aliquot of fresh electrolyte, a few drops of methyl orange-indigo carmine indicator were added to turn the solution grey. The solution was then titrated with 0.01 M HCl to turn any carbonate (and bicarbonate) anions into carbonic acid, and until the solution turned violet. In order to differentiate between quantifying carbonate and bicarbonate anions, the titrate volume obtained for bicarbonate anions (detailed in "Bicarbonate, and CO_2, Quantification", using the barium chloride titration method, was taken away from the titrate volume obtained via this method.[237] The difference in titrate volumes for a few samples were insignificant, and therefore it was deemed that the moles of carbonate anions in the electrolyte post-CO_2 capture were negligible via this method.

Freeze-drying Electrolytes

A VirTis SP Scientific sentry 2.0 freeze-drier was used to freeze-dry electrolyte samples, with temperatures held between -105 °C and -110 °C and a vacuum pressure of approx. 27 mTorr (3.6 x 10^{-5} bar).

3.7.7 Sustainable Materials

Seawater Collection and Analysis

Seawater (3 L) was collected from the east beach along the coast of the seaside town Whitby, North Yorkshire, UK, at 54° 29' 31.0" N 0° 36' 28.8" W during early July 2015 (Figure 112).
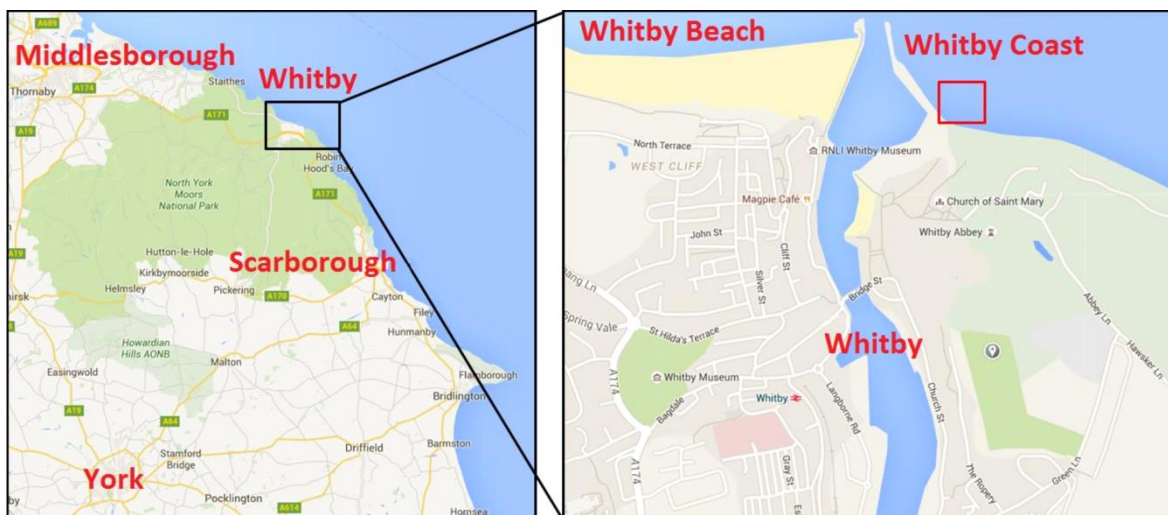
Figure 112: Geographical location of where seawater was collected.

All 3 L were filtered through cellulose nitrate membrane filters (GC Whatman, pore size 0.2 μm, 47 mm diameter) to remove any sand or solid particulates, as well as bacteria. The seawater was kept in sealable falcon bottles at -15 °C, to prevent the growth of any bacterial or fungi, and left to warm up to room temperature before using in any experiments. The seawater was analysed via ICP-MS to determine and quantify any trace elements present (Table 41).

Table 41: Quantification of trace elements in seawater via ICP-MS.[a,b]

Na / %	Mg / %	K / %	Ca / %	S / %
1.23 ± 5.1	0.15 ± 0.5	0.05 ± 0.4	0.05 ± 3.9	0.15 ± 6.6

a) A pure seawater sample was analysed and all elements that were detected are shown**.**
b) Errors quoted for each element are error percentages of quoted values.

4.0 Appendices

4.1 Appendix 1: Data for Chapter 2

4.1.1 Comparison of cyclic carbonate syntheses via CO_2 insertion into epoxides

All of the non-metal and metal based catalytic systems discussed in "Chapter 2: The Development of Chromium(III) Salophen Complexes for Cyclic Carbonate and Oxazolidinone Synthesis, 2.1 Introduction, 2.1.4 Carbon dioxide Insertion into Epoxides" are summarised in Table A1 and Table A2 respectively.

Table A1: Cyclic carbonate synthesis in the absence of metal complexes.
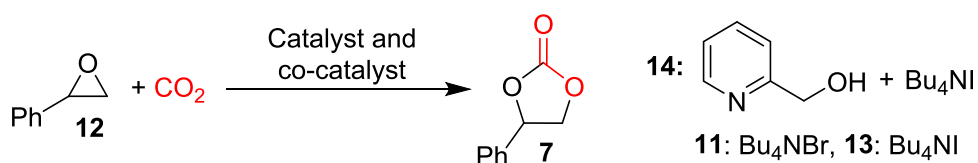
Catalyst	Co-catalyst	Substrate	Pressure[a] / bar	Temperature / °C	Time / h	Yield[b] / %	TOF[c] / h^{-1}
N/A	**11** and **13**	**12**	1	120	4	83	0.24
N/A	**14**	**12**	1	25	20	73	0.46
N/A	**14**	**12**	1	45	20	85	0.53

a) Pressure of CO_2.
b) Isolated yield of cyclic carbonate product.
c) TOF = mol of product / ((mol of catalyst) x time).

Table A2: Cyclic carbonate synthesis using metal salophen complexes.

11: Bu_4NBr; 13: Bu_4NI; 15: N-MeIm; 16: DMAP; 23: PPNBr

12, 21, 24, 36, 63

4, 7, 22, 25, 64

7, 12: R = Ph; 21, 22: R = CH_2Cl; 24, 25: R = ^nBu; 4, 36: R = CH_3; 63, 64: R = CH_2OMe
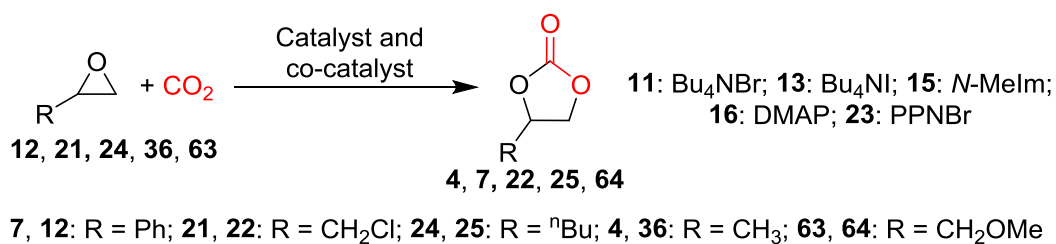
Catalyst	Co-catalyst	Substrate	Pressure[a] / bar	Temperature / °C	Time / h	Yield[b] / %	TOF[c] / h^{-1}
17	11	12	1	26	24	85[d]	1.42
18	11	12	1	26	24	91[d]	1.52
19	11	12	1	26	24	93[d]	1.55
20	13	21	10	30	2	91	91
20	23	24	10	90	2	36[d]	36,000
26	11	12	10	50	24	85	0.71
30	16	12	3.5	85	7	99[d]	14.1
30	16	12	3.5	75	12	99[d]	8.25
27	15	12	100	80	6	50[d]	24.3
27	11	12	1	25	24	20[d]	0.33
33	16	12	20	100	1.5	98[d]	65.3
34	-	36	6	20	20	45[d]	22.4
35	-	36	6	20	36	30[d]	8.19
42	11	12	1	25	24	98[d]	1.63
43	-	12	1	26	6	89	6.47
51	23	12	1	25	24	100[d]	2.78
51	11	12	1	25	24	100[d]	1.67

a) Pressure of CO_2.
b) Isolated yield of cyclic carbonate product.
c) TOF = mol of product / ((mol of catalyst) x time).
d) Conversion of epoxide into cyclic carbonate product, determined via GC or ^1H NMR spectroscopy.

Table A2 (cont.): Cyclic carbonate synthesis using metal salophen complexes.
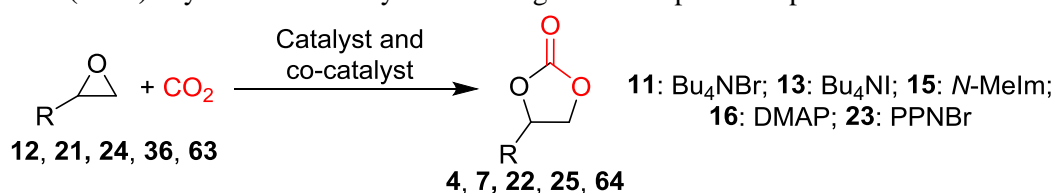
11: Bu_4NBr; 13: Bu_4NI; 15: N-MeIm;
16: DMAP; 23: PPNBr

12, 21, 24, 36, 63

4, 7, 22, 25, 64

7, 12: R = Ph; 21, 22: R = CH_2Cl; 24, 25: R = ^nBu; 4, 36: R = CH_3; 63, 64: R = CH_2OMe

Catalyst	Co-catalyst	Substrate	Pressure[a] / bar	Temperature / °C	Time / h	Yield[b] / %	TOF[c] / h^{-1}
57	11	12	1	25	24	100[d]	2.78
58	-	12	10	80	18	91[d]	10.1
61	-	63	10	85	18	100[d]	2.22

a) Pressure of CO_2.
b) Isolated yield of cyclic carbonate product.
c) TOF = mol of product / ((mol of catalyst) x time).
d) Conversion of epoxide into cyclic carbonate product, determined via GC or ^1H NMR spectroscopy.

4.1.2 Analysis of crystal Cry1

Experimental

Single crystals of $C_{10}H_{12.67}N_{0.67}O_{1.33}$ (**Cry1**) were grown from THF. A suitable crystal was selected and analysed on a SuperNova, Dual, Cu at zero, Eos diffractometer. The crystal was kept at 110.05 ± 10 K during data collection. Using Olex2[307] the structure was solved with the ShelXT[308] structure solution program using Direct Methods and refined with the ShelXL[309] refinement package using Least Squares minimisation. Crystal isolation and data collection was performed by Dr Adrian C. Whitwood, whom solved the crystal structure along with Rachel R. Bean from the University of York's Chemistry Department. Crystal data presented in Table A3-Table A6 were all provided by Dr Adrian C. Whitwood.

Table A3: Crystal data and structure refinement for **Cry1**.

Empirical formula	$C_{10}H_{12.67}N_{0.67}O_{1.33}$
Formula weight	163.54
Temperature/K	110.05(10)
Crystal system	monoclinic
Space group	C2/c
a/Å	17.8343(6)
b/Å	12.4405(4)
c/Å	13.0921(5)
$\alpha/°$	90
$\beta/°$	107.301(4)
$\gamma/°$	90
Volume/Å^3	2773.29(17)
Z	12
$\rho_{calc}g/cm^3$	1.175
μ/mm^{-1}	0.618
F(000)	1056.0
Crystal size/mm^3	$0.2008 \times 0.1607 \times 0.1298$
Radiation	CuKα ($\lambda = 1.54184$)
2Θ range for data collection/°	8.804 to 142.972
Index ranges	$-21 \leq h \leq 13, -15 \leq k \leq 14, -13 \leq l \leq 15$
Reflections collected	4991
Independent reflections	2640 [$R_{int} = 0.0124, R_{sigma} = 0.0171$]
Data/restraints/parameters	2640/0/168
Goodness-of-fit on F^2	1.061
Final R indexes [I>=2σ (I)]	$R_1 = 0.0367, wR_2 = 0.0967$
Final R indexes [all data]	$R_1 = 0.0414, wR_2 = 0.1009$
Largest diff. peak/hole / e Å^{-3}	0.23/-0.22

Table A4: Bond Lengths for **Cry1**.

Atom	Atom	Length / Å	Atom	Atom	Length / Å
O1	C9	1.3826(14)	C7	C6	1.4002(16)
O1	C11	1.4280(16)	C10	C5	1.3885(18)
O2	C6	1.3713(14)	C12	C12[1]	1.551(2)
N1	C13	1.4109(15)	C6	C5	1.4063(17)
N1	C12	1.4680(14)	C5	C4	1.5403(16)
C9	C8	1.3770(16)	C14	C15	1.3828(19)
C9	C10	1.3910(17)	C15	C15[1]	1.389(3)
C8	C7	1.3916(16)	C4	C3	1.5370(19)
C13	C13[1]	1.401(2)	C4	C1	1.535(2)
C13	C14	1.3907(16)	C4	C2	1.529(2)
C7	C12	1.5098(15)			

[1]1-X,+Y,3/2-Z

Table A5: Bond Angles for **Cry1**.

Atom	Atom	Atom	Angle / °	Atom	Atom	Atom	Angle / °
C9	O1	C11	117.23(9)	C7	C12	C12[1]	109.84(7)
C13	N1	C12	117.15(9)	O2	C6	C7	120.32(10)
O1	C9	C10	115.18(10)	O2	C6	C5	118.49(10)
C8	C9	O1	124.53(11)	C7	C6	C5	121.16(11)
C8	C9	C10	120.28(11)	C10	C5	C6	117.01(11)
C9	C8	C7	119.40(10)	C10	C5	C4	121.45(11)
C13[1]	C13	N1	119.80(6)	C6	C5	C4	121.46(11)
C14	C13	N1	120.88(11)	C15	C14	C13	121.01(12)
C14	C13	C13[1]	119.22(7)	C14	C15	C15[1]	119.72(8)
C8	C7	C12	118.25(10)	C3	C4	C5	111.22(11)
C8	C7	C6	120.00(10)	C1	C4	C5	108.85(10)
C6	C7	C12	121.35(10)	C1	C4	C3	110.02(13)
C5	C10	C9	122.13(11)	C2	C4	C5	111.35(12)
N1	C12	C7	111.79(9)	C2	C4	C3	107.15(12)
N1	C12	C12[1]	107.92(7)	C2	C4	C1	108.19(13)

[1]1-X,+Y,3/2-Z

Table A6: Torsion Angles for **Cry1**.

A	B	C	D	Angle / °	A	B	C	D	Angle / °
O1	C9	C8	C7	-179.72(10)	C7	C6	C5	C10	0.24(16)
O1	C9	C10	C5	-179.26(10)	C7	C6	C5	C4	176.91(10)
O2	C6	C5	C10	-177.61(10)	C10	C9	C8	C7	1.42(16)
O2	C6	C5	C4	-0.94(16)	C10	C5	C4	C3	-124.68(13)
N1	C13	C14	C15	173.97(11)	C10	C5	C4	C1	113.94(14)
C9	C8	C7	C12	171.16(9)	C10	C5	C4	C2	-5.25(17)
C9	C8	C7	C6	-1.70(16)	C12	N1	C13	C13[1]	-24.78(19)
C9	C10	C5	C6	-0.53(17)	C12	N1	C13	C14	158.78(11)
C9	C10	C5	C4	-177.20(11)	C12	C7	C6	O2	6.04(16)
C8	C9	C10	C5	-0.30(17)	C12	C7	C6	C5	-171.77(10)
C8	C7	C12	N1	143.02(10)	C6	C7	C12	N1	-44.22(14)
C8	C7	C12	C12[1]	-97.20(13)	C6	C7	C12	C12[1]	75.56(13)
C8	C7	C6	O2	178.68(10)	C6	C5	C4	C3	58.81(16)
C8	C7	C6	C5	0.87(16)	C6	C5	C4	C1	-62.57(16)
C13	N1	C12	C7	169.60(9)	C6	C5	C4	C2	178.24(12)
C13	N1	C12	C12[1]	48.69(14)	C11	O1	C9	C8	12.86(16)
C13[1]	C13	C14	C15	-2.5(2)	C11	O1	C9	C10	-168.23(10)
C13	C14	C15	C15[1]	0.1(2)					

[1] 1-X,+Y,3/2-Z

4.2 Appendix 2: Data for Chapter 3

4.2.1 Results and Discussion Part 1: Performing Electrochemical CO_2 Sequestration and Mineralisation. Applying a current to the aluminium-only anode cell in the absence of CO_2

Electrochemical Data

As discussed in "Chapter 3, Section 3.2.2, Carbon dioxide capture with an aluminium-only anode cell", upon the application of a 24 h 10 mA current to the aluminium-only anode cell in the absence of CO_2, higher pH levels were reported with no change in the electrode potentials (Figure A1).

Solid Analysis

A solid was formed during this experiment. Powder XRD analysis of the solid identified NaCl and $Al(OH)_3$ as the only crystalline phases, with the rising baseline indicating the presence of a secondary amorphous species (Figure A2).[278,310] No carbonate stretch was detected via FT-IR (DRIFT) analysis (Figure A3). TGA-IR analysis demonstrated that, as expected, negligible levels of carbon are captured in the solid (0.018 mmol, Figure A4). This indicates that the solid primarily contained $Al(OH)_3$ with NaCl crystallites on the surface.
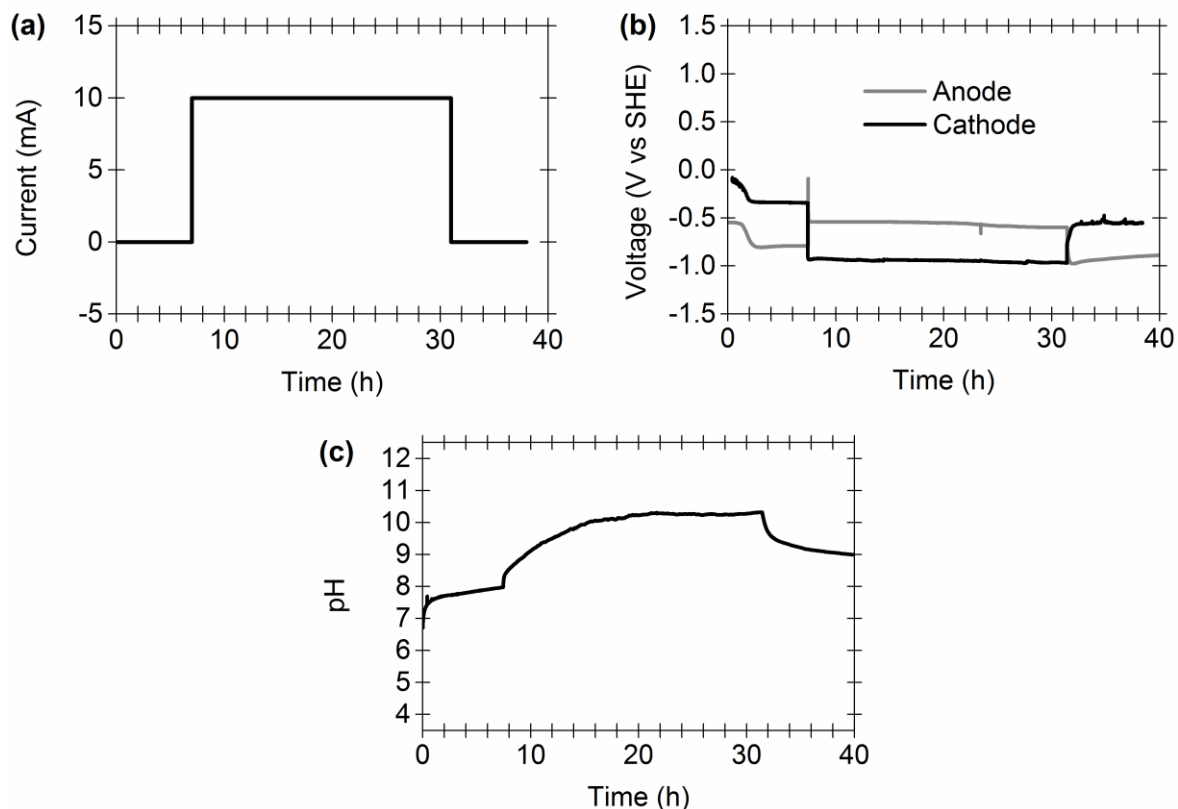
Figure A1: Carbon dioxide capture with 1 M NaCl in the aluminium-only anode cell in the absence of CO_2. (a) Programmed current-time steps; (b) Resultant changes to the electrochemical potential of the anode (grey line) and cathode (black line); (c) Corresponding changes in solution pH. Other reaction conditions: a continuous gas flow of 14.0 mL min^{-1} N_2, and 180 mL of 1 M NaCl.
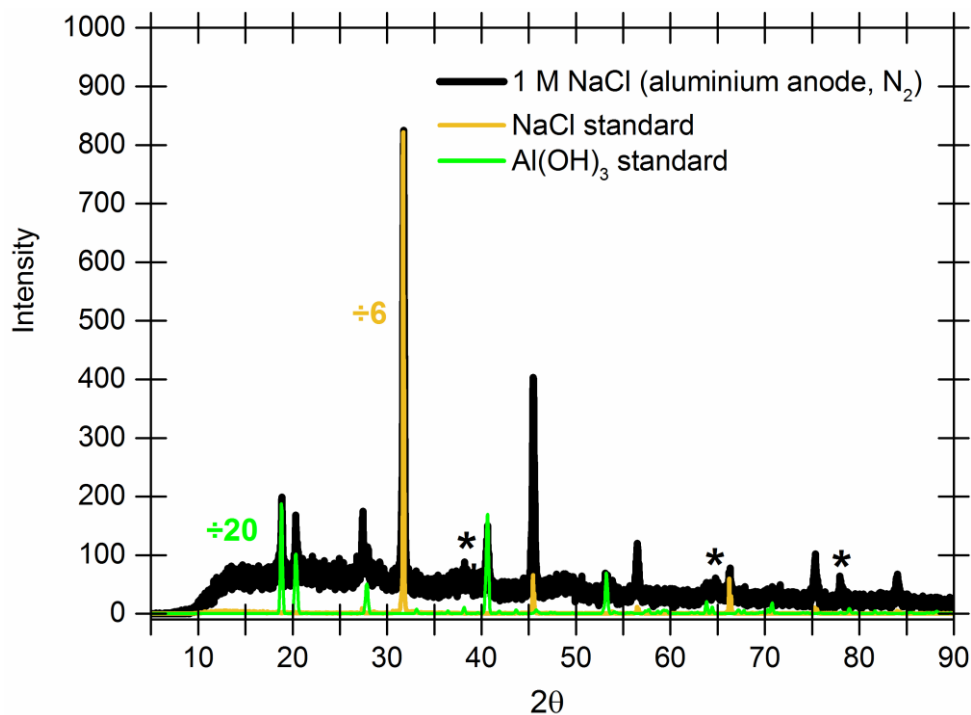
Figure A2: Powder XRD analysis of the electrochemically formed solid in the aluminium-only anode cell in the absence of CO_2, compared to NaCl and Al(OH)$_3$.[277,278,310]
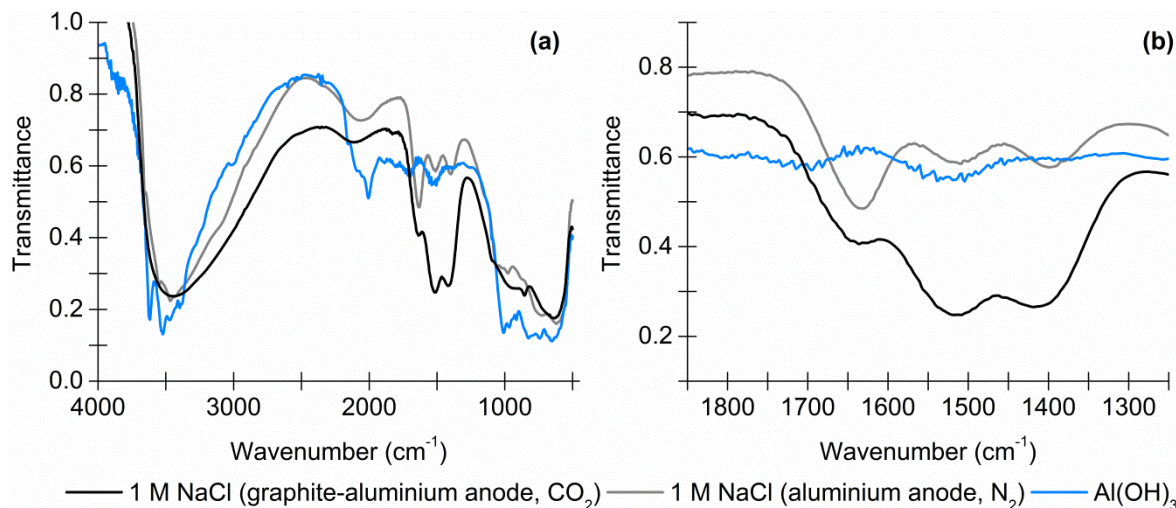
Figure A3: Comparing FT-IR (DRIFT) spectra of the precipitate isolated in the graphite-aluminium anode cell in the presence of CO_2 (black line), absence of CO_2 (grey line) and standard $Al(OH)_3$ (blue line). (a) Full spectrum; (b) Carbonyl stretch region.
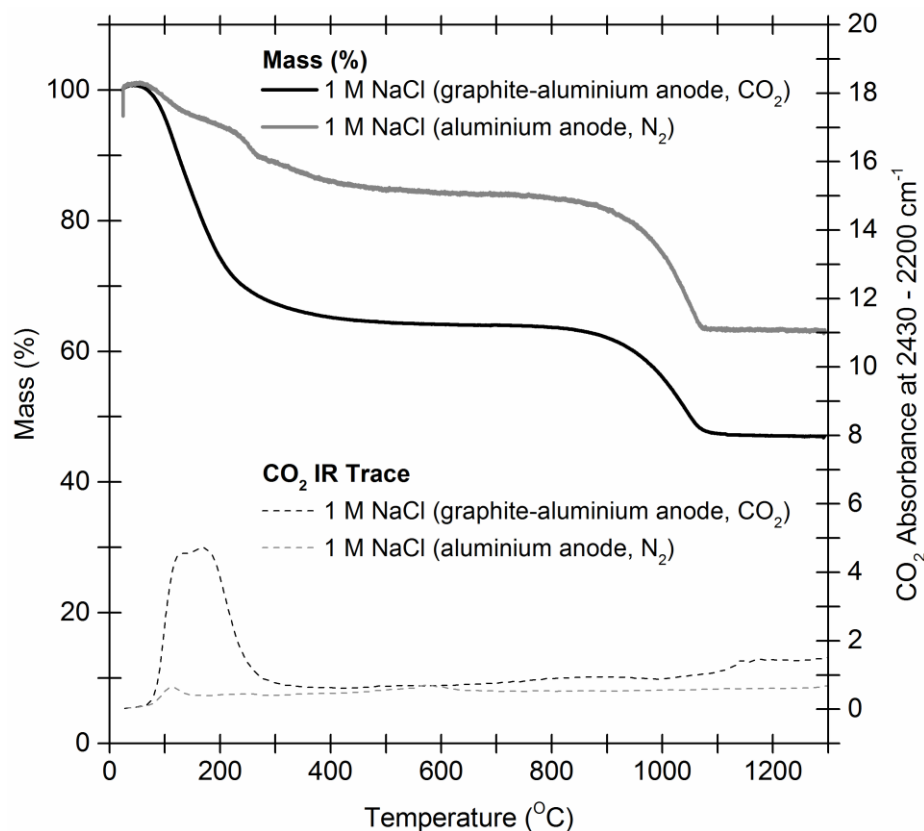
Figure A4: Comparing TGA-IR analysis and consequent CO_2 IR spectra of the precipitate isolated post-CO_2 capture in the graphite-aluminium anode cell (black line), and from the aluminium-only anode cell in the absence of CO_2 (grey line).

4.2.2 Results and Discussion Part 1: Performing Electrochemical CO_2 Sequestration and Mineralisation. Applying a current to the graphite-aluminium anode cell in the absence of CO_2

Electrochemical Data

As discussed in "Chapter 3, Section 3.2.3, Carbon dioxide capture with a graphite-aluminium anode cell, Carbon dioxide levels, anode and cathode voltages and pH levels", upon application of a 24 h 10 mA current to the graphite-aluminium anode cell in the absence of CO_2 (Figure A5), higher pH levels were reported with no change in the electrode potentials (akin to the results with the aluminium-only anode cell, Figure A1).
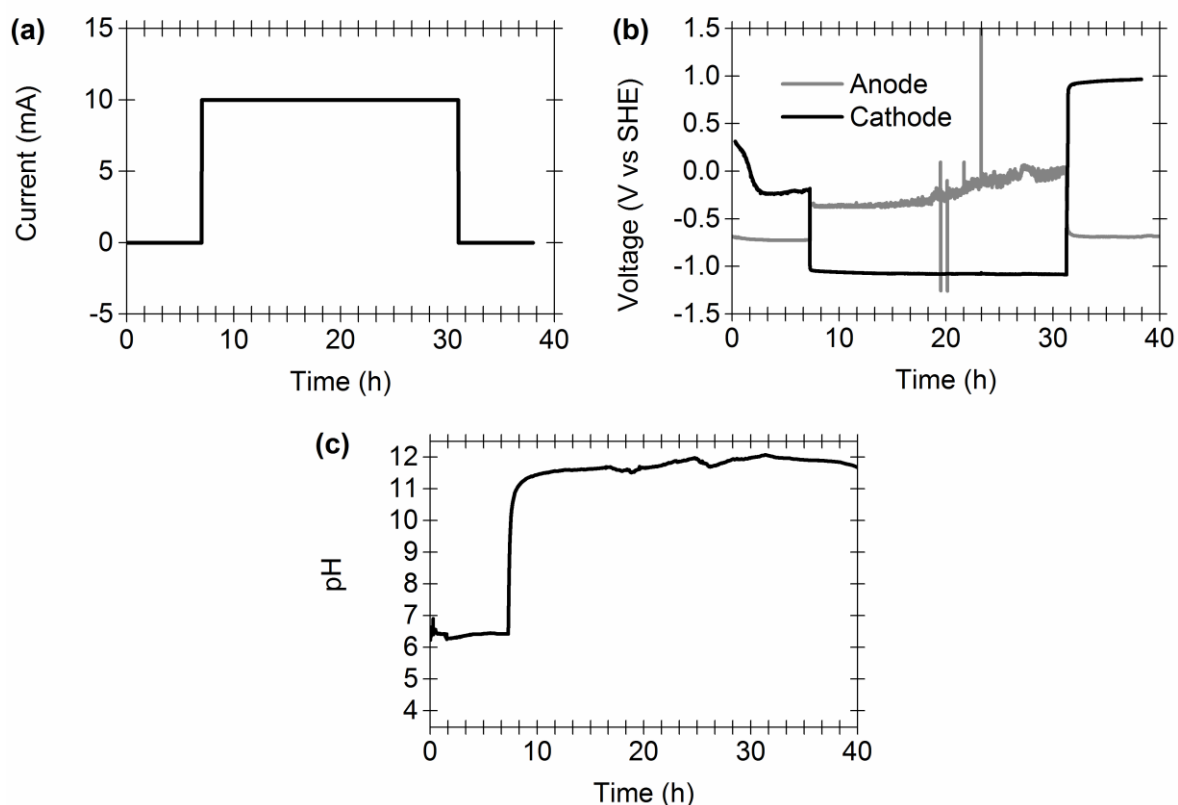
Figure A5: Carbon dioxide capture with 1 M NaCl in the graphite-aluminium anode cell in the absence of CO_2. (a) Programmed current-time steps; (b) Resultant changes to the electrochemical potential of the anode (grey line) and cathode (black line); (c) Corresponding changes in solution pH. Other reaction conditions: a continuous gas flow of 14.0 mL min^{-1} N_2, and 60 mL of 1 M NaCl.

The lack of solid formation can be expected as no CO_2 was flowed through the cell, and hence no aluminium hydroxycarbonate species would form. The Pourbaix diagram of

aluminium (Chapter 3, Section 3.2.2, Figure 47) suggests that the water soluble aluminium species Al(OH)$_4$⁻ would form at this high pH, hence no aluminium based solid was also isolated.[230,242]

4.2.3 Results and Discussion Part 1: Performing Electrochemical CO$_2$ Sequestration and Mineralisation. Data Summary

The key results obtained by promoting electrochemical CO$_2$ capture with 1 M NaCl in the anode cell and analysis of the solid as a result of CO$_2$ mineralisation, are summarised in Figure A6. Elemental analysis of the electrochemically formed solids obtained with different electrolytes, as well as levels of carbon captured in the electrolyte and solid, are summarised in Table A7. The energy requirements for carbon capture with different anodes in the electrochemical cell and electrolytes are summarised in Table A8.
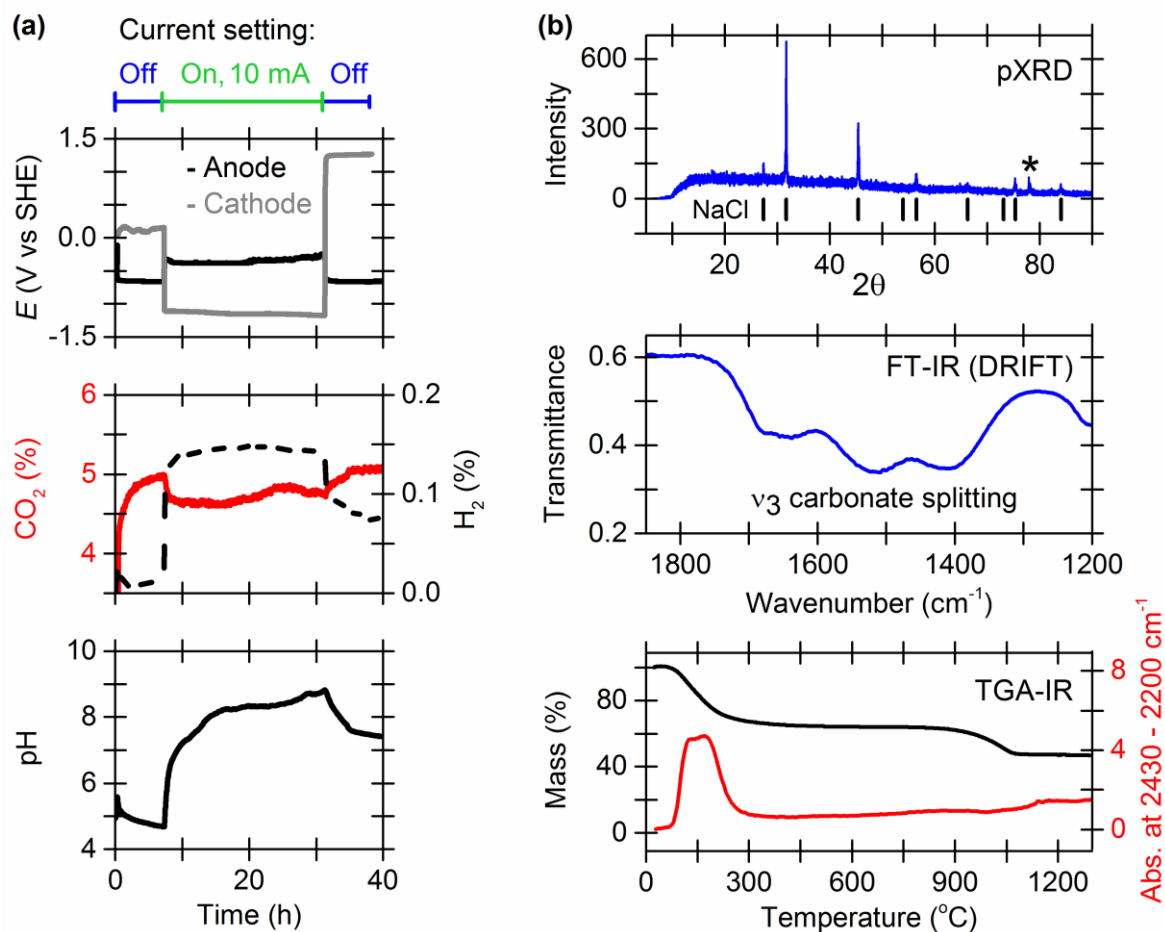
Figure A6: (a) Carbon dioxide fixation using an "on" 24 h 10 mA current setting with 1 M NaCl in the mixed graphite-aluminium anode cell and solid analysis. (top) The voltage of the graphite-aluminium anode and platinum cathode; (middle) CO_2 and H_2 content in the exit gas stream; (bottom) solution pH. (b) Analysis of the precipitate isolated after carbon capture. (top) Powder XRD, the broad featureless signal is due to disordered material, while the sharp features are assigned to crystalline NaCl (reference values shown by vertical black lines), * metal plate (Al) sample holder; (middle) FT-IR (DRIFT) analysis; (bottom) TGA-IR analysis.

Table A7: Sodium, aluminium and total carbon levels captured using different electrolytes in the graphite-aluminium anode cell.[a]

1 M Electrolyte	Solid mass / g	Na in solid[b] / mmol	Al in solid[b] / mmol	C in solid[c] / mmol	C in solution[d] / mmol	C total[e] / mmol
NaCl, Run 1[f]	0.62	7.2 ± 0.2	4.1 ± 0.4	0.6 ± 0.1	1.3 ± 0.1	1.9 ± 0.1
NaCl, Run 2[f]	0.63	6.2 ± 0.2	3.9 ± 0.2	1.0 ± 0.2	1.7 ± 0.1	2.7 ± 0.2
NaCl, Run 3[f]	0.46	3.4 ± 0.2	3.3 ± 0.3	1.0 ± 0.1	1.9 ± 0.1	2.9 ± 0.1
NaCl, Run 4[f]	0.60	8.4 ± 0.5	4.1 ± 0.4	1.1 ± 0.1	2.6 ± 0.1	3.7 ± 0.1
NaCl average	0.58 ± 0.08	6.3 ± 2.1	3.9 ± 0.4	0.9 ± 0.2	1.9 ± 0.5	2.8 ± 0.7
LiCl	0.34	1.6 ± 0.1	2.3 ± 0.1	0.4 ± 0.01	0.8 ± 0.1	1.2 ± 0.1
CsCl	0.96	5.4 ± 0.1	3.4 ± 0.2	0.8 ± 0.1	1.7 ± 0.1	2.5 ± 0.2

a) All molar values reported for sodium, aluminium and carbon detected in the solid and carbon in the solution post-CO_2 capture, correspond to the total moles of sodium aluminium and carbon in the total mass of solid and the total amount of carbon in the total volume of electrolyte, respectively.
b) Quantified via ICP-MS analysis.
c) Quantified via TGA-IR analysis.
d) Quantified via titration of electrolyte.
e) Combination of the total carbon captured in the total volume and mass of solution and solid respectively.
f) The four runs correspond to the four experiments in Figure 55.

Table A8: Energy required for CO_2 sequestration and mineralisation using different anodes and electrolytes.

Electrolyte and anode	E_{Cell} [a] / V	E_{Cell} energy[b] / J	C total[c] / mmol	Energy of C capture[d] / kJ mol^{-1}
NaCl, graphite anode	2.39	2065	1.4 ± 0.1[e]	1475
NaCl, aluminium anode	0.58	501	0.3 ± 0.02[f]	1670
NaCl, graphite-aluminium anode[h]	0.81 ± 0.05	700 ± 40	2.8 ± 0.7	250
LiCl, graphite-aluminium anode	0.80	695	1.2 ± 0.1	579
CsCl, graphite-aluminium anode	0.72	618	2.5 ± 0.2	247

a) Difference between the anode and platinum cathode voltage.
b) The E_{Cell} value is converted into watts (watt = voltage x current). Watts are equivalent to J s^{-1}, therefore J s^{-1} x time of current application is equivalent to joules.
c) Combination of the total carbon captured in the total volume and mass of solution and solid respectively.
d) (E_{Cell}/1000) ÷ (C total/1000).
e) Carbon captured in the electrolyte. No solid was formed.
f) Carbon captured in the electrochemically formed solid. No C was detected in the electrolyte.
h) Average results obtained from the four experiments in Figure 55.

4.2.4 Results and Discussion Part 2: Promoting Cost-effective and Sustainable Electrochemical CO_2 Capture and Mineralisation. Data Summary

A summary of the electrochemical data obtained for Section 3.4 is shown in Figure A7. The correlation between NaCl concentration and E_{Cell} for different experiments is summarised in Figure A8. The carbon capture levels and consequent energy requirements for all trialled systems is summarised in Table A9 and Table A10.
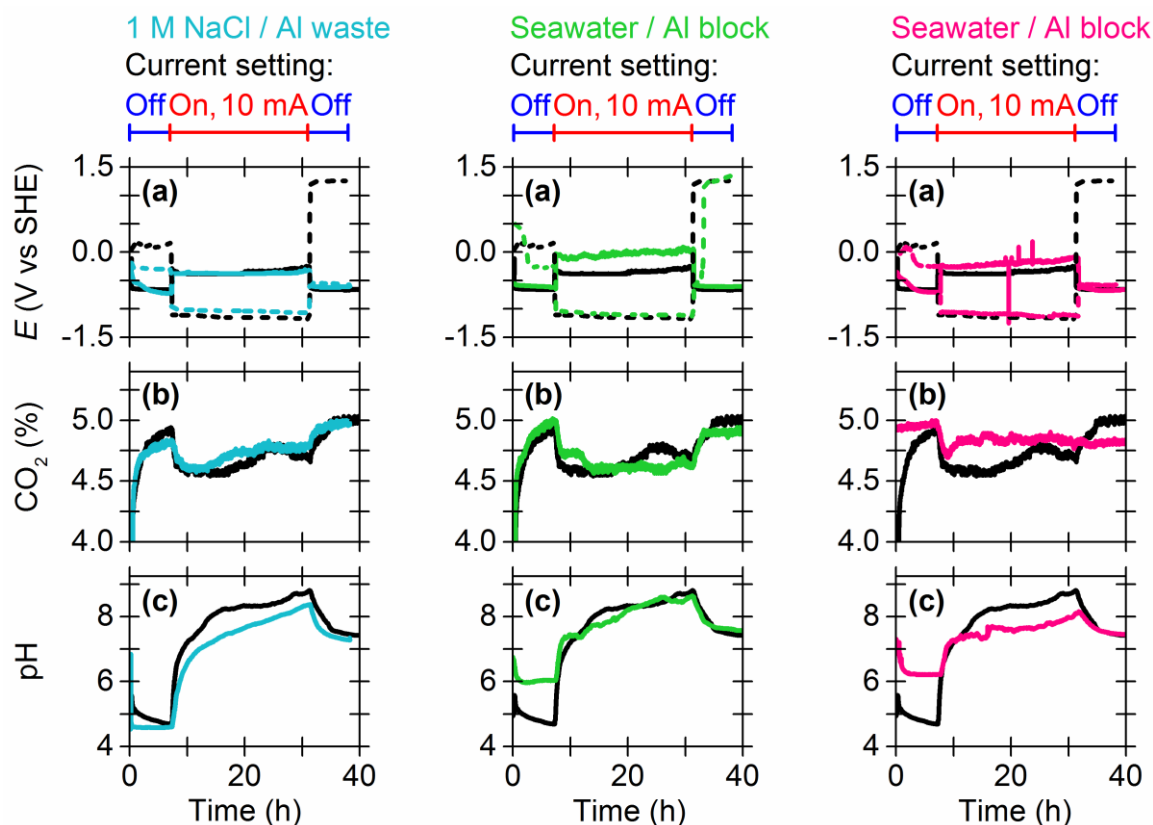
Figure A7: Comparing CO_2 capture with 1 M NaCl in the graphite-aluminium anode cell (black lines) to "waste" aluminium (aluminium foil, blue lines), seawater (green lines) and both combined (red lines). (a) Anode (solid line) and cathode (dashed line) voltages. (b) Carbon dioxide content in the exit gas stream. (c) Corresponding changes in solution pH. Other reaction conditions: a continuous gas flow of 0.7 mL min^{-1} CO_2 (5%) and 13.3 mL min^{-1} N_2.
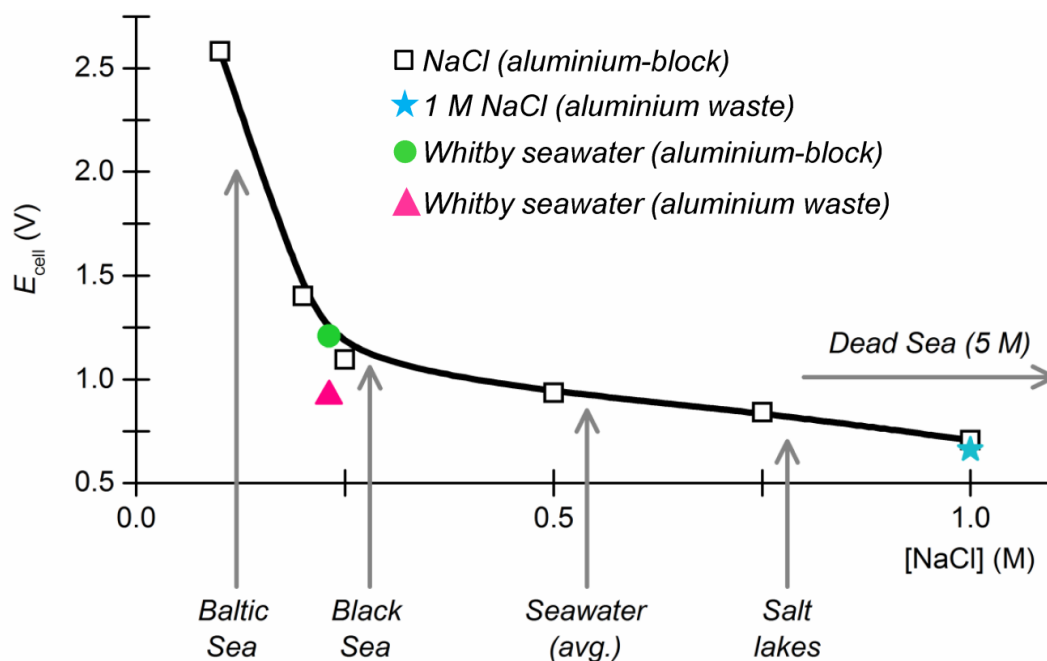
Figure A8: Difference between anode and cathode voltages, and thus E_{Cell}, as a function of NaCl concentration, with predictions for results that would be obtained using seawater samples from around the world, and results obtained using different sustainable materials.

Table A9: Carbon levels captured using experimental setups in Sections 3.2 and 3.4.[a]

Electrolyte	Cell (anode)	Solid mass / g	C in solid[b] / mmol	C in solution[c] / mmol	C total[d] / mmol
1 M NaCl	Graphite-aluminium	0.58 ± 0.08	0.9 ± 0.2[e]	1.9 ± 0.5[e]	2.8 ± 0.7
1 M NaCl	Graphite-aluminium[f]	0.39	0.3 ± 0.01	1.5 ± 0.1	1.8 ± 0.1
1 M NaCl	Graphite-aluminium	0.74 ± 0.15	1.0 ± 0.2[g]	3.7 ± 0.7[g]	4.7 ± 0.2
1 M NaCl	Graphite-aluminium (solar panel)	0.39	0.3 ± 0.07	1.9 ± 0.1	2.2 ± 0.1
1 M NaCl	"Waste" aluminium	0.61	1.1 ± 0.1	0.4 ± 0.01	1.5 ± 0.1
Seawater	Graphite-aluminium	0.42	0.6 ± 0.02	1.4 ± 0.1	2.0 ± 0.1
Seawater	"Waste" aluminium	0.36	0.2 ± 0.01	0.3 ± 0.01	0.5 ± 0.01

a) All molar values reported for carbon detected in the solid and solution post-CO_2 capture correspond to the total amount of carbon in the total volume of electrolyte and total mass of solid, respectively.
b) Quantified via TGA-IR analysis.
c) Quantified via titration of electrolyte.
d) Combination of the total carbon captured in the total volume and mass of solution and solid respectively.
e) Average values obtained from the four 24 h current-time experiments in Figure 55.
f) Temperature of stirrer hotplate, on which the graphite-aluminium block was placed, was set to 60 °C.
g) Average values obtained from the three 36 h current-time experiments in Figure 94.

Table A10: Comparison of E_{Cell} values and energy required for carbon capture using different energy sources, electrolytes and anode material.

Electrolyte	Cell (anode)	E_{Cell}[a] / V	E_{Cell} energy[b] / J	C total[c] / mmol	Energy of C capture[d] / kJ mol^{-1}
1 M NaCl	Graphite-aluminium	0.81[e]	700[e]	2.8 ± 0.7[e]	250
1 M NaCl	Graphite-aluminium[f]	0.52	453	1.8 ± 0.1	252
1 M NaCl	Graphite-aluminium	0.84[g]	1087[g]	4.7 ± 0.2[g]	231
1 M NaCl	Graphite-aluminium (solar panel)	0.83-0.94	718-813	2.2 ± 0.1	326-369
1 M NaCl	"Waste" aluminium	0.67	579	1.5 ± 0.1	386
Seawater	Graphite-aluminium	1.06	917	2.0 ± 0.1	459
Seawater	"Waste" aluminium	0.86	743	0.5 ± 0.01	1486

a) Difference between the anode and platinum cathode voltage.
b) The E_{Cell} value is converted into watts (watt = voltage x current). Watts are equivalent to J s^{-1}, therefore J s^{-1} x time of current application is equivalent to joules.
c) Combination of the total carbon captured in the total volume and mass of solution and solid respectively.
d) (E_{Cell}/1000) ÷ (C total/1000).
e) Average values obtained from the four 24 h current-time experiments in Figure 55.
f) Temperature of stirrer hotplate, on which the graphite-aluminium block was placed, was set to 60 °C.
g) Average values obtained from the three 36 h current-time experiments in Figure 94.

5.0 Abbreviations

Abbreviation, symbol or term	Definition
+I	Positive inductive effect
+M	Positive mesomeric effect
3QMAS	3-Quantum Magic-Angle Spinning
a.u.	Arbitrary units
AEM	Anode Exchange Membrane
ArC (NMR)	Aromatic Carbon
ArH (NMR)	Aromatic H
BAC	Basic Aluminium Carbonate / Basic $Al_2(CO_3)_3$
BMIM	1-Butyl-2-methylimidazolium
BNC	Bayonet Neill–Concelman
BPM	BiPolar Membrane
BPMED	BiPolar Membrane ElectroDialysis
br (NMR)	Broad
CCS	Carbon (dioxide) Capture and Storage
CDU	Carbon Dioxide Utilisation
CEM	Cathode Exchange Membrane
conv.	Conversion
COP21	21st Conference of the Conference Of Parties
CPMAS	Cross Polarisation Magic Angle Spinning
C_Q	Magnitude
CS	Carbon Surface
CV	Cyclic Voltammetry
d (NMR)	Doublet
DCM	Dichloromethane
DEC	Diethyl carbonate
dd (NMR)	Doublet of doublets
ddd (NMR)	Doublet of doublets of doublets
DL	Double Layer
DRIFT	Diffuse Reflectance Infrared Fourier Transform
$E_{1/2}$	Midpoint potential between anodic peak potential and cathodic peak potential
E_{Cell}	Cell potential / difference between anode and cathode voltages
EDA	Ethylene diamine
EDL	Electrical (or Electric) Double Layer
EI	Electron Ionisation
EMAR	Electrochemically-Mediated Amine Regeneration
EOR	Enhanced Oil Recovery
$E_{p,a}$	Anodic peak potential
$E_{p,c}$	Cathodic peak potential
equiv.	Equivalents
ESI	Electrospray ionisation
FT-IR	Fourier Transform-Infrared Spectroscopy
GC	Gas Chromatography
GHG	GreenHouse Gases
-I	Negative inductive effect

ICP-MS	Inductively Coupled Plasma-Mass Spectrometry
ICSD	Inorganic Crystal Structure Database
IEA	International Energy Agency
IEM	Ion Exchange Membrane
IHP	Inner Helmholtz Plane
IPCC	Intergovernmental Panel on Climate Change
IR	Infrared Spectroscopy
LDH	Layered Double Hydroxide
LHS	Left Hand Side
LIFDI	Liquid Injection Field Desorption Ionisation
-M	Negative mesomeric effect
m (NMR)	Multiplet
MAS	Magic Angle Spinning
MCFC	Molten Carbonate Fuel Cell
MCT	Mercury Cadmium Telluride
MQMAS	Multiple Quantum Magic-Angle Spinning
MS	Mass Spectrometry
MS (electrochemical)	Metal Surface
NMR	Nuclear Magnetic Resonance
OCED	Organisation for Economic Cooperation and Development
OHP	Outer Helmholtz Plane
p	Para
PCC	Precipitated Calcium Carbonate
P_Q	Quadrupolar product
PSD	Position Sensitive Detector
q (NMR)	Quartet
RF	Radio Frequency
RHS	Right Hand Side
s (NMR)	Singlet
sat.	Saturated
sat. aq.	Saturated aqueous
SEM-EDX	Scanning Electron Microscope-Energy Dispersive X-Ray Spectroscopy
SHE	Standard Hydrogen Electrode
ST (NMR)	Satellite Transitions
STA	Simultaneous Thermo Analysis
T1	Spin-lattice relaxation time
td (NMR)	A triplet of doublets
TGA-IR	ThermoGravimetric Analysis-Infrared Spectroscopy
TOF	Turnover Frequency
t_{on}	The moment in time in when a current was applied
UV-Vis	Ultraviolet–visible
XRD	X-Ray Diffraction
XRF	X-Ray Fluorescence
δ	NMR Chemical Shift
δ_C	Chemical shift of C environment
$\Delta_f G$	Gibbs free energy of formation
$\Delta_f H$	Enthalpy of formation
$\Delta_f S$	Entropy of formation

δ_H	Chemical shift of H environment
δ_{iso}	Isotopic shift
$\Delta_r G$	Gibbs free energy of reaction
$\Delta_r H$	Enthalpy of reaction
$\Delta_r S$	Entropy of reaction
η	Asymmetry (cross-sectional shape)
ν_2 (IR)	Bend
ν_3 (IR)	Antisymmetric stretch
ν_{rf}	Carrier frequency

6.0 References

1. *The State of World Population 2014: The Power of 1.8 Billion: Adolescents, Youth And The Transformation Of The Future*, United Nations Population Fund (UNFPA), New York, USA, 2014.

2. K. S. Lackner, in *Carbon Capture: Sequestration and Storage*, eds. R. E. Hester and R. M. Harrison, Royal Society of Chemistry, Cambridge, UK, 1st edn., 2009, vol. 29, ch. 1, pp. 1-40.

3. C. S. Song, *Catal. Today*, 2006, **115**, 2-32.

4. *Provisional UK Greenhouse Gas Emissions National Statistics 2014*, National Statistics, Department of Energy and Climate Change, London, UK, 2015.

5. M. North, in *Carbon Dioxide Utilisation: Closing the Carbon Cycle*, eds. P. Styring, E. A. Quadrelli and K. Armstrong, Elsevier, Oxford, UK, 1st edn., 2015, ch. 1, pp. 3-17.

6. G. Aydin, I. Karakurt and K. Aydiner, *Energy Policy*, 2010, **38**, 5072-5080.

7. R. W. Bentley, *Energy Policy*, 2002, **30**, 189-205.

8. N. Abas, A. Kalair and N. Khan, *Futures*, 2015, **69**, 31-49.

9. M. Aresta, A. Dibenedetto and E. Quaranta, *J. Catal.*, 2016, **343**, 2-45.

10. P. G. Jessop and W. Leitner, in *Chemical Synthesis using Supercritical Fluids*, eds. P. G. Jessop and W. Leitner, Wiley-VCH Verlag GmbH, Weinheim, Germany, 1st edn., 1999, ch. 1, pp. 1-136.

11. D. H. Gibson, *Coord. Chem. Rev.*, 1999, **185-6**, 335-355.

12. M. Aresta and A. Dibenedetto, *Dalton Trans.*, 2007, 2975-2992.

13. C. Huber and G. Wachtershauser, *Science*, 1997, **276**, 245-247.

14. M. Aresta, A. Dibenedetto and A. Angelini, *Chem. Rev.*, 2014, **114**, 1709-1742.

15. C. E. Housecraft and A. S. Sharpe, *Inorganic Chemistry*, Pearson Education Limited, Harlow, UK, 4th edn., 2012.

16. Earth's CO_2: Are we stabilizing yet?, https://www.co2.earth, (accessed 07/02/2017).

17. M. W. Chase, Jr., *J. Phys. Chem. Ref. Data, Monogr. 9*, 1998, 1-1951.

18. J. D. Cox, D. D. Wagman and V. A. Medvedev, *CODATA Key Values for Thermodynamics*, Hemisphere Pub Corp, New York, USA, 1989.

19. NIST database, http://webbook.nist.gov/chemistry/name-ser.html, (accessed 02/02/2017).

20. T. Matschei, B. Lothenbach and F. P. Glasser, *Cem. Concr. Res.*, 2007, **37**, 551-558.

21. S. Pacala and R. Socolow, *Science*, 2004, **305**, 968-972.

22. M. North and P. Styring, *Faraday Discuss.*, 2015, **183**, 489-502.

23. J. P. Verdon, J. M. Kendall, A. L. Stork, R. A. Chadwick, D. J. White and R. C. Bissell, *Proc. Natl. Acad. Sci. U. S. A.*, 2013, **110**, E2762-E2771.

24. M. Mikkelsen, M. Jorgensen and F. C. Krebs, *Energy Environ. Sci.*, 2010, **3**, 43-81.

25. P. Styring, E. A. Quadrelli and K. Armstrong, *Carbon Dioxide Utilisation: Closing the Carbon Cycle*, Elsevier, Oxford, 1st edn., 2015.

26. *IPCC Special Report on Carbon Dioxide Capture and Storage*, Intergovernmental Panel on Climate Change, Cambridge University Press, New York, USA, 2005.

27. D. Y. C. Leung, G. Caramanna and M. M. Maroto-Valer, *Renewable Sustainable Energy Rev.*, 2014, **39**, 426-443.

28. N. S. Spinner, J. A. Vega and W. E. Mustain, *Catal. Sci. Technol.*, 2012, **2**, 19-28.

29. C. G. Brundland, *Our Common Future, The World Commission on Environmental Development*, Oxford University Press, Oxford, UK, 1987.

30. R. A. Sheldon, *Chem. Soc. Rev.*, 2012, **41**, 1437-1451.

31. P. T. Anastas and J. C. Warner, *Green Chemistry: Theory and Practice*, Oxford University Press, Oxford, 1998.

32.   Green   Chemistry   Pocket   Guides,
      https://www.acs.org/content/acs/en/greenchemistry/what-is-green-
      chemistry/principles/green-chemistry-pocket-guides.html, (accessed 01/02/2017).

33.   M. Aresta, A. Dibenedetto and A. Angelini, *CO₂ Chemistry*, 2014, **66**, 259-288.

34.   T. Sakakura, J. C. Choi and H. Yasuda, *Chem. Rev.*, 2007, **107**, 2365-2387.

35.   A. T. Najafabadi, *Int. J. Greenhouse Gas Control*, 2013, **37**, 485-499.

36.   Y. A. Daza and J. N. Kuhn, *RSC Adv.*, 2016, **6**, 49675-49691.

37.   B. Schaffner, F. Schaffner, S. P. Verevkin and A. Borner, *Chem. Rev.*, 2010, **110**,
      4554-4581.

38.   C.-X. Miao, J.-Q. Wang and L.-N. He, *Open Org. Chem. J.*, 2008, **2**, 68-82.

39.   J. H. Clements, *Ind. Eng. Chem. Res.*, 2003, **42**, 663-674.

40.   M. North, R. Pasquale and C. Young, *Green Chem.*, 2010, **12**, 1514-1539.

41.   M. Aresta, A. Dibenedetto, A. Angelini and I. Papai, *Topics in Catalysis*, 2015, **58**,
      2-14.

42.   H. L. Parker, J. Sherwood, A. J. Hunt and J. H. Clark, *ACS Sustainable Chem.
      Eng.*, 2014, **2**, 1739-1742.

43.   V. Besse, F. Camara, C. Voirin, R. Auvergne, S. Caillol and B. Boutevin, *Polym.
      Chem.*, 2013, **4**, 4545-4561.

44.   A. Dibenedetto and A. Angelini, in *Advances in Inorganic Chemistry: CO₂
      Chemistry*, eds. M. Aresta and R. Van Eldik, Elsevier, Oxford, 1st edn., 2014, vol.
      66, ch. 2, pp. 25-81.

45.   C. M. Alder, J. D. Hayler, R. K. Henderson, A. M. Redman, L. Shukla, L. E.
      Shuster and H. F. Sneddon, *Green Chem.*, 2016, **18**, 3879-3890.

46.   A. A. G. Shaikh and S. Sivaram, *Chem. Rev.*, 1996, **96**, 951-976.

47.   C. Maeda, Y. Miyazaki and T. Ema, *Catal. Sci. Technol.*, 2014, **4**, 1482-1497.

48.   C. Martin, G. Fiorani and A. W. Kleij, *ACS Catal.*, 2015, **5**, 1353-1370.

49. J. W. Comerford, I. D. V. Ingram, M. North and X. Wu, *Green Chem.*, 2015, **17**, 1966-1987.

50. B. R. Buckley, A. P. Patel and K. G. U. Wijayantha, *Chem. Commun.*, 2011, **47**, 11888-11890.

51. M. Aresta, A. Dibenedetto and I. Tommasi, *Appl. Organometal. Chem.*, 2000, **14**, 799-802.

52. J. M. Sun, S. Fujita, B. M. Bhanage and M. Arai, *Catal. Commun.*, 2004, **5**, 83-87.

53. Q. B. Li, W. Y. Zhang, N. Zhao, W. Wei and Y. H. Sun, *Catal. Today*, 2006, **115**, 111-116.

54. H. Shi-yong, S.-g. Liu, J.-P. Li, N. Zhao, W. Wei and Y.-H. Sun, *J. Fuel Chem. Technol.*, 2007, **35**, 701-705.

55. Y. Du, D. L. Kong, H. Y. Wang, F. Cai, H. S. Tian, J. Q. Wang and L. N. He, *J. Mol. Catal. A: Chem.*, 2005, **241**, 233-237.

56. J. W. Comerford, S. J. Hart, M. North and A. C. Whitwood, *Catal. Sci. Technol.*, 2016, **6**, 4824-4831.

57. M. Tamura, M. Honda, Y. Nakagawa and K. Tomishige, *J. Chem. Technol. Biotechnol.*, 2014, **89**, 19-33.

58. K. Mueller, L. Mokrushina and W. Arlt, *Chem. Ing. Tech.*, 2014, **86**, 497-503.

59. M. Honda, M. Tamura, Y. Nakagawa and K. Tomishige, *Catal. Sci. Technol.*, 2014, **4**, 2830-2845.

60. B. H. Xu, J. Q. Wang, J. Sun, Y. Huang, J. P. Zhang, X. P. Zhang and S. J. Zhang, *Green Chem.*, 2015, **17**, 108-122.

61. J. J. Peng and Y. Q. Deng, *New J. Chem.*, 2001, **25**, 639-641.

62. F. W. Li, L. F. Xiao, C. G. Xia and B. Hu, *Tetrahedron Lett.*, 2004, **45**, 8307-8310.

63. V. I. Parvulescu and C. Hardacre, *Chem. Rev.*, 2007, **107**, 2615-2665.

64. J. M. Sun, S. Fujita and M. Arai, *J. Organomet. Chem.*, 2005, **690**, 3490-3497.

65.   R. H. Heyn, I. Jacobs and R. H. Carr, in *Advances in Inorganic Chemistry: CO$_2$ Chemistry*, eds. M. Aresta and R. Van Eldik, Elsevier, Oxford, UK, 1st edn., 2014, vol. 66, ch. 3, pp. 83-115.

66.   Y. Xiao, B. L. Chen, H. P. Yang, H. Wang and J. X. Lu, *Electrochem. Commun.*, 2014, **43**, 71-74.

67.   W. Li, N. Yang and Y. Lyu, *J. Org. Chem.*, 2016, **81**, 5303-5313.

68.   N. Della Ca, B. Gabriele, G. Ruffolo, L. Veltri, T. Zanetta and M. Costa, *Adv. Synth. Catal.*, 2011, **353**, 133-146.

69.   S. N. Riduan and Y. G. Zhang, *Dalton Trans.*, 2010, **39**, 3347-3357.

70.   J. Rintjema, W. S. Guo, E. Martin, E. C. Escudero-Adan and A. W. Kleij, *Chem. - Eur. J.*, 2015, **21**, 10754-10762.

71.   G. Fiorani, W. S. Guo and A. W. Kleij, *Green Chem.*, 2015, **17**, 1375-1389.

72.   M. Boudart, *Chem. Rev.*, 1995, **95**, 661-666.

73.   V. Calo, A. Nacci, A. Monopoli and A. Fanizzi, *Org. Lett.*, 2002, **4**, 2561-2563.

74.   H. Y. Ju, M. D. Manju, K. H. Kim, S. W. Park and D. W. Park, *J. Ind. Eng. Chem.*, 2008, **14**, 157-160.

75.   Y. Toda, Y. Komiyama, A. Kikuchi and H. Suga, *ACS Catal.*, 2016, **6**, 6906-6910.

76.   T. Ema, K. Fukuhara, T. Sakai, M. Ohbo, F. Q. Bai and J. Y. Hasegawa, *Catal. Sci. Technol.*, 2015, **5**, 2314-2321.

77.   S. Y. Liu, N. Suematsu, K. Maruoka and S. Shirakawa, *Green Chem.*, 2016, **18**, 4611-4615.

78.   L. Wang, G. Y. Zhang, K. Kodamaa and T. Hirose, *Green Chem.*, 2016, **18**, 1229-1233.

79.   P. P. Pescarmona and M. Taherimehr, *Catal. Sci. Technol.*, 2012, **2**, 2169-2187.

80.   D. Darensbourg, *Inorg. Chem.*, 2010, **49**, 10765-10780.

81.   M. North and C. Young, *Catal. Sci. Technol.*, 2011, **1**, 93-99.

82. C. J. Whiteoak, N. Kielland, V. Laserna, F. Castro-Gomez, E. Martin, E. C. Escudero-Adan, C. Bo and A. W. Kleij, *Chem. - Eur. J.*, 2014, **20**, 2264-2275.

83. J. Castro-Osma, C. Alonso-Moreno, A. Lara-Sanchez, J. Martinez, M. North and A. Otero, *Catal. Sci. Technol.*, 2014, **4**, 1674-1684.

84. J. Martinez, J. A. Castro-Osma, A. Earlam, C. Alonso-Moreno, A. Otero, A. Lara-Sanchez, M. North and A. Rodriguez-Dieguez, *Chem. - Eur. J.*, 2015, **21**, 9850-9862.

85. A. Decortes, A. Castilla and A. Kleij, *Angew. Chem., Int. Ed.*, 2010, **49**, 9822-9837.

86. M. North, S. C. Z. Quek, N. E. Pridmore, A. C. Whitwood and X. Wu, *ACS Catal.*, 2015, **5**, 3398-3402.

87. W. Clegg, R. W. Harrington, M. North and R. Pasquale, *Chem. - Eur. J.*, 2010, **16**, 6828-6843.

88. M. Taherimehr, A. Decortes, S. M. Al-Amsyar, W. Lueangchaichaweng, C. J. Whiteoak, E. C. Escudero-Adan, A. W. Kleij and P. P. Pescarmona, *Catal. Sci. Technol.*, 2012, **2**, 2231-2237.

89. M. V. Escarcega-Bobadilla, M. M. Belmonte, E. Martin, E. C. Escudero-Adan and A. W. Kleij, *Chem. - Eur. J.*, 2013, **19**, 2641-2648.

90. A. W. Kleij, M. Kuil, D. M. Tooke, M. Lutz, A. L. Spek and J. N. H. Reek, *Chem. - Eur. J.*, 2005, **11**, 4743-4750.

91. J. A. Castro-Osma, A. Lara-Sanchez, M. North, A. Otero and P. Villuendas, *Catal. Sci. Technol.*, 2012, **2**, 1021-1026.

92. T. P. Yoon and E. N. Jacobsen, *Science*, 2003, **299**, 1691-1693.

93. S. J. Wezenberg and A. W. Kleij, *Angew. Chem., Int. Ed.*, 2008, **47**, 2354-2364.

94. R. L. Paddock and S. T. Nguyen, *J. Am. Chem. Soc.*, 2001, **123**, 11498-11499.

95. D. J. Darensbourg, R. M. Mackiewicz, J. L. Rodgers, C. C. Fang, D. R. Billodeaux and J. H. Reibenspies, *Inorg. Chem.*, 2004, **43**, 6024-6034.

96. M. Alvaro, C. Baleizao, D. Das, E. Carbonell and H. Garcia, *J. Catal.*, 2004, **228**, 254-258.

97. R. L. Paddock and S. T. Nguyen, *Chem. Commun.*, 2004, 1622-1623.

98. T. Chang, L. L. Jin and H. W. Jing, *ChemCatChem*, 2009, **1**, 379-383.

99. D. J. Darensbourg and D. R. Billodeaux, *Inorg. Chem.*, 2005, **44**, 1433-1442.

100. J. Melendez, M. North and R. Pasquale, *Eur. J. Inorg. Chem.*, 2007, 3323-3326.

101. J. Melendez, M. North and P. Villuendas, *Chem. Commun.*, 2009, 2577-2579.

102. J. A. Castro-Osma, M. North and X. Wu, *Chem. - Eur. J.*, 2014, **20**, 15005-15008.

103. C. J. Whiteoak, G. Salassa and A. W. Kleij, *Chem. Soc. Rev.*, 2012, **41**, 622-631.

104. S. I. Vagin, R. Reichardt, S. Klaus and B. Rieger, *J. Am. Chem. Soc.*, 2010, **132**, 14367-14369.

105. J. A. Castro-Osma, M. North and X. Wu, *Chem. - Eur. J.*, 2016, **22**, 2100-2107.

106. C. Martin, C. J. Whiteoak, E. Martin, M. M. Belmonte, E. C. Escudero-Adan and A. W. Kleij, *Catal. Sci. Technol.*, 2014, **4**, 1615-1621.

107. J. Chun, S. Kang, N. Kang, S. M. Lee, H. J. Kim and S. U. Son, *J. Mater. Chem. A*, 2013, **1**, 5517-5523.

108. D. J. Darensbourg, W.-C. Chung and S. J. Wilson, *ACS Catal.*, 2013, **3**, 3050-3057.

109. X. Zhang, Y. B. Jia, X. B. Lu, B. Li, H. Wang and L. C. Sun, *Tetrahedron Lett.*, 2008, **49**, 6589-6592.

110. D. J. Darensbourg and R. M. Mackiewicz, *J. Am. Chem. Soc.*, 2005, **127**, 14026-14038.

111. A. Burrows, J. Holman, A. Parsons, G. Pilling and G. Price, *Chemistry³*, Oxford University Press, Oxford, 1st edn., 2009.

112. J. A. Castro-Osma, K. J. Lamb and M. North, *ACS Catal.*, 2016, **6**, 5012-5025.

113. D. J. Darensbourg, R. M. Mackiewicz, J. L. Rodgers and A. L. Phelps, *Inorg. Chem.*, 2004, **43**, 1831-1833.

114. D. J. Darensbourg, *Chem. Rev.*, 2007, **107**, 2388-2410.

115. R. Fuchs and C. A. Vanderwerf, *J. Am. Chem. Soc.*, 1954, **76**, 1631-1634.

116. A. Decortes, M. M. Belmonte, J. Benet-Buchholz and A. W. Kleij, *Chem. Commun.*, 2010, **46**, 4580-4582.

117. A. Decortes and A. W. Kleij, *ChemCatChem*, 2011, **3**, 831-834.

118. F. A. Carey and R. J. Sundberg, *Advanced Organic Chemistry: Part A: Structure and Mechanisms*, Springer-Verlag New York Inc., New York, 5th edn., 2007.

119. P. Jaramillo, P. Perez, R. Contreras, W. Tiznado and P. Fuentealba, *J. Phys. Chem. A*, 2006, **110**, 8181-8187.

120. P. Jaramillo, P. Fuentealba and P. Perez, *Chem. Phys. Lett.*, 2006, **427**, 421-425.

121. C. G. Swain and C. B. Scott, *J. Am. Chem. Soc.*, 1953, **75**, 141-147.

122. J. O. Edwards, *J. Am. Chem. Soc.*, 1954, **76**, 1540-1547.

123. V. D'Elia, J. D. A. Pelletier and J. M. Basset, *ChemCatChem*, 2015, **7**, 1906-1917.

124. A. Buonerba, A. De Nisi, A. Grassi, S. Milione, C. Capacchione, S. Vagin and B. Rieger, *Catal. Sci. Technol.*, 2015, **5**, 118-123.

125. C. J. Whiteoak, E. Martin, M. M. Belmonte, J. Benet-Buchholz and A. W. Kleij, *Adv. Synth. Catal.*, 2012, **354**, 469-476.

126. J. Qin, P. Wang, Q. Li, Y. Zhang, D. Yuan and Y. Yao, *Chem. Commun.*, 2014, **50**, 10952-10955.

127. J. A. Castro-Osma, M. North, W. K. Offermans, W. Leitner and T. E. Muller, *ChemSusChem*, 2016, **9**, 791-794.

128. D. J. Darensbourg and A. I. Moncada, *Inorg. Chem.*, 2008, **47**, 10000-10008.

129. J. A. Castro-Osma, A. Earlam, A. Lara-Sanchez, A. Otero and M. North, *ChemCatChem*, 2016, **8**, 2100-2108.

130. C. Beattie and M. North, *Chem. - Eur. J.*, 2014, **20**, 8182-8188.

131. V. Laserna, W. S. Guo and A. W. Kleij, *Adv. Synth. Catal.*, 2015, **357**, 2849-2854.

132. G. Zappia, P. Menendez, G. Delle Monache, D. Misiti, L. Nevola and B. Botta, *Mini-Rev. Med. Chem.*, 2007, **7**, 389-409.

133. T. Baronsky, C. Beattie, R. W. Harrington, R. Irfan, M. North, J. G. Osende and C. Young, *ACS Catal.*, 2013, **3**, 790-797.

134. G. P. Speranza and W. J. Peppel, *J. Org. Chem.*, 1958, **23**, 1922-1924.

135. C. Beattie and M. North, *RSC Adv.*, 2014, **4**, 31345-31352.

136. R. L. Paddock, D. Adhikari, R. L. Lord, M. H. Baik and S. T. Nguyen, *Chem. Commun.*, 2014, **50**, 15187-15190.

137. X. X. Zhang, W. Chen, C. F. Zhao, C. Li, X. A. Wu and W. Z. Chen, *Synth. Commun.*, 2010, **40**, 3654-3659.

138. A. Baba, M. Fujiwara and H. Matsuda, *Tetrahedron Lett.*, 1986, **27**, 77-80.

139. M. Fujiwara, A. Baba and H. Matsuda, *J. Heterocycl. Chem.*, 1988, **25**, 1351-1357.

140. G. P. Wu, S. H. Wei, X. B. Lu, W. M. Ren and D. J. Darensbourg, *Marcomol.*, 2010, **43**, 9202-9204.

141. B. Lin and D. L. Whalen, *J. Org. Chem.*, 1994, **59**, 1638-1641.

142. H. E. Gottlieb, V. Kotlyar and A. Nudelman, *J. Org. Chem.*, 1997, **62**, 7512-7515.

143. T. V. Hansen and L. Skattebøl, *Org. Synth.*, 2005, **82**, 64.

144. M. T. Sun, T. Q. Xu, W. Gao, Y. Liu, Q. L. Wu, Y. Mu and L. Ye, *Dalton Trans.*, 2011, **40**, 10184-10194.

145. G. W. Theaker, C. Morton and P. Scott, *Dalton Trans.*, 2008, 6883-6885.

146. C. T. Chen, J. Q. Kao, S. B. Salunke and Y. H. Lin, *Org. Lett.*, 2011, **13**, 26-29.

147. M. T. Sun, Y. Mu, Q. L. Wu, W. Gao and L. Ye, *New J. Chem.*, 2010, **34**, 2979-2987.

148. M. Braun, R. Fleischer, B. Mai, M. A. Schneider and S. Lachenicht, *Adv. Synth. Catal.*, 2004, **346**, 474-482.

149. T. S. Singh, P. C. Paul and H. A. R. Pramanik, *Spectrochim. Acta, Part A*, 2014, **121**, 520-526.

150. Q. Song, M. Jia, W. Ma, Y. Fang and Y. Huang, *Sci. China: Chem.*, 2013, **56**, 1775-1782.

151. S. Y. Liu and D. G. Nocera, *Tetrahedron Lett.*, 2006, **47**, 1923-1926.

152. C. T. Cohen, T. Chu and G. W. Coates, *J. Am. Chem. Soc.*, 2005, **127**, 10869-10878.

153. D. J. Covell and M. C. White, *Angew. Chem., Int. Ed.*, 2008, **47**, 6448-6451.

154. A. Berkessel and M. Brandenburg, *Org. Lett.*, 2006, **8**, 4401-4404.

155. A. Martinsen and J. Songstad, *Acta Chem. Scand., Ser. A*, 1977, **31**, 645-650.

156. C. J. Devlin and B. J. Walker, *J. Chem. Soc., Perkin Trans. 1*, 1974, 453-460.

157. Y. A. Rulev, Z. Gugkaeva, V. I. Maleev, M. North and Y. N. Belokon, *Beilstein J. Org. Chem.*, 2015, **11**, 1614-1623.

158. X. Liu, S. Zhang, Q. W. Song, X. F. Liu, R. Ma and L. N. He, *Green Chem.*, 2016, **18**, 2871-2876.

159. J. A. Martens, A. Bogaerts, N. De Kimpe, P. A. Jacobs, G. B. Marin, K. Rabaey, M. Saeys and S. Verhelst, *ChemSusChem*, 2017, **10**, 1039-1055.

160. *The Global Status of CCS: 2016 Summary Report*, Global CCS Institute, Australia, 2016.

161. E. S. Rubin, H. Mantripragada, A. Marks, P. Versteeg and J. Kitchin, *Prog. Energy Combust. Sci.*, 2012, **38**, 630-671.

162. *Introduction to Industrial Carbon Capture and Storage*, Global Carbon Capture and Storage Institute, Australia, 2016.

163. E. S. Rubin, J. E. Davison and H. J. Herzog, *Int. J. Greenhouse Gas Control*, 2015, **40**, 378-400.

164. *20 Years of Carbon Capture and Storage - Accelerating Future Deployment*, International Energy Agency, Paris, France, 2016.

165. CO$_2$ Capture Project (CCP), http://www.co2captureproject.com/index.html, (accessed 07/01/2017).

166. M. Peters, B. Kohler, W. Kuckshinrichs, W. Leitner, P. Markewitz and T. E. Muller, *ChemSusChem*, 2011, **4**, 1216-1240.

167. A. Hasanbeigi, L. Price and E. Lin, *Renewable Sustainable Energy Rev.*, 2012, **16**, 6220-6238.

168. G. T. Rochelle, *Science*, 2009, **325**, 1652-1654.

169. J. D. McDonald, D. Kracko, M. Doyle-Eisele, C. E. Garner, C. Wegerski, A. Senft, E. Knipping, S. Shaw and A. Rohr, *Environ. Sci. Technol.*, 2014, **48**, 10821-10828.

170. R. Sabouni, H. Kazemian and S. Rohani, *Environ. Sci. Pollut. Res.*, 2014, **21**, 5427-5449.

171. G. A. Olah, G. K. S. Prakash and A. Goeppert, *J. Am. Chem. Soc.*, 2011, **133**, 12881-12898.

172. A. B. Rao and E. S. Rubin, *Environ. Sci. Technol.*, 2002, **36**, 4467-4475.

173. P. Luis, *Desalination*, 2016, **380**, 93-99.

174. H. W. Pennline, E. J. Granite, D. R. Luebke, J. R. Kitchin, J. Landon and L. M. Weiland, *Fuel*, 2010, **89**, 1307-1314.

175. A. Azdarpour, M. Asadullah, E. Mohammadian, H. Hamidi, R. Junin and M. A. Karaei, *Chem. Eng. J.*, 2015, **279**, 615-630.

176. C. L. Sabine, R. A. Feely, N. Gruber, R. M. Key, K. Lee, J. L. Bullister, R. Wanninkhof, C. S. Wong, D. W. R. Wallace, B. Tilbrook, F. J. Millero, T. H. Peng, A. Kozyr, T. Ono and A. F. Rios, *Science*, 2004, **305**, 367-371.

177. K. Z. House, C. H. House, D. P. Schrag and M. J. Aziz, *Environ. Sci. Technol.*, 2007, **41**, 8464-8470.

178. K. Caldeira and M. E. Wickett, *Nature*, 2003, **425**, 365-365.

179. K. S. Lackner, *Annu. Rev. Energy*, 2002, **27**, 193-232.

180. V. Alvarado and E. Manrique, *Energies*, 2010, **3**, 1529-1575.

181. R. Zevenhoven and J. Fagerlund, *Mineralisation of Carbon Dioxide (CO$_2$)*, CRC Press, Taylor & Francis Inc, Cambridge, UK, 2010.

182. R. Zevenhoven, S. Eloneva and S. Teir, *Catal. Today*, 2006, **115**, 73-79.

183. A. A. Olajire, *J. Pet. Sci. Eng.*, 2013, **109**, 364-392.

184. Y. W. Chiang, R. M. Santos, J. Elsen, B. Meesschaert, J. A. Martens and T. Van Gerven, *Chem. Eng. J.*, 2014, **249**, 260-269.

185. S. Y. Pan, A. Chiang, E. E. Chang, Y. P. Lin, H. Kim and P. C. Chiang, *Aerosol Air Qual. Res.*, 2015, **15**, 1072-1091.

186. M. L. Druckenmiller and M. M. Maroto-Valer, *Fuel Process. Technol.*, 2005, **86**, 1599-1614.

187. G. M. Bond, J. Stringer, D. K. Brandvold, F. A. Simsek, M. G. Medina and G. Egeland, *Energy & Fuels*, 2001, **15**, 309-316.

188. K. E. Kelly, G. D. Silcox, A. F. Sarofim and D. W. Pershing, *Int. J. Greenhouse Gas Control*, 2011, **5**, 1587-1595.

189. A. J. Bard and L. R. Faulkner, *Electrochemical Methods: Fundamentals and Applications*, John Wiley and Sons, New York, USA, 2nd edn., 2001.

190. M. D. Eisaman, K. Parajuly, A. Tuganov, C. Eldershaw, N. Chang and K. A. Littau, *Energy Environ. Sci.*, 2012, **5**, 7346-7352.

191. *Carbon Footprint of Electricity Generation*, Parliamentry Office of Science and Technology, London, UK, 2006.

192. J. Qiao, Y. Liu, F. Hong and J. Zhang, *Chem. Soc. Rev.*, 2014, **43**, 631-675.

193. C. Costentin, M. Robert and J. M. Saveant, *Chem. Soc. Rev.*, 2013, **42**, 2423-2436.

194. J. L. White, M. F. Baruch, J. E. Pander, Y. Hu, I. C. Fortmeyer, J. E. Park, T. Zhang, K. Liao, J. Gu, Y. Yan, T. W. Shaw, E. Abelev and A. B. Bocarsly, *Chem. Rev.*, 2015, **115**, 12888-12935.

195. J. Winnick, H. Toghiani and P. D. Quattrone, *AIChE J.*, 1982, **28**, 103-111.

196. J.-H. Wee, *Renewable Sustainable Energy Rev.*, 2014, **32**, 178-191.

197. E. J. Granite and T. O'Brien, *Fuel Process. Technol.*, 2005, **86**, 1423-1434.

198. M. D. Eisaman, L. Alvarado, D. Larner, P. Wang and K. A. Littau, *Energy Environ. Sci.*, 2011, **4**, 4031-4037.

199.   M. D. Eisaman, L. Alvarado, D. Larner, P. Wang, B. Garg and K. A. Littau, *Energy Environ. Sci.*, 2011, **4**, 1319-1328.

200.   V. J. Frilette, *J. Phys. Chem.*, 1956, **60**, 435-439.

201.   D. Shuto, H. Nagasawa, A. Iizuka and A. Yamasaki, *RSC Adv.*, 2014, **4**, 19778-19788.

202.   A. Iizuka, K. Hashimoto, H. Nagasawa, K. Kumagai, Y. Yanagisawa and A. Yamasaki, *Sep. Purif. Technol.*, 2012, **101**, 49-59.

203.   A. M. Appel, J. E. Bercaw, A. B. Bocarsly, H. Dobbek, D. L. DuBois, M. Dupuis, J. G. Ferry, E. Fujita, R. Hille, P. J. A. Kenis, C. A. Kerfeld, R. H. Morris, C. H. F. Peden, A. R. Portis, S. W. Ragsdale, T. B. Rauchfuss, J. N. H. Reek, L. C. Seefeldt, R. K. Thauer and G. L. Waldrop, *Chem. Rev.*, 2013, **113**, 6621-6658.

204.   M. C. Stern, F. Simeon, H. Herzog and T. A. Hatton, *Energy Environ. Sci.*, 2013, **6**, 2505-2517.

205.   M. C. Stern and T. A. Hatton, *RSC Adv.*, 2014, **4**, 5906-5914.

206.   S. Porada, L. Weinstein, R. Dash, A. van der Wal, M. Bryjak, Y. Gogotsi and P. M. Biesheuvel, *ACS Appl. Mater. Interfaces*, 2012, **4**, 1194-1199.

207.   S. Porada, R. Zhao, A. van der Wal, V. Presser and P. M. Biesheuvel, *Prog. Mater. Sci.*, 2013, **58**, 1388-1442.

208.   T. Brousse, D. Belanger and J. W. Long, *J. Electrochem. Soc.*, 2015, **162**, A5185-A5189.

209.   A. Ghosh and Y. H. Lee, *ChemSusChem*, 2012, **5**, 480-499.

210.   A. Gonzalez, E. Goikolea, J. A. Barrena and R. Mysyk, *Renewable Sustainable Energy Rev.*, 2016, **58**, 1189-1206.

211.   S. Bose, T. Kuila, A. K. Mishra, R. Rajasekar, N. H. Kim and J. H. Lee, *J. Mater. Chem.*, 2012, **22**, 767-784.

212.   B. Kokoszka, N. K. Jarrah, C. Liu, D. T. Moore and K. Landskron, *Angew. Chem., Int. Ed.*, 2014, **53**, 3698-3701.

213.   L. L. Zhang and X. S. Zhao, *Chem. Soc. Rev.*, 2009, **38**, 2520-2531.

214.   R. Kotz and M. Carlen, *Electrochim. Acta*, 2000, **45**, 2483-2498.

215.   A. G. Pandolfo and A. F. Hollenkamp, *J. Power Sources*, 2006, **157**, 11-27.

216.   E. Frackowiak and F. Beguin, *Carbon*, 2001, **39**, 937-950.

217.   C. Liu and K. Landskron, *Chem. Commun.*, 2017, **53**, 3661-3664.

218.   D. Karabelli, J. C. Lepretre, F. Alloin and J. Y. Sanchez, *Electrochim. Acta*, 2011, **57**, 98-103.

219.   A. Chandan, M. Hattenberger, A. El-Kharouf, S. Du, A. Dhir, V. Self, B. G. Pollet, A. Ingram and W. Bujalski, *J. Power Sources*, 2013, **231**, 264-278.

220.   S. Y. Pan, E. E. Chang and P. C. Chiang, *Aerosol Air Qual. Res.*, 2012, **12**, 770-791.

221.   A. Sanna, M. Uibu, G. Caramanna, R. Kuusik and M. M. Maroto-Valer, *Chem. Soc. Rev.*, 2014, **43**, 8049-8080.

222.   Q. Liu and M. M. Maroto-Valer, *Fuel Process. Technol.*, 2012, **98**, 6-13.

223.   R. J. Gilliam, V. Decker, N. A. Knott, M. Kostowskyj, B. Boggs and K. Farsad, *Gas Diffusion Anode and CO$_2$ Cathode Electrochemical System*, US Patent, No: 7,993,500, 2011.

224.   R. J. Gilliam, B. K. Boggs, V. Decker, M. A. Kostowskyj, S. Gorer, T. A. Albrecht, J. D. Way, D. W. Kirk and A. J. Bard, *J. Electrochem. Soc.*, 2012, **159**, B627-B628.

225.   R. J. Gilliam, T. A. Albrecht, N. Jalani, N. A. Knott, V. Decker, M. Kostowskyj, B. Boggs, A. Gorer and K. Farsad, *CO$_2$ Utilization in Electrochemical Systems*, US Patent, No: 8,357,270, 2013.

226.   A. Mehmood, E. Jang, N. Lee, K. D. Jung and H. Y. Ha, *Electrochim. Acta*, 2015, **180**, 845-851.

227.   A. Mehmood, M. I. Iqbal, J. Y. Lee, J. Hwang, K. D. Jung and H. Y. Ha, *Electrochim. Acta*, 2016, **219**, 655-663.

228. J. D. Jones, *Removing Carbon Dioxide from Waste Streams through co-generation of Carbonate and/or Bicarbonate Minerals*, US Patent, No: 7,727,374, 2010.

229. H. Xie, T. Liu, Z. Hou, Y. Wang, J. Wang, L. Tang, W. Jiang and Y. He, *Environ. Earth Sci.*, 2015, **73**, 6881-6890.

230. E. Deltombe and M. Pourbaix, *Corrosion*, 1958, **14**, 16-20.

231. W. I. Al Sadat and L. A. Archer, *Sci. Adv.*, 2016, **2**.

232. J. E. O'Reilly, *Biochim. Biophys. Acta, Bioenerg.*, 1973, **292**, 509-515.

233. Y. Wang, Y. Song and Y. Xia, *Chem. Soc. Rev.*, 2016, **45**, 5925-5950.

234. A. J. Bard, R. Parsons and J. Jordan, *Standard Potentials in Aqueous Solutions*, CRC Press, Taylor & Francis Inc, New York, USA, 1985.

235. R. G. Compton and G. H. W. Sanders, *Electrode Potentials*, Oxford University Press, Oxford, UK, 1996.

236. F. J. Vidal-Iglesias, J. Solla-Gullon, A. Rodes, E. Herrero and A. Aldaz, *J. Chem. Educ.*, 2012, **89**, 936-939.

237. G. H. Jeffery, J. Bassett, J. Mendham and R. C. Denney, *Vogel's Textbook of Quantitative Chemical Analysis*, Bath Press, Longman Scientific and Technical, Avon, UK, 5th edn., 1989.

238. K. Ichikawa, *Chem. - Eur. J.*, 2007, **13**, 10176-10181.

239. O. Izgec, B. Demiral, H. Bertin and S. Akin, *Transp. Porous Media*, 2008, **72**, 1-24.

240. S. K. Lower, Carbonate equilibria in natural waters, http://www.chem1.com/acad/webtext/pdf/c3carb.pdf, (accessed 11/11/2016).

241. J.-P. Randin, in *Encyclopedia of Electrochemistry of the Elements*, ed. A. J. Bard, Marcel Dekker Inc., New York, USA, 1st edn., 1976, vol. VII, ch. VII-1, pp. 2-291.

242. L. L. Pesterfield, J. B. Maddox, M. S. Crocker and G. K. Schweitzer, *J. Chem. Educ.*, 2012, **89**, 891-899.

243. P. A. Malachesky, in *Encyclopedia of Electrochemistry of the Elements*, ed. A. J. Bard, Marcel Dekker Inc., New York, USA, 1st edn., 1976, vol. VI, ch. VI-I, pp. 64-165.

244. N. Jiang, B. You, M. L. Sheng and Y. J. Sun, *Angew. Chem., Int. Ed. Engl.*, 2015, **54**, 6251-6254.

245. Z. Xing, Q. Liu, A. M. Asiri and X. Sun, *ACS Catal.*, 2015, **5**, 145-149.

246. S. Morra, F. Valetti, V. Sarasso, S. Castrignano, S. J. Sadeghi and G. Gilardi, *Bioelectrochemistry*, 2015, **106**, 258-262.

247. J. Petrovic and G. Thomas, *Reaction of Aluminium with Water to Produce Hydrogen*, U.S. Department of Energy, Washington, United States of America, 2010.

248. E. R. Andersen and E. J. Andersen, *Method for Producing Hydrogen*, US Patent, No: 6,638,493, 2002.

249. A. A. Mazhar, S. T. Arab and E. A. Noor, *Journal of Applied Electrochemistry*, 2001, **31**, 1131-1140.

250. T. Hagyard and J. R. Santhiapillai, *J. Appl. Chem*, 1959, **9**, 323-330.

251. C. J. Serna, J. L. White and S. L. Hem, *J. Pharm. Sci.*, 1978, **67**, 1144-1147.

252. C. J. Serna, J. C. Lyons, J. L. White and S. L. Hem, *J. Pharm. Sci.*, 1983, **72**, 769-771.

253. P. Tarte, *Spectrochim. Acta Mol. Biomol. Spectrosc.*, 1967, **A 23**, 2127-2143.

254. J. M. Saniger, *Mater. Lett.*, 1995, **22**, 109-113.

255. B. H. Stuart, *Infrared Spectroscopy: Fundamentals and Applications*, John Wiley and Sons Ltd, Chichester, UK, 2004.

256. H. W. Papenguth, R. J. Kirkpatrick, B. Montez and P. A. Sandberg, *Am. Min.*, 1989, **74**, 1152-1158.

257. S. Lin and J. Selig, *J. Alloys Compd.*, 2010, **503**, 402-409.

258. L. W. Finger and R. M. Hazen, *J. Appl. Phys.*, 1978, **49**, 5823-5826.

259. S. M. Beekman, *Basic aluminum carbonate and glycine composition and method of making same*, Reheis Company Inc., US Patent, No: 2,802,773, 1953.

260. S. M. Beekman, *Process for perparing basic aluminium carbonate gels substantially free from foreign anions and fibrous collodial alumina monohydrate of a boehmite crystal lattice structure*, Beekman, Stewart M., US Patent, No: 4,500,444, 1982.

261. K. Wefers and C. Misra, *Oxides and Hydroxides of Aluminium*, Alcoa Laboratories Alcoa Laboratories 1987.

262. K. J. D. MacKenzie and M. E. Smith, *Multinuclear Solid-State NMR of Inorganic Materials*, Elsevier Science Technology, Pergamon, Amsterdam, Netherlands, 1st edn., 2002.

263. G. E. Bacon and N. A. Curry, *Acta Crystallogr.*, 1956, **9**, 82-85.

264. M. Dusek, G. Chapuis, M. Meyer and V. Petricek, *Acta Crystallogr., Sect. B: Struct. Sci.*, 2003, **59**, 337-352.

265. B. Bureau, G. Silly, J. Y. Buzare, C. Legein and D. Massiot, *Solid State Nuclear Magnetic Resonance*, 1999, **14**, 181-190.

266. G. Bardossy and J. L. White, *Science*, 1979, **203**, 355-356.

267. R. L. Frost and M. J. Dickfos, *Spectrochim. Acta, Part A*, 2008, **71**, 143-146.

268. A. C. Ferrari, *Solid State Commun.*, 2007, **143**, 47-57.

269. J. T. Kloprogge, H. D. Ruan and R. L. Frost, *J. Mater. Sci.*, 2002, **37**, 1121-1129.

270. W. O. Milligan and J. L. McAtee, *J. Phys. Chem.*, 1956, **60**, 273-277.

271. P. P. Reichertz and W. J. Yost, *J. Chem. Phys.*, 1946, **14**, 495-501.

272. H. D. Ruan, R. L. Frost and J. T. Kloprogge, *J. Raman Spectrosc.*, 2001, **32**, 745-750.

273. T. Selvam, A. Inayat and W. Schwieger, *Dalton Trans.*, 2014, **43**, 10365-10387.

274. E. Conterosito, L. Palin, D. Antonioli, D. Viterbo, E. Mugnaioli, U. Kolb, L. Perioli, M. Milanesio and V. Gianotti, *Chem. Eur. J.*, 2015, **21**, 14975-14986.

275. X. Q. Hou and R. J. Kirkpatrick, *Inorg. Chem.*, 2001, **40**, 6397-6404.

276. L. Huang, J. Wang, Y. Gao, Y. Qiao, Q. Zheng, Z. Guo, Y. Zhao, D. O'Hare and Q. Wang, *J. Mater. Chem. A*, 2014, **2**, 18454-18462.

277. A. Belsky, M. Hellenbrandt, V. L. Karen and P. Luksch, *Acta Crystallogr., Sect. B: Struct. Sci.*, 2002, **58**, 364-369.

278. G. Bergerhoff and I. D. Brown, *Crystallographic Databases*, International Union of Crystallography, Chester, England, 1987.

279. J. P. Thiel, C. K. Chiang and K. R. Poeppelmeier, *Chem. Mater.*, 1993, **5**, 297-304.

280. N. Iyi and T. Sasaki, *J. Colloid Interface Sci.*, 2008, **322**, 237-245.

281. M.-C. Lin, F.-T. Chang and J.-Y. Uan, *J. Mater. Chem.*, 2010, **20**, 6524-6530.

282. M.-C. Lin, F.-T. Chang and J.-Y. Uan, *J. Mater. Chem. A*, 2013, **1**, 14773-14782.

283. C. M. Li, M. Wei, D. G. Evans and X. Duan, *Small*, 2014, **10**, 4469-4486.

284. M. Ahtee, *Ann. Acad. Sci. Fenn., Ser. A6*, 1969, **313**, 1-11.

285. J. W. Akitt, *Multinuclear NMR*, Plenum Press, New York, 2nd edn., 1989.

286. Fuel Prices and Carbon Intensity (our calculations), The Energy Saving Trust, http://www.energysavingtrust.org.uk/about-us/our-calculations, (accessed 02/04/2017).

287. The International Aluminium Institute, The Aluminium Story, http://www.thealuminiumstory.com/, (accessed 31/01/2017).

288. The International Aluminium Institute, Recycling Aluminium, http://recycling.world-aluminium.org/home/, (accessed 31/01/2017).

289. *Electricity Information 2016*, International Energy Agency, Paris, France, 2016.

290. *Carbon Footprint of Electricity Generation*, Parliamentary Office of Science and Technology, London, UK, 2011.

291. L. D. Talley, G. L. Pickard, W. J. Emery and J. H. Swift, *Descriptive Physical Oceanography: An Introduction.*, Academic Press, Elsevier, London, UK, 6th edn., 2011.

292.   The International Aluminium Institute, Aluminium mass flow chart 2013-2014, http://www.world-aluminium.org/statistics, (accessed 25/08/2016).

293.   H. S. Harned and R. Davis, *J. Am. Chem. Soc.*, 1943, **65**, 2030-2037.

294.   J. J. Carroll, J. D. Slupsky and A. E. Mather, *J. Phys. Chem. Ref. Data*, 1991, **20**, 1201-1209.

295.   K. Mazloomi, N. B. Sulaiman and H. Moayedi, *Int. J. Electrochem. Sci.*, 2012, **7**, 3314-3326.

296.   J. K. Stolaroff, D. W. Keith and G. V. Lowry, *Environ. Sci. Technol.*, 2008, **42**, 2728-2735.

297.   M. Yoo, S.-J. Han and J.-H. Wee, *J. Environ. Manage.*, 2013, **114**, 512-519.

298.   M. Mahmoudkhani and D. W. Keith, *Int. J. Greenhouse Gas Control*, 2009, **3**, 376-384.

299.   M. L. Doche, J. J. Rameau, R. Durand and F. Novel-Cattin, *Corros. Sci.*, 1999, **41**, 805-826.

300.   R. Gastineau, D. D. Holmquist, K. Redding and C. M. McDaniel, *Water Quality with Vernier*, Vernier Software & Technology, Oregon, USA, 2015.

301.   K. Havens, *Climate Change: Effects on Salinity in Florida's Estuaries and Responses of Oysters, Seagrass, and Other Animal and Plant Life*, IFAS Extension, University of Florida, Florida, USA, 2015.

302.   The International Aluminium Institute, Primary Aluminium Smelting Energy Intensity, http://www.world-aluminium.org/statistics/primary-aluminium-smelting-energy-intensity/#data, (accessed 10/10/2016).

303.   J. Wilcox, *Carbon Capture*, Springer, New York, UK, 2012.

304.   C. Yver, M. Schmidt, P. Bousquet, W. Zahorowski and M. Ramonet, *J. Geophys. Res.: Atmos.*, 2009, **114**.

305.   P. K. Madhu, A. Goldbourt, L. Frydman and S. Vega, *Chem. Phys. Lett.*, 1999, **307**, 41-47.

306. Y. Millot and P. P. Man, *Solid State Nucl. Magn. Reson.*, 2002, **21**, 21-43.

307. O. V. Dolomanov, L. J. Bourhis, R. J. Gildea, J. A. K. Howard and H. Puschmann, *J. Appl. Crystallogr.*, 2009, **42**, 339-341.

308. G. M. Sheldrick, *Acta Crystallogr., Sect. A: Found. Adv.*, 2015, **71**, 3-8.

309. G. M. Sheldrick, *Acta Crystallogr., Sect. C: Struct. Chem.*, 2015, **71**, 3-8.

310. R. Rothbauer, F. Zigan and H. Odaniel, *Z. Krist.*, 1967, **125**, 317-337.